

MODELLING INTERCONNECTIONS IN c-SI SOLAR
PHOTOVOLTAIC MODULES FOR IMPROVED RELIABILITY
IN KUMASI IN SUB-SAHARAN AFRICA

KNUST

By

Frank Kwabena Afriyie Nyarko

BSc. Mechanical Engineering, KNUST

MSc. Engineering Design, Loughborough University, UK

The Brew-Hammond Energy Center

Department of Mechanical Engineering

College of Engineering

KNUST

Kumasi, Ghana.

A thesis submitted to the School of Graduate Studies of KNUST, Kumasi in partial fulfillment of the requirements for the award of the degree of Doctor of Philosophy (PhD) in Mechanical Engineering.

November 2019.

ACKNOWLEDGMENT

I wish to express my profound gratitude to my supervisor Professor Gabriel Takyi for his vision in proposing this research and guiding me through this study. His supervision has been extremely crucial in bringing this work to fruition. The contributions of my second and third supervisors; Dr. Anthony Agyei-Agyemang and Professor Francis Kofi Forson have immensely improved the quality of work reported in this thesis.

The technical support provided by Dr. Mani and Sai Tatapudi at Arizona State University Photovoltaic Reliability Laboratory is greatly appreciated. I wish to also acknowledge the invaluable support received from my research assistant Mr. Benjamin Asaga. His commitment and dedication are unparalleled. I am also grateful for the support received from Dr. Hyginus E. Amalu of Teesside University, UK.

This acknowledgment cannot be complete without mentioning the financial support received from the USAID for the PRESSA project Sub-Grant no. 2000004829 through the US National Academy of Sciences. The researcher also acknowledges the support received from the Norwegian Programme for Capacity Development in Higher Education and Research for Development within the Fields of Energy and Petroleum (EnPE) led by Professor Samuel Muyiwa Adaramola of NMBU, Norway.

DEDICATION

I wish to dedicate this work to my Father in heaven (Almighty God) for giving me the strength and spirit of perseverance to carry out this study successfully. To my beloved late mother - Comfort Adu Serwah; I say thank you for pouring out all you had in me. Finally, and most especially, to my adorable wife Mrs. Gloria Afriyie Nyarko and my children; Hillary, Melinda, and Ursula. Thank you for inspiring me to the finish line.



ABSTRACT

The use of climate-specific temperature-cycling profile is critical in precisely quantifying the degradation rate and accurately determining the service fatigue life of the crystalline silicon photovoltaic (c-Si PV) module operating in various climates. A reliable in-situ outdoor weathering database is pivotal in generating the required climate-specific temperature cycle profile. This study concerns the prediction of the reliability of both SnPb and Pb-free solder interconnects in a c-Si PV module from a sub-Saharan Africa outdoor weathering conditions. The test site for this study is located at the College of Engineering, KNUST Ghana (latitude 6° 40" N and longitude 1° 37" W at an elevation of 250 m above sea level). The research utilizes a three-year (2012 to 2014) high-resolution data to generate temperature cycles profiles that are representative of the test site climate. Subsequently, the generated temperature cycles were used in numerical investigations to examine the impact of these temperature cycle loads on the creep damage in the solder used as cell interconnecting material.

The study involved an initial determination of the accurate constitutive model of EVA (encapsulant) for thermo-mechanical analysis of the c-Si solar cell. Furthermore, the life (number of cycles to failure) of the interconnecting solders were predicted using Finite Element Analysis (FEA) software (Ansys 18.2). The Garafalo-Arrhenius creep model was used to study the creep behaviour of the interconnecting solders since creep is the main damaging mechanism in the solder. Finally, the effects of temperature dwells and ramps were investigated from the change in Accumulated Creep Energy Density (ACED) profiles at the respective load steps for temperature ramps and dwells. Analysis of the data on temperature variation and thermally induced stresses showed that the test site has a temperature profile with a ramp rate of 8.996 °C/hr, a hot dwell time of 228 minutes, and a cold dwell time of 369 minutes.

Maximum and minimum module temperatures of 58.9 °C and 23.7°C, respectively; in a cycle time of 86400 s (24 hrs) were recorded. Results from the numerical study showed that the linear viscoelastic material model (LVMM) of EVA generated the most consistent response to the thermo-mechanical analysis. Additionally, life cycle prediction results of soldered interconnections from ACED revealed that SnPb solder interconnections are likely to last longer (23.4 years) under the sub-Saharan African test region compared with Pb-free solder interconnects (13.69 years). Finally, a study on the effects of temperature dwells and ramps on creep damage of interconnections showed that the temperature ramps (heating and cooling load steps) accounted for approximately 80% of the creep damage in the soldered interconnections.

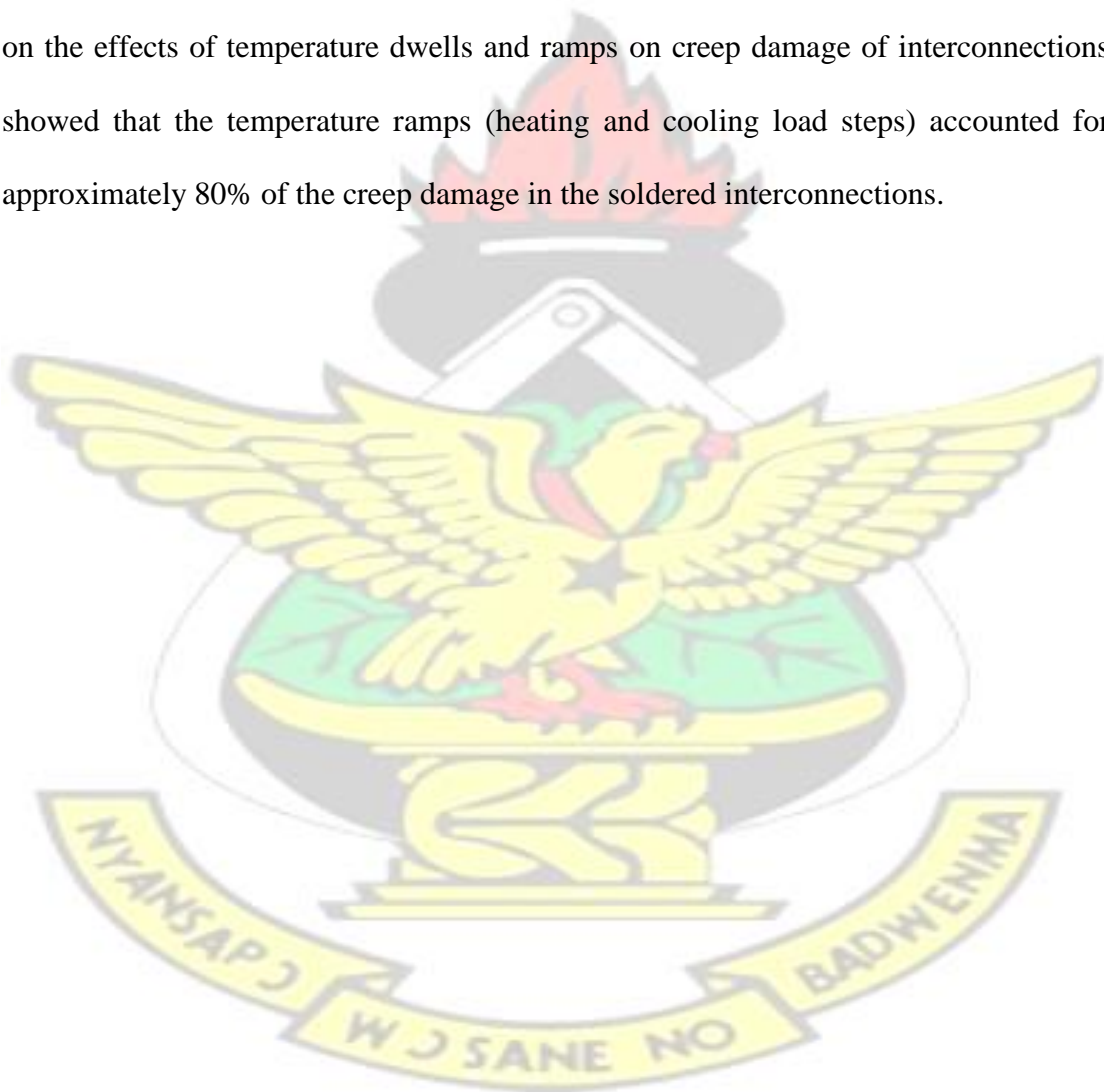


TABLE OF CONTENTS

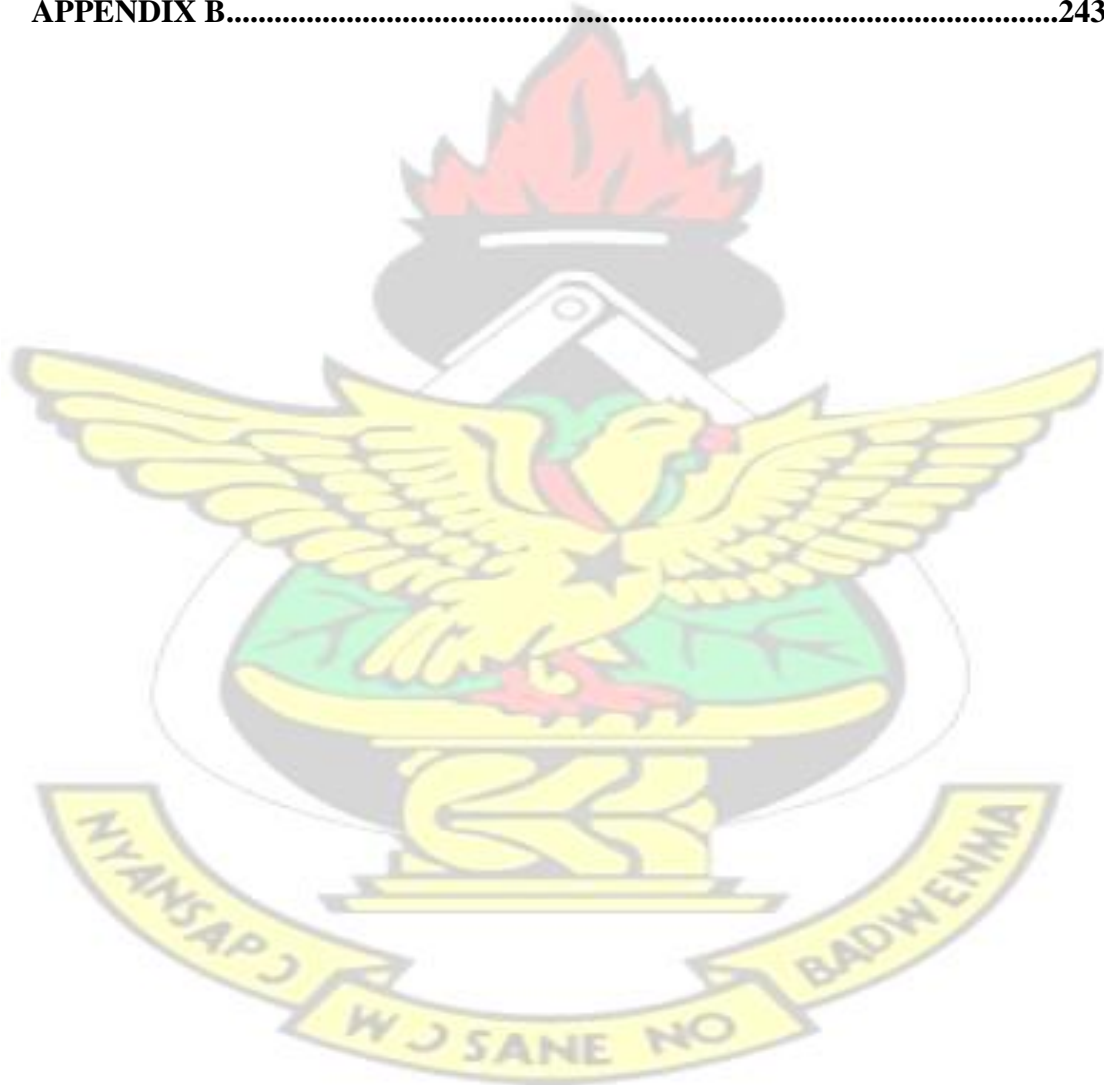
DECLARATION	ii
ACKNOWLEDGMENT	iii
DEDICATION	iv
ABSTRACT	v
TABLE OF CONTENTS	vii
LIST OF TABLES	xii
LIST OF FIGURES	xiii
NOMENCLATURE	xvii
CHAPTER ONE: INTRODUCTION	1
1.0 Introduction	1
1.1 Background.....	1
1.2 Motivation or Justification for the Study.....	3
1.3 Aim and Objectives of the Study:.....	4
1.4 Programme of Work for the Study	5
1.5 Significant findings.....	9
1.7 Publications from the Study	11
CHAPTER TWO: LITERATURE REVIEW	12
2.1 Introduction	12
2.2 Assembly and Manufacturing Processes	12
2.3 Solar Cell Efficiency	15
2.4 Interconnection Technology and Reliability	18
2.5 State-of-the-Art in c-Si PV Module Interconnection Technologies.....	20
2.5.1 Conventional Front-to-Back Cell Interconnection Technology	20
2.5.2 Back Contact (BC) Solar Cell Interconnection Technologies	23
2.5.2.1 Emitter Wrapped Through (EWT) Cell Interconnection	24
2.5.2.2 Metallization Wrap Through (MWT) Cell Interconnection.....	25
2.5.2.2 Back-Junction Back-Contact (BJ-BC) Interconnection	27
2.5.2.3 Alternate p-and n-type solar cell interconnection	28
2.5.2.4 Pin-Up Modules (PUM) interconnection	29
2.5.2.5 Silver solar cells	32
2.5.2.6 Spherical silicon solar cell interconnection.....	34
2.5.2.7 Solar Cells with Flexible Electrode Wire Grid (Day 4 Electrode)....	36
2.6 R&D Challenges and Interconnection Technologies Evaluation of c-Si PV Module for Tropical Climate Suitability	37
2.6.1 The Cell Interconnection Techniques	38
2.6.2 Interconnect Peel Strength	40

2.6.3 Average Fill Factor (FF)	41
2.6.4 Shading Losses.....	42
2.7 Effect of Tropical Climate on Interconnection Degradation Factors on Reliability of the c-Si PV Module.....	44
2.7.1 Corrosion of Soldered Joints and Electrical Contacts by Water Vapour Ingress into Encapsulant.....	44
2.7.2 Induced Thermo-Mechanical Stress on Soldered Joints Occasioned by Module Temperature cycling	47
2.7.3 Intermetallic Compound (IMC) Growth in Soldered Interconnections in PV Module Caused by Thermal Soaking and Aging	48
2.7.4 Presence of Micro-Cracks in PV Module Caused by Vibrations resulting from hail Storms and High Winds.....	50
2.8 Review of Solar PV Cell-Material Constitutive Models for Thermo-mechanical Reliability Prediction	51
2.8.1 Glass.....	52
2.8.2 EVA (Encapsulant)	53
2.8.2.1 Temperature-Dependent Linear Elasticity of EVA.....	54
2.8.2.2 Linear Elasticity of EVA.....	55
2.8.2.3 Linear Viscoelasticity of EVA	55
2.8.3 Silicon	59
2.8.4 Copper ribbons.....	61
2.8.5 Solder (SnAgCu, Sn/Pb).....	63
2.8.6 IMC's (Cu ₃ Sn, Cu ₆ Sn, Ag ₃ Sn).....	68
2.8.7 Aluminium Rear Contact	69
2.8.8 Silver (Ag) Busbars.....	70
2.8.9 Tedlar Backsheet.....	71
2.9 Review of Life Prediction Models for Thermal Cycling Analysis.....	72
2.10 Summary.....	78
CHAPTER THREE: METHODOLOGY	81
3.1 Introduction	81
3.2 Method for Data Analysis and generation of ATC temperature profiles	81
3.2.1 Description of Experimental Setup.....	81
3.2.2 Site Climatic Data and Thermal Analysis.....	84
3.2.3 Temperature Signal 'Rainflow' cycle Counting Algorithm	84
3.2.4 Estimation of Temperature Cycle Ramp rates and Dwell Times	87
3.3 Method for Geometric Modelling, Finite Element Analysis and Cell Material Modelling	89
3.3.1 Geometric modelling of solar cell.....	90
3.3.2 Mesh Generation.....	92

3.3.3 Solar Materials and Properties	94
3.3.3.1 Linear viscoelastic model of EVA	98
3.3.4 Thermal Loads and boundary conditions.....	100
3.3.5 Analysis Settings.....	100
3.3.6 Finite Element Analysis	102
3.3.7 Processing of Numerical Results	102
3.3.8 Post-processing	103
3.4 Summary.....	104
CHAPTER FOUR: GENERATION OF SPVM THERMAL CYCLES.....	105
4.1 Introduction	105
4.2 Methodology.....	109
4.3 Results and Discussions.....	110
4.3.1 Daily temperature cycle profile	110
4.3.2 Temperature Gradient of Thermal Cycle Profile	113
4.3.3 Results from Module Temperature ‘Rainflow’ Counting Analysis.....	114
4.3.4 Evaluating Heating and Cooling Rates of the PV Module	115
4.3.5 Results from Evaluation of Temperature Dwell Times of the PV Module.....	117
4.3.6 Generating in-situ Temperature Cycle (ATC) Profile using the Logged Data	119
4.3.7 Comparison of critical parameters of the generated ATC profile for test region with IEC 61215 Test qualification.	120
4.3.7.1 Ramp Rate	122
4.3.7.2 Dwell time	122
4.3.7.3 Temperature gradient and temperature cycle boundary conditions	123
4.4 Summary.....	124
CHAPTER FIVE: IMPACT OF CONSTITUTIVE BEHAVIOUR OF EVA ON SOLDERED INTERCONNECTIONS of SPVM.	125
5.1. Introduction	125
5.2. Methodology.....	128
5.3. Results and Discussion	130
5.3.1 Study on equivalent Von-Mises stress in EVA.....	130
5.3.2 Evaluation of maximum principal strains in EVA.....	134
5.3.3 Study on time-dependent equivalent creep strain in Solder joint.	137
5.3.4 Evaluation of Strain Energy and Strain Energy Density of Solder joint.	140
5.3.4.1 Evaluation of Strain Energy of Solder Joint.....	140
5.3.4.2 Evaluation of Strain Energy Density of a soldered joint.....	142

5.3.5 Study on interconnect deformation	143
5.4. Summary.....	146
CHAPTER SIX: LIFE PREDICTION OF Pb-FREE AND SnPb SOLDERED JOINTS	148
6.1 Introduction	148
6.2 Methodology.....	151
6.3 Results and Discussion	152
6.3.1 Study on Von-Mises Equivalent stress of solder joint.....	152
6.3.2 Study on equivalent creep strain of solder joint.....	156
6.3.3 Study on solder joint stress-strain hysteresis loops.....	161
6.3.4 Evaluation of Accumulated Creep Strain of Solder Interconnections ...	163
6.3.5 Evaluation of the solder joint accumulated creep energy density.....	168
6.3.6 Life Prediction of Soldered Joint in Cell Interconnection	173
6.4. Summary.....	177
CHAPTER SEVEN: EFFECTS OF TEMPERATURE RAMPS AND DWELLS ON DAMAGE OF SOLDERED INTERCONNECTIONS	179
7.1 Introduction	179
7.2 Methodology.....	182
7.3 Results and discussions	184
7.3.1 Evaluation of change in Accumulated Creep Energy Density (ACED) of solder joint.....	184
7.3.2 Study on Creep Damage distribution from Thermal cycles.....	185
7.3.2.1 Damage Distribution from TRA thermal cycle.....	185
7.3.2.2 Damage Distribution from 2012 thermal cycle.....	186
7.3.2.3 Damage distribution from 2013 thermal cycle.....	188
7.3.2.4 Damage distribution from 2014 thermal cycle.....	188
7.3.3 Study on Damage Accumulation profile at Temperature Load Steps ...	189
7.3.3.1 Damage profile at Cold dwell load step at the start of Thermal Cycle	189
7.3.3.2 Damage at Cold Dwell load step at the end of thermal cycles.....	192
7.3.3.3 Damage profile at maximum Temperature Dwell (Hot Dwell load step).....	193
7.3.3.4 Damage Profile at Heating (Ramp Up) load step.....	194
7.3.3.5 Damage Profile at Cooling Ramp Down load step	196
7.3.4 Generating Accumulated Creep Damage Functions for Soldered Joint Life Prediction	197
7.3.4.1 Damage Functions for Pb-free Soldered Interconnections	200
7.2.4.2 Damage Functions for PbSn Interconnections	201

7.3.4.3 Damage in Pb-free Interconnections	202
7.3.4.4 Damage in Pb-Sn Interconnections	203
7.4 Summary	205
CHAPTER 8- CONCLUSIONS AND RECOMMENDATIONS FOR FURTHER WORK	207
8.1 Conclusions	207
8.2 Recommendations for Further Work.....	209
REFERENCE	211
APPENDICES	229
APPENDIX A	229
APPENDIX B.....	243



LIST OF TABLES

Table 2-1: Comparison of interconnection techniques (Kontges et al., 2014)	41
Table 2-2: Comparison of cell interconnection technologies for c-Si solar cells in PV modules	43
Table 2 - 3: Material description for layers solar within a typical PV module.....	52
Table 2-4: Mechanical Properties of Glass	53
Table 2 - 5: WLF parameters for EVA (Eitner et al., 2010).....	57
Table 2 - 6: Viscoelastic Material Model for EVA with 26 Maxwell Arms	57
Table 2-7: Lists the Mechanical properties of silicon determined from a 3-point bending test.	61
Table 2-8: Mechanical Properties of Copper	62
Table 2-9: Bilinear model for the constitutive behaviour of copper ribbons	62
Table 2-10: Elastic Properties and Thermal Expansion Coefficient of Lead-free and Tin-Lead Solders (Cuddalorepatta, Dasgupta, et al., 2010).....	64
Table 2-11: Constitutive Equations for Predicting the Thermo-mechanical Response of Solders.	66
Table 2-12: Creep Parameters for Garofalo-Arrhenius model	68
Table 2-13: Mechanical Properties of Cu ₃ Sn and Ag ₃ Sn IMCs	69
Table 2-14: Mechanical Properties of Aluminium Rear Contact	70
Table 2 - 15: Mechanical Properties of Silver Busbar	71
Table 2-16: Elastic Properties of Isovoltal Icosolar 2442 from Tensile Testing with Mean Value and Largest Distance to Minimum or Maximum value	71
Table 2 - 17: Summary of selected solder joint fatigue models	74
Table 3-1: Technical Specification of PV Modules Installed at Test Site	84
Table 3-2: Geometric Properties of layer materials in solar PV module.....	91
Table 3-3: Mechanical Properties of Isotropic linear elastic cell materials.....	96
Table 3 - 4: Mechanical Properties of temperature dependent Young's modulus cell materials.....	97
Table 3-5: Mechanical Properties of Anisotropic cell material (Silicon)	98
Table 3-6: Linear viscoelastic properties of cell material (EVA).....	99
Table 3 - 7: Mechanical and Creep Properties of Pb-free and PbSn solders in solar cell.....	100
Table 4-1: Summary of recorded daily temperature for years 2012, 2013 and 2014	111
Table 4 - 2: Summary of observed heating and cooling rates and maximum ramp rates.....	117
Table 4-3: Summary of the parameters of the temperature cycle profiles.....	118
Table 4-4: Summary of ATC profile parameters for Test Region and IEC 61215....	121
Table 5 - 1: Solar Cell Material constitutive model.....	129
Table 5 - 2: Thermal load and boundary conditions	129
Table 6 - 1: Percentage change in Accumulated creep Strain	166
Table 6 - 2: Expected Life of solder interconnects from outdoor module temperature cycle profiles.....	176

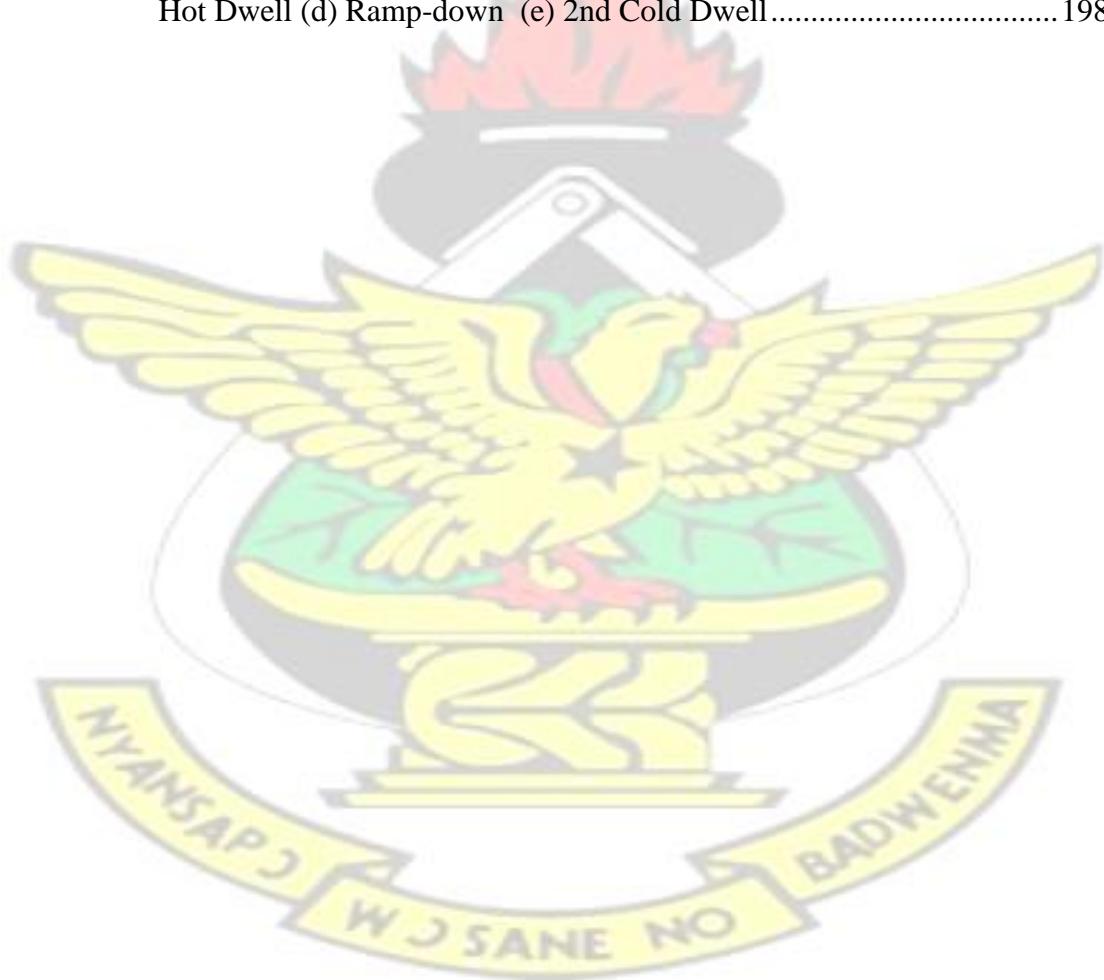
LIST OF FIGURES

Figure 1-1: Programme of Work for PhD Study	8
Figure 2-1: The Assembly Process Flow of c-Si PV Module.....	13
Figure 2-2: c-Si PV Module Lamination Process	15
Figure 2-3: Best Research Solar Cell Efficiencies Reported by NREL (© NREL 2015).....	16
Figure 2-4: Exploded view of a typical solar PV-module	17
Figure 2-5: Selective Laser Soldering of a 3-busbar Solar Cell (Jeong et al., 2012)...	19
Figure 2-6: Conventional Front-to-Back Cell Interconnection Technology.....	21
Figure 2-7: Schematic Drawing of a Cell for Shingled Cells Interconnection	23
Figure 2-8: Schematic Cross-Section of the EWT Solar Cell.....	25
Figure 2-9: MWT Cell Interconnection	26
Figure 2-10: Schematic n-type BJ-BC Silicon Solar Cell	28
Figure 2-11: (a) Conventional Module Interconnection: each cell backside is connected with the front side of the subsequent solar cell (b) Innovative Interconnection using Alternating p-type and n-type Solar Cells (Kopecek et al., 2006b).....	29
Figure 2-12: Schematic of Pin-UP Module Cell Interconnection.....	30
Figure 2 - 13: Interconnection for a PUM one Cell Laminate	31
Figure 2-14: Current Innovations in PUM Development (Franklin et al., 2006)	32
Figure 2-15: Schematic Drawing of Silver Cells	33
Figure 2 - 16: Schematic of Spherical Cell.....	35
Figure 2-17: SP100 Fabrication Process (Rubin and Schneider, 2007).....	36
Figure 2-18: Schematic of Day 4 Electrode.....	36
Figure 2-19: Ranking of possible interconnection techniques in terms of induced mechanical stress.....	40
Figure 2-20: shows a schematic I-V curve of an illuminated PV module	42
Figure 2 - 21: Microstructure of Silver Finger-Solder-Copper Ribbon Interface(Dutta, 2003).....	49
Figure 2 - 22: Layer structure of a typical PV module	52
Figure 2-23: Elastic modulus of EVA versus temperature, for different relaxation times (Paggi et al., 2011).....	54
Figure 2-25: Isothermal relaxation curves for EVA obtained by experiments (Eitner et al., 2011b).....	56
Figure 2 - 26: Mastercurve and Prony fit for shear modulus G of EVA.(Eitner et al., 2011b).....	56
Figure 2-27: Model of the Rear Face of a Silicon Solar Cell with Corresponding Microstructural Features (Popovich et al., 2013)	69
Figure 3-1: Outdoor Monitoring Set-up at College of Engineering KNUST, Kumasi, Ghana.....	83
Figure 3-2: Monitoring Station for Outdoor Test Set-up at College of Engineering KNUST, Kumasi, Ghana.....	83
Figure 3 - 3: Flowchart for rainflow counting	86

Figure 3 - 4: Typical temperature cycle	87
Figure 3 - 5: Flowchart for computing dwell times; (a) lower dwell (b) upper dwell ..	88
Figure 3-6: General finite element flow methodology	90
Figure 3 - 7: Geometric model flow chart	92
Figure 3 - 8: Mesh generation flow chart.....	93
Figure 3 - 9: Meshed geometry of cell-to-cell interconnection	93
Figure 3 - 10: Solar cell architecture for front-to-back cell interconnection	94
Figure 3 - 11: Engineering Data flow chart	95
Figure 3-12 Elastic Modulus of EVA versus temperature at 2-minute relaxation time.....	96
Figure 3 - 13: Post Processing flow chart	103
Figure 4-1: Conventional front-to-back cell interconnection technology in c-Si PV module	108
Figure 4-2: Distribution of recorded daily module temperatures for 2012, 2013 and 2014.....	111
Figure 4-3: Daily temperature profile (monthly average) observed for 2012 - 2014	112
Figure 4-4: Frequency distribution of daily module temperature (monthly average) gradients observed for 2012-2014 at the test site.....	113
Figure 4 - 5: Distribution of cycles counted for each year (2012-2014)	115
Figure 4 - 6: Cumulative frequency distribution of heating rates at test site.....	116
Figure 4 - 7: Cumulative frequency distribution of cooling rates from 2012 to 2014	116
Figure 4-8: Monthly average distribution of hot dwell times (2012-2014).....	117
Figure 4-9: Monthly average distribution of cold dwell times (2012-2014)	118
Figure 4-10: in-situ thermal cycle profiles fitted onto the real-time module temperature profile for 2012-2014.	120
Figure 4 - 11: Plots of a twelve-cycle profile of (a) the IEC 61215 Test Qualification and (b) the Test Region Average (TRA).....	121
Figure 5 - 1: Equivalent von-Mises stress distribution in EVA for (a) tin-lead solder and (b) lead-free solder interconnection for different EVA material constitutive models.....	131
Figure 5-2: Equivalent von-Mises Stress in EVA versus Thermal Cycles @ TRA ..	133
Figure 5-3: Maximum Principal Strains distribution in EVA material from a TRA Cycle.....	135
Figure 5-4: Maximum Principal Strain Cycles	136
Figure 5-5: Equivalent Creep Strain Distribution in Interconnecting Solder	138
Figure 5-6: Time Response of Equivalent Creep Strain in Interconnecting Solder ..	139
Figure 5-7: Strain Energy Distribution in solder for the different material models of EVA.....	141
Figure 5-8: Strain Energy Density profiles versus thermal cycles	142
Figure 5-9: Distribution of Total Deformation of Interconnection.....	144
Figure 5-10: Total deformation Profiles of Interconnections versus Thermal Cycles	145

Figure 6-1 Equivalent von-Mises Stress Distribution on PbSn-solder and Pb-free (Sn3.8Ag0.7Cu) solder for: (i) TRA and (ii) 2012 thermal cycles.	152
Figure 6-2 Equivalent von-Mises Stress Distribution on PbSn-solder and Pb-free (Sn3.8Ag0.7Cu) solder for: (iii) 2013 and (iv) 2014 thermal cycles.	153
Figure 6-3 Equivalent non-Mises stress response of SnPb-solder and Pb-free (Sn3.8Ag0.7Cu) solders for: (a) TRA, (b) 2012, (c) 2013 and (d) 2014 thermal cycles.	154
Figure 6-4 Equivalent Creep Strain distribution on PbSn-solder and Pb-free (Sn3.8Ag0.7Cu) Solder for: (i) TRA, (ii) 2012 thermal cycles	157
Figure 6-5 Equivalent Creep Strain distribution on PbSn-solder and Pb-free (Sn3.8Ag0.7Cu) Solder for: (iii) 2013 and (iv) 2014 Thermal cycles. ..	158
Figure 6-6 Equivalent Creep Strain Response of PbSn and Pb-free Solder interconnection versus Thermal cycles for: (a) TRA, (b) 2012, (c) 2013 and (d) 2014 thermal cycles	159
Figure 6-7 Superimposed Plots of Equivalent Creep Strain versus Thermal Cycles	160
Figure 6-8 Plot of hysteresis loop (a) SnPb-solder interconnection (b) Pb-free solder interconnections.....	162
Figure 6-9 Accumulated Creep Strain Damage Distribution in PbSn and Pb-free Solder Interconnection for: (i) TRA and (ii) 2012 Thermal Cycles.....	164
Figure 6 - 10 Accumulated Creep Strain damage distribution in PbSn and Pb-free solder interconnect for (i) 2013 and (ii) 2014 thermal cycles.	165
Figure 6-11 Accumulated creep Strain response for PbSn and Pb-free solder for: (a) TRA, (b) 2012, (c) 2013 and (d) 2014 thermal cycles	167
Figure 6 - 12 Accumulated Creep Energy Density Distribution at the end of 12 Thermal cycles for; (i) TRA and (ii) 2012 Thermal cycles.....	169
Figure 6 - 13 Accumulated Creep Energy Density Distribution at the end of 12 Thermal cycles for; (i) 2013 and (ii) 2014 thermal cycles.	170
Figure 6 - 14 Column distribution of Accumulated Creep Energy Density for 2012, 2013, 2014 and TRA thermal cycles.	171
Figure 6 - 15 Accumulated Creep Energy Density (ACED) response over the 12 thermal cycles for: (a) TRA, (b) 2012, (c) 2013 and (d) 2014 thermal cycles	172
Figure 6-16: Change in Accumulated Creep Energy Density vrs Thermal Cycles for; 2012, 2013, 2013, 2014 and TRA thermal cycles.	174
Figure 6 - 17 Expected Life of solder interconnection under 2012, 2013, 2014 and TRA thermal cycling.	176
Figure 7-1: Relationships between Thermal Cycle Parameters	179
Figure 7 - 2: Typical daily thermal cycle	183
Figure 7-3: Change in ACED over daily thermal cycles	184
Figure 7-4: Change in ACED distribution from TRA thermal cycle for (a) Pb-free (b) PbSn interconnections	186
Figure 7-5: Change in ACED distribution from TRA thermal cycle for: (a) Pb-free (b) PbSn interconnections	187

Figure 7-6: Change in ACED distribution from 2013 thermal cycle for: (a) Pb-free (b) PbSn interconnections	188
Figure 7-7: Change in ACED distribution from 2013 thermal cycle for: (a) Pb-free (b) PbSn interconnections	189
Figure 7-8: Damage Accumulation from cold dwell at start of thermal cycle (1st Cold dwell load step)	190
Figure 7-9: Damage Accumulation from cold dwell at end of thermal cycle (2nd Cold dwell load step)	192
Figure 7-10: Damage Accumulation from hot dwell load step.....	193
Figure 7-11: Damage Accumulation from Ramp-up load step.....	195
Figure 7-12: Damage Accumulation from Ramp-up load step.....	196
Figure 7 - 13: Change in ACED in Pb-free solder (a) 1St Cold Dwell (b) Ramp-up (c) Hot Dwell(d) Ramp-down (e) 2nd Cold Dwell.....	197
Figure 7 - 14: Change in ACED in PbSn Solder (a)1st cold Dwell (b) Ramp-up (c) Hot Dwell (d) Ramp-down (e) 2nd Cold Dwell.....	198



NOMENCLATURE

(a)	ABBREVIATION
SPV	Solar Photovoltaic
UV	Ultra Violet
MTTF	Mean Time to Failure
MTBF	Mean Time Before Failure
IMC	Intermetallic Compound
EVA	Ethylene Vinyl Acetate
STC	Standard Test Conditions
ATC	Accelerated Test Cycle
FEA	Finite Element Analysis
EL	Electroluminescence
NREL	National Renewable Energy Laboratories, USA.
ARC	Anti-Reflective Coating
JB	Junction Box
EWT	Emitter Wrap Through
MWT	Metallization Wrap Through
WLF	William-Landel-Ferry
BSF	Back Surface Field
ACED	Accumulated Creep Energy Density
BGA	Ball Grid Array
FC	Flip Chip
LMMM	Linear Viscoelastic Material Model
TRA	Test Region Average
LEMM	Linear Elastic Material Model
TDEMM	Temperature-Dependent Linear Elastic Material Model
HPC	High Productivity Computing
CSG	Constructive Solid Geometry
CAD	Computer-Aided Design
FEM	Finite Element Modelling
CTE	Coefficient of Thermal Expansion
R ²	Correlation Co-efficient

(c)

SYMBOLS

I_{oc}	Open Circuit Current
V_{oc}	Open Circuit Voltage
$A(T(t))$	WLF Shift Function
C_1, C_2	Calibration constants for WLF shift function
T_g	Glass Transition Temperature
ν	Poisson Ratio
G	Shear Relaxation Modulus
K	Bulk Relaxation Modulus
λ_i	Shear Relaxation time
G_i	Relative moduli
$\dot{\epsilon}_{cr}$	Creep Strain
s^*	Saturation Value of s
$\dot{\epsilon}_p$	Plastic strain rate
ϕ_i	Relative Modulus of i th Spring-damper in Maxwell's model
T_r	Reference temperature of WLF shift function (K)
T_{ref}	Stress-free Temperature or initial Temperature (K)
G_0	Instantaneous Shear Modulus
G_∞	Long-term Shear Modulus
C_1, C_2, C_3, C_4	Garafalo-Arrhenius Constants
α	Thermal expansion coefficient
$\Delta\epsilon/2$	Total Strain Amplitude
ρ	Density (kg/m^3)
σ_y	Yield Strength
$\dot{\gamma}$	Total Shear Strain
ϵ'_f	Fatigue Ductility Coefficient
c	Fatigue Ductility exponent
σ'_f	Fatigue strength coefficient
b	Fatigue strength (Basquin's) exponent
ϵ_{acc}	Accumulated creep strain
$\Delta\bar{W}_{total}$	Total strain energy
W_0, k	Fatigue coefficients
W_{acc}	Accumulated Creep Energy Density
ΔW_{acc}	Change in Accumulated Creep Energy Density
N_f	Fatigue Life (Number of Cycles to Failure)
L_{years}	Life of PV Module (years)
ΔW_{ave}	Average Change in Strain Energy Density
T_p	Moving Ref. Temperature Point
T_Y	The First and Second Temperature Points
T_X	The Second and Third Temperature Points
T_{peak}	Maximum cycle temperature
T_{valley}	Lowest cycle temperature
ΔT	Temperature gradient
C_{11}, C_{12}, C_{44}	Elastic constants for Silicon
$E_{\langle 100 \rangle}, E_{\langle 110 \rangle}, E_{\langle 111 \rangle}$	Young Modulus of Silicon at different Crystallographic Directions

X_{cs}	Cold dwell load step at the start of each thermal cycle (1 st cold dwell)
X_{ce}	Cold dwell load step at the end of each thermal cycle (2 nd cold dwell)
X_{ru}	Load steps from Temperature ramp-ups
X_{rd}	Load steps from Temperature ramp-downs
X_{hd}	Load steps from Hot Dwell
$(\Delta W_{acc})_{cs}$	Change in ACED from 1 st Cold Dwell
$(\Delta W_{acc})_{ce}$	Change in ACED from 2 nd cold Dwell
$(\Delta W_{acc})_{ru}$	Change in ACED from Temperature Ramp-ups
$(\Delta W_{acc})_{rd}$	Change in ACED from Temperature Ramp-downs
$(\Delta W_{acc})_{hd}$	Change in ACED from Hot Dwells
L_s	Number of Thermal load steps



CHAPTER ONE: INTRODUCTION

1.0 Introduction

This chapter discusses the background and justification of the study. Additionally, it sets out the aims and objectives of the research. Furthermore, the chapter presents the programme of work for the study and an overview of the structure of this report.

1.1 Background

The warranty period of Solar Photovoltaic (SPV) modules has increased rapidly and significantly in recent years. The industry aims to develop an SPV system that can attain a thirty-year field service life by the year 2020 (Hulstrom, 2005, Quintana et al., 2002). This effectively translates to the power degradation rate of between 0.5% and 1.0% per year (maximum) of the PV module. However, the current reported annual power degradation rate is between 0.5% and 10% (Rosenthal et al., 1993, Sørensen and Watt, 2006). Several factors account for the degradation of installed SPV modules. Key amongst these factors is the exposure of the solar PV modules to a range of cyclic temperatures coupled with elevated temperature during their operations. The cyclic thermal loading induces thermo-mechanical damage in the soldered joint in the SPV module interconnections. Operations under a range of currents and voltages play a significant role in accumulating power degradation in the SPV modules. The band-gap of ultraviolet (UV) light incident on the SPV cells impacts on the degradation rate. A huge variation in weather conditions also significantly increases the degradation rate.

The cumulative contributions of these factors on the degradation of SPV modules operating in a tropical climate are critical. (Macben, 2015) demonstrated that the degradation and failure mechanisms of SPV modules are location dependent. Other factors associated with packaging material, interconnection, soldered joint, adhesion;

CHAPTER ONE: INTRODUCTION

delamination, moisture accumulation, and semiconductor device thermal challenges degrade the module performance and reduce its power output, which increases the SPV module reliability concerns. SPV modules installed in hot-humid climates such as the sub-Saharan ambient experience a significant increase in moisture accumulation. Moisture penetration of SPV modules account for several degradation mechanisms such as: weakening of the adhesive bonds within laminated surface leading to delamination and loss of passivation (Morita et al., 2003), corrosion of cell from the Silicon Nitride (Si-N_x) Anti-Reflective Coating (ARC), or the corrosion of metallic materials such as solder bonds and Silver fingers. All these degradation mechanisms lead to significant loss of SPV module performance. At present, there are no standard methods to determine long-term SPV module performance on the field. The industry-standard certification tests (IEC 61215, UL 1703) are presently used in determining the 'infant mortality' rate of SPV modules. The IEC 61215 (IEC61215, 1993) thermal cycling test standard requires modules to be subjected to 200 cycles from $-40\text{ }^\circ\text{C}$ to $85\text{ }^\circ\text{C}$. Modules recording at least 5% relative power degradation are deemed to have failed the test. Understanding degradation mechanisms in SPV modules is, therefore, a crucial step in attempting to mitigate their effect.

Field modules installed in sub-Saharan ambient experience temperature swings of about $35.6\text{ }^\circ\text{C}$ (average) each day. The outdoor weathering effects expose PV modules to direct sunlight in an alternating day/night cycles which exposes modules to thermal load due to the variation in the coefficient of thermal expansion of constituent materials forming the individual cells in the module (Park et al., 2014). The daily temperature swings induce fatigue-related failure mechanism occasioned by a mismatch of the respective temperature coefficients of thermal expansion of silicon, glass, copper, and solder bonded together. One effect of soldered joint degradation is the formation of

CHAPTER ONE: INTRODUCTION

micro-cracks across the entire joint area. This could result in an increase in electrical resistance across the soldered joint. This phenomenon affects SPV module output power significantly.

1.2 Motivation or Justification for the Study

The growth of the PV industry largely depends on the ability to accurately predict power delivery over the course of time. The two key cost drivers are the efficiency with which sunlight is converted into power and the change in the efficiency of the PV module over time. Accurate quantification of power decline over time, also known as degradation rate is essential to all stakeholders (utility companies, investors, and researchers). Financially, the degradation of a PV module or system is equally important. As explained by (Hulstrom, 2005), a higher degradation rate translates directly into less power produced and therefore reduced future cash flows. Inaccuracies in determining degradation rates lead directly to increased financial risk (Quintana et al., 2002).

The failure of soldered joints in solar PV modules and other electronic devices has been demonstrated to increase at elevated temperatures (Amalu and Ekere, 2012b). This makes it imperative to understand the behaviour of soldered joints at high temperatures in order to accurately predict soldered bond reliability and solar PV module reliability as a whole. Accurate prediction of Mean Time to Failure (MTTF) or Mean Time Before Failure (MTBF) of a PV module is critical as it offers the opportunity for module maintenance or replacement in good time. The integrity of solar PV cell-to-cell interconnections can greatly be improved if the static structural parameters of the joints are optimized within the assembly.

Most computer modelling studies involving the use of solder geometric models of soldered joints often fail to account for the intermetallic (IMC) layers formed between

CHAPTER ONE: INTRODUCTION

the solder and the copper ribbon interface on one side and the solder and silver fingers on the other side. In addition, the use of a fewer number of thermal cycles (up to six thermal cycles) has been a common practice in predicting the thermo-mechanical reliability of soldered joints in microelectronic devices.

The use of a fewer number of cycles and the exclusion of IMC layers in modelling studies often yield inaccurate data in simulation output. This practice could, therefore, lead to a poor interpretation of the effects and inexact prediction of damage and the life of the soldered joint in the interconnect. (Amalu and Ekere, 2012b), observed that the non-inclusion of IMC in models used to predict the number of cycles for fatigue failure (N_f) of soldered joints is one of the causes of discrepancy between the value of assembled component solder joints fatigue life obtained by experiments and the estimated value from modelling studies.

An in-depth understanding of the thermo-mechanical behaviour of cell-to-cell interconnects in SPV modules is key in improving the operational reliability of the module. SPV installations in the sub-Saharan Africa region are expected to be around 1156 MW by 2020 (REN21, 2014). This is expected to generate an estimated 1823 GWh of electricity. With the flood of PV modules into the sub-region, renewable energy has been regarded as the solution to the region's energy problem. For this reason and others discussed, more reliable information on the effect of interconnection degradation due to thermal cycling on the reliability and durability of the modules has to be obtained for the sub-Saharan region.

1.3 Aim and Objectives of the Study:

The aim of this research work is to study soldered interconnections in c-Si photovoltaic modules in sub-Saharan Africa for improved thermo-mechanical reliability.

CHAPTER ONE: INTRODUCTION

The Objectives of the study are to:

- i. generate temperature cycle profile from an in-situ climatic condition for accurate prediction of thermomechanical degradation of c-Si photovoltaic module in Kumasi in sub-Saharan Africa.
- ii. evaluate the impact of encapsulant (EVA) constitutive behaviour on interconnect damage in c-Si Solar PV Modules installed in Kumasi in sub-Saharan Africa.
- iii. evaluate the effect of the operating module temperature cycle (test region thermal cycle) on creep damage and fatigue life of interconnection in photovoltaic modules.
- iv. evaluate the effects of temperature ramp rates and dwell times on degradation of interconnections on SPV modules operating in Kumasi in sub-Saharan Africa.

1.4 Programme of Work for the Study

The study began with an extensive review of relevant and related previously published works. The main focus of the literature review was to identify the gaps in knowledge in the thermo-mechanical reliability of cell interconnections in photovoltaic modules subjected to accelerated temperature cycles. Four gaps in knowledge in the sub-Saharan ambient were identified namely;

- i. the discrepancies in temperature cycle profiles (ramp rates, dwell times, maximum and minimum module temperatures) between standard test conditions (STC) and operating temperatures of PV modules operating in sub-Saharan tropical ambient are yet to be investigated.

CHAPTER ONE: INTRODUCTION

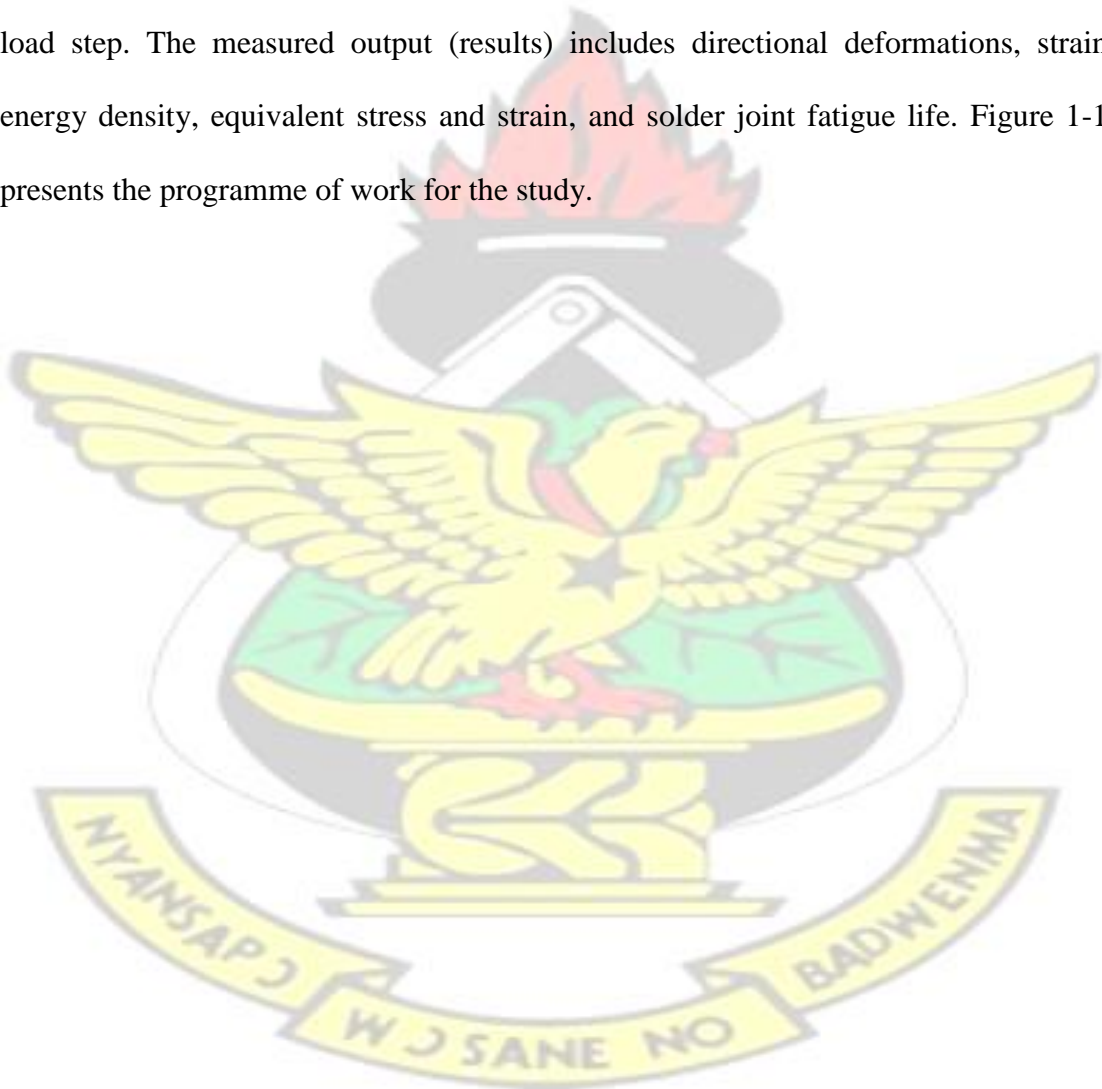
- ii. the discrepancies in creep damage between standard test conditions (STC) and operating temperatures of SnPb and Pb-free solder interconnections in PV modules operating in the sub-Saharan African region are yet to be investigated.
- iii. the effect of actual operating temperatures on fatigue life of SnPb and Pb-free solder interconnections in PV modules installed in sub-Saharan African climatic conditions are yet to be studied.
- iv. the effects of temperature ramp rates on the degradation of SnPb and Pb-free solder interconnections on SPV modules operating in Sub-Saharan African regions are yet to be investigated.

The four gaps identified, form an integral part of the studies carried out in this study. Data analysis and experimental models were designed to investigate these concerns. The study focused on quantitative damage evaluation on the joints while taking into consideration the presence of intermetallic compound (IMC) layers within the bulk solder. It will also present a realistic strain range in PV Cell assemblies subjected to strain load. The accumulated damage and fatigue life of the joints of the various interconnections were determined.

The study employed field module temperature data logged at five-minute intervals for three years (2012-2014). The test site is a sub-Saharan ambient (College of Engineering, KNUST, Kumasi, Ghana, on latitude $6^{\circ} 40''$ N and longitude $1^{\circ} 37''$ W, and elevation of 250 m above sea level). Geometric models of solar cells were developed using constructive solid geometry and boundary representation techniques. The temperature data were analysed to evaluate the accelerated test cycle (ATC) parameters such as the ramp rates, dwell times, temperature gradients and maximum and minimum temperatures. The ATC profiles generated were used as thermal conditions in the finite element analysis (FEA) of the solar cell geometric model. The

CHAPTER ONE: INTRODUCTION

solid models of the solar cell were developed and exported into ANSYS finite element modelling software to perform a static structural analysis on them. The modelling procedure involved importing the solar cell geometry from a CAD system into Ansys, adding engineering data which is made up of SPV cell material properties, the non-linear meshing of geometry to respond to material non-linearities, as well as applying thermal loading and boundary conditions. Finally, appropriate analysis settings were selected and simulation was successfully run to achieve convergence for every thermal load step. The measured output (results) includes directional deformations, strain energy density, equivalent stress and strain, and solder joint fatigue life. Figure 1-1 presents the programme of work for the study.



CHAPTER ONE: INTRODUCTION

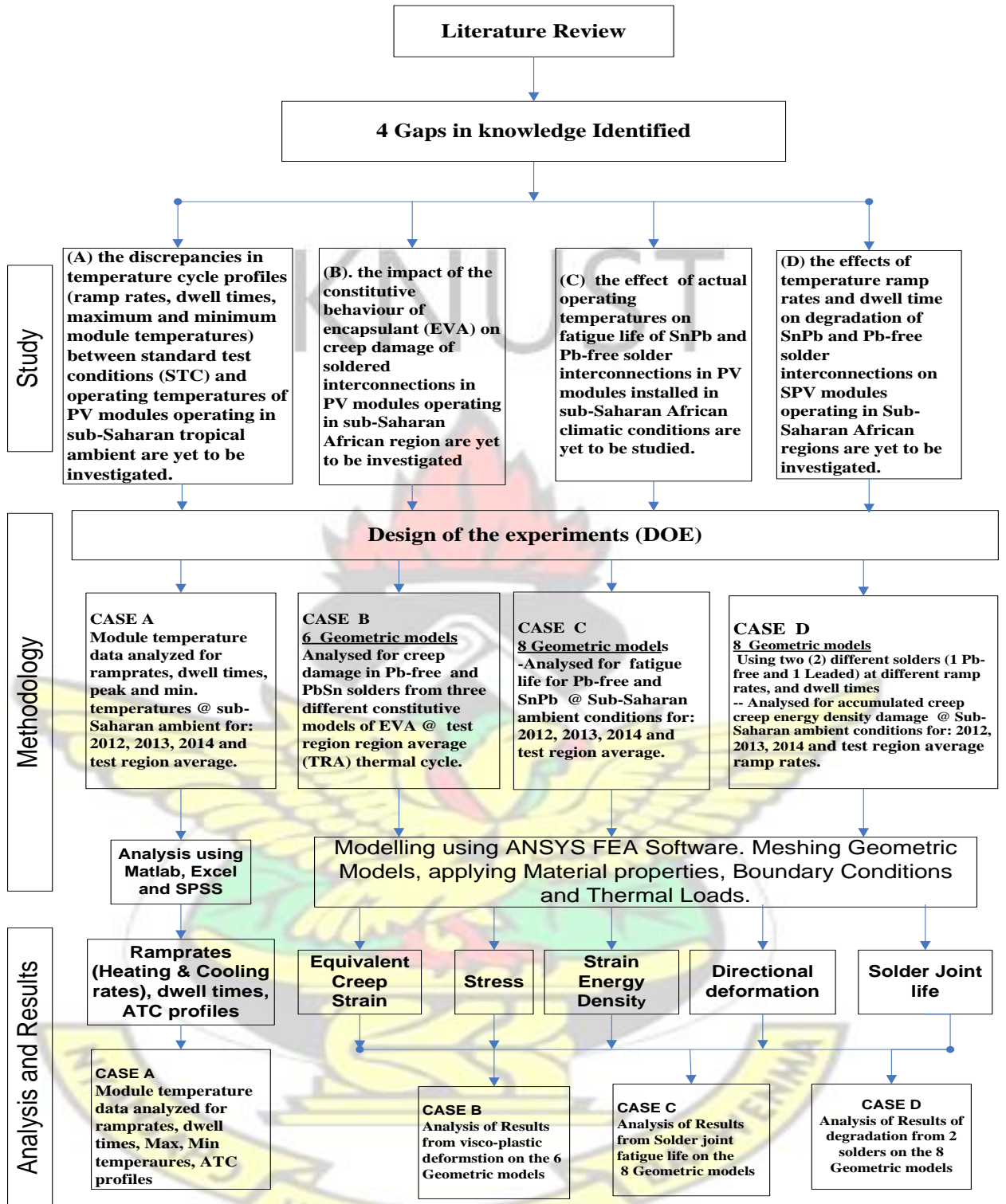


Figure 1-1: Programme of Work for PhD Study

CHAPTER ONE: INTRODUCTION

1.5 Significant findings

The following represent some significant findings from the study:

- i. The generated TRA cycle has magnitudes of the critical parameters of ramp rate, hot and cold dwell times, maximum and minimum temperatures of 8.996 °C/hr, 228 minutes (hot dwell), 369 minutes (cold dwell), 58.9 °C and 23.7 °C, respectively.
- ii. The percentage differences between the values of TRA parameters and the values of corresponding parameters of the IEC 61215 standards for terrestrial PV modules qualification are -91%, 2180%, 3590%, -30.7%, -159.3%, -71.8%, respectively. Furthermore, the percentage difference of the generated cycle time from the IEC61215 cycle time is about 747 % (86400 s versus 10200 s). This shows that field conditions are totally different from IEC 61215 test conditions.
- iii. Using LVMM in the study of the EVA material, the lowest change in equivalent Von-Mises stress of 0.55% was registered in the EVA when the interconnecting solder was changed from SnPb to Pb-free.
- iv. It was observed, that the maximum equivalent Von-Mises stress occurred at a less critical region (cell-gap region) for EVA as LVMM compared with the LEMM and the TDEMM. In addition, the total interconnect deformation remained the lowest using LVMM as the constitutive behaviour of EVA.
- v. At the test site, the Pb-free and SnPb solder interconnections are expected to achieve an average of 7944 cycles (13.69 years) and 12814 cycles (23.4 years), respectively. The solder interconnects will achieve the maximum life (cycles/years) under the 2014 thermal cycle loading. The SnPb solder interconnection is expected to achieve 14,153 cycles (25.85 years) whilst the

CHAPTER ONE: INTRODUCTION

Pb-free soldered interconnection is expected to achieve 9249 cycles (16.89 years).

- vi. The results show that the ramp-down (cooling) load steps generated the highest damage in the soldered interconnections. The ramp-up load steps closely followed this. Overall, the ramp-up and ramp-down load steps accounted for average values of 78% and 88% of the total damage per cycle in the interconnections. It was observed further that, the 1st cold dwell load steps generated the lowest change in ACED in the interconnections.
- vii. A study of the damage profiles from the five different load steps in each thermal cycle showed that the first two thermal cycles can be predicted using logarithmic functions and the remaining ten thermal cycles predicted using sixth-order polynomial functions. The damage functions developed are expected to accurately predict the accumulated creep energy density damage (W_{acc}) for a given number of load steps. This will reduce considerably the computational time required for a higher number of thermal cycles

1.6 Thesis Overview

Chapter One presents an overview of the research work presented in this thesis. This chapter is presented under seven subsections including the background to objectives through to motivation and outline of the thesis. The chapter also outlines significant findings and contributions to the study. Subsequently, Chapter Two presents a literature review covering manufacturing, efficiency, interconnection technology and reliability, and thermo-mechanics of solar PV modules. Presented in Chapter Three are the methodology involving solar PV module temperature analysis, solar cell geometry and material modelling, and finite element analysis. Chapter Four discusses the results from the generation of temperature cycles from in-situ climatic conditions. In Chapter Five,

CHAPTER ONE: INTRODUCTION

the effect of the constitutive behaviour of EVA on solder joint degradation is examined. The life of solder joints under the real outdoor temperature cycle is predicted in Chapter Six. Furthermore, the effects of temperature ramp rates and dwell times to solder joint life are presented in Chapter Seven. Finally, the conclusions and recommendations for future work from this study are presented in Chapter Eight.

1.7 Publications from the Study

The output from this study is expected to generate 5 manuscripts for publication namely;

- i. Robust crystalline silicon photovoltaic module (c-Si PVM) for the tropical climate: future facing the technology (*Manuscript under review*)
- ii. Nyarko, F. K. A., Takyi, G., Amalu, E. H., & Adaramola, M. S. (2018). Generating temperature cycle profile from an in-situ climatic condition for accurate prediction of thermo-mechanical degradation of c-Si photovoltaic module. *Engineering Science and Technology, an International Journal*. doi:<https://doi.org/10.1016/j.jestch.2018.12.007>
- iii. Impact of EVA constitutive behaviour on soldered joint reliability in c-Si solar cells (*Manuscript ready for publication*)
- iv. Life prediction of soldered joints in c-Si solar PV modules under field thermal cycling (*Manuscript ready for publication*)
- v. Effects of temperature ramp rates and dwell times on creep damage and fatigue life of c-Si solar cell interconnection. (*Manuscript ready for publication*)

CHAPTER TWO: LITERATURE REVIEW

2.1 Introduction

The efficient design of a robust c-Si PV module for the tropics demands that effective manufacturing techniques and processes be adopted. It is also imperative that factors affecting solar cell efficiency and power output be designed for. The integrity of solder interconnection in c-Si PVM impacts both the Power Conversion Efficiency (PCE) and Power Output (PO). Therefore, knowledge of the operations of silicon solar cells and the thermo-mechanical response of the interconnection are vital in its effective design. Additionally, accurate modelling of the respective constitutive behaviour of the constituent materials in the SPV cell assembly is necessary for a reliable reliability assessment of SPV module interconnection.

This chapter presents and discusses the manufacturing processes, efficiency, interconnection technology and reliability of solar PV modules. It also presents a brief review of the basic thermo-mechanical principles of SPV laminates and reviews the various material constitutive models and life prediction models used in investigating the thermo-mechanical response of the SPV module.

2.2 Assembly and Manufacturing Processes

Sorted cells of defined efficiency band are stacked to minimise mismatch issues. The cells are usually of the same colour class. A quality check is performed to identify front and back visual defects. Cells are interconnected in a stringing and tabbing process per power requirement. The stringed cells are checked to ensure there is no cell breakage or chipping. A further check is conducted to ensure that cell to cell gap and the pull strength (> 2 Newton) of ribbons on front and back bus bars are implemented. Figure 2-1 shows an illustration of an assembly process of c-Si PV module. A back sheet of

CHAPTER TWO: LITERATURE REVIEW

appropriate dimension with no contamination on either side is cut as well as the front and back EVA. The strings are connected using string connectors and fixed EVA tapes.



Figure 2-1: The Assembly Process Flow of c-Si PV Module

The correct position of the EVA fixing tape and the right placement and directions of strings are ensured. Generally, the layup sequence involved; Glass-Front EVA – connected strings – Back EVA– Back Sheet. Dark IV curves are taken to correct faults at interconnections before lamination. An Electroluminescence (EL) of the cell strings is also verified in the process. Defects associated with this assembly process include

CHAPTER TWO: LITERATURE REVIEW

black cell, dry solder, broken cell, shorted string, and wrong interconnection. The lamination process is the main crystallizing step in the PV-module assembly. Lamination protects the SPV module from the harsh environmental conditions that it is expected to endure throughout the module's 25-year design service life. Thus, a reliable module lamination is critical in ensuring that cells attain their designed life. The lamination process is preceded by a gel test. This is performed to determine the insoluble fraction of cured EVA. The gel test is expected to yield 75% of cross-linked material. A peel test with over 40 N magnitude force between Glass to EVA and EVA to Backsheet is conducted. Poor lamination could lead to delamination of EVA from edges or inside the module. Delamination leads to corrosion of the cells during exposure to the environment. Poor lamination traps air bubbles inside the module. The occurrence leads to cell corrosion. Poor gel content ($< 75\%$ of cross-linked material) leads to gradual seepage of moisture into the module which culminates in cell corrosion. The lamination process consists of three main steps. These are shown in Figure 2-2. After lamination, excess EVA and back sheet protruding from the glass are trimmed before the module is framed. Framing process involves pressing silicone-filled short and long frames with all sides of the laminated edges such that the laminate is uniformly covered. The junction box is then fixed and the module is ready for electrical safety testing.

Modules are tested for safety before it becomes market-ready. The tests include insulation, high pot (test for high voltage insulation), wet leakage and ground continuity. A flash test is performed to check the current-voltage (I-V) characteristics of the module. Final quality assurance of the Electroluminescence (EL) test, for identification of any defects (cracks in the cells), is performed to certify the module for packaging and dispatch.

CHAPTER TWO: LITERATURE REVIEW

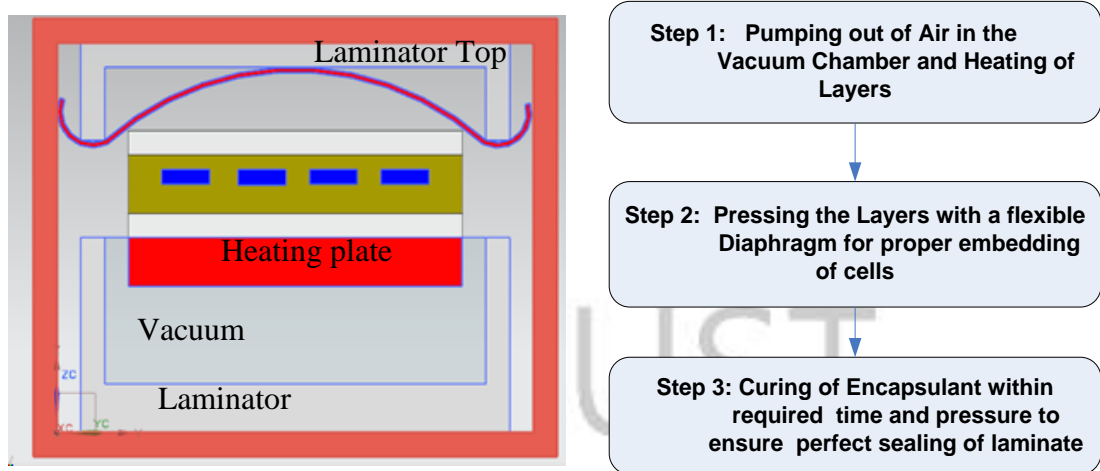


Figure 2-2: c-Si PV Module Lamination Process

2.3 Solar Cell Efficiency

C-Si PV module manufacturing spans over half a century – representing its biggest share of manufacturing. It accounted for a manufacturing share of approximately 90% of solar cells produced in 2008 (S. Kluska, 2008, Saga, 2010). Silicon material is abundant in nature and represents over 26% of the Earth's crustal material with a very negligible environmental impact (Saga, 2010). Silicon solar cells remain dominant in the PV industry. The reported cell efficiencies presented in Figure 2-3 shows that c-Si cells provide high-energy conversion efficiencies compared to other commercial solar cells and modules. Its efficiency is about 27.6%. A significant increase in the installation of solar PV in the tropical ambient is projected by the year 2020. The c-Si PV cell is the most feasible alternative for meeting this requirement because it is the most appropriate for large-scale production (REN21, 2014).

CHAPTER TWO: LITERATURE REVIEW

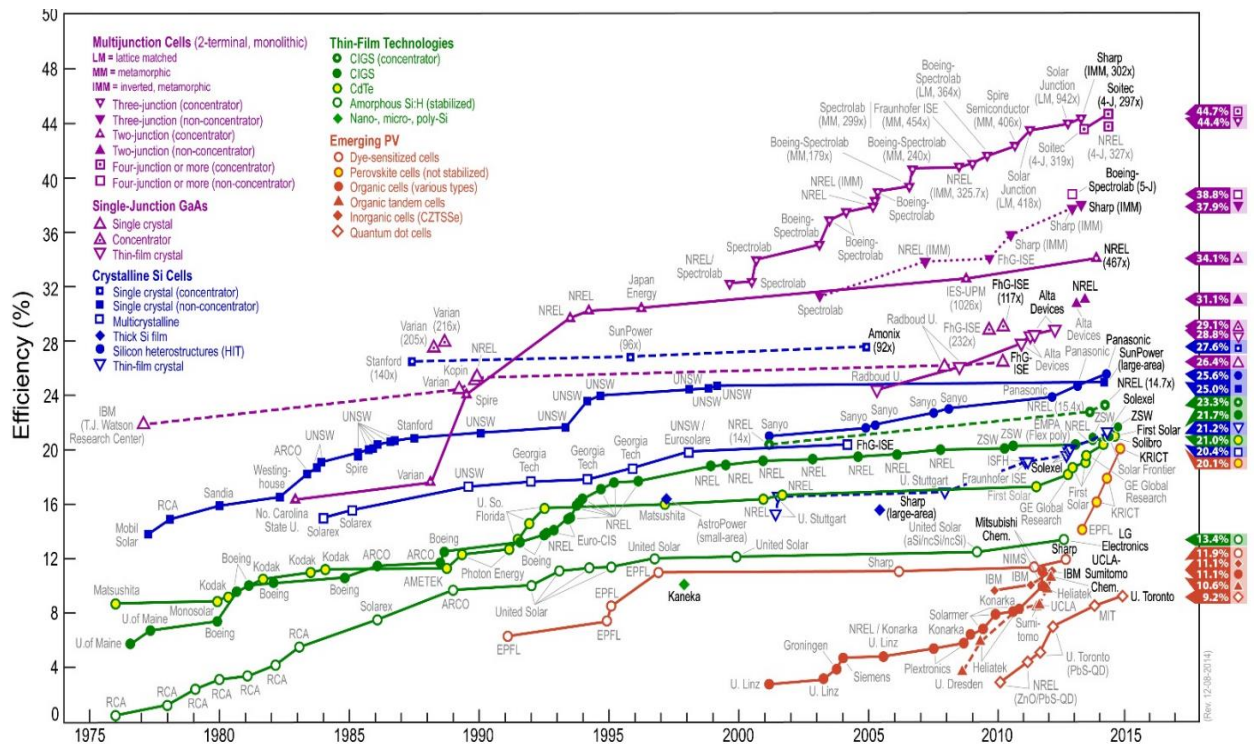


Figure 2-3: Best Research Solar Cell Efficiencies Reported by NREL (© NREL 2015)

In general, solar cells are manufactured from thin wafer discs with a thickness of about 200 μm (Klengel et al., 2011). The various manufacturing steps involved in the production of silicon cells include etching, coating, screen printing, and firing. Conventional solar cells have a metallization grid on the front side, which collects the light-generated charge. This grid is connected to busbars. Current is transferred through the PV-module from one cell to another by means of flat copper ribbons soldered to the busbars. The copper ribbons provide a conduit for current transfer from one cell to a neighbouring cell in a series interconnection referred to as strings. A typical solar PV-module is made up of a transparent cover glass with anti-reflective coating (ARC), an encapsulant made from ethylene-vinyl acetate (EVA), a rear support layer of Tedlar material, a frame and a Junction Box with connecting cables as schematically represented in Figure 2-4. The module provides mechanical support to the crystalline silicon solar cell as well as protection to the electrical interconnections from harsh

CHAPTER TWO: LITERATURE REVIEW

environmental conditions. The PV-module is hermetically sealed to prevent water or water vapour from corroding the electrical contacts.

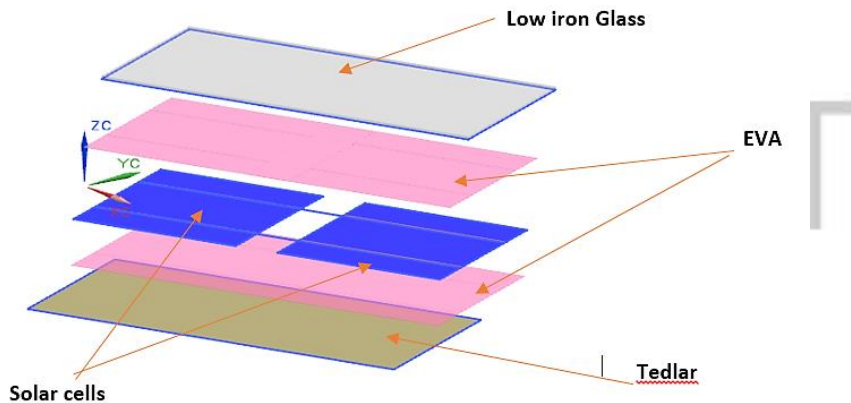


Figure 2-4: Exploded view of a typical solar PV-module

Various components of the solar PV module play important and unique roles during the module manufacturing as well as operation in the field. A solar cell should possess good solderable pads with no printing defects or micro-cracks. The EVA encapsulant must be optically transparent (360 nm minimum) with low thermal resistance. It must also offer a firm adhesion between solar cells. The Tedlar back sheet should exhibit high thermal resistance and low moisture permeability. The glass cover (with ARC) must not trap air bubbles or have chipping at the edges. The Junction Box (JB) houses the by-pass diodes and connecting cables. A typical JB can take any of the following configurations (IP X(Y));

- IP 65- total protection against dust ingress, low-pressure water jets from any direction permitting a limited ingress of water.
- IP 67- total protection against dust ingress, short periods of water exposure.

A 1.6 mm x 0.23 mm ribbon and a 5 mm x 0.22 mm string bus connector are the two main types of interconnecting ribbons used in assembling solar cells. A connecting

CHAPTER TWO: LITERATURE REVIEW

ribbon has a copper core with solder coating on the top and bottom sides. A typical PV solder coating thickness is approximately (25 ± 10) μm . The backbone of the module structure consists of short and long anodized Aluminum frames. The frames have perforations (holes). Each perforation has specific functionality. There are installation holes used for fixing modules for various structures. It contains drain holes used to drain water from rain and melting snow. There are also ground symbols with holes, which are for grounding the module. It has holes in the hollow part of the frame, which primarily provide ventilation to keep the module at a uniform temperature.

2.4 Interconnection Technology and Reliability

The performance of a PV module is highly affected by the interconnection technology used to connect the cells. In response to the miniaturization-manufacturing trend, coupled with the drive for a cheaper PV module, there has been a steady reduction in the thickness of silicon wafers in the solar PV module. Recently, a wafer thickness of below 200 microns is being used in the manufacture of solar cells (Klengel et al., 2011). The reduction is expected to continue to a projected value below 100 μm by 2020 (Wendt et al., 2009). (Gabor et al., 2006) have argued that thinner cells may lead to cost reduction and increased module performance. However, the reliability of such fragile cells remains a major concern. Currently, the cell interconnection technique commonly used in the industry involves IR (infrared) soldering of copper ribbons to form strings of interconnection between separate cells. This procedure usually leads to the formation of micro-cracks on the wafer (especially for long strings of thin cells). This is a challenging reliability concern for PV modules. The IR soldering technique, which produces a continuous line of solder, induces high mechanical stress in the soldered joint resulting in accelerated fatigue damage in the soldered joint. A selective laser soldering technique where a number of single solder spots (7-8 spots evenly distributed

CHAPTER TWO: LITERATURE REVIEW

on each busbar (Figure 2-5)) are applied on the copper ribbons mitigates the situation. Selective laser soldering has been reported to induce minimal mechanical damage to the soldered joint, with the potential to improve production yield (Guo and Cotter, 2004).

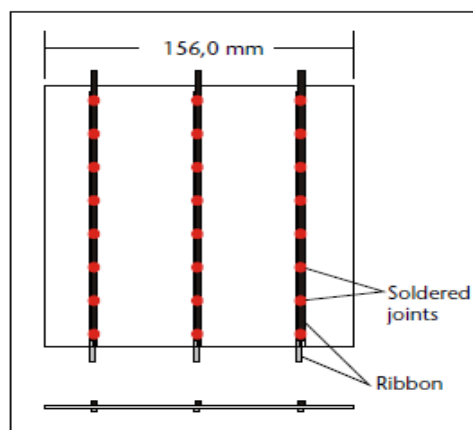


Figure 2-5: Selective Laser Soldering of a 3-busbar Solar Cell (Jeong et al., 2012)

Simultaneous stringing and tabbing process where soldering is done on the front and back metallization of the cell results in a single thermal cycle. The resulting balancing effect of the front and back surfaces reduces the bow experienced by the wafer. Reducing shadowing losses by reducing the width of the copper ribbons remains a research concern. With reduced wafer thickness, wafer breakage during stringing and tabbing process is also expected to rise. Usually, a reliable soldered joint is achieved with good solder wettability of the surface. Good substrate wettability ensures good adhesion to the soldered component (Schneller et al., 2016). For solar cells, the soldered components consist of two metals; Silver (Ag) from the cell busbar and Copper (Cu) from interconnection. Theoretically, solder joint failure is registered in three main locations. These are at the copper interconnect/solder; at the silver busbar/solder and within the solder itself. It is reported that the dominant failure sites are the Ag/solder interface as well as within the solder itself (Jeong et al., 2012, Cuddalorepatta et al.,

CHAPTER TWO: LITERATURE REVIEW

2006). The main cause of failure at these sites is the mismatch of the coefficient of thermal expansion (CTE) of the bonded materials. The influence of interconnection technology on the performance and long-term power degradation is very critical in the PV module design. Interconnections are expected to be designed to minimize global CTE mismatch induced stress on the solder joint while keeping electrical resistance at the minimum (Schneller et al., 2016). The next section discusses various cell interconnection technologies currently used in the manufacture of SPV modules.

2.5 State-of-the-Art in c-Si PV Module Interconnection Technologies

Several interconnection technologies are employed in the design and manufacture of c-Si PV modules. In this section, two key technologies (conventional front-to-back cell and back-contact solar cell interconnections) are presented and discussed. The section presents further information on the configurations of back-contact solar cell design.

2.5.1 Conventional Front-to-Back Cell Interconnection Technology

Figure 2-6 displays schematically the architecture of conventional front-to-back cell interconnection technology. The configuration consists of a front metal electrode and back contacts on the cell material. A solder-coated copper ribbon with high electrical conductivity is connected along the top face of a cell and soldered to the back of a neighbouring cell. This interconnection ensures current transfer across respective cells in a series connection (Klengel et al., 2011). The configuration has metallization which enables it to interface with two different materials - the Si wafer and the solder-coated Cu ribbon.

CHAPTER TWO: LITERATURE REVIEW

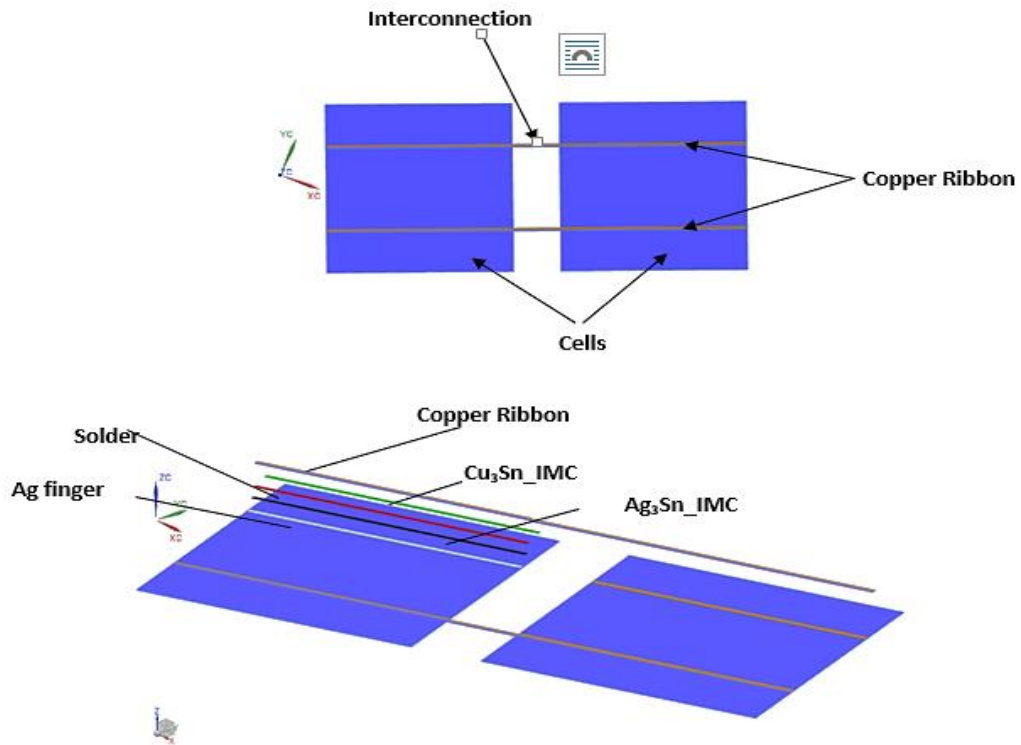


Figure 2-6: Conventional Front-to-Back Cell Interconnection Technology

In solar cells, electrons generated from the Si wafer are transferred to the Ag metal fingers. The contact between the silicon wafer and the silver finger must, therefore, be of higher integrity for efficient electron transfer (Davis et al., 2016). A screen printing method deposits silver fingers on the silicon wafer, generating an unbroken H-pattern of small and tall fingers linked by wider busbars. In order to minimise optical losses, the Ag metal fingers must have a large aspect ratio (narrow and tall). This also maximizes the cross-sectional area for increased conductivity (Neuhaus and Münzer, 2008, Chen et al., 2011).

The screen printing process enables optimized system production. This process is succeeded by baking out the solvent and then firing the cell at elevated temperatures of about 4800 °C. Contacts for both front and rear are formed at the same time (Davis et al., 2016).

CHAPTER TWO: LITERATURE REVIEW

The conventional front-to-back interconnection geometry introduces a kink in the copper ribbons as they connect the back to the front side. This geometric distortion induces stresses in the copper ribbons during manufacture, which is further aggravated by high thermal loading during operation in tropical ambient temperatures. The findings from degradation studies of many field-aged PV modules with this interconnect technology (Tossa et al., 2016, Cañete et al., 2014, Elibol et al., 2017, Balaska et al., 2017) report the claim. This cell interconnection technology remains dominant in the PV industry. However, new interconnection schemes are emerging which show a significant departure from the conventional structure. Current research reports of interconnection based on parallel Cu wires known as the Smartwire (Faes et al., 2014) or Multibusbars approaches (Braun et al., 2013) where a conventional full-area Al-BSF and standard screen printing for the front contact have been used for a 6" Czochralski Silicon (Cz-Si) multi-busbar solar cells and efficiencies of up to 19.5% recorded. This method of interconnection is receiving a lot of attention because it allows for greater cell effectiveness (by reduced shading) and reduced cost because of reduced consumption of Ag. Efficient mini-modules with little silver consumption and with or without copper-based metallization has been demonstrated by (A. Faes et al., 2016). The new mini-modules continues to show promising results.

An emerging interconnection technique known as ‘shingled cell interconnection’ (shown in Figure 2-7), where narrow cells are arranged in a manner that each cell overlaps a little with the other is currently under research and development. In this architecture, the busbars are connected back-to-front through a joint material. This design gives high-efficiency modules because shading losses are not caused by busbars or ribbons and the active region is nearly 100% of the total region (Beaucarne, 2016)

CHAPTER TWO: LITERATURE REVIEW

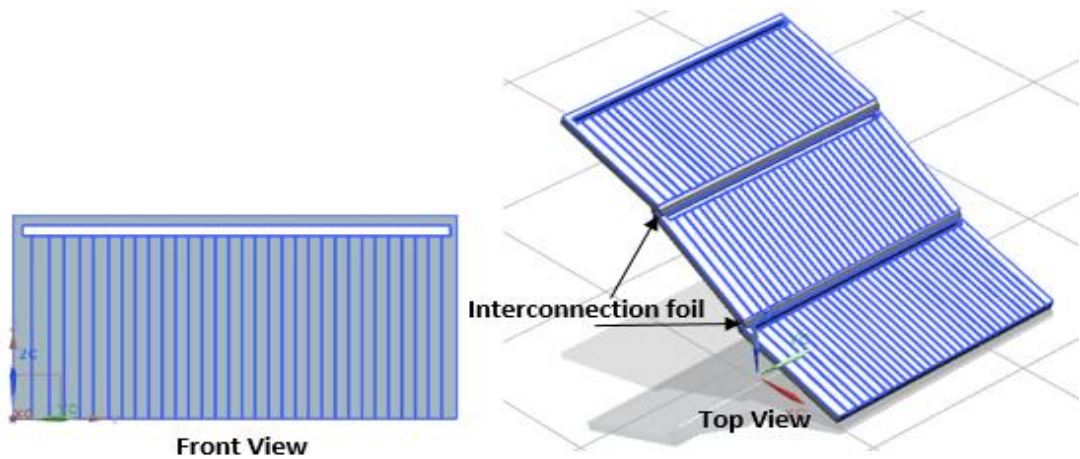


Figure 2-7: Schematic Drawing of a Cell for Shingled Cells Interconnection

2.5.2 Back Contact (BC) Solar Cell Interconnection Technologies

The back-contact (BC) solar cells require a unique interconnection design. In a conventional interdigitated back-contacted solar cell (IBC), the rear sides of neighbouring cells are joined.

This contrasts with conventional solar cells in which the front sides are joined with the rear sides of neighbouring cells. The BC interconnect design has a gridless front surface which improves light trapping and passivation. Charge recombination losses are also eliminated since all contacts appear at the rear of the cell.

There are several configurations of BC cells which include the following:

- i. Emitter Wrap through (EWT)
- ii. Metallization Wrap Through (MWT).
- iii. Back-Junction back-contact (BJBC).
- iv. Alternate p-and n-type.
- v. Pin-up modules (PUM).
- vi. Silver solar cells.

CHAPTER TWO: LITERATURE REVIEW

vii. Spherical solar cell.

viii. Cells with electrode wire grid (Day 4 Electrode).

The subsequent sub-sections present and discuss the various BC architectures listed.

2.5.2.1 Emitter Wrapped Through (EWT) Cell Interconnection

The design of the EWT cells enables a multiplicity of interconnection routes to be gathered via both the front and back surfaces connected in parallel (Kerschaver and Beaucarne, 2006). The configuration enables the performance of EWT cells to be nearly independent of the cell thickness to diffusion length ratio (Kray et al., 2001). The vias are formed by indentations that have been patterned and etched photolithographically. The indentations may not penetrate the wafer (Leistiko, 1994) or barely penetrate through the wafer (Hall and Soltys, 1980).

The prevailing front surface diffusion reduces any limitation posed by contact size and spacing up to the levels attained in screen printing. However, according to (Eikelboom et al., 2002), within the precision of printed screen technology theoretically deduced optimal design is difficult to accomplish. Therefore, (Gee et al., 1993) propose buried EWT cell design technology, since it is possible to form grooves and vias in a single step, thus ensuring excellent alignment. It is reported that cell efficiencies in small fields (6cm^2) were recorded at up to 21.4% (Schonecker et al., 2002). EWT cells have relatively low diffusion length to cell thickness ratio. However, screen-printed large EWT cells have high series resistance, which limits the size factor. Figure 2-8 illustrates the cross-sectional schematic of EWT solar cell technology.

CHAPTER TWO: LITERATURE REVIEW

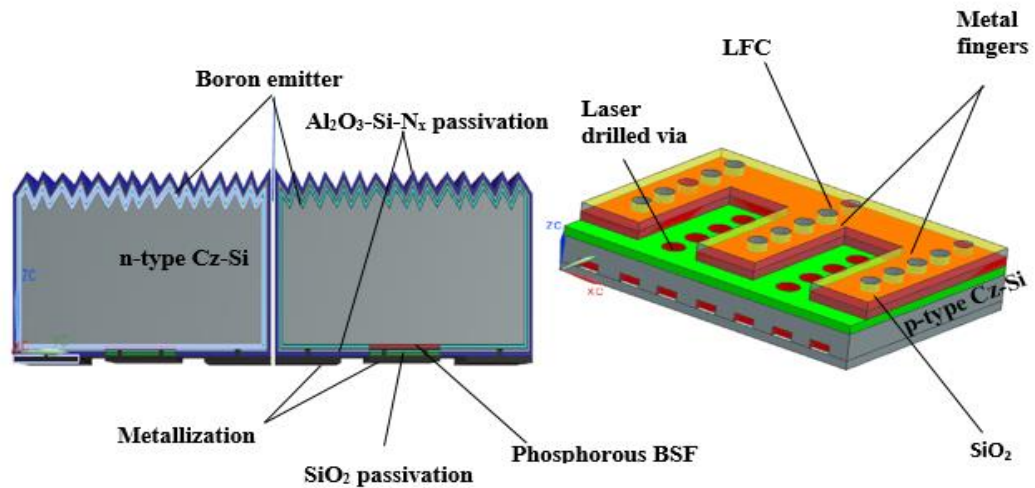


Figure 2-8: Schematic Cross-Section of the EWT Solar Cell

The metallization involved in creating cell interconnection of EWT shows a linear pattern of metal fingers. Induced stresses from the manufacturing of these metal fingers are generally low compared with front-to-back cell interconnection. Additionally, the metallization is somewhat 'shielded' from a direct incidence of thermal radiation due to her position in the cell architecture. EWT cell interconnections are therefore expected to register relatively lower induced thermo-mechanical stresses from elevated ambient temperatures.

2.5.2.2 Metallization Wrap Through (MWT) Cell Interconnection

Solar cell architecture for the back and back (BJBC) has a finger framework and a bar that collects the current from each finger (Schulte-Huxel et al., 2015). Only at the back ends are the corresponding cells connected, since the terminals are designed for base and emitter. Therefore, the interconnection, which is a versatile PCB, replaces the traditional assembly with the copper ribbons. The flexible PCB interconnection is less susceptible to induced thermo-mechanical damage at elevated temperatures compared with the conventional H-patterned interconnect. This is because the interconnect

CHAPTER TWO: LITERATURE REVIEW

technique involved in connecting the respective cells yields a comparatively lower manufacturing induced stress.

This cell structure does not eliminate front shading losses as both polarities on the back surface have a metal grid on the front surface coupled with interconnection pads (Kerschaver and Beaucarne, 2006). However, the losses are decreased considerably by putting the interconnection pads and solder strips at the back. Typically, conventional H-pattern solar cells with screen-printed contacts indicate a front-side shading of about 7%. This value is decreased to 4.1% by implementing the MWT idea as there are no busbars on the front side (Thaidigsmann et al., 2012). Unlike EWT, the length of the space charge region's surface termination in MWT cells is limited. This can be reduced with a dense metal-insulator, which separates the transmitter from silicon to the front surface and the metal contact as shown in Figure 2-9.

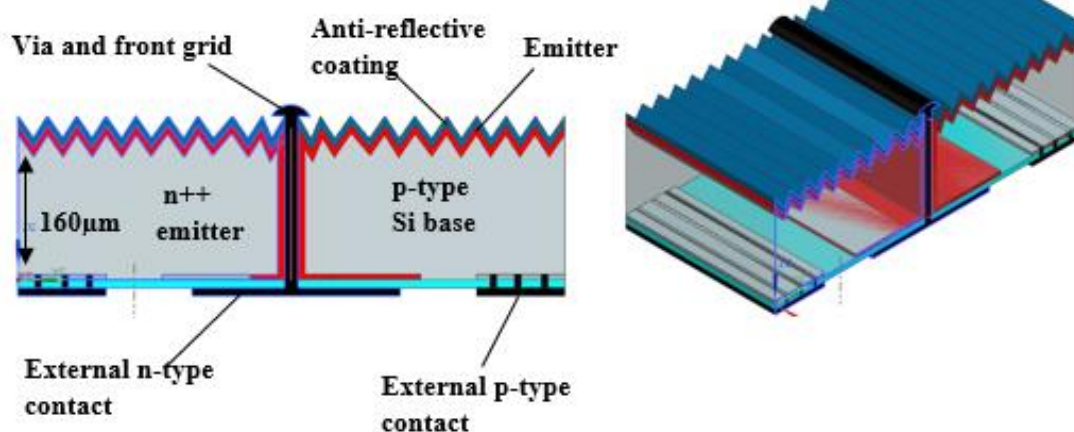


Figure 2-9: MWT Cell Interconnection

According to (Kerschaver and Beaucarne, 2006), an optimal combination of the rear surface pads and expanded emitter region at the cell back can be achieved. In such configuration, the rear pads are not restricted to interconnection as their only function. (Lamers et al., 2012) reported of some MWT solar cells that have initial superior energy

CHAPTER TWO: LITERATURE REVIEW

yield compared with conventional solar cells. Increased cell efficiencies were accomplished at more than 17% for c-Si (Hoenig et al., 2010) and by more than 20% for Cz-Si (Lohmuller et al., 2011). The improvement in efficiency is achieved by decreasing the front shadow because the electrical contacts are achieved at the back of the cell. This specific system also reduces the cost of manufacturing by reducing the mass per cell of the silver (Hendrichs et al., 2013). The presence of vias in the junction of the MWT cell structure renders it sensitive to reverse bias current. The ‘through’ hole metallization pattern has also been observed to promote the formation of hot spots on the cell surface.

2.5.2.2 Back-Junction Back-Contact (BJ-BC) Interconnection

The back-junction and back-contact (BJ-BC) solar cell architecture feature an interdigitated finger structure and busbar that collects the current from individual fingers (Schulte-Huxel et al., 2015). The p^+ and n^+ junctions are located on the rear side of the device. There is practically no metallization pattern on the front surface and therefore no feature on the surface that shadows the incident photon flux (Kerschaver and Beaucarne, 2006). In addition, a low series resistance of the metal pattern is achieved as the metallization can cover about one-half of the back surface. Unlike front-contacted cells, current conduction in BJ-BC cells is not through the emitter and therefore there is no trade-off between grid shading and series resistance losses. Thus, the rear function can be optimized in terms of the lowest saturation current only (Meier et al., 2010). Research simulation and measurements recorded indicate that the BJ-BC solar cell busbar areas decrease the Fill Factor and short circuit current density (Schulte-Huxel et al., 2015).

Figure 2-10 shows a schematic drawing of an n-type BJ-BC silicon solar cell.

CHAPTER TWO: LITERATURE REVIEW

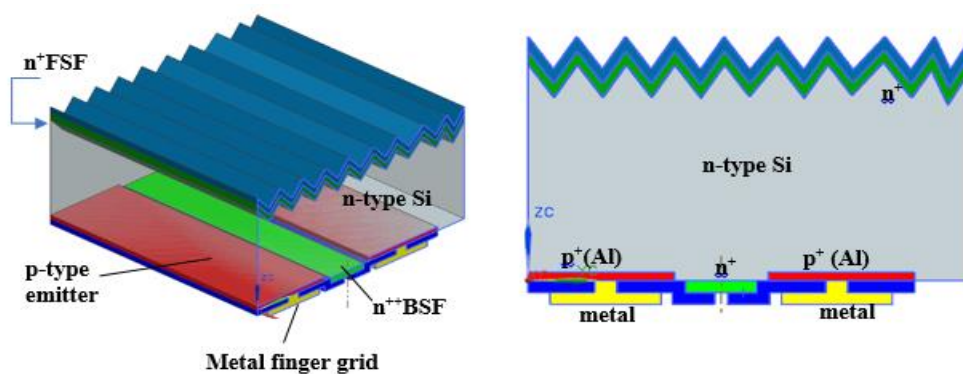


Figure 2-10: Schematic n-type BJ-BC Silicon Solar Cell

The photo-generated carriers are close to the surface and thus travel throughout the bulk region to the back metal contacts to be gathered. A higher average distance (lifetime) is required for carriers to travel to reach the backside region before recombination since there are no vias present. The diffusion length covered by carriers in BJ-BC cells is expected to be longer than the silicon wafer thickness to guarantee optimum cell efficiency. Therefore, using a thinner wafer is an advantage for a BJ-BC solar cell architecture (Guo and Cotter, 2004). BJ-BC cells have coplanar cell interconnection geometry that ensures the uniform linear expansion of metal contacts at elevated temperatures. At elevated temperatures, induced excess thermo-mechanical strain from an expansion of metal contacts due to differences in their CTEs is thus minimised.

2.5.2.3 Alternate p-and n-type solar cell interconnection

In the development of alternative p- and n-type silicon solar cells bifacial screen-printed cells are used. The design deploys alternating p- and n-type semiconductors arranged in a manner to permit the interconnection of equivalent sides on front-to-front and back-to-back of cells next to each other (Buck et al., 2006). Investigations from (Kopecek et al., 2005) reveal that, in contrast to the p-type, the n-type is not prone to boron oxygen-related light-induced degradation. The schematic of the technology is shown in Figure 2-11.

CHAPTER TWO: LITERATURE REVIEW

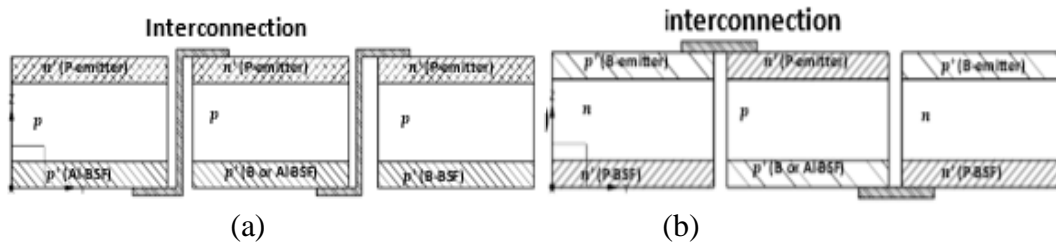


Figure 2-11: (a) Conventional Module Interconnection: each cell backside is connected with the front side of the subsequent solar cell (b) Innovative Interconnection using Alternating p-type and n-type Solar Cells (Kopecek et al., 2006b)

In addition to a phosphorus-diffused region, both solar cells have Plasma Enhanced Chemical Deposition of Vapor in SiNx as an Emitter in the p-type and as an FSF in an n-type cell (Kopecek et al., 2006b). The main distinguishing feature between the p-type and n-type is the Ag-Al pad at the rear side. The pad is printed straight on the substrate at the p-type interconnection, whereas in the n-type the pad is either printed onto p+ or the Al rear contact, to prevent cell shunting. (Kopecek et al., 2006b) The alternate p-and n-type solar cell interconnection method has a number of advantages over conventional PV-modules. These include simplified interconnection, closer cell assembly (to be aesthetic) and high output during the production of the module. In addition to these advantages, the technology (using the bifacial cells) leads to an increase in power output as compared to standard mono-facial modules (Kopecek et al., 2006a). The elegant interconnection geometry that reveals a straight horizontal short-spanned connection in the alternate front-to-front and back-to-back lay-up ensures a uniform horizontal expansion of the interconnection. The arrangement eliminates any potentially high bending stresses as may be registered in the conventional H-patterned cell interconnection.

2.5.2.4 Pin-Up Modules (PUM) interconnection

The pin-up module (PUM) is a type of back-contact solar cells designed with a structured back foil interconnection and a restricted amount of wafer holes (Zarmai et

CHAPTER TWO: LITERATURE REVIEW

al., 2015b). The holes form vias and contain pins that serve as interconnection material at the rear (Bultman JH, 2012, Bultman et al., 2001). The cell has a similar geometry as a conventional cell with metallization at both front and rear sides. The only distinguishing feature with the standard cell is the presence of vias and the configuration of the interconnection. Apart from being visually more appealing than conventional modules, PUM offers several performance improvements such as reduction in shadowing losses due to the absence of busbars, reduction in resistance losses as current is collected at holes equally spaced over the wafer and good alignment during screen printing of metal contacts (Weeber et al., 2006). The schematic of PUM cell interconnection is shown in Figure 2-12.

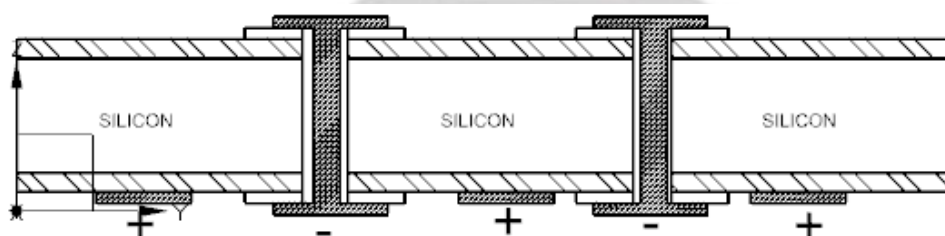


Figure 2-12: Schematic of Pin-UP Module Cell Interconnection

The interconnection is achieved by means of a metal foil produced to specification (Bultman JH, 2012). There are several interconnection methods utilised in PUM. These interconnection methods include; manual soldering, localised infrared soldering, ultrasonic bonding, dispensing of conductive adhesives and thermal arc spraying (Bultman et al., 2001).

The two most popular methods of this technology are the localised infrared soldering and the thermal arc spraying technique. Usually, the localised infrared soldering is preferred over the other as the soldering area at the front of the cell is relatively small. In thermal arc spraying, a metal powder is sprayed onto the surface of a foil and

CHAPTER TWO: LITERATURE REVIEW

subsequently into vias in the cell. The interconnection realised is further laminated with plastic. Thermal arc spraying has the potential of forming a good connection but the mechanical strength generated by this interconnection method is not fully qualified. In principle, a thin foil can be used. However, since metal foil of such thickness is not readily available, a 50 μm thick foil is usually used (Bultman et al., 2000).

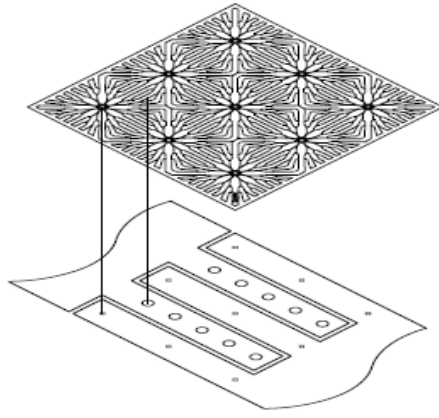


Figure 2 - 13: Interconnection for a PUM one Cell Laminate

The regular method for interconnection of PUM Cells involves the use of standard localised soldering technique to solder the pins to the front side of the silicon wafer. This is because the soldering region accessible in front of the cell is comparatively tiny. This soldering technique ensures that thermal stresses on the cells are minimised. Induced damage from the manufacture of the soldered joint from localised soldering is minimised. Also, this interconnection is not expected to be highly stressed at elevated temperatures as compared with the standard H-patterned interconnection. Some innovations in PUM development are shown in Figure 2-14.

CHAPTER TWO: LITERATURE REVIEW

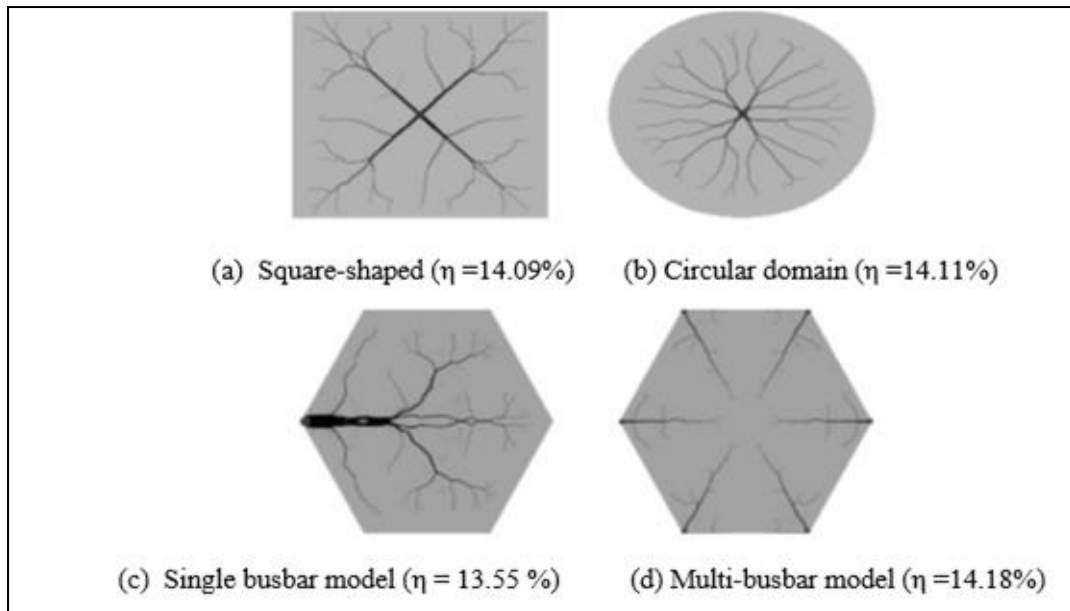


Figure 2-14: Current Innovations in PUM Development (Franklin et al., 2006)

The busbar (denoted by red) is located at the centroid of the geometry. The busbar extends from the centroid through the cell to the rear of the cell where all the interconnections are made. Generally, the circular-shaped PUM is expected to yield slightly high efficiencies compared with a square-shaped PUM. This is because for circular cells, the distance of the farthest point from the busbar is shorter and that leads to relatively lower resistive losses (Weeber et al., 2006). The efficiency range of (13-14%) has so far been achieved for the new PUM interconnections.

2.5.2.5 Silver solar cells

Silver cells are made up of monocrystalline silicon, which is very thin. The manufacturing technique involved in the production of silver cells allows for economic usage of silicon processed per module; with a reported 90-95% reduction by (Franklin et al., 2006). The main step in forming the silvers is by micromachining deep and narrow grooves through the thick silicon wafers. The completed cells are subsequently removed and rotated through 90° for the larger area to form the sun-facing surface of the cell (Weber et al., 2004).

CHAPTER TWO: LITERATURE REVIEW

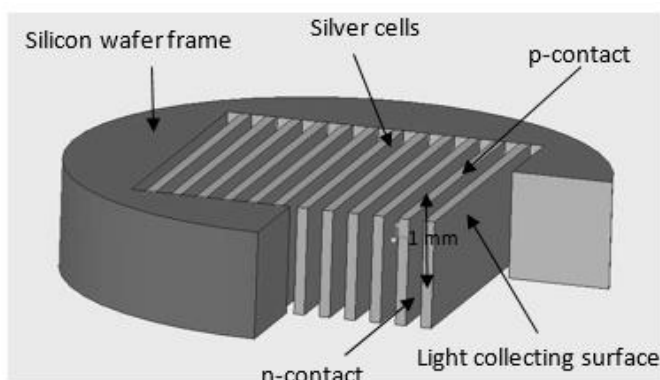


Figure 2-15: Schematic Drawing of Silver Cells

The metal contacts used for interconnection are located on the side of the silver - occupying a small fraction of the total surface of the cells. This arrangement eliminates shading due to metallization. Furthermore, doping below the contact could be made heavy resulting in excellent, low resistivity contacts with minimized recombination losses (Deenapanray et al., 2006). Figure 2-15 presents the schematic of solar silver cells.

Silver cells by design are comparatively thinner (approximately $50\ \mu\text{m}$) having emitter diffusion surfaces at the front and rear. This configuration provides an extremely elevated internal quantum efficiency. With a comparatively tiny minority carrier diffusion in the bulk of the cell, high open-circuit voltages are feasible. This is an additional benefit since the range of majority carrier drift in the bulk area from the cell terminals is sufficiently big (around $1000\ \mu\text{m}$). A large majority of carrier drift leads to series resistance losses. This situation can only be mitigated by the use of low resistivity substrates (which have reduced diffusion length) (which have reduced diffusion length) are used (Franklin et al., 2006).

Distributed series resistance losses present a major loss mechanism for the silver cell interconnects. Wider cells or cells operating under concentrated illumination are particularly affected. A strongly associated loss mechanism is ascribed to a region of

CHAPTER TWO: LITERATURE REVIEW

strongly compensated silicon that results from the overlap of the diffusion from phosphorus at the emitter sidewall and boron at the sliver cell edge. The loss results in a decreased fill factor and open-circuit voltage, which corresponds to a separate non-ideal recombination element. The current research aimed at innovating a simplified cost-effective manufacturing process capable of delivering cell efficiencies beyond 20% with superior energy yield is being advanced.

2.5.2.6 Spherical silicon solar cell interconnection

The spherical (Sphelar) cell has a wrapped-up single-crystalline p-n junction reception surface that has enabled three-dimensional light capture and large reduction of silicon usage per square metre of the module. The Sphelar solar cell employs a special manufacturing process technology that takes place under space-like conditions of microgravity. The process involves dripping molten silicon into a drop tube. As the molten silicon drops in a free-fall, it moulds into spheres due to the surface tension of the droplets. This process results in the economic usage of silicon and the energy used in silicon cell production as compared with conventional technologies. According to (Taira et al., 2008), the basic concept of Spherical cells is that a spherical sunlight reception surface can capture sunlight 3-dimensionally. This operation improves the power generation capacity to maximum potential. Sphelar cells have comparatively higher efficiency than conventional cells having only one planar surface to capitalize upon sunlight. The schematic of spherical cell technology is presented in Figure 2-16.

CHAPTER TWO: LITERATURE REVIEW

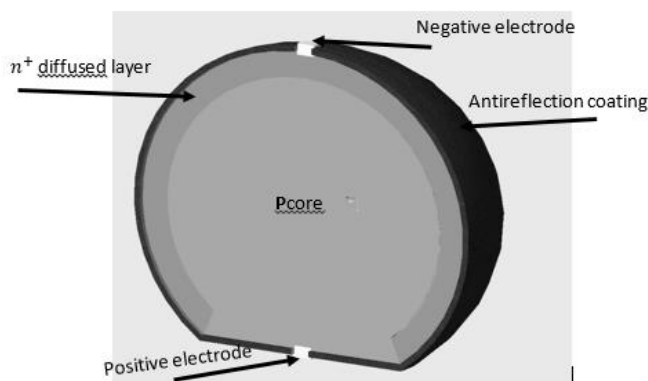


Figure 2 - 16: Schematic of Spherical Cell

The cell interconnection - consisting of small silver and aluminum electrodes on top and bottom of the spheres are formed to produce a link between the emitter and the base. The electrode arrangement enables an even distribution of generated current. Serial and or parallel cell interconnections can easily be facilitated (Taira et al., 2008). If one outfitted the underside of the cell with a reflective material, the yield could be significantly enhanced (Biancardo et al., 2007). The resulting interconnect geometry created by low-temperature ECAs exhibits less induced stresses in the interconnect material. At elevated ambient temperature operation, the interconnection is likely to experience relatively lower thermal stresses. A Novel monodispersed spherical TiO_2 aggregate with a diameter of 100 nm (SP100), which is the smallest TiO_2 spheres (or beads) reported thus far, has been prepared by controlled hydrolysis and hydrothermal reaction (figure 2-17). SP100 exhibits photovoltaic conversion efficiency of 18.41% with JSC of $22.91\text{mA}/\text{cm}^2$, VOC of 1,049 mV and FF of 0.759 (Wu et al., 2017).

CHAPTER TWO: LITERATURE REVIEW

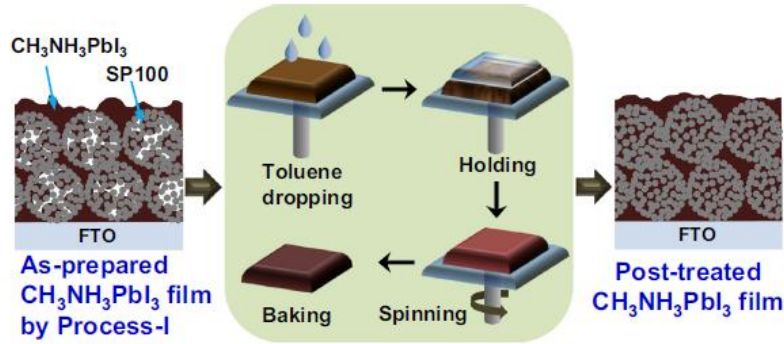


Figure 2-17: SP100 Fabrication Process (Rubin and Schneider, 2007)

2.5.2.7 Solar Cells with Flexible Electrode Wire Grid (Day 4 Electrode)

The solar cells with a flexible electrode wire grid are also known as Day4TM Electrode. The solar cell technology is realized from a transparent compound of an adhesive and polymeric film with an embedded copper wire grid. The adhesive offers dual functionality by giving support as housing for cables during the manufacturing of the electrode, and adhesion fixation on the solar cell through a conventional lamination step (Rubin and Schneider, 2007). The technology is shown in Figure 2-18.

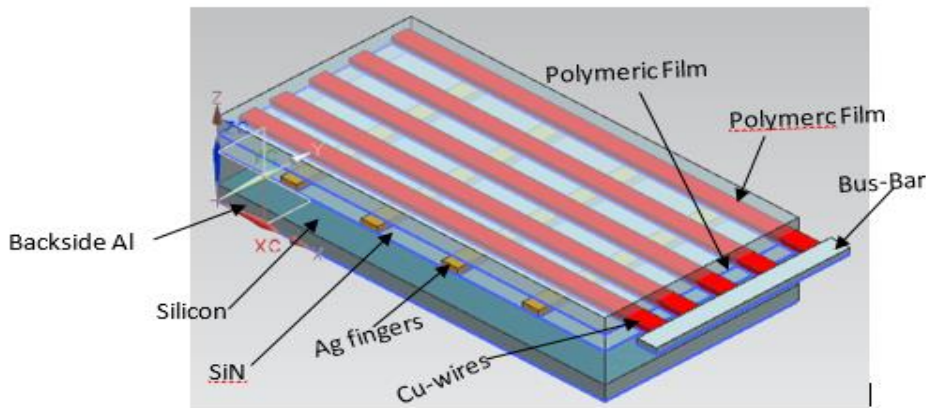


Figure 2-18: Schematic of Day 4 Electrode

The flexible nature of the electrode wire ensures a reliable cell interconnection. The design configuration ensures a stable fill-factor with almost no losses with reference to the cell-level fill factor. The reduced frontal metallisation range and the larger BSF rear

CHAPTER TWO: LITERATURE REVIEW

passivation on Day4 solar cells significantly increase the open-circuit voltage (V_{oc}). Although a slightly greater shading appears to occur from cells in 1-side lay-up using a 4-mm gap, an increase in the current of encapsulation is compensated for this. In comparison to conventional reference cells, (Rubin and Schneider, Rubin and Schneider, 2007) reported a 0.1% increase in efficiency for Day4 cells in 1-side lay-up when compared with standard reference cells. Furthermore, (Rubin and Schneider, Rubin and Schneider, 2007) reported a 50% reduction in the number of wires used for a 2-side lay-up which resulted in a reduction of cell shading (down to less than 6%) and with fill factor still at a higher level compared with standard cells. Day4 solar cells contacting architecture provides more than 2000 contacting points on the front side of the solar cell when compared with only two busing lines from standard solar cells. This unique contacting scheme secures a high interconnection redundancy against cell breakage. Experimental results from (Rubin and Schneider 2007) show only a small or no loss in cell power from cell breakage. At elevated temperatures, the narrow/tiny-sectioned wires resulting in a nearly negligible thermal expansion and therefore a stable interconnection takes up the induced thermal stresses.

2.6 R&D Challenges and Interconnection Technologies Evaluation of c-Si PV Module for Tropical Climate Suitability

In this section, the characteristics of the various interconnection techniques presented and discussed in the preceding sections are evaluated and compared for their suitability for application in a tropical ambient. The factors considered include; cell interconnection technique, interconnection peel, and residual strengths, average Fill Factor (FF), shading losses and Power Conversion Efficiency (PCE).

CHAPTER TWO: LITERATURE REVIEW

2.6.1 The Cell Interconnection Techniques

The normal soldering method, often through infrared heating, leads to heating at the required soldering temperature of the entire tab-cell-tab envelope for interconnection. On cooling, induced shear stress levels are high. The interface of the silicon cell and the silver solder alloy develop micro-cracks. Crack propagation leads to removal and premature failure. A proposed new technology is spot soldering where the tab-cell interface is heated locally. However, suitable process technology is laser soldering. In this process, the laser beam is directed with precision to the required spot, lowering the temperature at which the joint is formed and this is desirable to minimize induced stress level (de Jong et al., 2005). In addition to the traditional solder bumping, there are generally five different cell interconnection techniques used for the realization of the various cell interconnection technologies discussed. These techniques include; Infrared reflow (IR) soldering, laser spot soldering, an electrically conductive adhesive (ECA), thermal arc spraying and ultrasonic welding.

A soldering paste (a sticky combination of powdered solder and flux) is used in IR reflow soldering to momentarily attach the cell interconnectors. The whole assembly is then exposed to controlled heat that melts the solder (Wikipedia, 2017). The IR reflow soldering allows for the least time for solder grain growth over liquid solder temperature, which leads to the formation of a more reliable solder joint. (Bergenthal, 1995). Laser soldering generally utilizes a liquid solder to allow the components to be joined and provide mechanically and electrically stable contact when solidified (Ogochukwu, 2013). A controlled laser beam is utilized in transferring energy to the spot where the soldering is taking place. The absorbed energy then heats the solder to its melting temperature, leading to the soldering of the contact upon cooling. This method eliminates mechanical contact entirely contact (Raga, 2011).

CHAPTER TWO: LITERATURE REVIEW

Laser spot soldering, previously described in section 2.3, Figure 2-6, delivers single solder spots amounting to 7-8 per busbar. The spot is evenly distributed over the busbar (Wirth, 2010). Such distribution impacts minimum mechanical damage on the soldered joint. Electrically Conductive Adhesives (ECA) are metal-filled silicon-based adhesives that help to create a reliable interconnection of solar cells – yielding high conductivity and flexibility while potentially reducing material costs (Corporation, 2013. Accessed: 2017 January 14). A good conductive adhesive is not only determined by the electrical and mechanical properties after curing but also depends on the curing characteristics (De Jong et al., 2004, Liu et al., 1998). The mechanical strength of adhesives is generally defined in terms of their shear strength and is dependent on the dimensions and materials of the test vehicles (De Jong et al., 2004). ECA offers increased flexibility and durability that improve the overall stability of the PV module under thermal stress.

Thermal arc spraying involves heating metal powder with a thermal arc and spraying on the surfaces to be joined. This process leads to the realization of a very durable mechanical adhesion on the metal contacts whilst ensuring that cell and interconnecting material are kept at a lower temperature (Bultman et al., 2002). Ultrasonic welding employs a combination of friction and cold pressure welding applied at overlapped surfaces of interconnects to be welded together (Gochermann, 1990). The process assumes an existing contact pressure during the welding. Contact forces and ultrasonic energy are applied simultaneously in such a manner that the required forces and the developing deformation of the parts being welded are greatly reduced. The key benefit of this interconnection technique is a reduction in induced mechanical stress build-up

CHAPTER TWO: LITERATURE REVIEW

in the joint. Figure 2-19 presents the ranking of various interconnection technique in terms of induced mechanical stress magnitude.

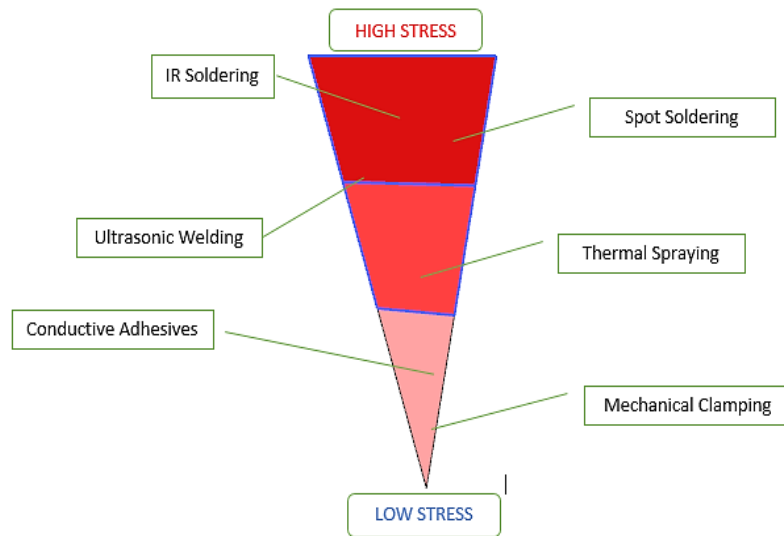


Figure 2-19: Ranking of possible interconnection techniques in terms of induced mechanical stress.

2.6.2 Interconnect Peel Strength

Peel strength of solar cell interconnection is the average load per unit width of bond line required to separate bonded interconnection ribbons where the angle of separation is 180 degrees (Ametektest, 2017). Peel strength is defined as the average force per unit width of bonded interconnection materials. Peel strength is part of the solar cell testing standard DINEN 50461 and offers a very simple and quick approach to measure the strength of adhesion of interconnector ribbons to solar cell metallization (Eitner and Rendler, 2014). Table 2-1 presents the peel strengths of various cell interconnection techniques discussed in section 4.1. It can be observed from the table that IR reflow soldering delivers interconnection with the highest peel strength (2-16) N. However, as shown in Figure 2-19, IR soldering introduces the highest induced mechanical stress in the interconnection. Mechanical clamping with unknown peel strength delivers a relatively lower induced mechanical stress in the interconnection which positively

CHAPTER TWO: LITERATURE REVIEW

impacts the durability of the joint formed. At elevated PV module operating temperatures, characteristic of tropical climates, the joints formed are expected to be subjected further to induce thermo-mechanical stress.

The challenge, therefore, is to have an interconnection technique that can maintain the integrity of the joints formed under this harsh ambient condition. Table 2-1 summarizes the results of the investigation by (Kontges et al., 2014). The findings indicate that soldering causes stress on the cell. The situation aggravates when more thick ribbons are used. In terms of longterm reliability, soldering offers better stability than clamping. Using ECA could be a compromise between higher power degradation and lower mechanical strength. A decreased ribbon thickness could be adopted to decrease the stress in cells during soldering. This will be a situation of reducing total cost, bearing in mind that greater losses come with encapsulation of thinner ribbons.

Table 2-1: Comparison of interconnection techniques (Kontges et al., 2014)

Ribbon Interconnection	Clamped	Soldered	Glued(ECA)
Long term stability	-	+	+
Mechanical stability	+	0	+

2.6.3 Average Fill Factor (FF)

The Fill Factor (FF) is the ratio of the maximum power of the PV module to the virtual power (PT) that would result if V_{mpp} would be the open-circuit voltage and I_{mpp} would be the short-circuit current. FF is a performance indicator that measures the quality of the solar cell or PV module (Kontges et al., 2014). Although it cannot be practically achieved, an ideal PV module technology would produce a perfectly rectangular I-V curve in which the maximum power point coincided with short circuit current (I_{sc}) and open-circuit voltage (V_{oc}) (Sathyanarayana et al., 2015).

CHAPTER TWO: LITERATURE REVIEW

The FF can be interpreted graphically as the ratio of the area of the blue rectangle to the area of the green rectangle shown in Figure 2-20.

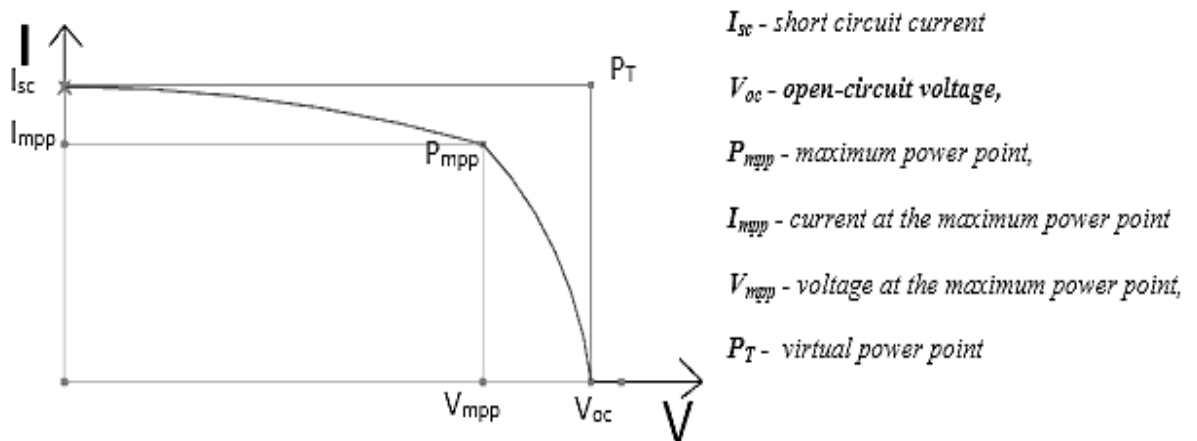


Figure 2-20: shows a schematic I-V curve of an illuminated PV module.

2.6.4 Shading Losses

Losses from shadowing (optical losses) are triggered by the presence of metal on the top layer of the solar cell that keeps light from entering the cell (Baccouch et al., 2016). Shading losses are measured by the transparency of the top surface of the cell, which is affected by the width of the metal lines on the surface and the spacing of the metal lines. (pveducation, Accessed: 2017 January 10). Table 2-2 presents a tabular evaluation of the various interconnection technologies.

CHAPTER TWO: LITERATURE REVIEW

Table 2-2: Comparison of cell interconnection technologies for c-Si solar cells in PV modules

Cell Interconnect Technology	Interconnection Technique	Interconnection Peel Strength (N)	Interconnection Residual Stress (MPa)	Average FF (%)	Shading losses (% of front cell area)	PCE (Maximum) (%)		
						Cell	Module	
							Lab.	Commercial
1. Conventional Front-to-Back (H- patterned cell)	IR soldering/ Laser spot soldering (Ribbon-front-to-back)	2-16 (Kraemer et al., 2013)	49-355 (Novotny et al., 2006) N/A	71.8-75.4 (Bultman JH, 2012, Weeber et al., 2006)	7 (Thaidigsmann et al., 2012)	18 (Granek and Reichel, 2010)		
2. Emitter Wrapped Through (EWT)	Laser soldering/ Electrical Conductive Adhesive (ECA) (Edge Tab - back contact)	1-5 (Schmidhuber et al., 2005, Schmitt et al., 2008) 0.3-1 (Bennett I, 2013)	N/A 15 - 19.5 (Hasan and Sasaki, 2016)	80 - 81 (Kiefer et al., 2011, Kray et al., 2001)	3	21.6 (Kiefer et al., 2011)		
3. Metallization Wrap Through	Laser soldering/ ECA (conductive foil /ribbon)	1-5 (Schmidhuber et al., 2005, Schmitt et al., 2008) 0.3-1 (Bennett I, 2013)	N/A 15-19.5 (Hasan and Sasaki, 2016)	76.6-78.4 (Lohmuller et al., 2011, Thaidigsmann et al., 2012)	4.1 (wikipedia, 2017)	17.8 (Lamers et al., 2012, Wirth, 2010)	17 (Lamers et al., 2012)	
4. BJ-BC	IR soldering (ribbon - back contact)	2-16 (Kraemer et al., 2013)	49-355 (Novotny et al., 2006)	80.5 (Schulte-Huxel et al., 2015)	0 (Schulte-Huxel et al., 2015)	24 (Granek and Reichel, 2010)	22 (Schulte-Huxel et al., 2015)	23.4 (Schulte-Huxel et al., 2015)
5. Alternate p- and n-type cell	IR soldering (Ribbon-equivalent sides)	2-16 (Kraemer et al., 2013)	49-355 (Novotny et al., 2006)	71.5 - 82.1 (Buck et al., 2006, Kopecek et al., 2006b, Bordihn et al., 2016)	1.6 - (Alam et al., 2002)	21.8 (Alam, Chan et al.)		
6. HoneyComb Design (HD)	IR soldering/ ECA (Ribbon/Adhesive)	2-16 (Kraemer et al., 2013) 0.3-1 (Bennett I, 2013)	49-355 (Novotny et al., 2006) 15 - 19.5 (Hasan and Sasaki, 2016)	68 (Huang et al., 2012)	0 (Huang et al., 2012)	19.8 (Zhao et al., 1999)	16.6 (Huang et al., 2012)	
7. PUM cell	IR soldering/ Thermal arc Spraying (foils with patterned conductors)	2-16 (Kraemer et al., 2013) N/A	49-355 (Novotny et al., 2006) N/A	72-74.8 (Bultman JH, 2012, Weeber et al., 2006)	6.5 (Bultman JH, 2012)	16.7 (Peike et al., 2013)	13.8 (Baccouch et al., 2016)	12.2 (Baccouch, Sakli, et al.)
8. Silver solar cells	Solder bump (substrate support bond)	1 - 5 (Schmidhuber et al., 2005, Schmitt et al., 2008)	N/A	81 (Franklin et al., 2006)	0 (Franklin et al., 2006)	20 (Franklin et al., 2006)	18.5 (Franklin et al., 2006)	
9. Spherical solar cells	Ultrasonic welding (substrate support bond)	2 - 5 (Rubin and Schneider)	N/A	77.4-77.9 (Biancardo et al., 2007)	0 (Biancardo et al., 2007)	23.54 (Biancardo et al., 2007)	-----	-----
10. Cell with flexible electrode wire	ECA (Day4 electrode wire)	0.3-1 (Bennett I, 2013)	15-19.5 (Hasan and Sasaki, 2016)	79 (Rubin and Schneider, 2007)	6 (Rubin and Schneider, 2007)	17 (Rubin and Schneider, 2007)	-----	-----

CHAPTER TWO: LITERATURE REVIEW

2.7 Effect of Tropical Climate on Interconnection Degradation Factors on Reliability of the c-Si PV Module.

Tropical climates are characterised by an average daily ambient temperature of 26 °C. The solar cell temperature rises to an average high of about 65 °C at mid-day and an average low of about 15 °C at mid-night. Tropical climates also experience high rainfall with occasional high winds and thunderstorms. An average relative humidity of about 85% is usually recorded. The above conditions increase the rate of degradation of interconnections of installed solar PV modules operating in the region. This section presents and discusses four factors accelerating the degradation of soldered joints in crystalline silicon (c-Si) PV modules operating in tropical climates. This section presents the review under four sub-headings namely: Corrosion of Soldered Joints, Induced Thermo-mechanical stress, Intermetallic Compound (IMC) growth, and Development of Microcracks.

2.7.1 Corrosion of Soldered Joints and Electrical Contacts by Water Vapour Ingress into Encapsulant.

Corrosion may be defined as a process of deterioration of materials due to chemical, physical or electrochemical reactions with the environment. The corrosion of metals typically proceeds as an electrochemical reaction since electrons may migrate in the metal and ions can be released to the environment (Peike et al., 2013). The tropical climates are best described as hot and humid. The weather situation facilitates moisture intrusion into cells within the PV-module. When moisture permeates through the PV-module back sheet or through edges of module laminates, it leads to cell corrosion that result to increase in leakage currents. EVA has relatively high diffusivity compared to most polymers and this makes it easier for moisture to enter the PV modules. According to (Kempe, 2006), the variation of diffusivities of polymers is by orders of magnitude.

CHAPTER TWO: LITERATURE REVIEW

Significant reductions in water intrusion of cells are therefore feasible using encapsulant materials with lower diffusivities. Keeping a module completely dry for the PV module warranty period of 25 years may require low diffusivity materials such as Aclar (Polychlorotrifluoroethylene). However, most low diffusivity materials (including Aclar) have challenges associated with adhesion. The use of such encapsulants could result in unacceptable delamination under environmental exposure which would allow water to diffuse into the module easily. Subsequently, the presence of water in the PV module could accelerate the corrosion of the solar cells (Park et al., 2013). Corrosion has a significantly negative impact on the resistance properties of soldered joints, cell metallization, cell interconnection bus-bars and junction-box terminations (Wenham et al., 1994, Park et al., 2013). In turn, the effect reduces power produced by cells—leading to a drop in performance of the PV module. One other key function of the encapsulant is to provide mechanical support to protect the cells against breakage caused by impact during manufacture. Unfortunately, materials with high mechanical strength such as PET and Aclar generally have low glass transition temperature (T_g) (Cuddihy et al., 1986). This property makes Aclar and PET unsuitable for use as encapsulant materials (Cuddihy et al., 1983). Materials with low T_g have porous atomic structures and exhibits significant mobility. The porous structure tends to produce high diffusivities. Thus, the presence of low-modulus and low- T_g is in conflict with low diffusivity. This situation severely limits potential benefits from materials that have low diffusivities which are potential substitutes for EVA. Even with impermeable front and back-sheets, moisture is still able to penetrate the system and reach the centre of PV module in about two years due to the high diffusivity of EVA (Kempe, 2006).

CHAPTER TWO: LITERATURE REVIEW

There is a growing interest in research focusing on water vapour limiting encapsulants capable of outperforming EVA in this regard. This is mainly due to the relatively high susceptibility of thin-film PV modules to water vapour (Kim and Han, 2013). (Kim and Han, 2013) identifies ionomer and PVB as potential candidates offering higher protection from environmental exposure for thin-film than EVA. Edge seal materials with low-diffusivity and desiccant are being investigated by several manufacturers (Kempe et al., 2010). These materials are capable of preventing moisture ingress over the lifetime of a module. Polyisobutylene (PIB) uniquely provides a very low moisture-permeability and diffusivity, as well as a low glass transition temperature (Boyd and Pant, 1991, Lundberg et al., 1969). Other edge seal materials (e.g. epoxies) can have very low diffusivities but they are hard and brittle and could easily crack or delaminate in a large module (Kempe et al., 2010).

Though moisture is able to reach the centre of a module with impermeable front and back-sheets, it does not account for moisture-induced performance loss. However, moisture can saturate the outer few centimeters in a few months, enhancing the corrosive process that can short out the entire cells (Grossiord et al., 2012). The supersaturation of water around the edges of SPV modules also accelerates delamination. The oxidative degradation of EVA may decrease the diffusivity of water, but it will increase the solubility of water by the introduction of more polar groups leading to a greater amount of water ingress (Sangaj and Malshe, 2004). Alternative encapsulants with superior adhesional strength and lower diffusivities could offer better protection against hydrolytic reactions in the module. Although it has been experimentally demonstrated by (Kempe, 2006) that even a typical PV module will still approach equilibrium with the outside environment over 20 to 30-year lifetime of the

CHAPTER TWO: LITERATURE REVIEW

module, the volume of water necessary to accelerate corrosion processes varies with the PV technology.

2.7.2 Induced Thermo-Mechanical Stress on Soldered Joints Occasioned by Module Temperature cycling

Tropical climatic conditions induce thermo-mechanical stresses in PV-modules due to module temperature cycling. Abrupt weather change represents a major long-term reliability concern in the PV-industry. Stresses are transferred easily from one cell to the adjacent interconnected cell as well as to the interconnectors. Locally induced stresses partly result from module temperature change. The induced stresses are caused majorly by the mismatch in the magnitude of the coefficients of thermal expansion (CTE) of the different materials which include glass, interconnection, silicon wafer and Ag fingers that are bonded together in a PV module.

According to (Gonzalez et al., 2011), the higher CTE of glass relative to the cells makes the cells separate from each other occasioned by an increase in temperature during the day. This causes tensile stress in the interconnection. (Gonzalez et al., 2011) further observed that cells are pushed to each other upon cooling at night to temperatures lower than the stress-free temperature condition, which causes compressive stress in the interconnection. The compressive stresses could lead to mechanical instability in the interconnection due to its thickness ($-10\ \mu\text{m}$). PV module design is trending towards larger cells with shorter cell-to-cell interconnections. The challenge with this new design is that large cells tend to exhibit significant relative displacements between cells. Owing to the shorter gap between cells, the capacity of modules to accommodate the deformation is jeopardised.

CHAPTER TWO: LITERATURE REVIEW

The thermal cycling load for natural weathering caused by the alternation between day and night in the tropical climatic region is expected to be much lower compared with the IEC test conditions for thermal cycling at 125 K. The maximum temperature gradients observed for roof mounting in the region lie in the neighbourhood of 60 K. The highest yearly average of 37 K has also been reported. In this regard, the 125 K temperature gradient stipulated by IEC 61215 entails a much higher load on the materials due to thermo-mechanical stress. However, the larger number of cycles in long-term operation (approximately 9000 cycles for 25 years) at relatively lower temperature gradients may yield different material fatigue characteristics.

2.7.3 Intermetallic Compound (IMC) Growth in Soldered Interconnections in PV Module Caused by Thermal Soaking and Aging

Two types of IMC: Cu_6Sn_5 (η) and Cu_3Sn (ϵ) are generally formed from the reaction between Sn and Cu in solar PV interconnection soldering (Choi et al., 2002, Mei et al., 1992, Prakash and Sritharan, 2001). A number of researchers including (Deng et al., 2003, Tu and Thompson, 1982) explain that the Cu_6Sn_5 phase is typically formed above the melting point of the solder, while Cu_3Sn phase is generally produced during low-temperature thermal aging (100 °C to 175°C) by diffusion between Cu and Cu_6Sn_5 . Investigations by Dutta (Dutta, 2003) show the microstructures of SnPb63 and SnAg3.5 solders as containing Pb and Ag_3Sn grains respectively suspended in the Sn matrix. According to (Meydbray et al., 2007) the solder interface has a thin brittle intermetallic layer. In crystalline silicon PV modules, the intermetallic (IMC) layers are formed between the solder and the copper ribbon interface on one side and the solder and silver fingers on the other side (Figure 2-21). As the solder is subjected to cyclic thermo-mechanical stress, it undergoes microstructural coarsening and the intermetallic layer

CHAPTER TWO: LITERATURE REVIEW

thickens. This changes that occur in the microstructure of the intermetallic layer also promotes crack formation and propagation.

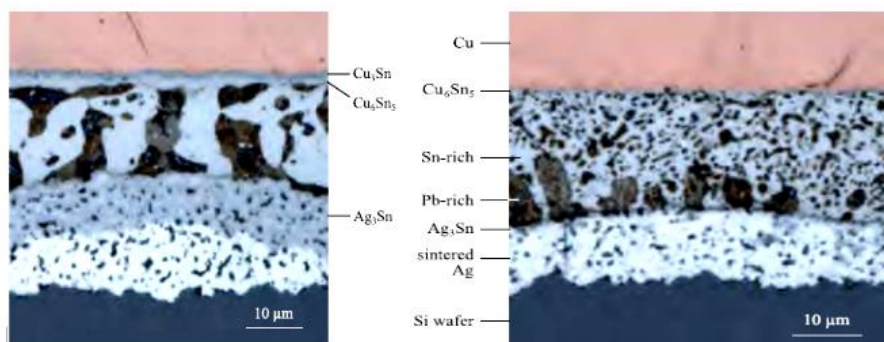


Figure 2 - 21: Microstructure of Silver Finger-Solder-Copper Ribbon Interface(Dutta, 2003)

The size (thickness) of an IMC layer greatly impacts on the reliability of the soldered joint. (Pratt et al., 1994) and (Protsenko et al., 2001) observed in their studies that a thin layer of IMC between the solder and Cu substrate improves bonding between the solder and the substrate but thicker IMC may have an adverse impact on the toughness of the soldered joints and interconnections. Several researchers have investigated the influence of IMC on the shear behaviour of solder/Cu joints. According to (Alam et al., 2002, Chan et al., 1998, Pang et al., 2001a, Miao and Duh, 2001); increasing thermal aging time or aging temperature leads to an increase in the thickness of the IMC layer. (Deng et al., 2005) further explains that the growth of intermetallic phases in the joint, both during soldering and lifetime, affects the quality of the joint and its reliability in terms of the mechanical response to applied loads. From research, isothermal aging severely impacts on several important material properties of solders such as; stiffness (modulus), yield stress, ultimate strength, and strain to failure. In their study, (Ma et al., 2006) observed a sharp change in the creep response of lead-free solders, recording a 100 times increase in the steady-state (secondary) creep strain rate (creep compliance) of Sn-Ag-Cu solders that were simply aged at room temperature.

CHAPTER TWO: LITERATURE REVIEW

In tropical climates, ambient temperatures are persistently above room temperature with an average daily high of 60 °C and an average of eight hours of continuous sunshine. Thus, the thermal soaking and aging of solder interconnections in PV modules are likely to occur through continuous exposure of modules over long periods of elevated tropical temperature. The mechanical properties of the IMC layer at the solder interconnections in the module is likely to deteriorate. The change is expected to adversely impact on the strength of the solder interconnections.

2.7.4 Presence of Micro-Cracks in PV Module Caused by Vibrations resulting from hail Storms and High Winds

Microcracks can develop in a cell of PV module during manufacturing, transportation or exposure in service. Repeated climatic events such as snow loads, hailstorms or strong winds increase the crack size and cause its propagation (Köntges et al., 2013, Kohn et al., 2009, Pingel et al., 2009b, Assmus et al., 2011). Tropical climates are characterized by occasional hailstorms and high winds which can trigger cracks in the front glass and in the cell of the PV-module. Wind loads are highly dynamic and thus triggers oscillations. Dynamic loads are known to induce fatigue loads on the materials - especially on PV-cells and connecting wires (Wiese et al., 2010b). When cracks develop in the interconnection circuit of cells, they may create potential locations for heating if both interconnections of a cell are affected by material fatigue. In the worst case, arcing may occur if the conditions for arc ignition are fulfilled (Herrmann et al., 2010, Reil et al., 2012).

Defects from micro-cracks coupled with poor electrical contacts tend to reduce the lifetime of the PV-module in the field (Chaturvedi et al., 2013).

The orientation of a crack could have a varied impact on the power delivery of a PV module. According to (Köntges et al., 2011, Grunow et al., 2005), a single crack that is

CHAPTER TWO: LITERATURE REVIEW

oriented in a way that leads to an electrical separation of a relevant part of the cell could severely affect the power delivery of a PV module. In contrast, cracks that do not lead to an interconnection break marginally affect the performance of a PV module. A detailed complementary study on crack formation after the mechanical load test also demonstrated that many cracks, about 50%, were found parallel to the busbars, thus causing maximum degradation in cell and overall module performance (Kajari-Schröder et al., 2011). These cracks may lead to the disconnection of cell parts and thus power loss (Morlier et al., 2015). High winds cause dynamic loading on PV-cells and can create contact problems from bad soldering of cell interconnection. This could result in increased power losses from PV-modules. Investigations from (Koch et al., 2010) revealed that dynamic mechanical loading affects the mechanical robustness of solder contacts in PV-modules and this could lead to a total interconnection failure.

2.8 Review of Solar PV Cell-Material Constitutive Models for Thermo-mechanical Reliability Prediction

A typical PV module with conventional front-to-back cell interconnection geometry is made of crystalline silicon cells with a number of different materials interconnected and encapsulated. Figure 2-22 presents a layer structure of a standard PV module.

CHAPTER TWO: LITERATURE REVIEW

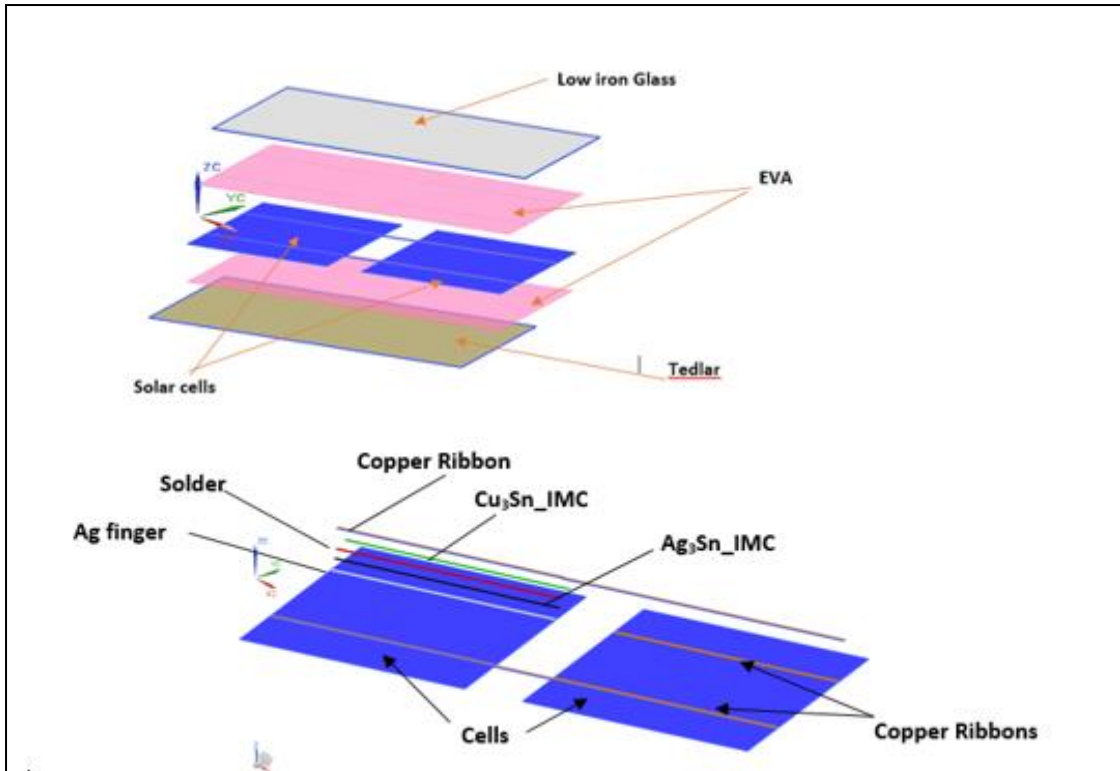


Figure 2 - 22: Layer structure of a typical PV module

Table 2 - 3: Material description for layers solar within a typical PV module

Layer	Material
1 Glass	Glass
2 Encapsulant	EVA (Ethylene Vinyl Acetate)
3 Solar Cell	Silicon
4 Interconnector	Copper
5 Busbar	Silver fingers
6 Rear contact	Aluminum
7 Interconnecting Material	Solder (SnPb, SnAgCu)+ IMC (Cu ₃ Sn, Ag ₃ Sn)
8 Backsheet	Tedlar

2.8.1 Glass

Typically, the glass used for PV modules is tempered with a small iron content with 3.2 mm or 4 mm thickness. The glass offers the PV module mechanical rigidity. It also protects the encapsulated cell from impact from hail storms and harsh weather conditions. It further insulates the solar cell circuit (Quintana et al., 2002). The low iron content leads to greater sunlight transmission. On the other side, the passage of ultraviolet sunlight is unwanted as it damages the underlying polymeric encapsulant and leads to enhanced module degradation (Eitner, 2011). Doping the glass with cerium

CHAPTER TWO: LITERATURE REVIEW

allows the glass to absorb short wavelengths (Quintana et al., 2002). In order to improve the optical properties, a number of module producers use glass with unique surface therapy. The module glass is either textured (Blieske et al., 2003) or coated with an anti-reflection layer (P. Morgensen, 2004., Neander et al., 2006, Eitner, 2011). The mechanical properties of glass in the literature are well-documented Glass exhibits isotropic linear elasticity. Table 2-4 lists the mechanical properties of Glass.

Table 2-4: Mechanical Properties of Glass

Material	Young's Modulus(E) (GPa)	Poisson ratio ν	Density(ρ) g/cm ³	CTE(α) $\times 10^{-6}$ 1/K	Reference
Glass	73	0.23	2.5	8	(Brueckner,1991, Eitner et al., 2011a)

2.8.2 EVA (Encapsulant)

The most frequently used lamination material for photovoltaic modules is EVA (ethylene vinyl acetate). It includes extra substances, such as peroxides, UV-stabilizers, and antioxidants, like all other photovoltaic encapsulation products based on EVA (Eitner et al., 2011a). The copolymer of ethylene and vinyl acetate is ethylene-vinyl acetate (EVA). It is an incredibly elastic material that can be sintered into a rubber-like porous material, yet with great toughness. The porous elastomeric material is three times as flexible as low-density polyethylene (LDPE), with a tensile elongation of 75% at a peak temperature of 205 °F (96 °C) (Porex, 2017). This flexible porous plastic material has outstanding barrier properties, low-temperature toughness, stress cracking resistance, waterproof hot-melt adhesive properties, and ultraviolet radiation resistance. After lamination, the EVA is classified as an elastomer. Crosslinking is an irreversible process that means that a laminated EVA sheet can not soften again without the removal of the covalent nuclear bonds. Unlike thermosets, EVA cannot be re-formed. Unlike thermosets, it is not possible to reshape EVA. A number of studies have established that

CHAPTER TWO: LITERATURE REVIEW

the properties of EVA depend on time and on temperature (Behnken et al., 2003, Liang et al., 2017, Eitner et al., 2009). In this section, the three material models that have been used to predict the behaviour of EVA namely: linear elasticity, temperature-dependent linear elasticity, and linear viscoelasticity are reviewed.

2.8.2.1 Temperature-Dependent Linear Elasticity of EVA

Tensile relaxation tests performed by (Eitner et al., 2010) generated isothermal relaxation curves. These curves were further used by (Paggi et al., 2011) to generate isochronal curves at chosen relaxation times over temperature. Figure 2-23 presents the elastic modulus of EVA versus temperature for different relaxation times.

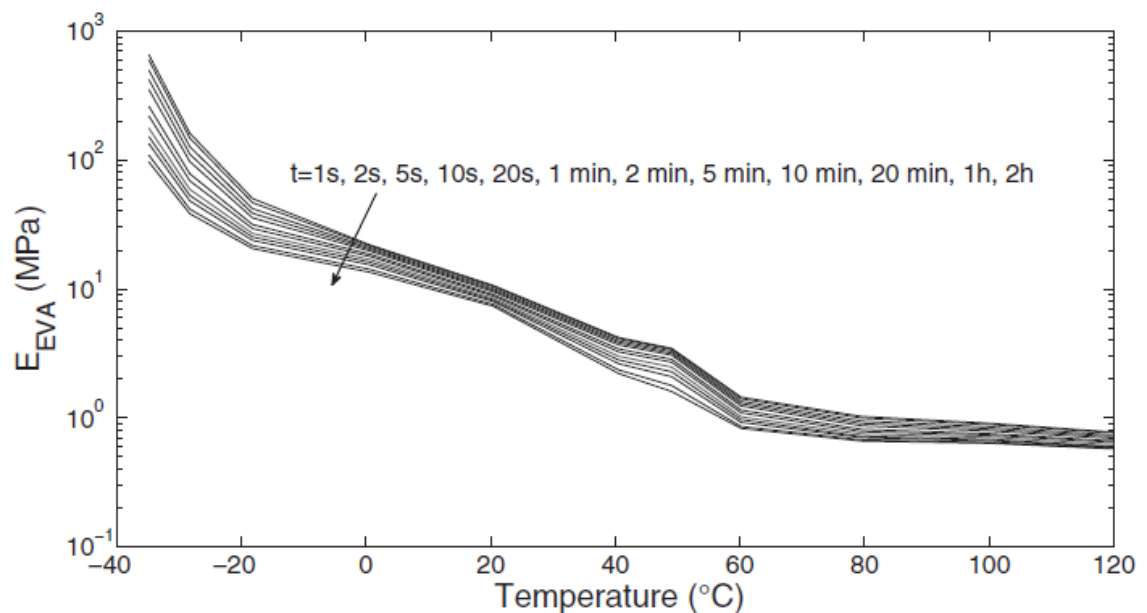


Figure 2-23: Elastic modulus of EVA versus temperature, for different relaxation times (Paggi et al., 2011)

From Figure 2-23 the young modulus of EVA assumes a constant value of 0.5 MPa regardless of relaxation time at temperatures beyond 70 °C. However, Young's modulus increases at lower temperatures below 70 °C and assumes values ranging from 0.5 MPa to 1 GPa based on the moment of relaxation. In the thermo-mechanical analysis,

CHAPTER TWO: LITERATURE REVIEW

Young's modulus versus temperature data at a selected relaxation time could be used to study the temperature-dependent behaviour.

2.8.2.2 Linear Elasticity of EVA

For linear elastic simulations, a minimum and maximum value for Young's modulus are selected with a fixed Poisson's ratio ($\nu = 0.499$). From Figure 2-23, a maximum and minimum Young's modulus of 0.5 MPa and 1 GPa respectively can be selected as extrema values.

2.8.2.3 Linear Viscoelasticity of EVA

Overall, in relation to shear relaxation modulus $G(t)$ and mass relaxation module $K(t)$, the constitutive equation of isotropic viscoelastic materials can be formulated as (Xu and Jiang, 2017, Paggi and Sapora, 2015, Eitner, 2011):

$$\sigma = \int_{-\infty}^t G(t - \tau)e(\tau)d\tau + Ktr(e(t)) \quad (2.1)$$

The scalar time functions are then both $G(t)$ and $K(t)$. Generally, for polymers of up to a few percent ranges, the hypothesis of linearity is true. Nonlinear viscoelastic behaviour begins above that stage (Eitner et al., 2010). The relations above are a generalization of the Maxwell material and indeed the integral equation can be defined as a generalized Maxwell model by making $G(t)$ to assume the Prony series form (Xu and Jiang, 2017, Paggi and Sapora, 2015):

$$G(t) = G_{\infty} + \sum_{i=1}^N G_i \exp\left(-\frac{t}{\lambda_i}\right) \quad (2.2)$$

CHAPTER TWO: LITERATURE REVIEW

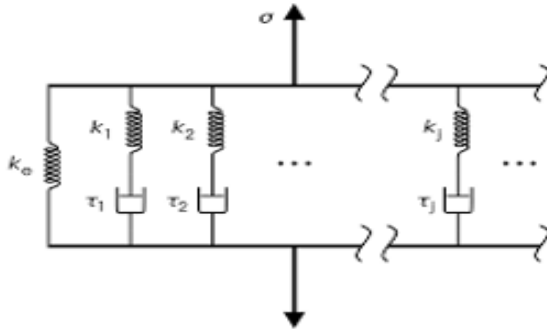


Figure 2 - 24: The Maxwell-Weichert or the Generalized Maxwell model

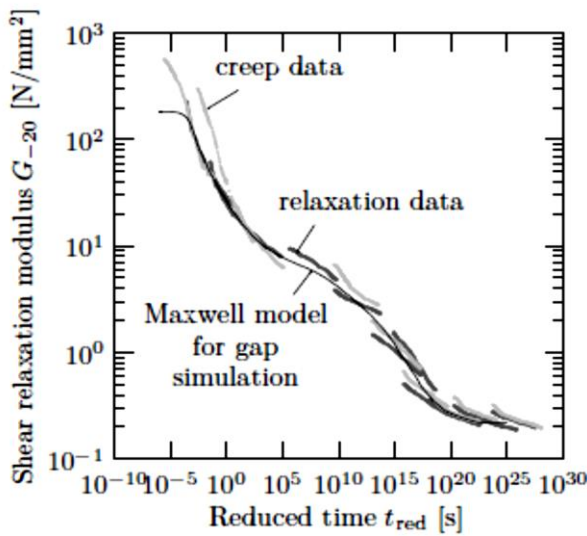


Figure 2 - 26: Mastercurve and Prony fit for shear modulus G of EVA. (Eitner et al., 2011b)

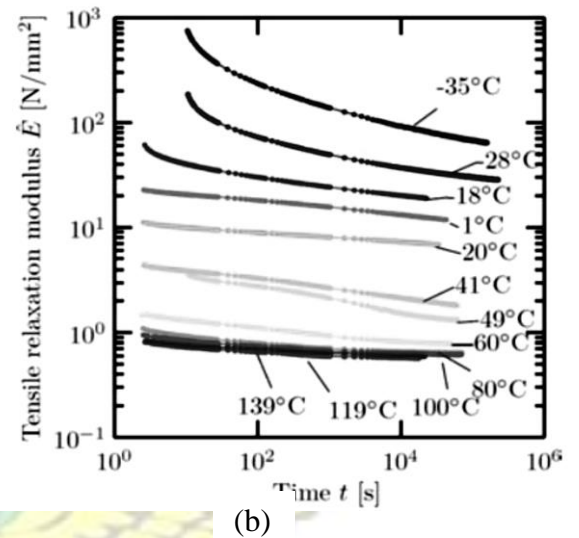


Figure 2-25: Isothermal relaxation curves for EVA obtained by experiments (Eitner et al., 2011b)

Uniaxial relaxation tests must be done and traditionally interpreted using rheological models to accurately determine and model the temperature-dependent properties of EVA. such as Maxwell's model (Ojo and Paggi, 2016). A detailed study of the procedures to obtain the properties of EVA using the classical Maxwell model has been presented by (Eitner et al., 2011b). A number of constitutive models for predicting the linear viscoelastic response of EVA including; Maxwell model, 3-parameter model and the Generalised Maxwell model reviewed by (Eitner et al., 2011b), show that the Generalised Maxwell Model with 26 Maxwell arms provides a good linear viscoelastic

CHAPTER TWO: LITERATURE REVIEW

response for EVA when used with the Prony Series and William-Landel-Ferry (WLF) shift function. The WLF shift is given by (Williams et al., 1955) :

$$\log_{10}\alpha_{T_{ref}}(T) = \frac{-C_1(T - T_{ref})}{C_2 + T - T_{ref}} \quad (2.3)$$

Table 2-5 presents the WLF parameters for EVA and Table 2-6 also presents the viscoelastic material model for EVA with 26 Maxwell Arms.

Table 2 - 5: WLF parameters for EVA (Eitner et al., 2010)

T _{ref} [°C]	C ₁ [-]	C ₂ [°C]
-20	48.44	172.55

Table 2 - 6: Viscoelastic Material Model for EVA with 26 Maxwell Arms (Hasan et al., 2013)

Maxwell parameters			Maxwell parameters			Maxwell parameters		
Arm	Shear Relaxation time λ_i (s)	Relative moduli G_i (MPa)	Arm	Shear Relaxation time λ_i (s)	Relative moduli G_i (MPa)	Arm	Shear Relaxation time λ_i (s)	Relative moduli G_i (MPa)
0	-	0.24	10	10^6	0.8	20	10^{16}	0.3
1	0.001	90	11	10^7	0.6	21	10^{17}	0.25
2	0.01	40	12	10^8	0.7	22	10^{18}	0.12
3	0.1	19	13	10^9	0.8	23	10^{19}	0.07
4	1	11	14	10^{10}	0.8	24	10^{20}	0.03
5	10	7	15	10^{11}	0.7	25	10^{21}	0.02
6	10^2	4	16	10^{12}	0.6	26	10^{22}	0.02
7	10^3	2.5	17	10^{13}	0.56			
8	10^4	1.4	18	10^{14}	0.48			
9	10^5	1	19	10^{15}	0.5			

Other methods based on fractional calculus have also been proposed to accurately predict the linear viscoelastic response of EVA (Di Paola et al., 2013, Paggi and Sapora, 2015, Di Paola et al., 2011) defined by:

CHAPTER TWO: LITERATURE REVIEW

$$\sigma(t) = a \frac{d^\alpha \epsilon}{dt^\alpha} \quad \alpha \in (0,1) \quad (2.4)$$

The relaxation $E(t)$ assumes the power law of the form:

$$E(t) = a \frac{t^{-\alpha}}{\Gamma(1 - \alpha)} \quad (2.5)$$

a (with SI unit of Pa s α) has the mechanical meaning from stiffness ($\alpha = 0$) to viscosity ($\alpha = 1$). Time t is measured in seconds. To obtain the relaxation modulus $E(t)$ of the EVA during cooling using the fractional model, fitted parameters are plotted against a change in temperature with respect to the reference temperature to determine a and α as functions of temperature change.

Due to modification in the material microstructure of EVA at $\Delta T \approx 84$ °C, two different correlations are used to accurately fit the experimental data. These are given as (Paggi and Sapora, 2015):

$$\alpha = \begin{cases} -6.5 \times 10^{-7} \Delta T^3 + 1 \times 10^{-4} \Delta T^2 - 0.0093 \Delta T + 0.225 & \Delta T \leq 84 \text{ }^\circ\text{C} \\ -1.2 \times 10^{-7} \Delta T^3 + 5.4 \times 10^{-5} \Delta T^2 - 0.0083 \Delta T + 0.474 & \Delta T > 84 \text{ }^\circ\text{C} \end{cases} \quad (2.6)$$

$$a = \begin{cases} 733.5 \exp - 0.26 \Delta T + 81.2 \exp - 0.04 \Delta T & \Delta T \leq 84 \text{ }^\circ\text{C} \\ 6.5 \times 10^6 \exp - 0.17 \Delta T + 1.7 \exp - 0.004 \Delta T & \Delta T > 84 \text{ }^\circ\text{C} \end{cases} \quad (2.7)$$

Although the fractional calculus model has the advantage over the Prony series because it only involves two parameters (a and α) to accurately model the EVA's viscoelastic behaviour, unlike the generalized Maxwell model, it is not currently present in some commercial Finite Element Modelling (FEM) packages as standard options. However, it is possible to code as a user-defined constitutive relation in most FEM packages.

CHAPTER TWO: LITERATURE REVIEW

2.8.3 Silicon

Crystalline silicon has an ordered crystal structure, ideally lying in a predetermined place with each atom. Miller indices define the crystal orientation in single crystalline silicon fabric. Silicon has a cubic symmetrical cubic structure and thus (100), (010) are equal planes and referred jointly to '{100}' braces. Similarly, the direction of the crystal is described using square brackets and jointly described using triangular brackets ' $\langle 100 \rangle$ ' (Pveducation, 2013). A conventional Silicon cell features a phosphorous or boron-doped Silicon 150–350 nm profound diffusion layer, a Silicon Nitride passivation layer (anti-reflective coating) approximately 80 nm thick. Silicon has a 15–25 μm thick metallization grid. For effective carrier transport, the H-like pattern silver paste at the front (split into two device components in particular; contact busbars and contact fingers). A 25–50 μm thick aluminum metallization at the back (contact pads) to boost mechanical contact and collect current from the metallized region and a front surface of 2–15 μm high randomly distributed pyramids to boost the transmission of photons into the silicon absorber (Eitner et al., 2011b, Glunz et al., 2012). Crystalline silicon cells are produced of normal 125 mm / 125 mm or 156 mm / 156 mm pseudo-square or full-square cells (see Figure 2-4). The studied crystalline silicon is generally oriented in the direction of $\langle 100 \rangle$ i.e. the edges of the Silicon cells are parallel to the direction of $[100]$. As cubic symmetry holds in this direction, it follows that:

$$E_{\langle 100 \rangle} = E_{\langle 010 \rangle} = E_{\langle 001 \rangle} = E_x = E_y = E \quad (2.8)$$

Silicon is a brittle material that shows basically no ductile effects at all. The curve depicting the stress-strain relationship in Silicon is linear to fracture. Therefore, linear elasticity is the right model to describe monocrystalline silicon mechanics. However, owing to the crystallographic structure, it has anisotropic material characteristics. The elastic constants, therefore, have distinct values for distinct loading directions. The

CHAPTER TWO: LITERATURE REVIEW

wafer coordinate system matches the materials coordinate system for a wafer cut out of a monocrystalline ingot with the normal surface in $\langle 100 \rangle$ -direction and edges along the $\langle 010 \rangle$ -and $\langle 001 \rangle$ -direction. According to Greenwood (Greenwood, 1988), the matrix C of the constituent equation written in the form of a matrix becomes:

$$C = \begin{bmatrix} C_{11} & C_{12} & C_{12} & 0 & 0 & 0 \\ C_{12} & C_{11} & C_{12} & 0 & 0 & 0 \\ C_{12} & C_{12} & C_{11} & 0 & 0 & 0 \\ 0 & 0 & 0 & C_{44} & 0 & 0 \\ 0 & 0 & 0 & 0 & C_{44} & 0 \\ 0 & 0 & 0 & 0 & 0 & C_{44} \end{bmatrix} \quad (2.9)$$

With the values given in Table 2-7 for C_{11} , C_{12} , and C_{44} . The matrix C structure usually applies to any material with cubic symmetry (Bower, 2009). C is inverted in order to calculate Young's module in the x-direction and then holds for a uniaxial stress state such as:

$$\varepsilon_{11} = \frac{C_{11} + C_{12}}{C_{11}^2 + C_{11}C_{12} - 2C_{12}^2} \sigma_{11} \quad (2.10)$$

$$E_x = C_{11} - 2 \frac{C_{12}^2}{C_{11} + C_{12}} \quad (2.11)$$

CHAPTER TWO: LITERATURE REVIEW

Table 2-7: Lists the Mechanical properties of silicon determined from a 3-point bending test.

Quantity	Unit	Value	Reference
C_{11}	[GPa]	164.8	(Greenwood, 1988)
C_{12}		63.5	
C_{44}		79.0	
$\left(\frac{dC_{11}}{dT}\right)/C_{11}$	$[10^{-6} 1/K]$	-122	(Greenwood, 1988)
$\left(\frac{dC_{12}}{dT}\right)/C_{12}$		-162	
$\left(\frac{dC_{44}}{dT}\right)/C_{44}$		-97	
$E_{<100>}$	[GPa]	129.5	(Greenwood, 1988)
$E_{<110>}$		168.0	
$E_{<111>}$		186.6	
$\left(\frac{dE_{<100>}}{dT}\right)/E_{<100>}$	$[10^{-6} 1/K]$	-63	(Greenwood, 1988)
$\left(\frac{dE_{<110>}}{dT}\right)/E_{<110>}$		-80.3	
$\left(\frac{dE_{<111>}}{dT}\right)/E_{<111>}$		-45.6	
$\alpha(T = 220K)$	$[10^{-6} 1/K]$	1.717	(Lyon et al., 1977)
$\alpha(T = 260K)$		2.225	(Lyon et al., 1977)
$\alpha(T = 300K)$		2.614	(Roberts, 1981)
$\alpha(T = 340K)$		2.915	(Roberts, 1981)
$\alpha(T = 420K)$		3.342	(Roberts, 1981)

2.8.4 Copper ribbons

Copper is a metallic material whose characteristics are well recognized. The copper used for solar cell interconnection is a highly conductive soldered ribbon strip along the length of the cell, the extended part of which is soldered to the back of a neighboring cell to enable current transfer from the front of one cell to the back of a neighboring cell in series connections (Kopecek et al., 2006a, Zarmai et al., 2015b). Copper has excellent electrical conductivity of around $58 \times 10^{-6} / \Omega m$. which is, after silver, the highest value of all metals (Roos et al., 2017). The size of a typical ribbon for Silicon

CHAPTER TWO: LITERATURE REVIEW

cell is 130 μm thick and 2 mm wide while the solder coating has a thickness of 20 μm .

Table 2-8 lists the mechanical properties for copper in general.

Table 2-8: Mechanical Properties of Copper

Copper Type	Copper	Copper, hard drawn	Copper, soft wrought	Copper	Copper	Copper	Pure Copper	Copper ribbon (type 1)
E(GPa)	117	124.1	103.4	120	100-130	125		86.1
ν (-)				0.34		0.34		
α (10^{-6} 1/K)	17				16.8	17.7	16.5	
ρ (g/cm ³)	8.907				8.93	8.93	8.96	
Reference	(Brady et al., 1956)	(Brady et al., 1956)	(Brady et al., 1956)	(Hornbogen and Warlimont, 2006)	(Nicht auf den Aufschwung, 2008.)	(Pintat et al., 2000)	(Shackelford et al., 2016)	(Wiese, Meier, et al. 2010)

A recent study by (Wiese et al., 2010b) on the mechanical properties of copper ribbons used in solar modules finds Young's modulus, E, of plated copper ribbons to be significantly lower than those of pure copper. (Wiese et al., 2010b) also determined the temperature dependence of the Young's modulus ($dE/dT = -0.056$ GPa/K for $T = (40, \dots, 120^\circ\text{C})$) and constructed a bilinear model to include plastic deformation. The researchers discovered that for linear elastic deformation behaviour of the copper, for strain values below 1% and for higher strains, the Hooke's law was not applicable. Presented in Table 2-9 are the model parameters for copper ribbons derived from extrapolation calculations.

Table 2-9: Bilinear model for the constitutive behaviour of copper ribbons (Herrmann et al., 2010)

Temperature (T) (°C)	Young's Modulus (E) (GPa)	Yield stress (σ_y) (MPa)	Hardening Coefficient (h)
-40	91.5	116.2	1000
25	85.7	95.5	1000
125	82.0	62.6	1000
225	79.2	30.0	1000

CHAPTER TWO: LITERATURE REVIEW

A temperature-dependent bilinear model could, therefore, be used in modelling of the environmental loadings during the operation of PV modules.

2.8.5 Solder (SnAgCu, Sn/Pb)

Solar cells are usually soldered to interconnect into strings to create a PV module. Until recently, the predominant choice of soldering substances was eutectic or near-eutectic tin/lead (Sn / Pb) solder (Melting Temperature $T_M=183^\circ\text{C}$) thanks to excellent longevity and reliability (Hongtao et al., 2006). Though restriction on the use of certain Hazardous Substances (RoHS) guidelines which took effect from 1st July 2006, prohibits the use of Sn/Pb solder since Pb is a hazardous material, the PV industry is excluded from this directive. Regardless of the toxicity of Pb based solders ($\text{Sn}_{60}\text{Pb}_{40}$ and $\text{Sn}_{62}\text{Pb}_{36}\text{Ag}_2$), the PV industry continues to use them for soldering cell interconnections (Geipel et al., 2017). Nevertheless, research continues in the quest to finding suitable solder alternatives.

Currently, there are different alloy options for high-temperature electronics soldering. However, SnAg and SnAgCu alloys remain the most studied and widely used solder materials in the PV manufacturing industry. These lead-free solders are predominantly tin-based with melting points (220°C) that are in excess of 40 K above conventionally used solders for cell interconnection. Using lead-free solders may result in higher thermal stress for the cells with a considerably higher amount of cell damage (Nieland et al., 2007). One other key issue affecting the use of lead-free solders in PV module manufacture is wettability. To enhance wettability, a more aggressive flux media is required. However, care should be taken to remove flux residues as they tend to restrict module lamination that can also offer long-term reliability issues.

CHAPTER TWO: LITERATURE REVIEW

Solder alloys are generally known to display nonlinear visco-plastic behaviour. The main components of the deformation are elastic, plastic and creep strains (Cuddalorepatta et al., 2010). The thermo-mechanical response of solders can be represented by constitutive models made from a combination of elastic, plastic, viscoelastic and visco-plastic/creep models (Sitaraman and Kacker, 2005). It is essential to use a model that correctly defines the lead-free solder along with suitable model constants because the thermo-mechanical reliability of PV modules is mainly dependent on solder joints ' fatigue and creep behaviour. The Young's modulus of solder has been discovered to depend on temperature. Table 2-10 enlists the elastic properties for SnPb and Pb-free solders.

Table 2-10: Elastic Properties and Thermal Expansion Coefficient of Lead-free and Tin-Lead Solders (Cuddalorepatta, Dasgupta, et al., 2010)

SnAgCu-Solder			SnPb-Solder		
Temperature (°C)	Young's Modulus (GPa)	Poisson's Ratio	Temperature (°C)	Young's Modulus (GPa)	Poisson's Ratio
-50	57.30	0.3	-70	38.1	0.4
-25	55.79	0.3	20	30.2	0.4
0	54.22	0.3	140	19.7	0.4
25	52.62	0.3			
50	50.97	0.3			

Table 2-11 lists the various constitutive models used in predicting the thermo-mechanical response of solders. The Garofalo-Arrhenius model (Amalu and Ekere, 2012b, Zhang et al., 2013, Zarmai et al., 2015a) using accumulated creep strains and dissipated strain energy density which involves exponential dependence on temperature and a hyperbolic sine dependence on high stress is widely accepted for the characterization of solder alloys. This model is used in this study to formulate the creep response of the solders and IMCs. Other popular constitutive models are; the Double

CHAPTER TWO: LITERATURE REVIEW

Power-law [58-60] and Annand's model (Cheng et al., 2000, Zhang et al., 2014, Wilde et al., 2000).

The creep parameters of SnAgCu and SnPb solder for the Garofalo-Arrhenius model are listed in Table 2-12.

KNUST



CHAPTER TWO: LITERATURE REVIEW

Table 2-11: Constitutive Equations for Predicting the Thermo-mechanical Response of Solders.

S/N	Modelling approach	Prediction model	Constitutive equation	Ref.
1	Accumulated creep strains and dissipated strain energy density (Exponential dependence on T: sine-hyperbolic dependence on σ (high stress))	Garofalo-Arrhenius	$\dot{\epsilon}_{cr} = c_1 [\sinh(c_2 \sigma)]^{c_3} \exp\left(\frac{-C_4}{T}\right)$	(Amalu and Ekere, 2012b, Zhang et al., 2013, Zarmai et al., 2015a)
2	Power-exponential dependence on T: power-law dependence on grain size (d) and on stress(σ)	Modified Dorn	$\dot{\epsilon}_{cr} = \frac{AGb}{KT} \left(\frac{b}{d}\right)^P \left(\frac{\sigma}{G}\right)^n D_0 \exp\left(-\frac{Q}{KT}\right)$	(Jones and Ashby, 2011)
3	Two-term model with exponential dependence on T; power-law dependence on σ (different dependencies at low and high stresses)	Double-power law	$\dot{\epsilon}_{cr} = A_1 \exp\left(\frac{-H_1}{KT}\right) \left(\frac{\sigma}{\sigma_n}\right)^{n_1} + A_2 \exp\left(\frac{-H_2}{KT}\right) \left(\frac{\sigma}{\sigma_n}\right)^{n_2}$	(Wiese and Wolter, 2004, Syed, 2006, Schubert et al., 2003)
4	Exponential dependence on T: sine-hyperbolic dependence on σ (high stress)	Garafalo-hyperbolic sine	$\dot{\epsilon}_{cr} = A [\sinh(\alpha \sigma)]^n \exp\left(\frac{-H_1}{KT}\right)$	(Schubert et al., 2003, Pang et al., 2003)
5	Exponential dependence on T; sine-hyperbolic dependence on stress (s is the deformation resistance and h_0 is the hardening/softening constant)	Anand	$\dot{\epsilon}_p = A \left[\sinh\left(\frac{\xi \sigma}{S}\right) \right]^{1/m} \exp\left(\frac{-Q}{KT}\right)$ $\dot{s} = \{h_0 (B)^a \frac{B}{ B }\} \dot{\epsilon}_p, \quad B = 1 - \frac{s}{s^*}$ $s^* = \hat{s} \left[\frac{\dot{\epsilon}_p}{A} \exp\left(\frac{Q}{kT}\right) \right]^n$	(Cheng et al., 2000, Zhang et al., 2014, Wilde et al., 2000)
6	Energy-partitioning (Shear strain)	[Elastic(el)+ plastic(pl) + Primary Creep(pcr) + Secondary creep(scr)]	$\gamma = \gamma_{el} + \gamma_{pl} + \gamma_{pcr} + \gamma_{scr}$	(Zhang et al., 2004)

CHAPTER TWO: LITERATURE REVIEW

			$\gamma = \frac{\tau}{G} + \left(\frac{\tau}{C_{pl}}\right)^{1/n} + \gamma_{pcr-sat} \left(1 - \exp(-A_{pcrt})\right) + A(\sinh(\alpha\tau))^n \exp\left(\frac{-Q}{RT}\right)$	
7	Strain damage evolution	Internal damage variable coupled with a unified viscoplastic model	$D = 1 - e^{-\Delta e - \Delta\phi / N_0 k T / \bar{m}_0}$ $\Delta e - \Delta\phi = \frac{1}{\rho} \left(\int_{\varepsilon_0}^{\varepsilon} \sigma_{ij} d\varepsilon_{ij}^{vp} \right) - \int_{t_0}^t \frac{1}{\rho} \frac{\partial q_i}{\partial x_i} dt + \int_{t_0}^t \dot{\gamma} dt$	(Tang and Basaran, 2003)
8	Energy dissipation based.	Steady-state creep model	$\frac{d\varepsilon_s}{dt} = C_{ss} [\sinh(\alpha\sigma)]^n \exp\left(\frac{-Q_a}{kT}\right)$	(Darveaux and Banerji, 1992)
9	Power law on stress: k is the initial yield stress, R is the isotropic hardening, K and n represent material constants, tensors S0 and X0 are the deviatoric parts of stress and back stress tensors	Chaboche	$\dot{\varepsilon} = \frac{3}{2} \dot{p} \frac{S' - X'}{J(S' - X')} \dot{p}$ $= \left\langle \frac{J(S' - X') - R - k}{K} \right\rangle^n$ $J(S' - X') = \sqrt{\frac{3}{2}} (S' - X') : J(S' - X')$	(Chaboche and Rousselier, 1983)

CHAPTER TWO: LITERATURE REVIEW

Table 2-12: Creep Parameters for Garofalo-Arrhenius model

Solder Material	C_1 (1/s)	C_2 (MPa) ⁻¹	C_3	C_4	Reference
SnAgCu	2.78E+05	2.45E-08	6.41	6500	(Amalu and Ekere, 2016, Zarmai et al., 2015a)
SnPb	$\frac{926 \times (508 - \theta)}{\theta}$	$\frac{1}{37.78 \times 10^6 - 74414 \times \theta}$	3.3	6360	(Deplanque et al., 2005)

Where θ is the temperature in Kelvin (K).

2.8.6 IMC's (Cu₃Sn, Cu₆Sn, Ag₃Sn)

The presence and impact of IMC's (Cu₃Sn, Ag₃Sn) in solar cell interconnects have been discussed in detail in section 2.6.3 and will not be repeated here. A number of researchers (Kumar and Jung, 2013, Deng et al., 2004, R.J. Fields) have determined the properties of Cu₃Sn and Ag₃Sn experimentally. Though Cu₃Sn and Ag₃Sn exhibit slight anisotropy from research, assuming isotropic behaviour for the IMC's is a fair approximation. In the thermo-mechanical analysis, the IMCs are modelled as linear elastic materials exhibiting creep (tensile creep behaviour). Table 2.13 lists the mechanical properties of Cu₃Sn and Ag₃Sn IMCs.

CHAPTER TWO: LITERATURE REVIEW

Table 2-13: Mechanical Properties of Cu_3Sn and Ag_3Sn IMCs

Material	Young's Modulus(E) (GPa)	Poisson ratio ν	Density(ρ) kg/m^3	CTE(α) $\times 10^{-6}$ 1/K	Reference
Cu_3Sn	80 - 153	0.3	8900	23	(Kumar and Jung, 2013, Deng et al., 2004, R.J. Fields, T. Siewert, 2002)
Ag_3Sn	77.06 - 82.6	0.347	-	-	(Kumar and Jung, 2013, Deng et al., 2004, R.J. Fields)

2.8.7 Aluminium Rear Contact

The conductive aluminum paste on the rear-side of the silicon wafer creates a uniform, high-quality back surface field (BSF). A uniform BSF with strong adhesion to the Si-wafer improves the efficiency of the solar cell. (Popovich et al., 2013) showed in their work that the Al-BSF layer has a complex composite-like microstructure, consisting of three main components: 1) spherical (3-5 μm) hyper-eutectic Al-Si particles, surrounded by a thin aluminum oxide layer (150 - 200 nm); 2) a bismuth-silicate glass matrix (3.3%) and 3) pores (14%).

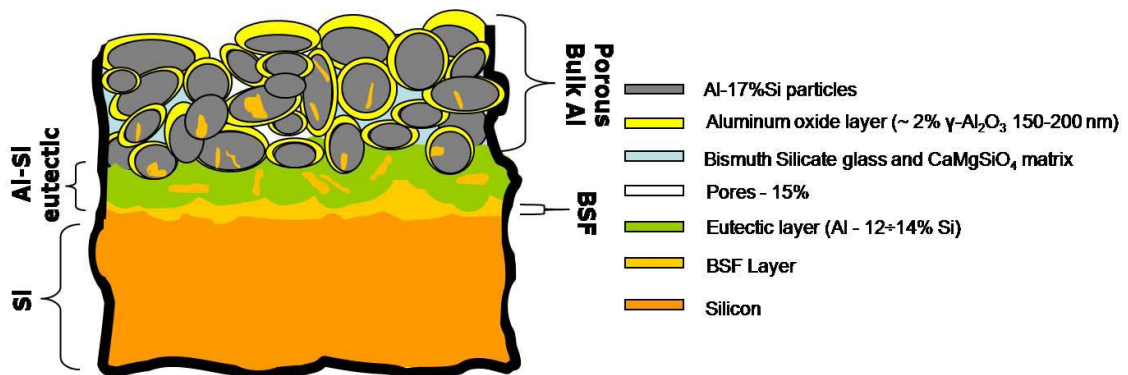


Figure 2-27: Model of the Rear Face of a Silicon Solar Cell with Corresponding Microstructural Features (Popovich et al., 2013)

CHAPTER TWO: LITERATURE REVIEW

(Popovich et al., 2013) further established that the eutectic layer can induce some plasticity at the outer fibre preventing the formation of critical micro-cracks at the silicon wafer surface. Young's modulus obtained from their research by a nano-indentation test was found to be 44.5 GPa which showed a good agreement with Young's modulus from the theoretical calculation. However (Wiese et al., 2010a) used Young's modulus of Aluminium paste of 6 GPa in their analysis of technological and mechanical problems in interconnection technologies for photovoltaic modules. (Chen, 2008) in their work on residual stress and bow analysis for silicon solar cells induced by soldering used Young's modulus of 3.5 GPa. Table 2-12 lists the mechanical properties used for the thermo-mechanical analysis of SPV modules.

Table 2-14: Mechanical Properties of Aluminium Rear Contact

Young's Modulus E (GPa)	Poisson ratio (ν)	CTE α ($10^{-6}/K$)	Yield Strength (σ_y) (MPa)	Reference
3.5	0.35	23.1	28.3	(Chen, 2008)
6.0	0.35	11.9	28.3	(Wiese et al., 2010a)

2.8.8 Silver (Ag) Busbars

In conventional silicon solar cells, metallization for busbars is achieved using rectangular-shaped strips printed on the front and rear side of the cell. Busbars conduct the direct current produced by the solar cell from the incoming photon. The busbars are made of copper and plated with silver to improve current conductivity (front side) as well as to reduce oxidization (rear side) (Niclas, 2016). A high-performance, high-quality silver paste should offer features such as good printability, fine line and high aspect ratio. It must possess a high screen life, solderability as well as efficiency and reliability (Mohamed M. Hilali, 2004). The mechanical properties of silver paste for busbars are listed in Table 2-15.

CHAPTER TWO: LITERATURE REVIEW

Table 2 - 15: Mechanical Properties of Silver Busbar

Young's Modulus E (GPa)	Poisson ratio (ν)	CTE α ($10^{-6}/K$)	Yield Strength (σ_y) (MPa)	Reference
72.4	0.37	10.4	26.423	(Zarmai et al., 2015a)

2.8.9 Tedlar Backsheet

The backsheet protects the encapsulated solar cells from external influences such as humidity, harsh ambient exposure, aggressive substances or scratches. It also serves as an electric insulating material. The most widely used backsheet is the Tedlar from DUPont. (Eitner et al., 2011a) performed sample test measurements at three different temperatures (20 °C, 80°C and -35°C). The test setup monitored the force, temperature, elongation strain and transverse strain. The summary of the test results is listed in Table 2-16.

Table 2-16: Elastic Properties of Isovolt Icosolar 2442 from Tensile Testing with Mean Value and Largest Distance to Minimum or Maximum value (Eitner et al., 2011a)

-35°C 3 Samples tested	20 °C 4 Samples tested	80°C 5 Samples tested	20°C Transverse 5 Samples tested
E [MPa]: 4015.0 ± 21.81	3584.5 ± 53.2	1966.9 ± 123.4	3790.4 ± 43.2
$\nu : 0.289 \pm 0.007$	0.271 ± 0.002	0.295 ± 0.009	0.301 ± 0.007

Though the test results from Table 2-16 reveal a slight anisotropy at room temperature, assuming isotropic material behaviour would be a good approximation. Thus the values $E=3.5$ GPa and $\nu = 0.29$ could be used in simulating material behaviour.

CHAPTER TWO: LITERATURE REVIEW

2.9 Review of Life Prediction Models for Thermal Cycling Analysis

Fatigue modelling can be described to consist of four primary steps namely;

- i. Selection of theoretical or constitutive equations with appropriate assumptions.
- ii. Translating the constitutive equation into an FEA program and creating the model.
- iii. Using the FEA results to create a model to predict the number of cycles to failure.
- iv. Testing and verifying the model using thermal cycling data.

In general, the total shear strain($\dot{\gamma}$) is given by:

$$\dot{\gamma} = \dot{\gamma}_{\text{elastic}} + \dot{\gamma}_{\text{plastic}} + \dot{\gamma}_{\text{creep}} \quad (2.12)$$

where, $\dot{\gamma}_{\text{elastic}}$, $\dot{\gamma}_{\text{plastic}}$ and $\dot{\gamma}_{\text{creep}}$ refers to the elastic, plastic and creep components of the shear strain.

Determining the magnitude of each of these components in actual life testing is practically difficult. Recent research efforts have been focused on constructing unified constitutive models and damage evolution models for solder joint fatigue life prediction. The review of fatigue models presented here are classified into five categories namely; stress-based, plastic strain-based, creep strain-based, energy-based, and damage based. Generally, stress-based fatigue models are based on the application of a force or stress to a component resulting in a strain. This typically applies to a vibrational or a physically stressed component. In the strain-based fatigue model, a strain is applied resulting in stresses within a component.

Thermal fatigue strains resulting from CTE mismatch lie in this category. The plastic strain-based fatigue model focuses on the time-independent effects whereas the creep strain accounts for the time-dependent effects. Solder by nature creeps when subjected

CHAPTER TWO: LITERATURE REVIEW

to thermal loading. The energy-based models, on the other hand, are based on evaluating the overall stress-strain hysteresis energy of the solder joint. The damage based models focus on calculating accumulated damage caused by crack propagation through the solder connection using a fracture mechanics approach. Table 2-17 presents a summary of selected solder joint fatigue models. In each category, a model is presented with the relevant equations and parameters, and applicable packages.



CHAPTER TWO: LITERATURE REVIEW

Table 2 - 17: Summary of selected solder joint fatigue models

S/N	Fatigue Model	Model Class (Parameter)	Model Equations and Constants	Coverage	Application	Reference
1	Coffin-Mason	Plastic Strain	$\frac{\Delta \epsilon_p}{2} = \epsilon'_f (2N_f)^c$ ϵ'_f - fatigue ductility coefficient c- fatigue ductility exponent	Low cycle fatigue	All	(Kilinski et al., 1991)
2	Total Strain (Coffin-Mason-Basquin)	Plastic + Elastic strain	$\frac{\Delta \epsilon}{2} = \frac{\sigma'_f}{E} (2N_f)^b + \frac{\Delta \epsilon_p}{2} = \epsilon'_f (2N_f)^c$ σ'_f -fatigue strength coefficient b-fatigue strength exponent (Basquin's exponent)	High and Low cycle Fatigue	All	(Kilinski et al., 1991)
3	Solomon	Plastic Shear Strain	$\Delta \gamma_p N_p^\alpha = \theta, \quad \theta = \frac{1}{\epsilon'_f}$ $\Delta \gamma_p$ -plastic shear strain range, α -material constant	Low cycle fatigue	All	(Pang et al., 1998)
4	Engelmaier	Total Shear Strain	$N_f = \frac{1}{2} \left[\frac{\Delta \gamma_t}{2\epsilon'_f} \right]^{1/c} \quad c = -0.442 - 6 \times 10^{-4} \bar{T}_s + 1.74 \times 10^{-2} \ln(1 + f)$ \bar{T}_s -the mean cyclic solder joint temperature in °C f- the cyclic frequency in cycles/day	Low cycle fatigue	Lead and leadless, TSOP	(Pang et al., 1998)
5	Miner	Superposition(plastic + creep)	$\frac{1}{N_f} = \frac{1}{N_p} + \frac{1}{N_c}$	Plastic shear and Matrix creep	PQFP, FCOB w/fill	(Pang et al., 1998, Yeo et al., 1996, Pang, 1997)

CHAPTER TWO: LITERATURE REVIEW

6	Knecht and Fox	Matrix creep (mc)	$N_f = \frac{C}{\Delta\gamma_{mc}}$	Matrix creep only	All	(Knecht and Fox, 1991)
7	Strain Range Partitioning (SRP)	Plastic and creep strain in tension and compression	$\frac{1}{N_f} = \frac{F_{pp}}{N_{pp}} + \frac{F_{cc}}{N_{cc}} + \frac{F_{cp}}{N_{cp}} + \frac{F_{pc}}{N_{pc}}$ <p>F_{ij}- fraction of total inelastic strain range of the hysteresis loop.</p>	Hysteresis Curve	All	(Kilinski et al., 1991)
8	Syed	Accumulation of creep strain per cycle	$N_f = ([0.022D_{gbs}] + [0.063D_{mc}])^{-1}$ $N_f = (0.106\varepsilon_{acc}^I + 0.045\varepsilon_{acc}^{II})^{-1}$ $N_f = (0.0468\varepsilon_{acc})^{-1}$ $N_f = (0.0513\varepsilon_{acc})^{-1}$ <p>ε_{acc}-accumulated creep strain D_{gbs}, D_{mc} accumulated equivalent creep strain per cycle for grain boundary sliding (gbs) and matrix creep (mc)</p>	Full Coverage	PBGA, SMD, NSMD	(Syed, 1996, Syed, 1997, Syed et al., 1999) (Syed, 2004)
9	Akay (based on Dasgupta)	Total strain energy	$N_f = \left(\frac{\Delta\bar{W}_{total}}{W_0} \right)^{1/k}$ <p>$\Delta\bar{W}_{total}$- total strain energy W_0, k - fatigue coefficients</p>	Joint geometry accounted for.	LLCC, TSOP	(Akay et al., 1997)
10	Liang	Stress/Strain energy density based	$\bar{N}_f = C(W_{ss})^{-m}$ <p>W_{ss}- stress-strain hysteresis energy density C and m - temperature-dependent material constants</p>	Isothermal low fatigue	BGA and leadless joint	(Liang et al., 1997)
11	Heinrich	Energy Density-based	$N_0 = 18083\Delta W^{-1.46}$	Hysteresis curve	BGA	(Wu et al., 1998)
12	Gustafsson (based on Darveaux)	Energy Density-based	$N_{\alpha w} = N_{0s} + \frac{a-(N_{0s}-N_{0p})\frac{d_{ap}}{dN}}{\frac{d_{as}}{dN} + \frac{d_{ap}}{dN}}$ <p>a-total possible crack length</p>	Hysteresis Curve	Leadless, PBGA	(Gustafsson, 1998)

CHAPTER TWO: LITERATURE REVIEW

13	Pan	Critical Accumulated Strain Energy (CASE)	$C = N_f^*(aE_p + bE_c)$ <p>C-critical strain energy density</p>	Hysteresis Curve	LCCC	(Pan, 1994)
14	Syed	Accumulated creep strain Energy density	$N_f = (0.0069W_{acc})^{-1}$ $N_f = (0.0015W_{acc})^{-1}$ $N_f = (0.0019W_{acc})^{-1}$ <p>W_{acc}- accumulated creep strain energy density per cycle</p>	Full Coverage	SAC405 alloys	(Syed, 2004)
15	Stolkarts	Damage Accumulation	$N_f = \frac{1 - (1 - d_f)^{k-1}}{(k + 1)L}$ <p>d_f-amount of damage ($d_f = 0.5$ for solders), k-material constant, $L = \int f dt$ f-initial rate of damage of remaining undamaged material in the representative volume element</p>	Hysteresis Curve and Damage evolution	All	(Stolkarts et al., 1998)
16	Norris and Landzberg	Temperature and Frequency	$\frac{N_{test}}{N_{use}} = \left(\frac{\Delta T_{test}}{\Delta T_{use}}\right)^2 + \left(\frac{f_{use}}{f_{test}}\right)^{1/3} \phi(T_{max})$ <p>f -is the thermal cycling frequency ΔT-temperature change ϕ- Arrhenius function at maximum temperature during test and use</p>	Test condition versus use conditions	All	(Mei, 1996)

CHAPTER TWO: LITERATURE REVIEW

From the summary of the review of selected fatigue models from Table 2-14, (Syed, 2004) models appear to be the most widely accepted and easier to apply. These models will be used in predicting the fatigue life of the soldered interconnections in this study. Creep strain energy density offers a more robust damage indicator in the soldered joint as it is based on the deformation that is internally stored throughout the volume of the joint during thermal loading. Thus the creep strain energy density captures the entire deformation in the joint. In practice, the change in accumulated creep energy density per cycle (ΔW_{acc}) averaged over the volume of solder is used for predicting the cycles of failure. The ΔW_{acc} is obtained by computing the average change in strain energy density (ΔW_{ave}) from the finite element analysis (FEA) results and then normalised with the volume of the solder used in generating the geometric model. Thus

$$\Delta W_{ave} = \frac{\sum_i^n W_2^i V_2^i}{\sum_i^n V_2^i} - \frac{\sum_i^n W_1^i V_1^i}{\sum_i^n V_1^i} \quad (2.13)$$

Where W_2^i , W_1^i is the total accumulated strain energy density in one element at the endpoint and the starting point of one thermal cycle respectively. V_2^i , V_1^i is the volume of an element at the endpoint and start point of one cycle respectively, and n is the number of selected elements used.

CHAPTER TWO: LITERATURE REVIEW

2.10 Summary

Interconnection technologies employed in the manufacture of the crystalline silicon photovoltaic (c-Si PV) module are reviewed for application in the manufacture of a robust PV module for increased thermomechanical reliability during operations in the tropical climate. The factors accelerating the degradation of solder joints in c-Si PV interconnection operating in tropical regions are also reviewed as well as the associated research and development challenges. The review identified back-contacted solar cells (BC) design as the architecture that potentially eliminates recombination losses. Similarly, the EWT cell architecture is found to record higher cell efficiencies up to 21.4% while the MWT cell design demonstrates initial superior energy yield compared with conventional solar cells. It is found that the alternate p- and n-type interconnections offer a simpler interconnection procedure and a higher yield during module fabrication while the Honeycomb design produces excellent packing density that reduces the 'double bounce' effect.

The review found that the amount of water necessary to accelerate the corrosion process in PV modules is yet to be quantified. It identified that the temperature cycling load from natural weathering in the tropical ambient is lower than the load from IEC 61215 test conditions.

However, the larger number of cycles produced by natural weathering test conditions within the region may culminate in different material fatigue yield characteristics. The research findings reveal that isothermal aging led to about 50% reductions in several key material properties including stiffness, yield strength, and ultimate strength. It is identified that a significant amount and intensity of hail storms and high winds that characterise the region make micro-cracks develop in the cells and cause untimely module failure. The phenomenon excessively increases the dynamic loads on the

CHAPTER TWO: LITERATURE REVIEW

modules and negatively impacts on module mechanical integrity and reliability. The elevated ambient temperatures increase the rate of IMC growth in the interconnection of modules – leading the modules operating in the region to increasing interconnection failure.

The constitutive models for solar PV materials and fatigue life prediction models for solders were reviewed in order to identify the proper material constitutive and life prediction models to be utilized in this study. Previous efforts in finite element modelling by a number of researchers have been reviewed. The review reveals discrepancies in the geometric models as well as material constitutive models of the solar cell which were deployed by various researchers in their respective studies. To improve the reliability of solar PV module interconnections, the PV module must be designed to withstand the outdoor weathering conditions it is expected to operate in. Thermal loading resulting from day and night temperature cycling induce fatigue damage within the soldered interconnections within the PV module resulting in total interconnection failure. Accurate thermal cycle profiles related to outdoor weathering conditions is necessary to ensure a reliable prediction of fatigue life.

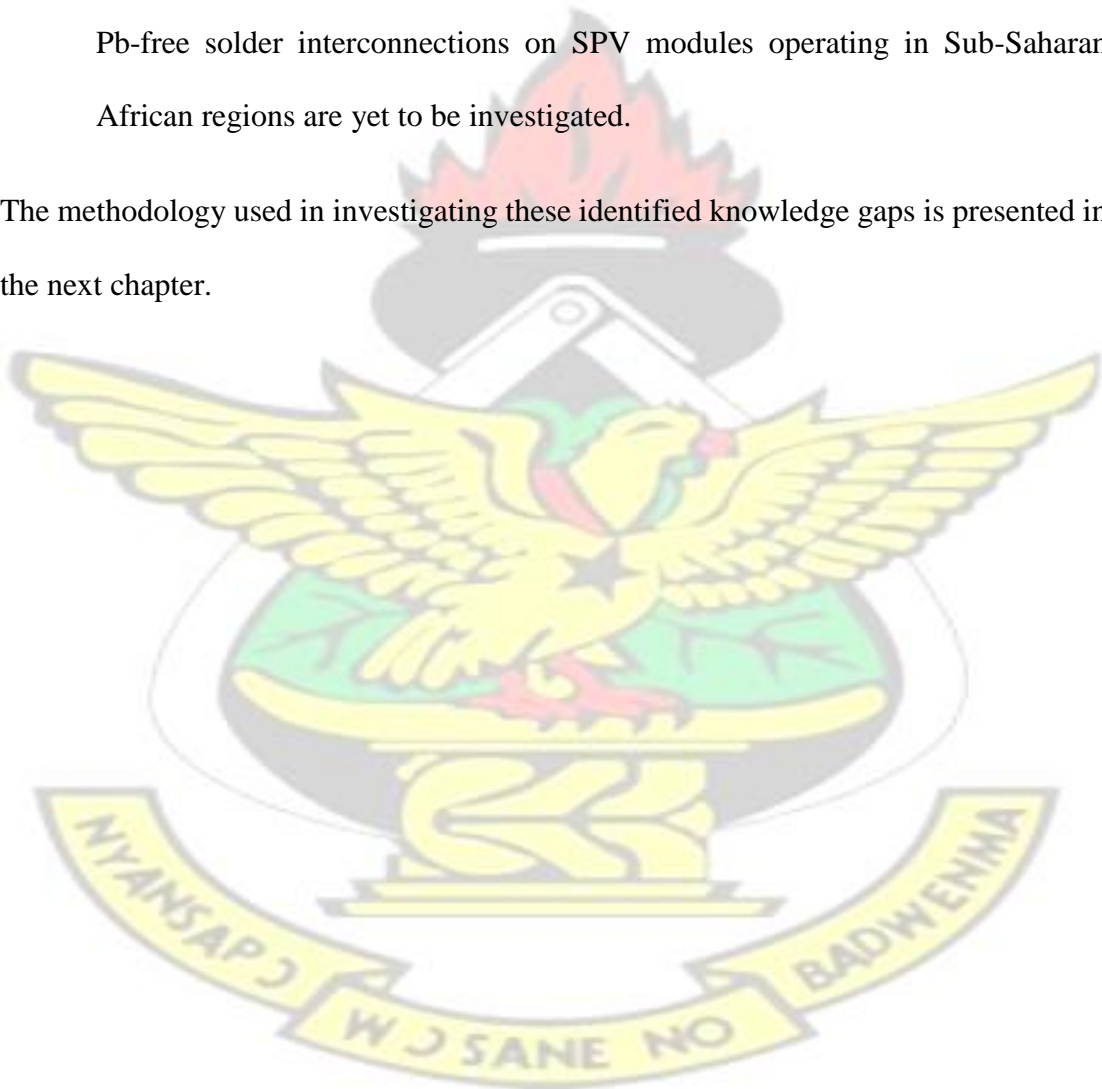
Based on the literature review, four gaps in knowledge were identified as :

- i. the discrepancies in temperature cycle profiles (ramp rates, dwell times, maximum and minimum module temperatures) between standard test conditions (STC) and operating temperatures of PV modules operating in sub-Saharan tropical ambient are yet to be investigated.

CHAPTER TWO: LITERATURE REVIEW

- ii. the impact of the constitutive model of encapsulant (EVA) on creep damage from operating temperatures of SnPb and Pb-free solder interconnections in PV modules operating in the sub-Saharan African region are yet to be investigated.
- iii. the effect of actual operating temperatures on fatigue life of SnPb and Pb-free solder interconnections in PV modules installed in sub-Saharan African climatic conditions are yet to be studied.
- iv. the effects of temperature ramp rates, dwell times on degradation of SnPb and Pb-free solder interconnections on SPV modules operating in Sub-Saharan African regions are yet to be investigated.

The methodology used in investigating these identified knowledge gaps is presented in the next chapter.



CHAPTER THREE: METHODOLOGY

3.1 Introduction

In this chapter, the method for collecting and analysing the module temperature data to generate the accelerated temperature cycle (ATC) profiles for installed PV modules is presented. Additionally, the derivation of solar cell geometry and constitutive material models are presented. The ATC profiles are generated by computing the rate of temperature rise (ramp-up) or fall (ramp-down), dwell times and maximum and minimum cycle temperatures.

The chapter also discusses the finite element modelling (FEM) methodology and outlines the mechanical properties of the assembled solar cell materials. The constitutive models used in modelling the response of the materials subjected to cyclic thermal loading are discussed. The geometry of the solar cell is generated using a constructive solid geometry (CSG) technique in Siemens PLM NX 11 computer-aided design (CAD) software that is compatible with ANSYS design modeller. The geometric model was subsequently imported into ANSYS finite element analysis software for static structural analysis to simulate the thermo-mechanical response of the PV cell.

3.2 Method for Data Analysis and generation of ATC temperature profiles

3.2.1 Description of Experimental Setup

Figure 3-1 shows the rig for monitoring the outdoor climate used for this study. The rig contains other types of crystalline silicon PV modules. However, only the mono-crystalline modules were used for this investigation. Figure 3-2 presents the sub-station that was used for the data collection. The rigs are located at the College of Engineering KNUST, Kumasi, Ghana. The system was installed in 2012 with financial assistance

CHAPTER THREE: METHODOLOGY

from The World Bank through Africa Renewable Energy Access programme (AFREA) under the project title: Capacity Upgrading for West African Partners in Renewable Energy Education. Table 3-1 lists the system specifications and capacity of the modules. The site location (College of Engineering, KNUST, Kumasi, Ghana) is on latitude 6° 40" N and longitude 1° 37" W, at an elevation of 250 m above sea level.

The modules are unshaded and mounted on an inclined rooftop with a tilt angle of 5°, and oriented toward the equator (southwards). Furthermore, a 4 kW SMA Sunny Boy DC-AC inverter (SB 3800) connects each of the various PV module technologies to the grid. There are five inverters connected and integrated to communicate with an SMA Sunny WebBox via a Bluetooth ad-hoc connection. Consequently, the SMA Sunny WebBox transmits the data output from the PV systems and stores on a dedicated server. Additionally, an SMA Sunny portal created on the dedicated server from the University network provided an online monitoring system. Calibrated platinum sensors (PT100) with a measurement accuracy of ± 0.5 °C, resolution of 0.1°C and positioned at the centre of each module (on the backside) measured the module temperatures. The data logged include; environment temperature, total insolation, module temperature, operating current and voltage, wind speed and total output power.

CHAPTER THREE: METHODOLOGY

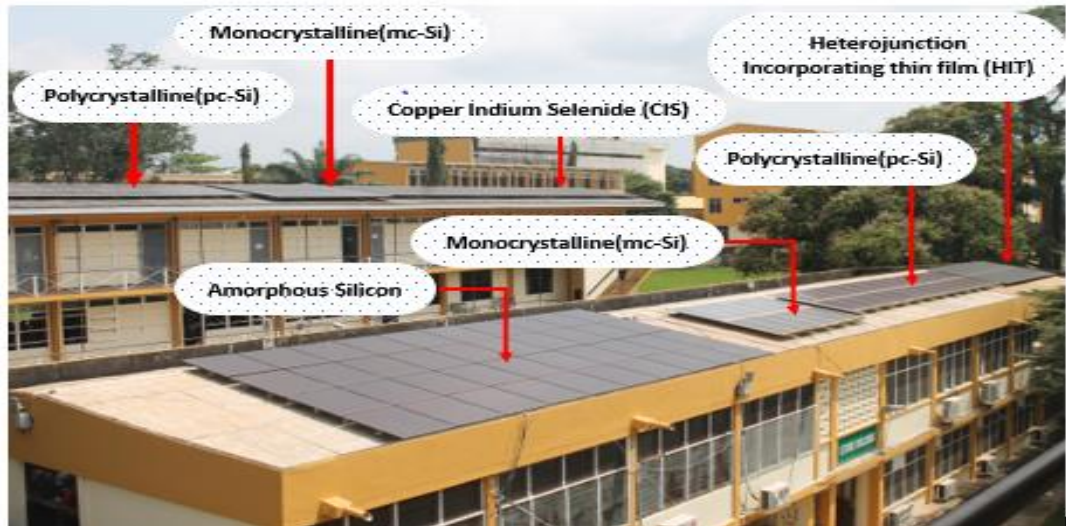


Figure 3-1: Outdoor Monitoring Set-up at College of Engineering KNUST, Kumasi, Ghana



Figure 3-2: Monitoring Station for Outdoor Test Set-up at College of Engineering KNUST, Kumasi, Ghana

CHAPTER THREE: METHODOLOGY

Table 3-1: Technical Specification of PV Modules Installed at Test Site

Cell Technologies	Amorphous Silicon	Monocrystalline Silicon	Polycrystalline Silicon	HIT	Copper Indium disulfide (CIS)
Model type	Schott ASI100	Schott GmbH Mono 190	Solar POLY 225	Sanyo H250E01	Sulfurcell SCG50-HV-F
Model×String	10×4	7×3	9×2	8×2	9×9
Total number of modules	40	21	18	16	81
Power per module (W)	100	190	225	250	50
Total module peak power (W)	4000	3990	4050	4000	4050
Voltage at nominal power (V)	30.7	36.4	29.4	34.9	36.8
Current at nominal power (A)	3.25	5.22	7.55	7.18	1.36
Open circuit voltage(V)	40.9	45.2	36.7	43.1	49.5
Open circuit current (A)	3.85	5.46	8.24	7.74	1.66
Maximum system voltage (V)	1000	1000	1000	1000	1000
Temperature coefficient of open circuit voltage (%/°C)	-0.33	-0.33	-0.33	-0.01	-0.26
Temperature coefficient of short circuit current (%/°C)	0.08	0.03	0.04	0.03	0.04
Temperature coefficient power (%/°C)	-0.20	-0.44	-0.45	-0.30	-0.30
Total surface area of PV system (m ²)	58.9	28.1	30.6	22.6	68.6
Nominal power of PV-module (kW)	4.0	3.99	4.05	4.0	4.05
Module efficiency (%)	6.9	14.5	13.7	18.0	6.1
NOCT	49	46	47.2	46	47

3.2.2 Site Climatic Data and Thermal Analysis

The data was collected at 5-minute intervals between the periods of March 2012 and December 2014. The study and data analysis was limited to the mono-crystalline PV-modules. The day/night module temperature profiles were generated for further thermomechanical modelling.

3.2.3 Temperature Signal 'Rainflow' cycle Counting Algorithm

Intra-day module temperature fluctuations caused by cloud movements have been demonstrated to have a more damaging effect on the c-Si PV module compared with day/night temperature gradient (Bosco and Kurtz, 2010). The highly unpredictable nature of cloud cover and subsequent fluctuation of irradiance presents a great difficulty in characterizing short-time intraday cycles. Cycle counting presents the best approach to stress-load analysis. Furthermore, the rainflow counting algorithm (Musallam and

CHAPTER THREE: METHODOLOGY

Johnson, 2012) offers the best cycle counting method for effectively compressing time-series data into peaks and valleys. The peaks and valleys in the temperature signal present reversal points at which half-cycles are determined. The algorithm counts a cycle by considering a moving reference temperature point of the sequence, say 'T_P', and a moving ordered three-temperature point subset T_X and T_Y with the following characteristics:

- The first and second temperature points are collectively named as T_Y
- The second and third temperature points are collectively named as T_X
- The absolute value of the difference between the amplitude of the first and second temperature point is the range of T_X denoted by r (T_X).
- Range of T_Y is denoted by r (T_Y)

Figure 3-3 displays the flowchart for the rainflow counting algorithm. The rainflow counting algorithm is generated using a MATLAB program and has been successfully deployed in this work to determine the number of temperature cycles experienced by the modules each year.

CHAPTER THREE: METHODOLOGY

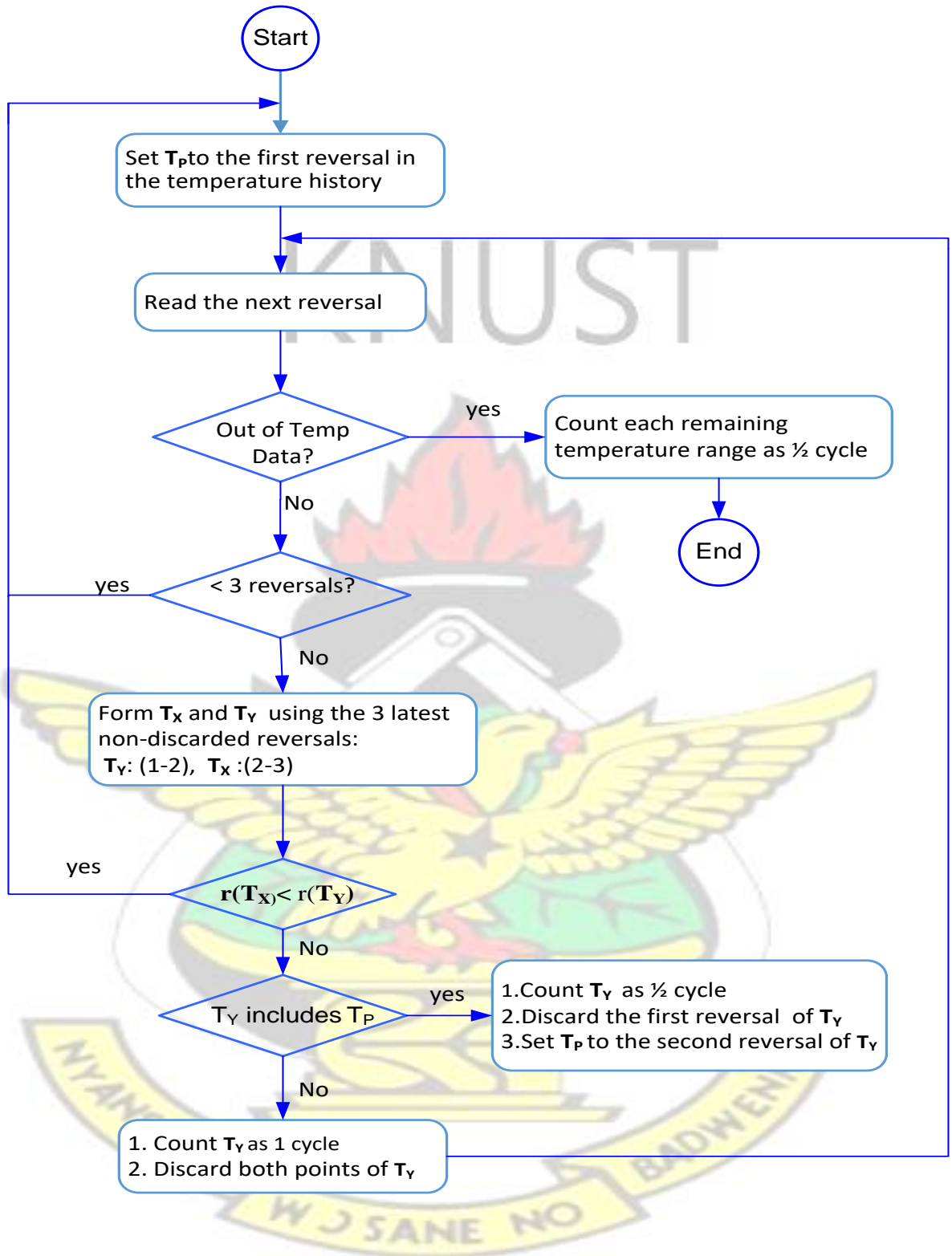


Figure 3 - 3: Flowchart for rainflow counting

CHAPTER THREE: METHODOLOGY

3.2.4 Estimation of Temperature Cycle Ramp rates and Dwell Times

Theoretically, the temperature dwell time for a PV module is the time the module records a zero temperature ramp. It is the time the module is soaked at a constant temperature. There are two main dwell times in a daily temperature cycle. The upper and lower dwells corresponding to the upper and lower temperature regimes. In this study, a module assumes a temperature dwell if the rate of temperature rise in an interval is lower than the mean ramp rate. Figure 3-4 assists to illustrate how to compute a dwell time from a typical temperature cycle with peak and valley temperatures.

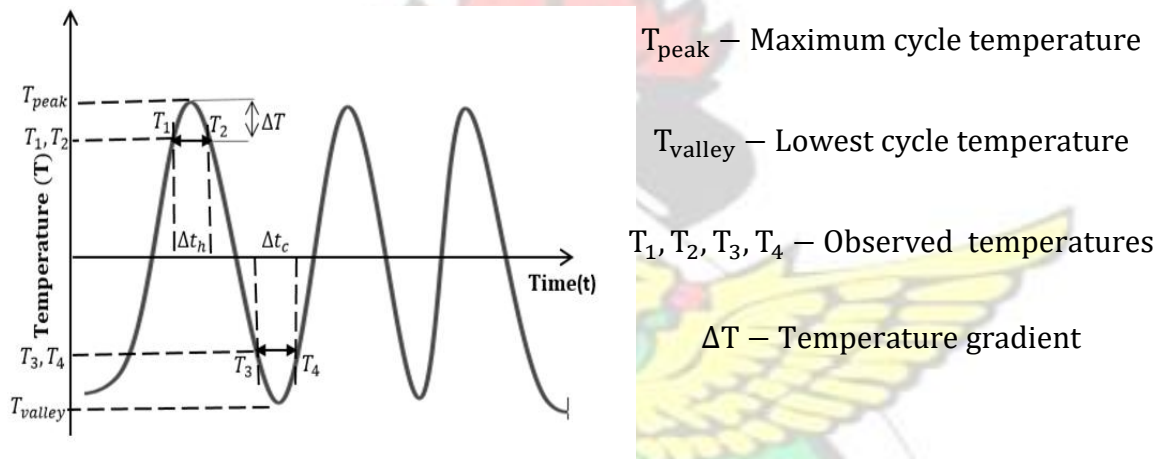


Figure 3 - 4: Typical temperature cycle

The analysis for evaluating the dwell times are as follows:

$$\Delta T = \text{mean ramp rate}(\text{°C}/\text{min}) \times (\text{temperature signal time interval (min)}) \quad (3.1)$$

The conditions for computing Δt_h hot dwell time range requires that:

$$\Delta t_h; \quad T_{peak} - T_1 \leq \Delta T \quad (3.2), \quad T_{peak} - T_2 \leq \Delta T \quad (3.3)$$

Similarly, conditions for computing Δt_c cold dwell time range requires that;

$$\Delta t_c; \quad T_3 - T_{valley} \leq \Delta T \quad (3.4), \quad T_4 - T_{valley} \leq \Delta T \quad (3.5)$$

CHAPTER THREE: METHODOLOGY

The huge size of the temperature data logged required an algorithm that could pick out the temperatures around the peaks and valleys and subsequently compute the dwell times. Figure 3-5 (a) and (b) show flowcharts of MATLAB algorithms used in computing the dwell times.

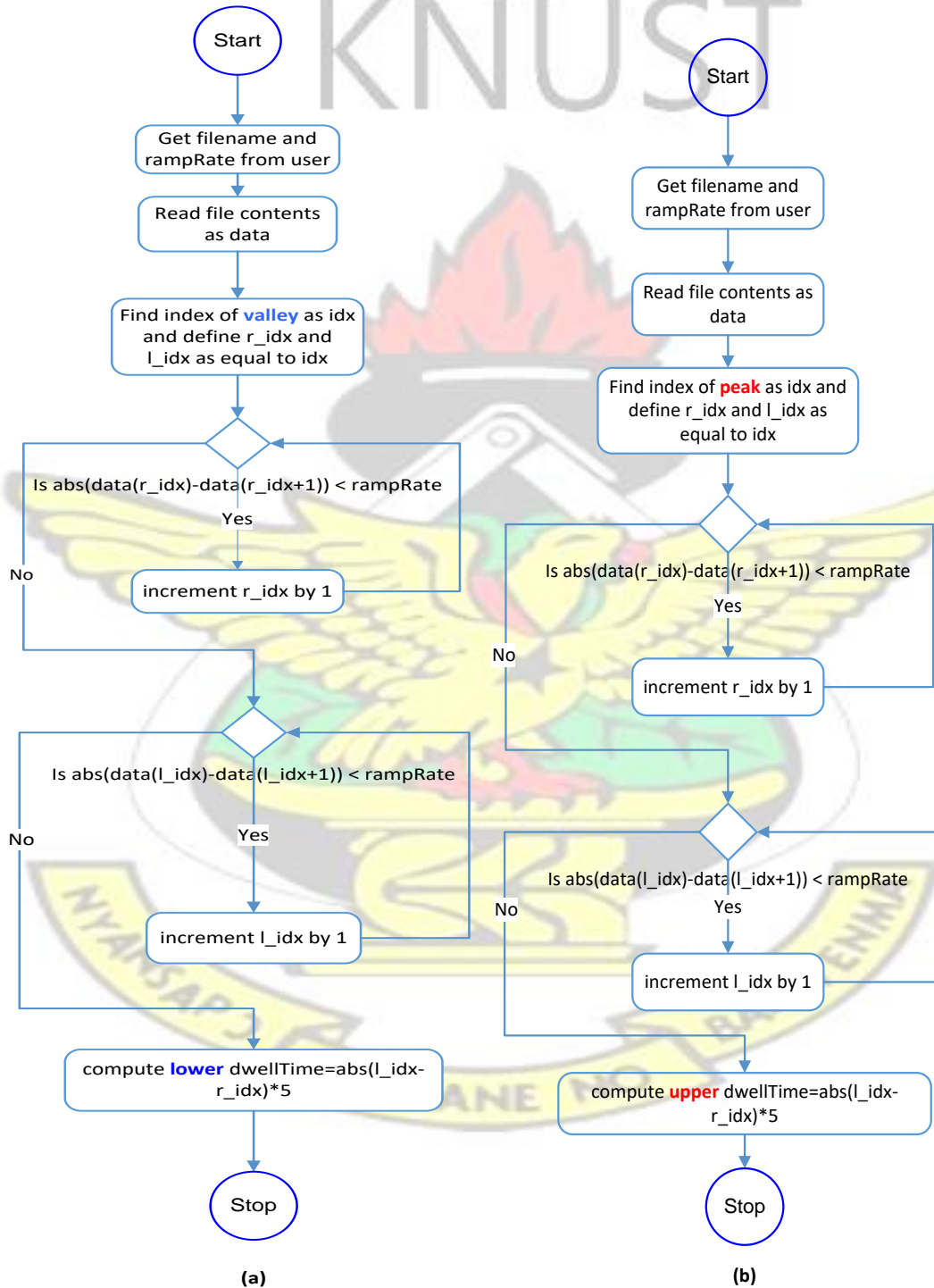


Figure 3 - 5: Flowchart for computing dwell times; (a) lower dwell (b) upper dwell

CHAPTER THREE: METHODOLOGY

The results from generating temperature cycles for the prediction of thermo-mechanical damage of the cell interconnections are presented and discussed in chapter 4 of this work.

3.3 Method for Geometric Modelling, Finite Element Analysis and Cell Material Modelling

The finite element method (FEM) is used extensively in photovoltaic and semiconductor industries for fatigue life prediction studies. The material matrix of the photovoltaic cell sub-assemblies is modelled via FEM routines to investigate the solder interconnect reliability. In the interconnect reliability study, strain energy, strain energy density, plastic work, stresses and strain magnitudes generated from the FEM simulation are inputted into the appropriate fatigue life prediction. In this study, an academic finite element software package known as ANSYS Workbench version 18.2 was used. The Static Structural analysis system containing the Mechanical APDL and Workbench solvers (structural and thermal physics) was used in modelling the PV cell matrix. The high productivity computing (HPC) resource used for this work is a Xi Workstation Server Computer resident at the Solar PV Reliability Laboratory, KNUST. Presented in Figure 3.6 is the general overview of the FEM simulation that was carried out.

CHAPTER THREE: METHODOLOGY

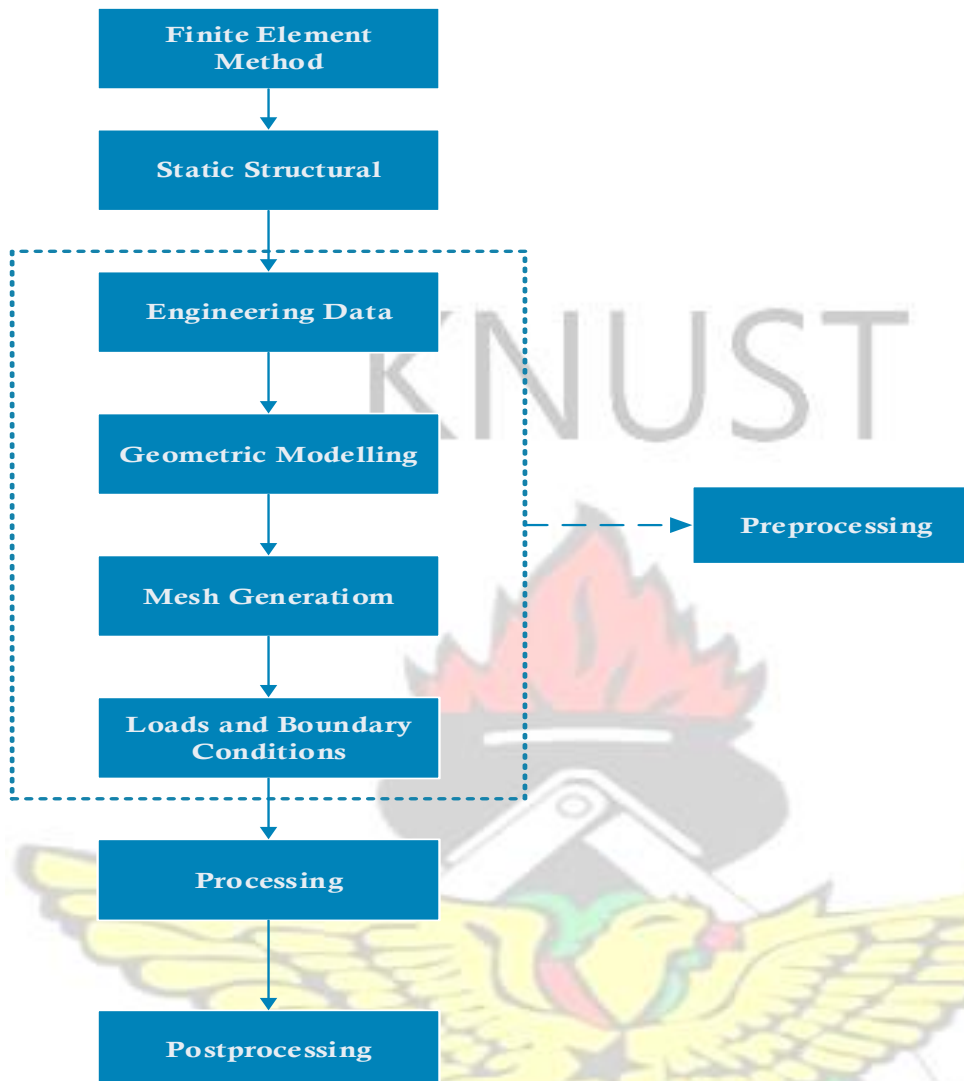


Figure 3-6: General finite element flow methodology

3.3.1 Geometric modelling of solar cell

The geometric assembly model of the solar PV was built in Unigraphics NX 11.0 a computer-aided design (CAD) software. This model was created using actual dimensions of a solar cell assembly. A quarter of the model was sliced from the general assembly (realistic) model to reduce the computation cost. The sliced model was converted into a Standard for the Exchange of Product (STEP). This is a CAD file format usually used to share 3D models between users with different CAD systems. This file was imported into ANSYS Workbench 18.2 (Design Modeller – a cell in the

CHAPTER THREE: METHODOLOGY

Static Structural Analysis system for creating and modifying geometries). A total of twenty-six (22) 3-dimensional representative geometric models of the H-patterned front-to-back interconnected c-Si solar cell assemblies were created by using a combination of Constructive Solid Geometry (CSG) and Boundary Representation (B-Rep) modelling technique. In general, the size of a mesh generated on a model for Finite Element Analysis (FEA) affects computational speed and accuracy of simulation results. A higher mesh density results in increased computational time, which could result in latency issues. To ensure that the simulation is optimized for accuracy and computational speed within the power of the computing resource, a quarter symmetry comprising of a cell-to-cell interconnect model was utilized in the FEA. Table 3-2 lists the various geometric parameters of the PV model.

Table 3-2: Geometric Properties of layer materials in solar PV module

Layer Material	Size (Length x Width)	Thickness(μm)	Ref
Glass	0.352 m x 0.156 m	3600	(Willeke and Weber, 2013)
EVA	0.352 m x 0.156 m	450	(Cuddalorepatta et al., 2010)
Silicon	0.156 m x 0.156 m	175	(Saga, 2010)
Copper Ribbons	0.156 m x 0.003 m	150	(Wiese et al., 2010b)
Solder	0.156 m x 0.003 m	20	(Wirth, 2010, I. Rogelj, 2012, Moyer et al., 2010)
IMC (Ag_3Sn , Cu_3Sn)	0.156 m x 0.003 m	4	(Choi et al., 2002, Mei et al., 1992, Prakash and Sritharan, 2001)
Aluminium Rear Contact	0.156 m x 0.156 m	25	(Chen, 2008, Wiese et al., 2010b)
Silver (Ag) Busbars	0.156 m x 0.003 m	50	(Wiese et al., 2010b, Zemen et al., 2012, Moyer et al., 2010)
Tedlar Backsheet	0.352 m x 0.156 m	175	(Armstrong and Hurley, 2010, Arangú et al., 2014)

CHAPTER THREE: METHODOLOGY

Figure 3-7 is a flow chart showing the development procedure of the geometric model assembly of the solar PV cell.

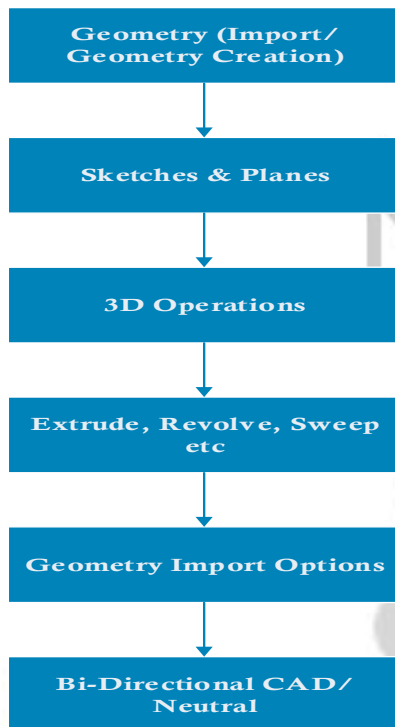


Figure 3 - 7: Geometric model flow chart

3.3.2 Mesh Generation

The sliced geometric model (quarter cell) was meshed using the ANSYS mesh creation engine (ANSYS Mesher). This engine discretizes the geometric model enabling equations to be solved at nodal locations. The mesh efficiency and accuracy were improved through refinement and sizing for high solution gradients and fine geometric details. For the focus of this research, selective mesh adjustment and refinement operations were carried out on the intermetallic compounds (IMC) and solder geometric models. ANSYS mesh refinement settings were applied to the IMC which is very thin whilst a face sizing setting was applied to the solder geometric models respectively. We applied a system default size of mesh element with an adaptive size function and a medium relevance center to the model to generate a mesh with a medium span angle

CHAPTER THREE: METHODOLOGY

center and minimum edge length. A total of 195,329 nodes and 49,075 elements constituted the resultant mesh statistics.

Fig. 3-8 shows the mesh generation flow chart and Figure 3-9 shows a meshed geometry of a cell interconnected with an adjacent cell.

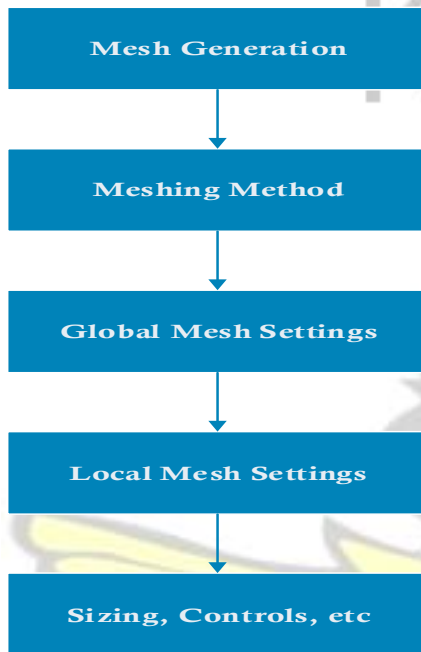


Figure 3 - 8: Mesh generation flow chart

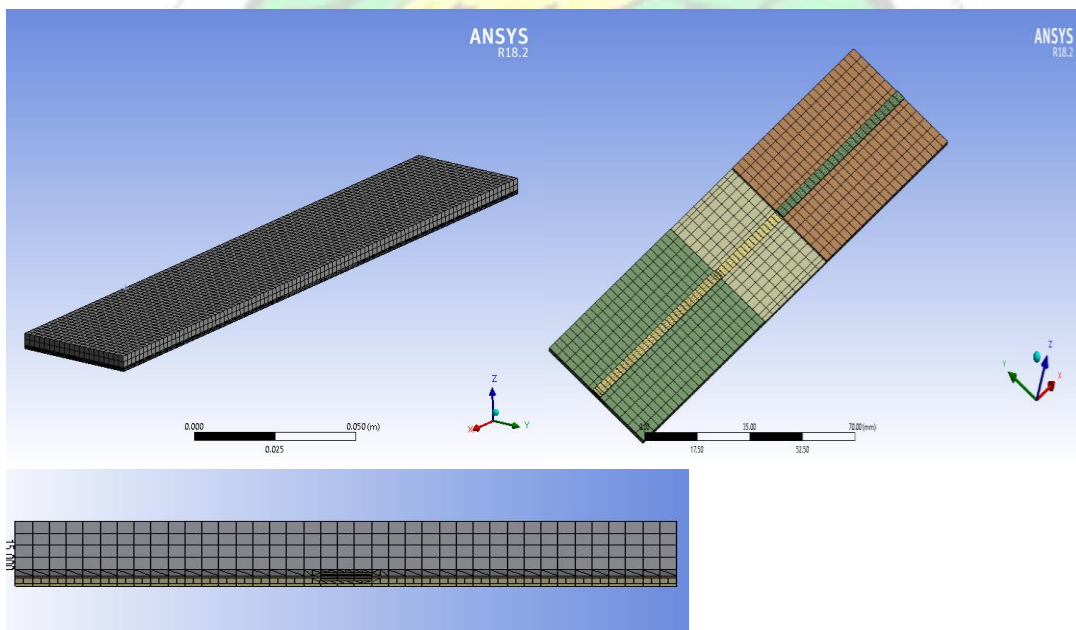


Figure 3 - 9: Meshed geometry of cell-to-cell interconnection

CHAPTER THREE: METHODOLOGY

3.3.3 Solar Materials and Properties

The geometric model of the solar cell has ten (10) different material matrices. These material matrices were created as subassemblies in the geometric model as started earlier. These materials include; glass, an encapsulant (ethylene vinyl acetate – EVA), solar cell (silicon), interconnector (copper), interconnecting material (solder – SnPb and SnAg, IMCs) and backsheet (Tedlar). Figure 3-10 depicts the material assembly matrix setup of the PV module used in the study.

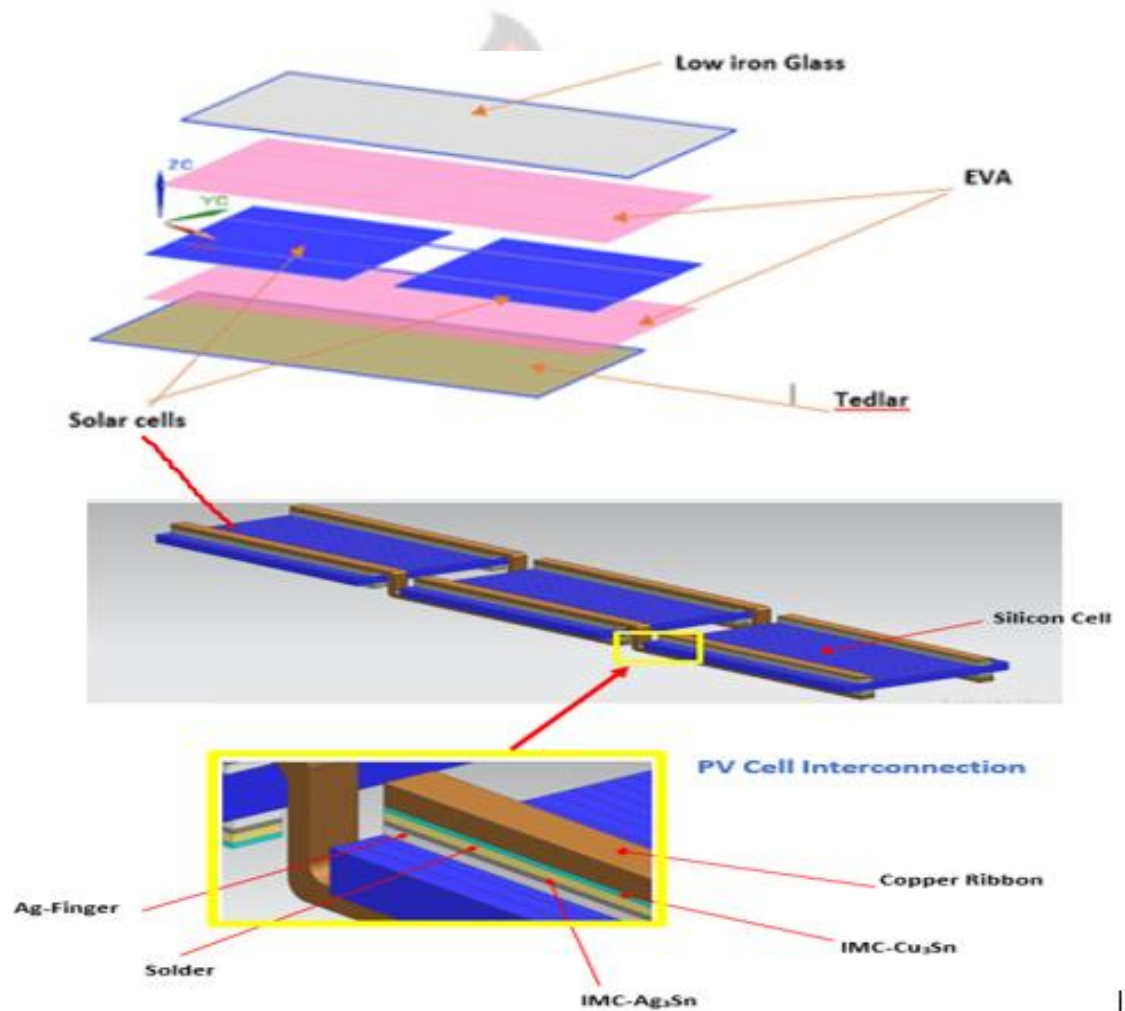


Figure 3 - 10: Solar cell architecture for front-to-back cell interconnection

The material assembly setup for the PV module assembly constitutes diverse material matrices which are characterized by their physical and engineering data. These diverse material matrices contribute partly or wholly to the fatigue life prediction of the solar

CHAPTER THREE: METHODOLOGY

cell assembly most especially the interconnection joint reliability. In this study, the solar PV model material matrices are classified under three (3) main material models namely; anisotropic, linear elastic, viscoelastic and visco-plastic. Figure 3-11 shows the overall material setup for the PV model used in this study. The constitutive behaviours and properties of respective solar cell materials have been reviewed exhaustively in chapter 2.

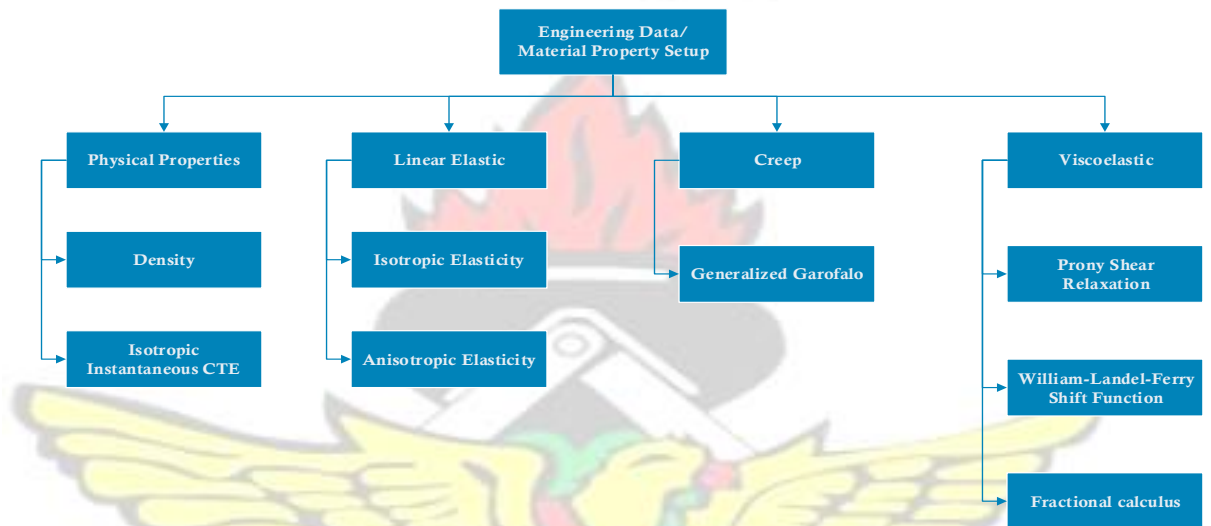


Figure 3 - 11: Engineering Data flow chart

The cell material properties are categorized as; Isotropic linear elastic, anisotropic, creep, Temperature-dependent linear elastic and linear viscoelastic materials. In this study, the behavior of EVA is examined under three different constitutive models namely: isotropic linear elastic, temperature-dependent Young's modulus (bilinear) and linear viscoelastic. The following tables describing the properties of the cell materials are thus extracted and presented:

CHAPTER THREE: METHODOLOGY

Table 3-3: Mechanical Properties of Isotropic linear elastic cell materials

Material	Young's Modulus(E) (GPa)	Poisson ratio ν	Density(ρ) kg/m ³	CTE(α) $\times 10^{-6}$ 1/K
Glass	73	0.23	2500	8
EVA*	1	0.4999	960	270
Cu ₃ Sn (IMC)	80 - 153	0.3	8900	23
Ag ₃ Sn (IMC)	77.06 - 82.6	0.347		
Aluminium	3.5	0.35		23.1
Ag Busbar	72.4	0.37		10.4
Tedlar (Backsheet)	3.5	0.29		

Table 3-4 lists the generated data and Figure 3-12 presents the corresponding graphical plot for Young's modulus of the EVA material versus temperature at a two-minute relaxation time.

Also listed in Table 3-4 are the temperature dependent properties of the copper ribbon interconnector.

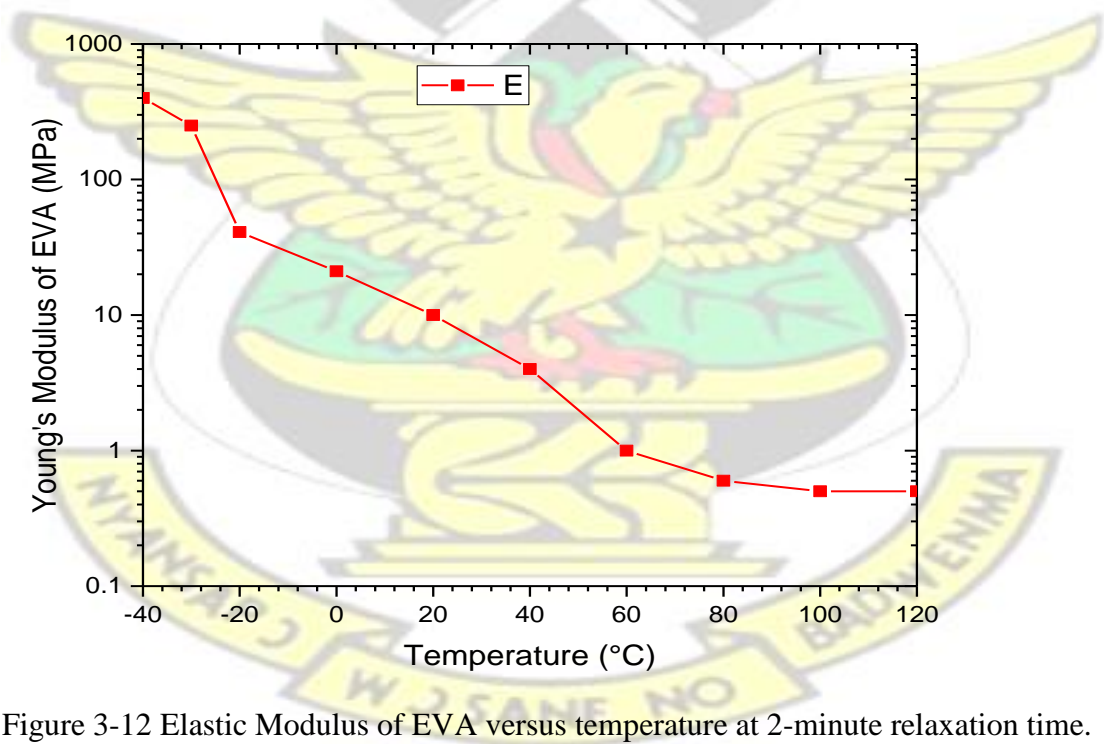


Figure 3-12 Elastic Modulus of EVA versus temperature at 2-minute relaxation time.

CHAPTER THREE: METHODOLOGY

Table 3 - 4: Mechanical Properties of temperature dependent Young's modulus cell materials

EVA**		Copper ribbon	
Temperature (°C)	Young's Modulus (E) (MPa)	Temperature (°C)	Young's Modulus (E) (GPa)
-40	400	-40	91.5
-30	250	25	85.7
-20	41	125	82.0
0	21	225	79.2
20	10		
40	4		
60	1		
0.6	0.6		
100	0.5		
120	0.5		

Silicon has anisotropic material properties that are due to the crystallographic structure.

There are thus different values of the elastic constants (C_{ij}) for different loading directions. The matrix C of the constitutive equation is given by equation (2.9).

$$C = \begin{bmatrix} C_{11} & C_{12} & C_{12} & 0 & 0 & 0 \\ C_{12} & C_{11} & C_{12} & 0 & 0 & 0 \\ C_{12} & C_{12} & C_{11} & 0 & 0 & 0 \\ 0 & 0 & 0 & C_{44} & 0 & 0 \\ 0 & 0 & 0 & 0 & C_{44} & 0 \\ 0 & 0 & 0 & 0 & 0 & C_{44} \end{bmatrix} \quad (2.9)$$

This matrix is subsequently set up in ANSYS™ with the elastic constants and other relevant material properties listed in Table 3-5.

CHAPTER THREE: METHODOLOGY

Table 3-5: Mechanical Properties of Anisotropic cell material (Silicon)

Quantity	Unit	Value	Ref.	Quantity	Unit	Value	Ref.	
C_{11}	[GPa]	164.8	(Greenwood, 1988)	$\left(\frac{dE_{<100>}}{dT}\right)/E_{<100>}$	[10 ⁻⁶ 1/K]	-63	(Greenwood, 1988)	
C_{12}		63.5				-80.3		
C_{44}		79.0				-45.6		
$\left(\frac{dC_{11}}{dT}\right)/C_{11}$	[10 ⁻⁶ 1/K]	-122	(Greenwood, 1988)	$\left(\frac{dE_{<110>}}{dT}\right)/E_{<110>}$	[10 ⁻⁶ 1/K]	1.717	(Lyon et al., 1977)	
$\left(\frac{dC_{12}}{dT}\right)/C_{12}$		-162				$\left(\frac{dE_{<111>}}{dT}\right)/E_{<111>}$	2.225	(Lyon et al., 1977)
$\left(\frac{dC_{44}}{dT}\right)/C_{44}$		-97				$\alpha(T = 220K)$	2.614	(Roberts, 1981)
$E_{<100>}$	[GPa]	129.5	(Greenwood, 1988)	$\alpha(T = 260K)$	[10 ⁻⁶ 1/K]	2.915	(Roberts, 1981)	
$E_{<110>}$		168.0		$\alpha(T = 300K)$		3.342	(Roberts, 1981)	
$E_{<111>}$		186.6		$\alpha(T = 340K)$				
				$\alpha(T = 420K)$				

3.3.3.1 Linear viscoelastic model of EVA

A number of FE packages including ANSYSTM declare the relaxation modulus as relative modulus (ϕ_i) where:

$$\phi_i = \frac{G_i}{G_0} \quad (2.4), \quad \phi_\infty = \frac{G_\infty}{G_0} \quad (3.1)$$

And

$$G_0 = G_\infty + \sum_{i=1}^n G_i \quad (3.2)$$

$$= G_0 \left(\frac{G_\infty}{G_0} + \sum_{i=1}^n \frac{G_i}{G_0} \right)$$

Recalling equation (2.2) we have:

$$G(t) = G_\infty + \sum_{i=1}^n G_i \exp\left(\frac{-t}{\lambda_i}\right) \quad (3.3)$$

$$G(t) = G_0 \left(\phi_\infty + \sum_{i=1}^n \phi_i \exp\left(\frac{-t}{\lambda_i}\right) \right) \quad (3.4)$$

CHAPTER THREE: METHODOLOGY

To determine the parameters in equation (3.4), n (a number of spring-dashpot) elements representing the material were selected with guessed values for (ϕ_i) and (λ_i) . Residuals were then calculated and brought to a minimum. The instantaneous shear modulus (G_0) is evaluated as follows:

$$\phi_{\infty} = 1 - \sum_{i=1}^n \phi_i \quad (3.5)$$

By substituting equation (3.5) into equation (3.4), the value of G_0 is computed.

The instantaneous Young's modulus (E_0) is calculated as follows:

$$E_0 = 2G_0(1+\nu) \quad (2.10)$$

Subsequently, E_0 was used in the FE package to simulate the viscoelastic response of EVA.

Table 3-6: Linear viscoelastic properties of cell material (EVA)

Maxwell parameters			Maxwell parameters			Maxwell parameters		
Arm	Shear Relaxation time λ_i (s)	Shear Modulus G_i (MPa)	Arm	Shear Relaxation time λ_i (s)	Shear modulus G_i (MPa)	Arm	Shear Relaxation time λ_i (s)	Shear modulus G_i (MPa)
1	0.0001219	0.5467175	11	10^6	0.0021774	21	10^{16}	0.0005575
2	0.0007823	0.2222377	12	10^7	0.0010461	22	10^{17}	0.0003087
3	0.0063471	0.0992664	13	10^8	0.0015563	23	10^{18}	0.000177
4	0.075255	0.0590673	14	10^9	0.0023002	24	10^{19}	0.0000112
5	1.261626	0.0265249	15	10^{10}	0.0008377	25	10^{20}	1.54E-08
6	15.7945	0.0136822	16	10^{11}	0.0013597	26	10^{21}	0.00000634
8	10333.19	0.0037958	18	10^{13}	0.00076	WLF constants		
9	99967.33	0.002486	19	10^{14}	0.0011088	$C_1 = 48.44$	$C_2 = 172.55^\circ\text{C}$	
10	1000001	0.0010978	20	10^{15}	0.0005415	$T_{\text{ref}} = -20^\circ\text{C}$		

The relevant creep properties of Pb-free and SnPb solders are presented in Table 3-7

CHAPTER THREE: METHODOLOGY

Table 3 - 7: Mechanical and Creep Properties of Pb-free and PbSn solders in solar cell

Pb-free solder (Sn3.8Ag0.7Cu)		Tin Lead solder (SnPb)		Generalized Garofalo		
					Pb-free solder(Sn3.8Ag 0.7Cu)	Tin Lead solder
Temperature (θ) (C)	Young's Modulus (GPa)	Temperature (θ) (C)	Young's Modulus (GPa)	C1	278000	$\frac{926 \times (508 - \theta)}{\theta}$
-50	57.3	-70	38.1	C2	2.45E-08	$\frac{1}{37.78 \times 10^6 - 74414 \times \theta}$
-25	55.79	20	30.2	C3	6.41	6.41
0	54.22	140	19.7	C4	6500	6500
25	52.62			CTE ($\times 10^{-6}$)	23.2	24
50	50.97					
75	49.29			Density (kg/m^3)	7500	8400
100	47.57					
				Poison	0.3	

3.3.4 Thermal Loads and boundary conditions

Thermal load cycling was used to simulate the behaviour of the solar PV module. The thermal condition load was used in this work to perform the analysis. The 12 thermal cycles comprising of the representative profiles generated for the years 2012, 2013, 2014 and TRA to be processed were loaded into the software including the number of steps and the steps end times. The load condition was applied to all the components of the solar photovoltaic cell assembly. The fixed support constraints were applied for all the edges of the one eight geometric model. This constraint was applied at the edges of the cell to depict the effects of the aluminum support bars of the panels during service.

3.3.5 Analysis Settings

The modelling of the solar cell consists of a thin plate with different material properties and they exhibit nonlinear attributes. For the effective characterization, modelling of these components including their material behaviours and settings were applied to the

CHAPTER THREE: METHODOLOGY

FEA software. The solver type was changed from the default to the Direct type since the Direct solver type allowed for a good convergence when carrying out a nonlinear analysis. Despite the benefits of using this solver, the processing times and the computational load on the CPU increases. Other settings such as weak springs, spring stiffness, Newton-Raphson, force convergence, contacts, pinball radius, displacement convergence, line search, stabilization and creep control settings were all modified to suit the thermal loading parameters such as ramp rates and temperature dwells. The model generated 154 contact regions with active connections across all contact points. A bonded contact type formulation with default trim tolerance of 0.49975 mm was used for modelling all the contacts created by the different materials in the cell assembly. Subsequently, advanced contact formulation settings that allow for small sliding were applied. Model analysis settings were set to detect contact on 'Gauss Point' during iterations. In addition, a nominal stiffness factor was set to update aggressively after each iteration from an initial standard value of 0.1. We deployed a direct solver in the computation of the numerical solution to improve the accuracy of simulation results. Furthermore, we activated the creep effects with a creep limit ratio of unity (1) to account for the creep behaviour of the solder material within the interconnection. Additionally, APDL commands (CUTCONTROL CRPLIMIT, PLSLIMIT) required to cut back the creep limit ratio and the plastic limit ratio was applied to control the creep and plastic limit of bonded cell materials during the numerical iterations. Default settings were applied to all the non-linear controls such as; Newton-Raphson option, force convergence, moment convergence, displacement convergence, and rotation convergence. Finally, we set the simulation output control to compute stresses and strains and to store results at all the iterative time steps (time points).

CHAPTER THREE: METHODOLOGY

3.3.6 Finite Element Analysis

The numerical study was carried out under the following simulation runs:

- Six (6) geometric models of the cell-to-cell interconnection assembly were simulated using the TRA thermal cycle with three different constitutive models of EVA material (namely; linear elastic, temperature-dependent linear elastic and linear viscoelastic) for both Pb-free and SnPb solder interconnects. This was necessary to establish the most appropriate constitutive model of EVA to be used in subsequent numerical studies.
- Eight (8) geometric models were simulated using 2012, 2013, 2014 and TRA thermal cycles. In each case, the cycles were simulated with Pb-free and SnPb solders as interconnecting solders. The output from these investigations was used to predict the life of interconnect from Accumulated Creep Energy Density (ACED).
- Eight (8) geometric models were simulated for 2012, 2013, 2014, TRA cycles with Pb-free, and SnPb solder interconnection for each cycle. The results from this investigation were extracted at time points for each of the five different load steps within the thermal cycle (cold dwell load step, ramp-up load step, hot dwell load step, ramp-down load step and cold dwell load step at the end of a cycle)

3.3.7 Processing of Numerical Results

After the boundary conditions were set, the simulation process was initialized and solved to generate the results based on the established parameters which include the material assignment, structural constraints and loads.

CHAPTER THREE: METHODOLOGY

3.3.8 Post-processing

Presented in Fig 3-13 is a flow chart showing some of the post-processing operations carried out.

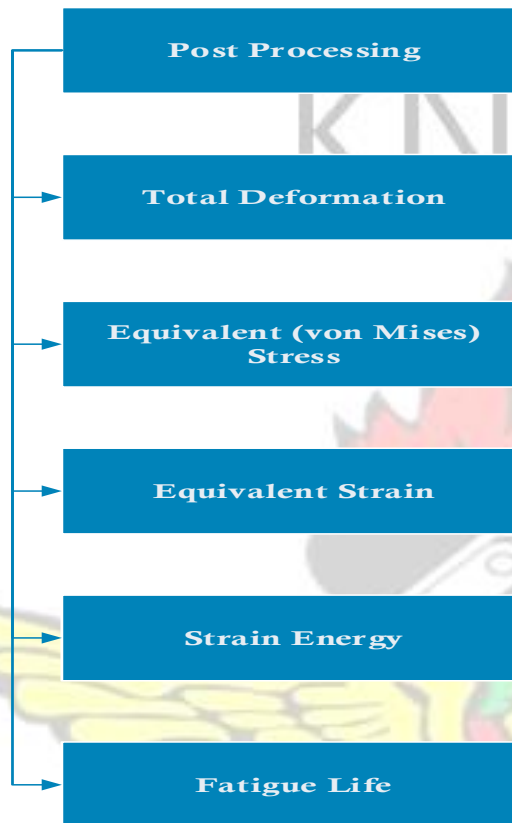


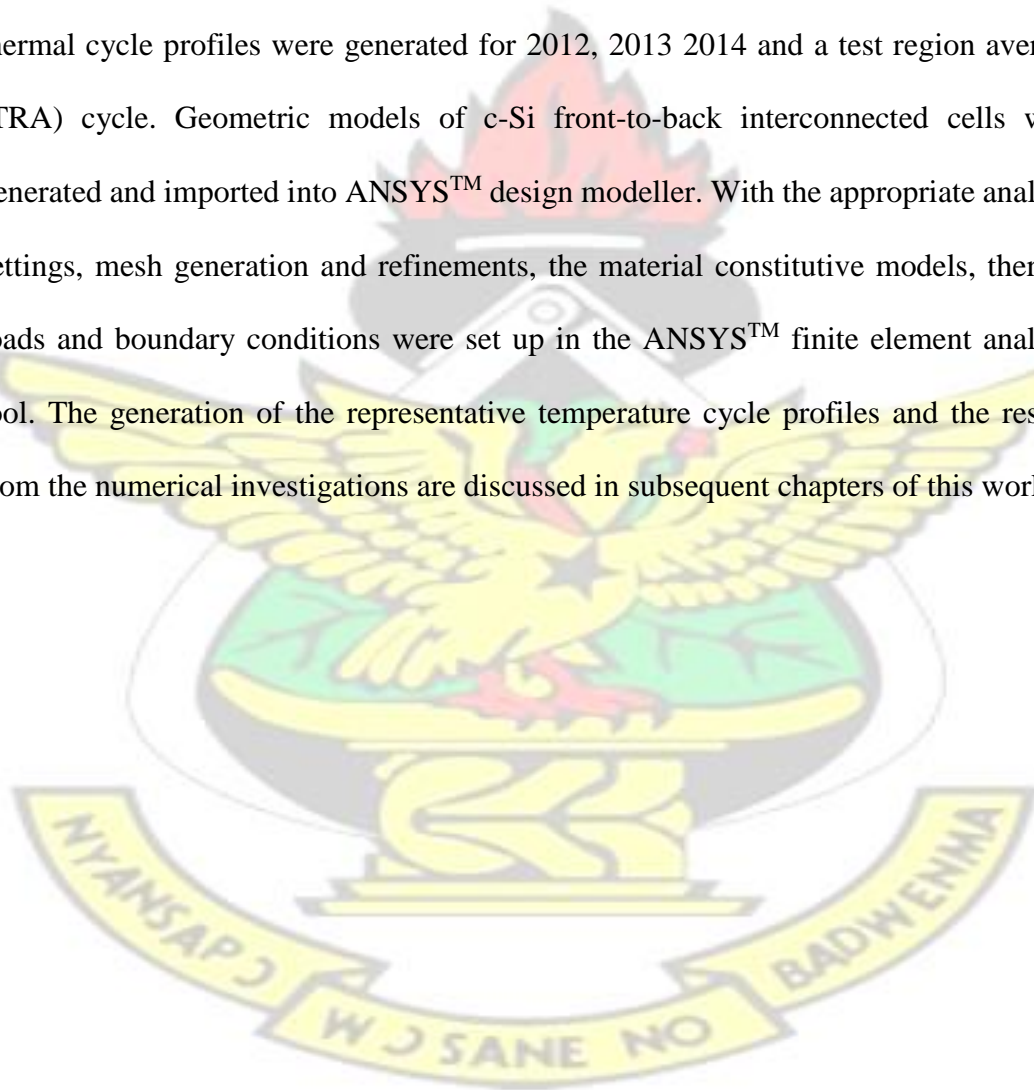
Figure 3 - 123: Post Processing flow chart

This procedure was carried out after the processing of the data inputted into the ANSYS™ Static Structural Analysis system. The desired results which include; total deformation, directional deformation, equivalent Von-Mises Stress, equivalent elastic strain, creep strain, strain energy density inter alia were generated from Mechanical APDL results file (.rst). User-defined results such as accumulated strain energy density and creep strain results were also generated during the post-processing operations.

CHAPTER THREE: METHODOLOGY

3.4 Summary

In this chapter, the thermal loads and boundary conditions resulting from real-time outdoor weathering of C-Si PV modules were generated for the test years spanning from March 2012 to December 2014. By the use of SMA Sunny WebBox, temperature data output from the PV systems were transmitted and stored on a dedicated server at 5-minute intervals. Subsequently, the data were analysed for temperature ramp rates and dwell times (hot and cold) and maximum and minimum temperatures. Furthermore, thermal cycle profiles were generated for 2012, 2013 2014 and a test region average (TRA) cycle. Geometric models of c-Si front-to-back interconnected cells were generated and imported into ANSYS™ design modeller. With the appropriate analysis settings, mesh generation and refinements, the material constitutive models, thermal loads and boundary conditions were set up in the ANSYS™ finite element analysis tool. The generation of the representative temperature cycle profiles and the results from the numerical investigations are discussed in subsequent chapters of this work.



CHAPTER FOUR: GENERATION OF SPVM THERMAL CYCLES

4.1 Introduction

The economics of the PV systems are based on their ability to deliver the rated power over their expected service lifetime, irrespective of their capacity (Dumbleton, 2012). The results from field studies conducted by a number of researchers have shown that outdoor degradation rates are much higher than expected. Studies have reported that installed modules experience annual power degradation rates of about 0.5% to 10%. In the tropical climate of eastern Nigeria, (Ike, 2013) studied the variation of the power output of field PV modules over a duration of the ambient temperature. The setup was mounted on an iron roof at an angle equivalent to the local latitude (site location; 6° 10' 0" North, 7° 4' 0" East). The author reported that power output degrades with an increase in ambient temperatures.

(Walsh et al., 2012) conducted a similar study involving the Singapore tropical climate on a rooftop at the National University of Singapore (site location; 1° 17' 44" N, 103° 46' 36" E). One significant finding from the study revealed that high year-round humidity is the greatest threat to the PV module durability. In addition, the researchers observed that high ambient temperatures and highly diffused light conditions have some negative effects on PV module output power. Furthermore, (Ogbomo et al., 2018) studied the effects of operating temperature on the degradation of solder joints in crystalline silicon photovoltaic modules. One of the key findings from their study shows that solder degradation increases with every 1°C cell temperature rise from Standard Test Conditions (STC). The study further observed module fatigue life, L (in years) decay, according to the power function ' $L = 721.48T^{-1.343}$ ', where T is the ambient temperature (in Kelvin). (McCormick and Suehrcke, 2018) on the other hand,

CHAPTER FOUR: GENERATION OF SPVM THERMAL CYCLES

investigated the effect of the intermittency of solar radiation on the performance of photovoltaic (PV) systems with battery storage. Consequently, they developed a model that simulated system energy flows with one-minute and hourly solar radiation values. Additionally, the researchers found that cloudy conditions caused significant fluctuations in system currents. Several researchers have also conducted related studies on the effects of temperature and irradiance on solar PV performance (Jamaly and Kleissl, 2017, Jamaly and Kleissl, 2018, Almeida et al., 2018, Anguera and Estrada, 2018, Bone et al., 2018).

A number of factors cause PV modules installed in the field to degrade. Exposure to a range of cyclic temperatures coupled with operations in elevated temperatures induces cyclic thermo-mechanical stresses in the solder joint interconnections in crystalline silicon photovoltaic (c-Si PV) modules. In addition, operations under a range of operating currents and voltages and the band-gap of ultraviolet (UV) light incident on the PV play a significant role in accumulating power degradation in PV modules. Huge variations in weather conditions also significantly increase the degradation rate. The contributions of these factors on the degradation of c-Si PV modules operating in the sub-Saharan climate are critical. (Macben, 2015) demonstrated in their report that the degradation and failure mechanisms of PV modules are location dependent.

Degradation of PV modules is by various failure mechanisms including:

- Corrosion of solder joints and electrical contacts by diffusion of water vapour into the encapsulated cell.
- Induced thermo-mechanical stress on solder joints occasioned by ambient temperature cycling.

CHAPTER FOUR: GENERATION OF SPVM THERMAL CYCLES

- Intermetallic (IMC) growth in solder interconnections caused by long-term exposure to high ambient temperature (thermal soaking and aging).
- Presence of micro-cracks caused by vibrations resulting from hailstorms and high winds.

The development of indoor tests that have the ability to predict real outdoor conditions accurately is quite challenging. A number of research findings suggest various methods which include expanding on the certification procedures outlined in the IEC 61215 thermal cycling test (TC 200) by increasing the number of cycles, increasing the temperature range or ramp rates (Owen-Bellini et al., 2015). Other studies have also used field data for PV reliability prediction. For instance, (Cuddalorepatta et al., 2010) in their study of the durability of Pb-free solder between copper interconnect and silicon in PV cells used a field condition with a temperature range between 63 °C and 17 °C from a data provided from a sponsoring company. (Park et al., 2014) on the other hand, used field data with a cycle time of 24 h: 23-67 °C; 390 min ramp up and 330 min ramp down; 2 h dwell in high temperature and 10 h in low temperature to estimate the degradation rate of multi-crystalline silicon. However, the authors did not demonstrate how they generated the temperature cycle parameters in their respective studies.

An improvement of the current IEC 61215 (TC 200) temperature profile that would lead to an improvement in the prediction of module long-term outdoor reliability remains a research task. Solar PV modules experience direct exposure to sunlight in an alternating day/night cycles in service. Furthermore, the exposure induces thermo-mechanical stress on the solder interconnection joints within the module. Figure 4-1 presents the architecture of a conventional c-Si PV cell interconnection.

CHAPTER FOUR: GENERATION OF SPVM THERMAL CYCLES

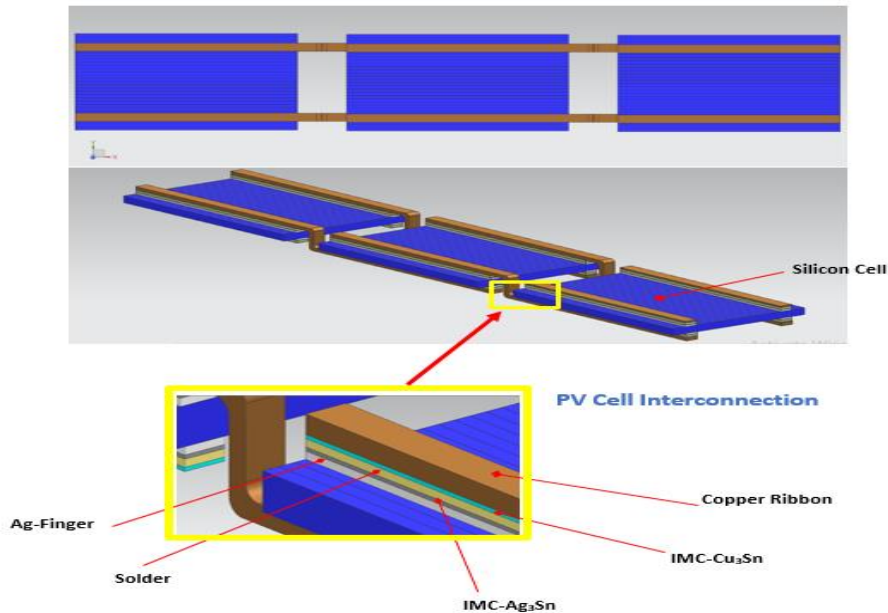


Figure 4-1: Conventional front-to-back cell interconnection technology in c-Si PV module

The conventional cell-to-cell interconnection architecture of c-Si PV modules involves connecting solder-coated copper (Cu) ribbons in a series arrangement. The ribbons connect the silver (Ag) electrodes deposited in the silicon crystal via solder bonds. These materials forming the interconnections of the module have a different coefficient of thermal expansion (CTE). (Park et al., 2014) explained that the variation in the CTE of constituent materials bonded together to form the module induces the thermo-mechanical stress. Consequently, the load effects culminate in the initiation and development of fatigue cracks in the soldered interconnection. Fatigue cracks in the joints increase module series resistance losses (R_s) and cause an overall drop in PV output power (Wenham et al., 1994). (Gonzalez et al., 2011) reported that the higher CTE mismatch between glass and cells may cause the cells to separate from the assembly. Furthermore, the high daily module temperatures aggravate the situation.

CHAPTER FOUR: GENERATION OF SPVM THERMAL CYCLES

Generally, an increase in temperature induces tensile stress in materials and thus in the interconnection. A decrease in temperatures lower than the stress-free temperature condition at night induces compressive stresses in the assembly and pushes the cells closer. A number of researchers have made significant contributions to the study of thermal cycling reliability of solder joints. However, the majority of the study focused primarily on flip-chip and BGA packages (Zhang et al., 2013, Zhang et al., 2008, Pang et al., 1998, Che and Pang, 2013). Research into thermal cycling of soldered interconnects in PV modules remain fewer in literature. This investigation involves a study of the in-situ operating module temperature of some field c-Si PV modules. The study uses a three-year data from 2012 to 2014 and develops a temperature cycle profile of each year. Consequently, the temperature profiles are used to generate a representative temperature profile for the test region.

4.2 Methodology

In this study, the thermal load cycles experienced by modules installed at a test site (College of Engineering, KNUST, Kumasi, Ghana latitude 6° 40" N and longitude 1° 37" W, and elevation of 250 m above sea level) were generated from real-time monitoring of module temperatures over a period of 3 years (from 2012 to 2014). Module temperatures were obtained by the use of platinum sensors with a resolution of 0.1°C and an accuracy of $\pm 0.5^\circ\text{C}$. The module temperatures generated at five-minute intervals were stored on a dedicated server. The methodology has been discussed in detail in chapter 3. The resulting large volume of data generated necessitated the development of an algorithm to select the peak temperatures in order to estimate the dwell times in a daily temperature cycle. Generally, a temperature dwell was assumed when the rate of temperature rise is below the average temperature ramp rate within the daily temperature cycle.

CHAPTER FOUR: GENERATION OF SPVM THERMAL CYCLES

The results of this study generated yearly temperature cycles for the 3-year period. Subsequently, a test region average (TRA) cycle was generated as a representative temperature cycle for c-Si PV modules at the test site. The resulting thermal cycles (for 2012, 2013, 2014 thermal cycles) served as thermal loads and boundary conditions for the numerical investigations using Finite Element Analysis (FEA).

4.3 Results and Discussions

The Sunny Webbox transmitted the high-resolution data logged at a 5-minute interval. The data were logged on a dedicated server from March 2012 to December 2014. The study and data analysis is limited to the monocrystalline PV-modules. This section discusses the observed climatic data and the analysis for the generation of temperature cycle profiles for the three years.

4.3.1 Daily temperature cycle profile

The data logged at a five-minute time interval produces 288 data points every 24 hrs. Figure 4-2 presents the distribution of module temperature signals observed during the study. Figure 4-2 shows that the modules recorded relatively higher frequencies of low-temperature signals (peaking around 23 °C) for each of the respective years (2012-2014). This observation is because the PV modules experience up to about 12 hrs of lower nighttime temperatures by virtue of the geographical location of the test site. As stated earlier, the module temperature data was logged from March 2012. Consequently, the size of the data points generated in 2012 was relatively smaller than that of the years 2013 and 2014. This may have accounted for the low concentration of temperature signals displayed for the year 2012. We further observed a mild year-to-year variation in temperature distribution between the years 2013 and 2014. The year

CHAPTER FOUR: GENERATION OF SPVM THERMAL CYCLES

2013 recorded slightly higher peaks in temperature signals between 30 °C and 60 °C compared with the year 2014.

Table 4-1 presents the statistics of some critical indices of the observed daily temperatures. It shows that the year 2012 recorded the minimum and maximum temperatures of 10.1°C and 73.2 °C, respectively. In addition, the temperature range of the year is the highest. The logged data were analyzed to produce plots of average daily temperature profiles of each month for the three years.

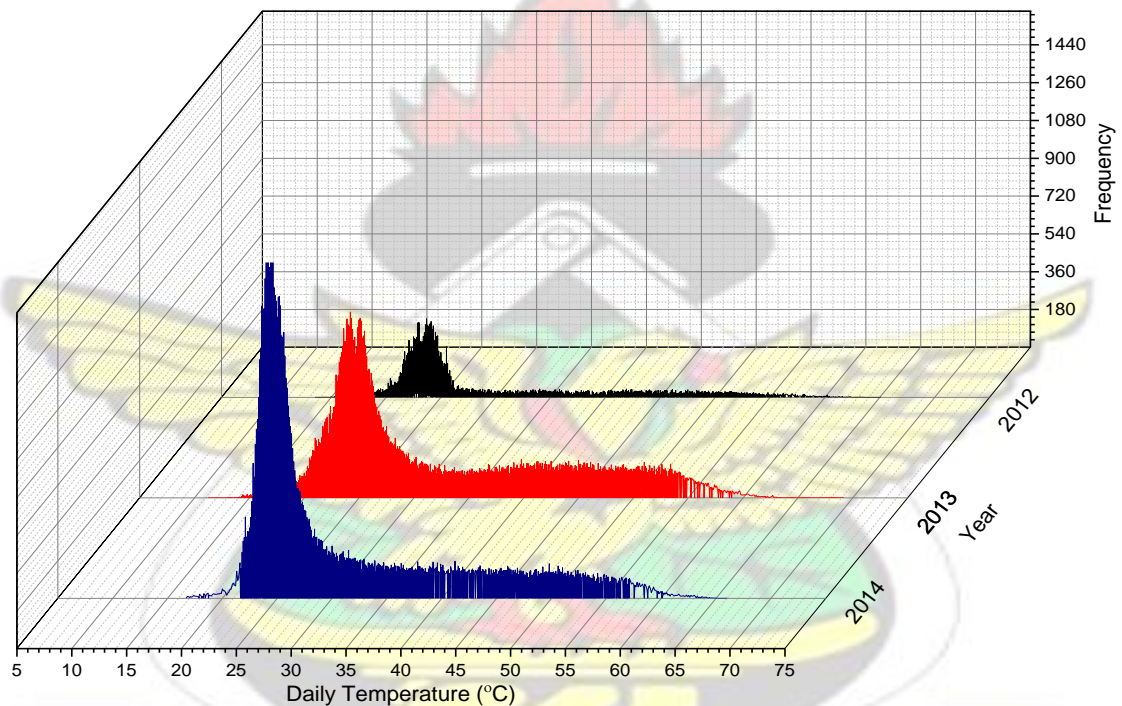


Figure 4-2: Distribution of recorded daily module temperatures for 2012, 2013 and 2014.

Table 4-1: Summary of recorded daily temperature for years 2012, 2013 and 2014

Year	2012	2013	2014
Mean	33.1	32.4	31.8
Minimum	10.1	18.5	20.2
Maximum	73.2	64.1	61.5
Std. Deviation	11.8	11.2	10.1
Range	63.0	45.6	41.3
Skewness	1.0	0.9	1.1

CHAPTER FOUR: GENERATION OF SPVM THERMAL CYCLES

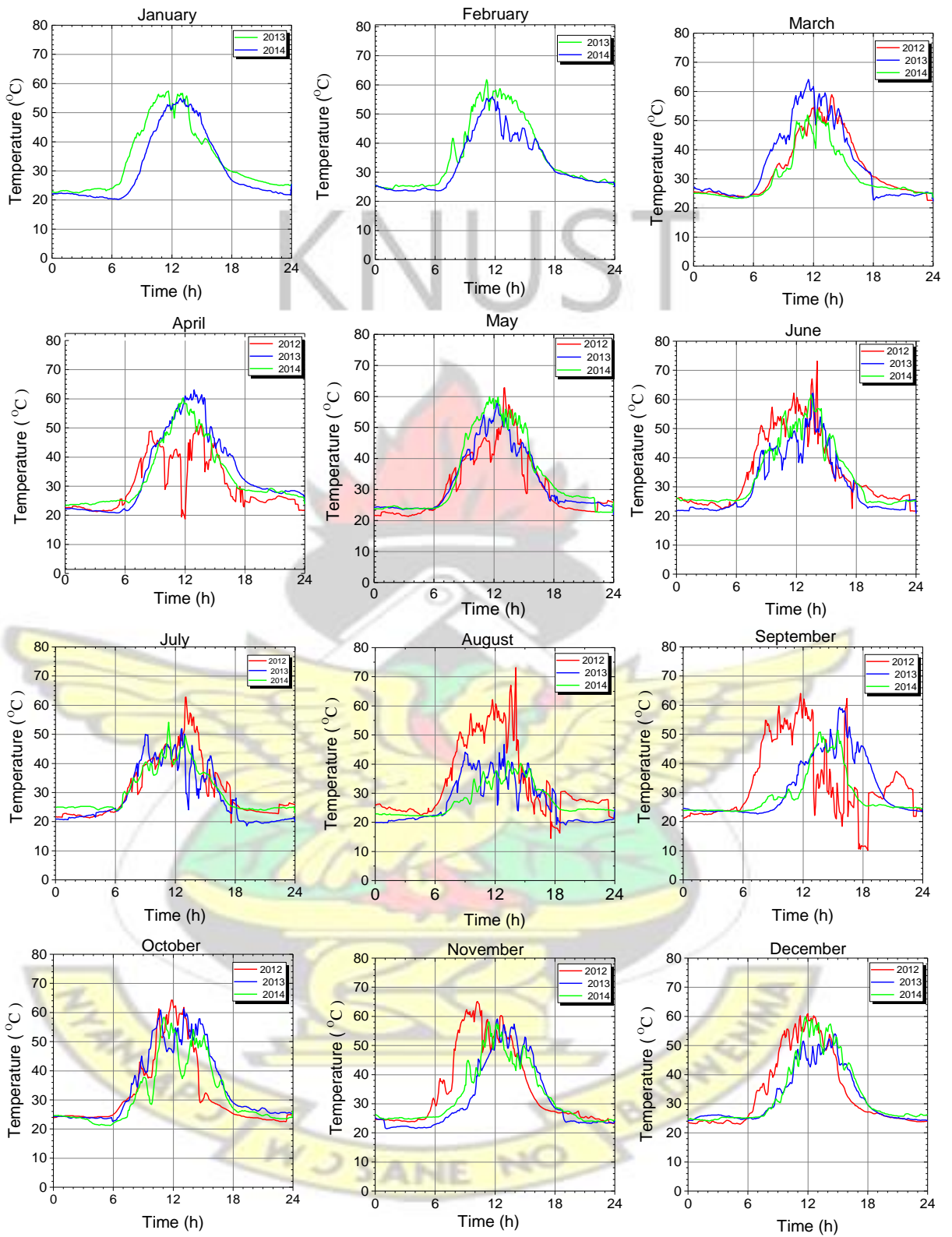


Figure 4-3: Daily temperature profile (monthly average) observed for 2012 - 2014

CHAPTER FOUR: GENERATION OF SPVM THERMAL CYCLES

Figure 4-3 presents the daily module temperature profiles (monthly average). The figure depicts that the average daily module temperature starts from around 20°C (midnight at local time, 00:00 hours) and slightly increases up to about 22°C at around 06:00 hours and peaks around 57°C at about 12:45 pm local time. Subsequently, the temperature decreases to around 22°C at about 1800 hours. Figure 4-3 shows that from the months of January to May, the year 2013 has the highest average daily temperatures while the year 2012 has the lowest values. Furthermore, it shows that from June to December, the year 2012 recorded the highest average daily module temperature while the year 2014 recorded the lowest.

4.3.2 Temperature Gradient of Thermal Cycle Profile

The daily temperature gradients of the cyclic temperature profile were determined from the logged module temperatures. The temperature gradients resulted from the difference between the peak daytime temperature and the minimum nighttime temperature.

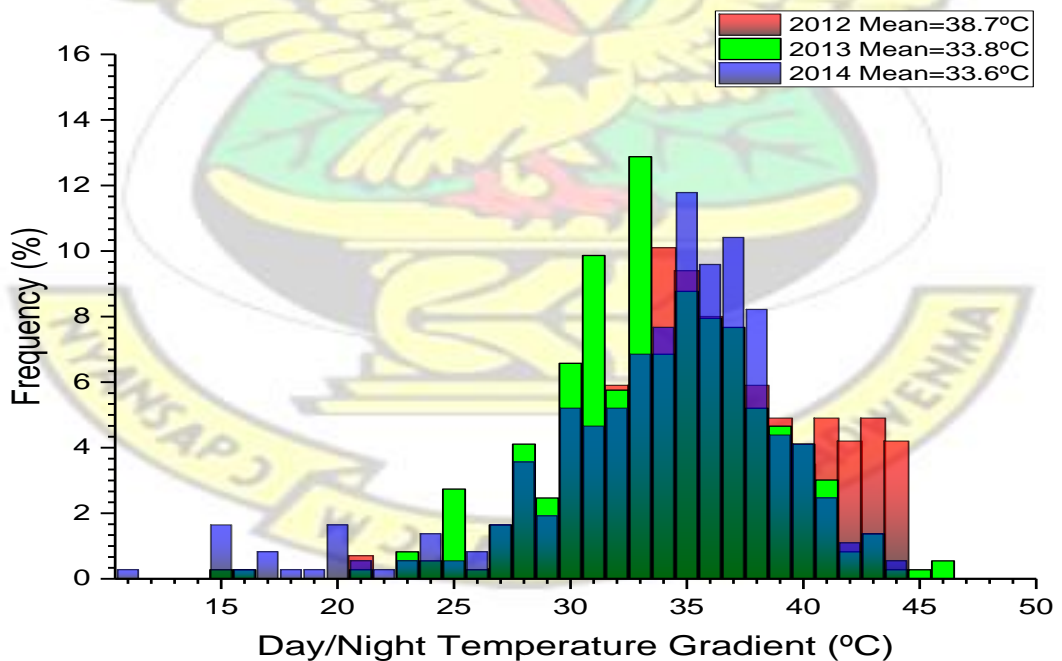


Figure 4-4: Frequency distribution of daily module temperature (monthly average) gradients observed for 2012-2014 at the test site.

CHAPTER FOUR: GENERATION OF SPVM THERMAL CYCLES

Figure 4-4 shows the distribution of temperature gradients for the mono c-Si PV module for the years 2012, 2013 and 2014. As observed in Figure 4.4, the yearly profiles are relatively similar.

The frequency distributions of the observed temperature gradients show curves with spikes, skewed towards higher temperature gradients. The mean temperature gradients of the modules are 38.7 °C, 33.8 °C and 33.6 °C for 2012, 2013 and 2014, respectively. The data compares well with results obtained from similar studies by (Herrmann et al., 2010).

4.3.3 Results from Module Temperature ‘Rainflow’ Counting Analysis

Figure 4-5 shows temperature cycles counted for the years 2012, 2013 and 2014 using the rainflow algorithm. Figure 4-5 revealed that sunrise and sunset ramping events correspond to low-frequency high-temperature range half-cycles. In addition, intra-day temperature fluctuations corresponded to short-range high-frequency temperature points. Typically, the tropical climate exhibits short-range high-frequency temperature ramping events mainly due to the presence of cloudy skies. More short-range ramping events were recorded for the year 2013 (28% over 2012) and 2014 (3% over 2012). The results trend closely with similar studies for a tropical climate by (Owen-Bellini et al., 2015)

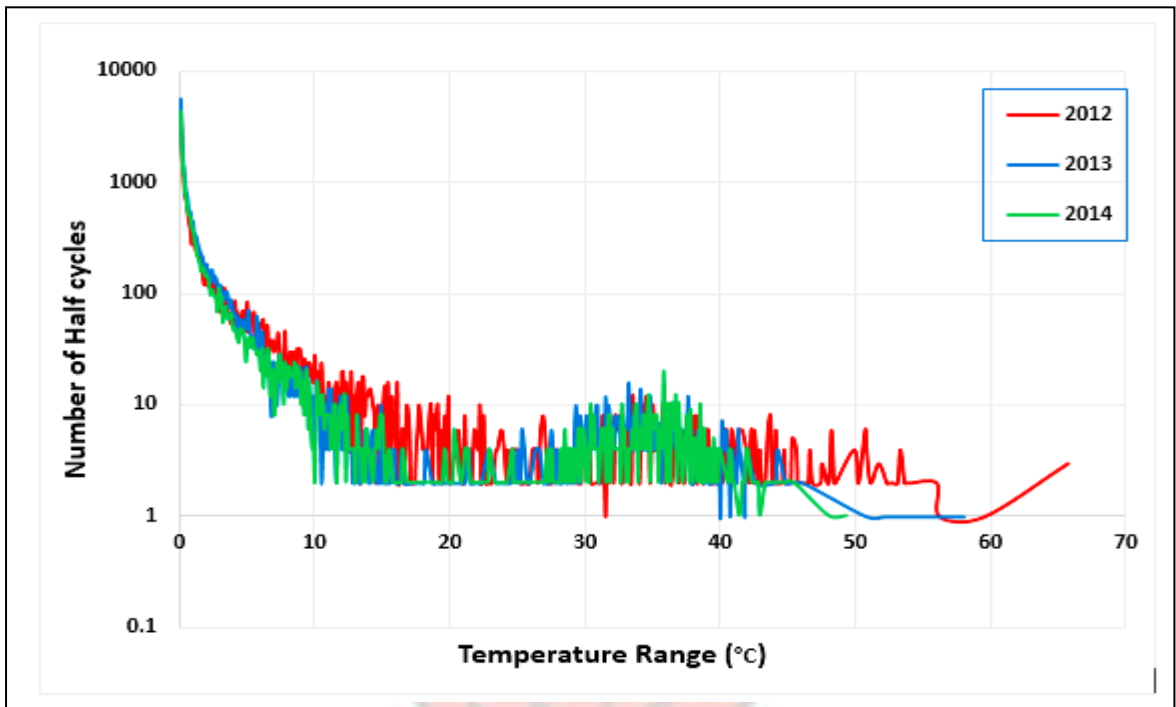


Figure 4 - 5: Distribution of cycles counted for each year (2012-2014)

4.3.4 Evaluating Heating and Cooling Rates of the PV Module

In this study, the heating and cooling rates of the monocrystalline silicon PV module were evaluated and analyzed using the IBM SPSS analysis tool (IBM). Figures 4.6 and 4.7 show the distribution of ramp rates obtained from the analyses of the data logged. The cumulative duration on the vertical axis evaluates the total time the PV module recorded a particular cooling/heating rate. From figure 4.6, the majority of ramp rates are well below 50 °C/h. Though there are ramp rates up and above the IEC 61215-test rate of 100 °C/h, the frequencies of their occurrence are relatively lower. Table 4-3 presents a summary of ramp rates recorded by modules for each test year. The mean ramp rates are very low (below 11 °C/h) for all the years. However, Table 4-3 depicts the occurrences of higher heating and cooling rates that are three times higher than the IEC 61215-test rate. Table 4-3 further reveals a percentage increase in maximum ramp rates of 238%, 147%, and 228% over the IEC 61215-ramp rate for years 2012, 2013 and 2014, respectively. The statistics are quite significant considering the fact that

CHAPTER FOUR: GENERATION OF SPVM THERMAL CYCLES

higher heating and cooling rates increase the damage accumulation that subsequently accelerates the degradation of soldered joints of the PV module (Skoczek et al., 2009).

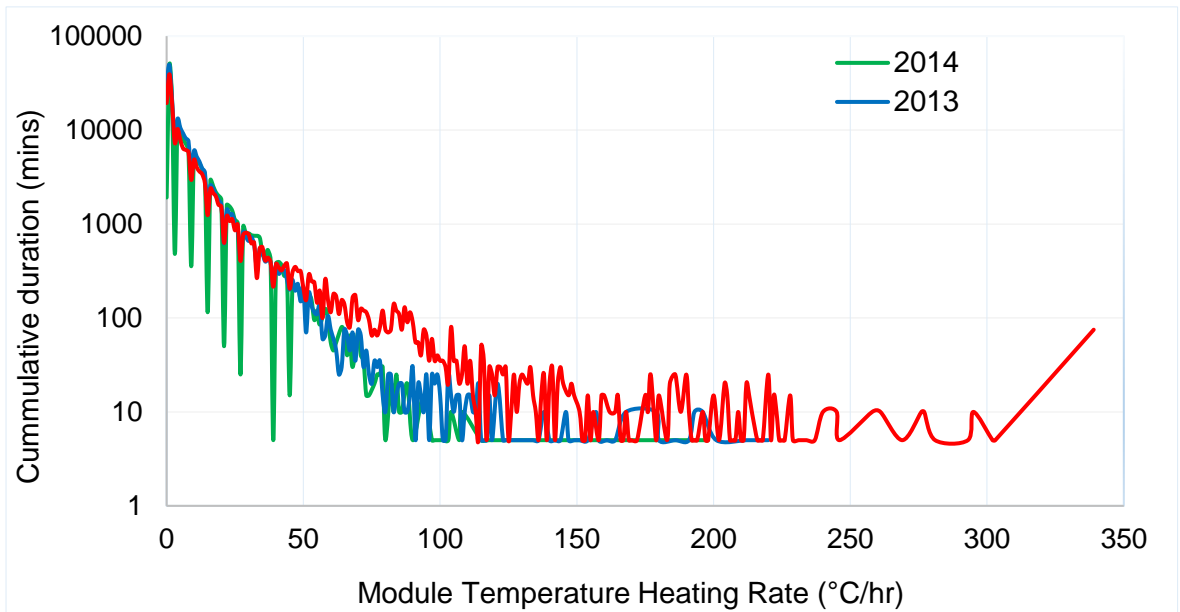


Figure 4 - 6: Cumulative frequency distribution of heating rates at test site

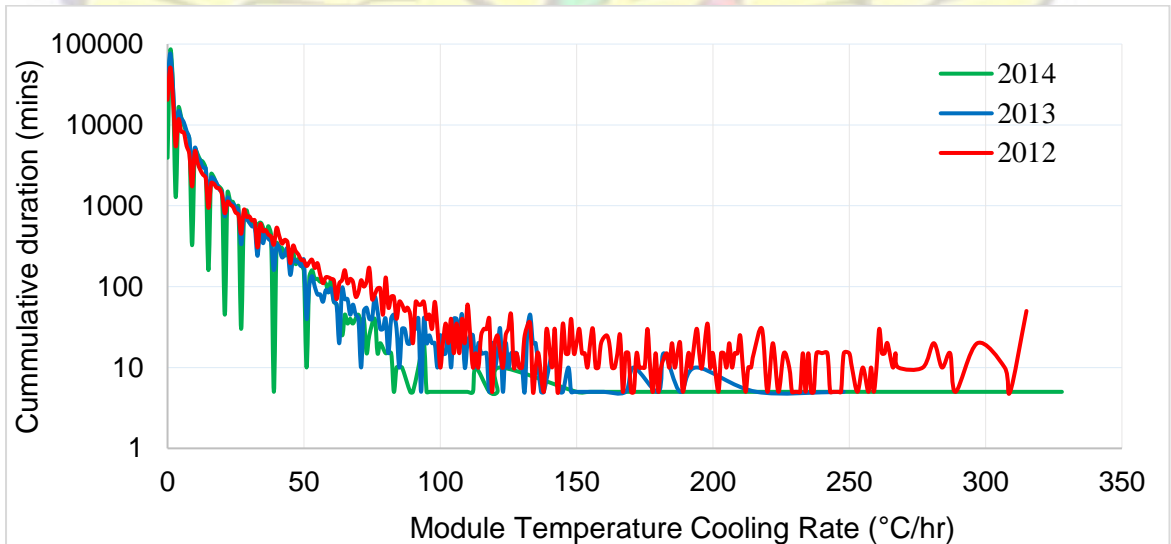


Figure 4 - 7: Cumulative frequency distribution of cooling rates from 2012 to 2014

CHAPTER FOUR: GENERATION OF SPVM THERMAL CYCLES

Table 4 - 2: Summary of observed heating and cooling rates and maximum ramp rates

Year	2012	2013	2014
Heating rates			
Mean (°C/h)	8.58	7.1	7.56
Maximum (°C/h)	339	220	198
% increase from IEC 61215 (100 °C/h)	238	120	98
Cooling rates			
Mean (°C/h)	10.44	10.2	10.1
Maximum (°C/h)	315	248	328
% increase from IEC 61215 (100 °C/h)	215	148	228
Maximum ramp rates			
Maximum heating rates(°C/h)	339	220	198
Maximum cooling rates (°C/h)	315	248	328
Maximum ramp rates(°C/h)	339	248	328
Maximum ramp rates(°C/min)	5.65	4.13	5.46
% increase from IEC 61215 (1.67°C/min)	238%	147%	228%

4.3.5 Results from Evaluation of Temperature Dwell Times of the PV Module

Figures 4-8 and 4-9 present a monthly average distribution of the dwell times (hot and cold) generated with the MATLAB algorithm. Table 4-3 lists the yearly average distribution of the hot and cold dwell times.

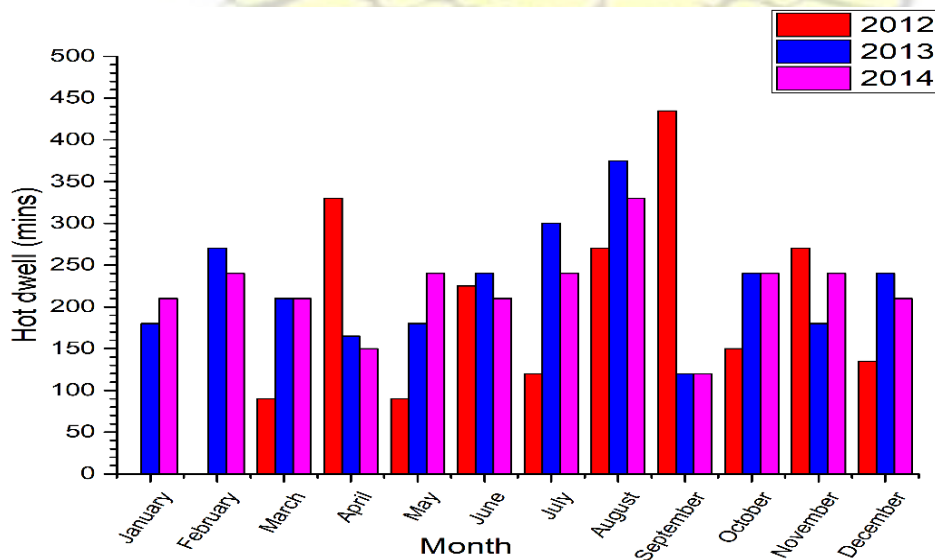


Figure 4-8: Monthly average distribution of hot dwell times (2012-2014)

CHAPTER FOUR: GENERATION OF SPVM THERMAL CYCLES

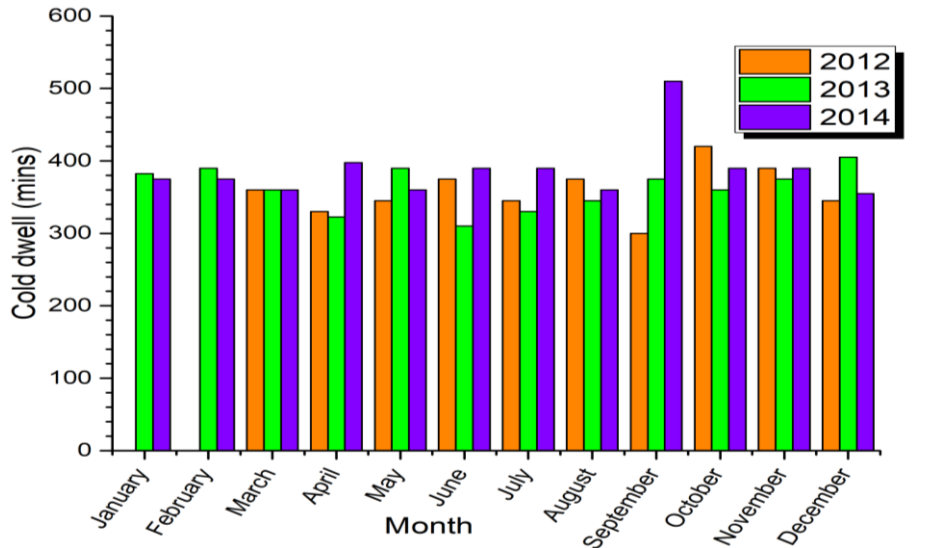


Figure 4-9: Monthly average distribution of cold dwell times (2012-2014)

Table 4-3: Summary of the parameters of the temperature cycle profiles

Test Year		2012	2013	2014	IEC 61215
Dwell time (min)	Mean Hot dwell	212	225	219	10
	Mean Cold dwell	359	357	390	10
Ramp rate ($^{\circ}\text{C}/\text{h}$)	Mean. Ramp rate	9.51	8.65	8.82	100
Mean module Hot Dwell Temperature (HDT)/ ($^{\circ}\text{C}$)		63.7	57.9	56.1	85
Mean module Cold Dwell Temperature (CDT)/ ($^{\circ}\text{C}$)		23.5	23	24.4	-40
Temperature gradient ($^{\circ}\text{C}$)		40.2	34.9	31.7	125

From Figures 4-8, 4-9 and Table 4-3 the cold dwell time remains constant averaging between 359-to-390 minutes with fewer spikes up to a maximum of 510 minutes. Furthermore, the year 2014 recorded the highest cold dwell times of 510 minutes, whilst the year 2012 recorded the highest hot dwell time of 435 minutes. The observed average hot and cold dwell times for the respective test years are far in excess of the 10-minute dwell time for the IEC 61215-test cycle. This is because SPV modules maintain near-constant peak temperatures for about three hours during the day, and maintain a near-constant temperature over long periods (over 6 hours) upon cooling at night.

CHAPTER FOUR: GENERATION OF SPVM THERMAL CYCLES

4.3.6 Generating in-situ Temperature Cycle (ATC) Profile using the Logged Data

In this section, the mean values of the ramp rates, dwell times, maximum and minimum temperatures experienced by the module in each of the respective years are used to generate in-situ temperature cycle profile representative of the test region. Table 4-3 presents a summary of the values of the critical parameters used to plot each temperature cycle profile of the years and the IEC 61215 condition. Figure 4-10 shows the actual daily temperature profiles recorded and fitted with a representative thermal cycle profiles for the respective years (2012-2014). The profiles show extended dwell times as well as overall cycle time. A typical daily cycle time completes in 86,400 s (24 hrs). As shown in Table 4, the mean daily temperature gradients for the generated cycles are relatively smaller when compared with the IEC 61215. A maximum of 40.2 °C recorded in 2012 whereas the IEC 61215 temperature gradient is 125 °C. The summary of the critical parameters presented in Table 4-3 shows that the effect of the employment of the IEC 61215 test on thermo-mechanical degradation qualification of the c-Si PV module is likely to be significantly different from the generated temperature cycles. For critical comparison, the temperature profiles (2012-2014) are combined and denoted as Test Region Average (TRA) cycle. Section 4.3.7 discusses the TRA cycle and the IEC 61215 cycle.

CHAPTER FOUR: GENERATION OF SPVM THERMAL CYCLES

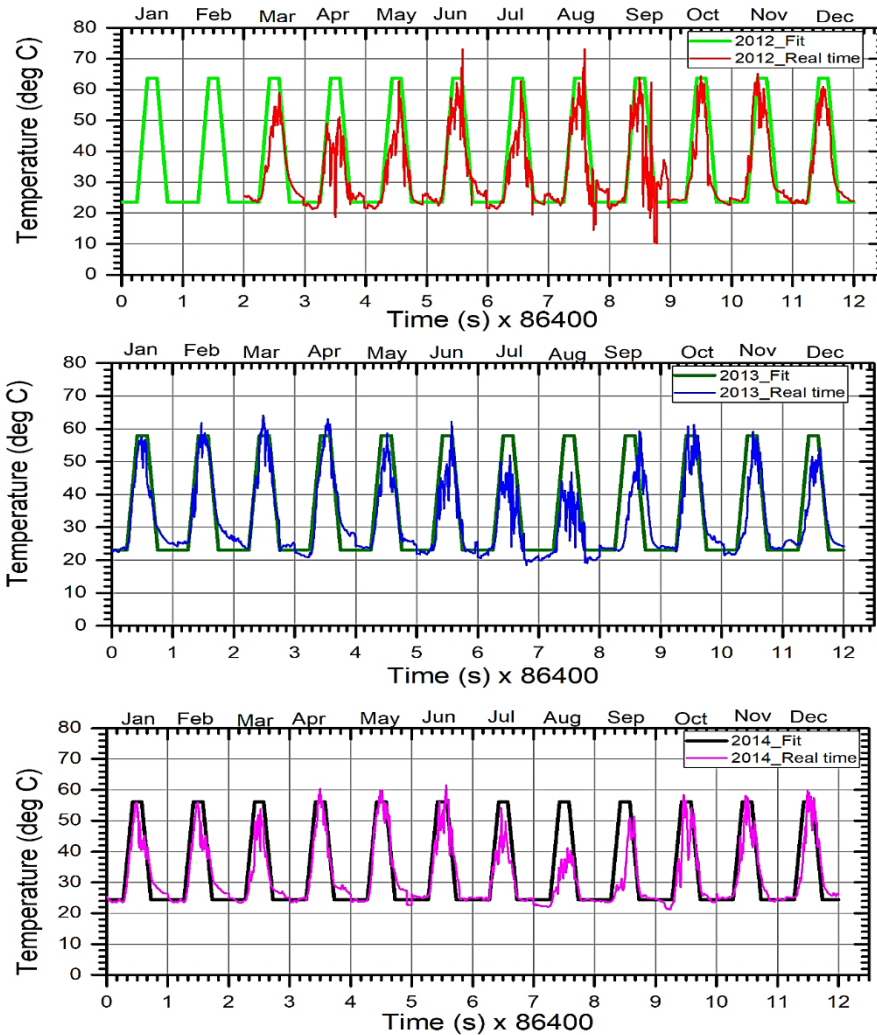


Figure 4-10: in-situ thermal cycle profiles fitted onto the real-time module temperature profile for 2012-2014.

4.3.7 Comparison of critical parameters of the generated ATC profile for test region with IEC 61215 Test qualification.

This section presents an ATC profile proposed to be representative of the test site. This is achieved by averaging the various cycle parameters such as the ramp rates, dwell times (Hot and Cold dwell), minimum module temperatures and maximum module temperatures. The section also discusses the critical parameters such as cycle time, ramp rates, dwell times and temperature gradients. Table 4-4 presents data analysis. Figure.4-11 (a) and (b) display the IEC 61215 profile and the generated TRA thermal cycle profile respectively. In general, the IEC 61215 features a relatively higher ramp

CHAPTER FOUR: GENERATION OF SPVM THERMAL CYCLES

rate of 100 °C/hr, shorter dwell time, short cycle time (10200 s) and a higher temperature gradient. The generated TRA profile, on the other hand, has relatively lower average ramp rates of 8.996 °C/hr, longer cold and hot dwell time, longer cycle time (86400 s) and lower temperature gradient.

Table 4-4: Summary of ATC profile parameters for Test Region and IEC 61215

ATC Profiles	Ramp Rates (°C/hr)	Dwell Times (min) Hot	Dwell Times (min) Cold	Maximum Temperature (°C)	Minimum Temperature (°C)	Temperature Gradient (°C)
Test Region						
Average (TRA)	8.996	228	369	58.9	23.7	35.2
IEC 61215	100	10	10	85	-40	125
% Difference	- 91 %	2180 %	3590%	- 30.7%	-159.3%	-71.8%

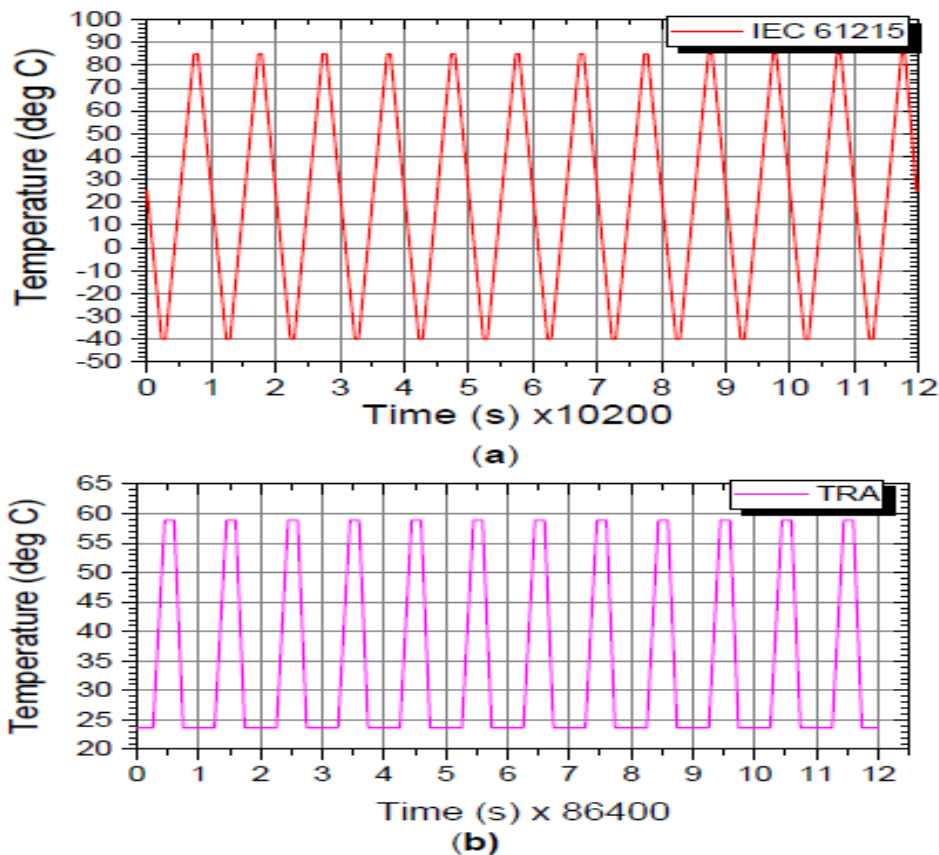


Figure 4 - 11: Plots of a twelve-cycle profile of (a) the IEC 61215 Test Qualification and (b) the Test Region Average (TRA).

CHAPTER FOUR: GENERATION OF SPVM THERMAL CYCLES

4.3.7.1 Ramp Rate

Table 4-3 shows that the ramp rate for the test region and the IEC 61215 are 8.996 °C/hr and 100°C/hr, respectively. The statistics demonstrate that the ramp rate of the test region (TRA) is 91 % at variance with the ramp rate for the IEC 61215-test cycle. A slower ramp rate leads to longer cycle time. The phenomenon accounts for the long completion of the temperature cycle in the sub-Saharan African TRA cycle. It is reported that cyclic strain energy increases with slower ramp rates in Pb-free (SAC) solder joints in chip resistor assemblies (Yoon et al., 2005).

The assertion is supported by similar research by (Clech, 2005) which concluded that thermal cycling with slower ramp rates leads to the largest reduction in shear strength. However, the results for tin-lead (SnPb) solder alloys appear to be on the contrary. For SnPb solders, results from studies conducted by (Sharma and Dasgupta, 2002, Clech, 2005) predicted a decrease in cyclic life with increasing ramp rates. Generally, short temperature cycle time accelerates the damage of the interconnection in the c-Si PV module by inducing a thermal shock in the system. It is significant to note that these studies reported on the solder joint lives in chip resistor assemblies. Studies on the effects of ramp rates on solder interconnections in the c-Si PV module are currently unavailable in the literature.

4.3.7.2 Dwell time

From Table 4-3 the hot and cold dwell times of the generated single cycle of the test region TRA are excessively higher than the IEC 61215. For instance, the hot dwell time of the test region is 2180 % at variance with the IEC 61215 dwell time. The difference in dwell time could have an adverse impact on the Mean Time to Failure (MTTF) of the c-Si PV module operating in the sub-Saharan Africa test site. Many studies

CHAPTER FOUR: GENERATION OF SPVM THERMAL CYCLES

conducted on eutectic soldered joints reported that the dwell time beyond certain limits has a minimal effect on the MTTF (Amagai, 1999, Sharma and Dasgupta, 2002, Zhai et al., 2003). Thus, an additional increase in dwell time will not produce additional damage beyond a certain limit. Other results show that due to rapid stress relaxation at the maximum cycle temperature, increasing the dwell time at high temperatures produces a little effect in creep damage of soldered joints (Schubert et al., 2002). However, the authors in (Schubert et al., 2002) observed a reduction in fatigue life due to increased creep strains at increased cold dwell time. Syed (Syed, 2001) reported that a longer dwell time causes more accumulated creep damage in the solder joint – thus lowering the fatigue life significantly.

It is therefore important to study the impact of dwell times on thermo-mechanical reliability of soldered interconnections in c-Si PV modules.

4.3.7.3 Temperature gradient and temperature cycle boundary conditions

Data from Table 4-3 shows that the profiles have average maximum module temperatures of 58.9 °C and 85 °C for the Test Region and the IEC 61215, respectively. The test region recorded an average minimum temperature of 23.7 °C whereas the IEC 61215 cycle has a minimum temperature ramp of -40 °C. The resulting temperature gradient of the test region is 35.2 °C. The value is lower than the IEC 61215 temperature gradient by about 71.8 %. (Pang et al., 2001b) reported an increase in accumulated creep strain range experienced by solder joints increases with temperature gradient. The increase leads to a decrease in the predicted fatigue life. (Pang et al., 2001b) further reported that creep exposure is greater for a higher temperature limit compared with a relatively lower temperature limit. These findings necessitate a critical investigation of the effect of these variables on the interconnection fatigue life of c-Si PV modules.

CHAPTER FOUR: GENERATION OF SPVM THERMAL CYCLES

4.4 Summary

This study analyzed the in-situ module temperature history of the monocrystalline silicon photovoltaic (c-Si PV) module operating in a sub-Saharan African climate. The temperature history consisted of a three-year observation period from 2012 to 2014. Analysis of the data yields a temperature cycle profile for the test site denoted as the TRA cycle. The study proposes the TRA cycle as a representative cycle of the sub-Saharan African test site. The generated TRA cycle has magnitudes of the critical parameters of ramp rate, hot and cold dwell times, maximum and minimum temperatures of 8.996 °C/h, 228 minutes (hot dwell), 369 minutes (cold dwell), 58.9 °C and 23.7 °C, respectively.

The percentage differences between the values of these parameters and the values of corresponding parameters of the IEC 61215 standards for terrestrial PV modules qualification are -91%, 2180%, 3590%, -30.7%, -159.3%, -71.8%, respectively. Furthermore, the percentage difference of the generated cycle time from the IEC61215 cycle time is about 747 % (86400 s versus 10200 s). These differences are huge and could explain the high failure rate that c-Si PV modules exhibit during operation in the sub-Saharan Africa region (Quansah and Adaramola, 2018).

The author of the current study proposes that the TRA cycle, which is location dependent, be used in finite element modelling of the PV system to predict thermo-mechanical degradation of soldered interconnects at the test site. This is necessary to quantify the differences in the rates of thermo-mechanical degradation in the region accurately. The results of the modelling will provide new knowledge to improve the reliability and increase the mean-time-to-failure of the PV modules operating in the sub-Saharan African climate.

CHAPTER FIVE: IMPACT OF CONSTITUTIVE BEHAVIOUR OF EVA ON SOLDERED INTERCONNECTIONS of SPVM.

5.1. Introduction

The global demand for energy continues to grow and that has made it imperative to consider sustainable energy sources. The Solar PV leads in the field of sustainable energy technologies capable of meeting the world's need for energy. However, the current high initial capital investment and relatively low lifetime pose a challenge to PV module uptake and installation (Kemausuor et al., 2011, Karekezi, 2002, Obeng and Evers, 2010, Obeng et al., 2008, Kankam and Boon, 2009). As a result, the industry continues to receive support in the form of government subsidy, as a means of encouraging user uptake. The degradation of the constituent parts of a solar PV module affects the reliability of the modules in the field. Consequently, the degradation leads to a gradual reduction in efficiency and eventual failure (Jellinek, 1989, McKellar and Allen, 1979, Emanuel and Buchachenko, 1987, Andrei et al., 1982). According to (Borri et al., 2018), cyclic loading which is a major cause of slow degradation of PV materials reduces the service life of PV modules. The field operating temperatures occasioned by day/night temperature cycle induces cyclic axial stress in the region between the silicon cells (interconnections) in the PV modules.

EVA, as an adhesive encapsulant and a key material in the cell assembly, suffers severely from this induced cyclic axial stress. The EVA acts as a protective layer by bonding the silicon cell to the front glass and the backsheet and thereby offering mechanical protection and electrical insulation (Badiee et al., 2016). EVA, like any other polymer, is stable at a certain range of operating temperatures where they possess the desired stiffness. EVA is soft and compliant within the operating temperatures; it is

CHAPTER FIVE: IMPACT OF CONSTITUTIVE BEHAVIOUR OF EVA ON SOLDERED INTERCONNECTIONS OF SPVM.

entropy elastic and has time-dependent material properties of creep and relaxation (Ehrenstein, 1999).

Although these facts about the viscoelastic constitutional behaviour of EVA is generally known, a number of investigations conducted into thermo-mechanical reliability of PV modules reveal variations in the constitutive models used in describing the material behaviour of the encapsulant (EVA). For instance, (Zarmai et al., 2015a) performed an optimization study on thermo-mechanical reliability of solder joints in a c-Si PV cell using finite element analysis (FEA) and the Taguchi method. In their study, the authors modelled EVA as a linear elastic material. Furthermore, (Herrmann et al., 2010) studied PV module degradation caused by thermo-mechanical stress using a linear elastic model for EVA during their numerical investigation. However, (Chen, 2008) investigated the residual stress and bow induced by soldering in the silicon cell interconnection by modelling EVA as temperature-dependent elastic perfectly plastic. In the study, (Chen, 2008) developed a 2D shell model of a single cell with aluminum BSF, copper, and solder to evaluate soldering induced damage. In another study, (Paggi et al., 2011) used analytical methods to investigate the thermo-elastic deformations in PV laminates by developing different approximate models based on the multi-layered beam theory. The authors (Paggi et al., 2011) used a temperature-dependent thermo-elastic property for studying the encapsulating polymer layer (EVA). Similarly, (Kraemer, 2014) performed a FEM stress analysis on different solar module concepts such as the front glass-backsheet assembly, glass-glass module for H-patterned cells and a back contact solar module under temperature cycling load. In the study by (Kraemer, 2014), the author modelled Young's modulus of EVA as temperature-dependent to describe the constitutive behaviour of EVA. In addition, (Amalu et al., 2018) analysed thermo-mechanical deformations in PV

CHAPTER FIVE: IMPACT OF CONSTITUTIVE BEHAVIOUR OF EVA ON SOLDERED INTERCONNECTIONS OF SPVM.

modules by modelling EVA material behaviour as having a temperature-dependent Young Modulus. (Ogbomo et al., 2018) also investigated the effect of operating temperature on the degradation of solder joints in crystalline silicon photovoltaic modules for improved reliability in hot climates using a temperature-dependent elastic model for EVA. Similarly, (Cuddalorepatta et al., 2010) in their study of the durability of Pb-free solder between copper interconnection and silicon in photovoltaic cells, modelled all cell materials other than solder as temperature-dependent linear elastic. On the other hand, other studies on thermo-mechanics of PV modules used viscoelastic models for studying the behaviour of EVA (Eitner et al., 2011b, Eitner et al., 2010, Eitner et al., 2011a). The pioneering research of (Eitner et al., 2010) on the viscoelastic behaviour of EVA has led to the adoption of the model in a number of recent studies as in (Hasan and Sasaki, 2016, Hasan and Arif, 2014, Hasan et al., 2013, Hasan and Sasaki, 2016, Song et al., 2018). In addition to the variations in the constitutive model for EVA in the above studies, there were varying levels of simplifications of the geometric models deployed in each of the studies. A key simplification of the solar PV model in most of the reviewed work was the absence of IMCs (intermetallic compounds) in the soldered interconnections of many models used in the various numerical investigations reported.

The constitutive behaviour of EVA as an encapsulant has a direct effect on soldered interconnections in solar PV modules. FE simulation results from (Shioda and Zenkoh, 2012) showed that an increase in Young's modulus of EVA led to higher stress in the solder bonds of solar cell interconnections. The findings were corroborated by (Mickiewicz et al., 2011) in a number of accelerated aging tests involving EVA and Silicones. In this study, we investigate the behaviour of the encapsulant (EVA) using

CHAPTER FIVE: IMPACT OF CONSTITUTIVE BEHAVIOUR OF EVA ON SOLDERED INTERCONNECTIONS OF SPVM.

three different constitutive models (linear elastic, temperature-dependent linear elastic and linear viscoelasticity). The geometric model used for this study attempts to completely define the solar cell by incorporating all material layers with their appropriate material behaviour in the cell assembly. The study uses the Finite Element Analysis (FEA) software (ANSYS 18.2) to simulate the thermo-mechanical stresses in the PV module for the temperature cycle generated from in-situ climatic conditions (Commission, 2005). Consequently, we examined the impact of the different constitutive models of EVA on damage on the solder and EVA material using both tin-lead ($\text{Sn}_{60}\text{Pb}_{40}$) and lead-free solder ($\text{Sn}_{3.8}\text{Ag}_{0.7}\text{Cu}$) for cell interconnection soldering. The results show the importance of incorporating the accurate constitutive model of EVA in the thermo-mechanical analysis of c-Si solar cells.

5.2. Methodology

The methodology for generating the TRA thermal cycle load and boundary conditions, solar cell material modelling, the finite element analysis has all been discussed exhaustively in chapter 3. In this investigation, we examine the impact of the three different constitutive models of EVA on cell interconnection damage from the generated test region average (TRA) thermal cycle.

The three constitutive models of the EVA material namely; linear elastic, temperature-dependent linear elastic and linear viscoelastic model were utilized in this study to predict the constitutive behaviour of the EVA during the static structural analysis of the encapsulated solar cell. This study was necessary in order to ascertain the most appropriate constitutive behaviour of the EVA material for modelling in subsequent investigations. Tables 5-1 and 5-2 present a summary of parameters for the numerical

CHAPTER FIVE: IMPACT OF CONSTITUTIVE BEHAVIOUR OF EVA ON SOLDERED INTERCONNECTIONS OF SPVM.

investigation. Results and discussions from this study are presented in the subsequent section.

Table 5 - 1: Solar Cell Material constitutive model

LAYER	MATERIAL	CONSTITUTIVE BEHAVIOUR
Glass	Glass	Isotropic linear elastic
Encapsulant	EVA (Ethylene vinyl Acetate)	<ol style="list-style-type: none"> 1. Linear elastic (LEMM) 2. Temperature dependent linear elastic (TDEMM) 3. Linear viscoelastic (LVMM)
Solar Cell	Silicon	Anisotropic (different elastic constants at different loading directions)
Interconnector	Copper	Bi-linear (Young's modulus changes with temperature)
Busbar	Silver fingers	Isotropic linear elastic
Rear contact	Aluminium	Isotropic linear elastic
Interconnecting Material	Solder (SnPb, SnAgCu)+ IMC (Cu ₃ Sn, Ag ₃ Sn)	Solder: Generalised Garafalo-Arrhenius model IMCs: Isotropic linear elastic
Backsheet	Tedlar	Isotropic linear elastic

Table 5 - 2: Thermal load and boundary conditions

Thermal cycle	Min. temp (°C)	Max. temp (°C)	Ramp-rate (°C/hr)
TRA	23.7	58	8.996

CHAPTER FIVE: IMPACT OF CONSTITUTIVE BEHAVIOUR OF EVA ON SOLDERED INTERCONNECTIONS OF SPVM.

5.3. Results and Discussion

5.3.1 Study on equivalent Von-Mises stress in EVA

Results from equivalent Von-Mises stress distribution evaluated across the EVA laminate from different constitutive models (linear elastic material model (LEMM), temperature-dependent linear elastic Young's modulus (TDEMM) and linear viscoelastic material model (LVMM)) for two main types of soldered interconnections (SnPb and Pb-free) are presented in Figure 5-1.

The stress distribution shows the highest equivalent stress damage in the EVA material when modeled as a linear elastic material with both SnPb and Pb-free solder interconnection. The viscoelastic model, on the other hand, recorded the lowest equivalent Von-Mises stresses in the EVA material for both types of solder interconnections utilized in the study. A Maximum stress of 4.857×10^7 Pa was recorded for EVA as a LEMM with a Pb-free solder interconnection. The LEMM with PbSn solder interconnection followed closely with a maximum equivalent stress value of 6.143×10^6 Pa. The TDEMM recorded maximum equivalent stress values of 3.0723×10^7 Pa and 3.1793×10^7 Pa at the end of the twelve (12) thermal cycles for the SnPb and Pb-free solder interconnections respectively. However, the LVMMs recorded much lower equivalent stresses in the EVA. A maximum of 525.83 Pa was recorded for the SnPb interconnection whereas the Pb-free solder interconnection recorded maximum equivalent stress of 522.96 Pa.

CHAPTER FIVE: IMPACT OF CONSTITUTIVE BEHAVIOUR OF EVA ON SOLDERED INTERCONNECTIONS OF SPVM.

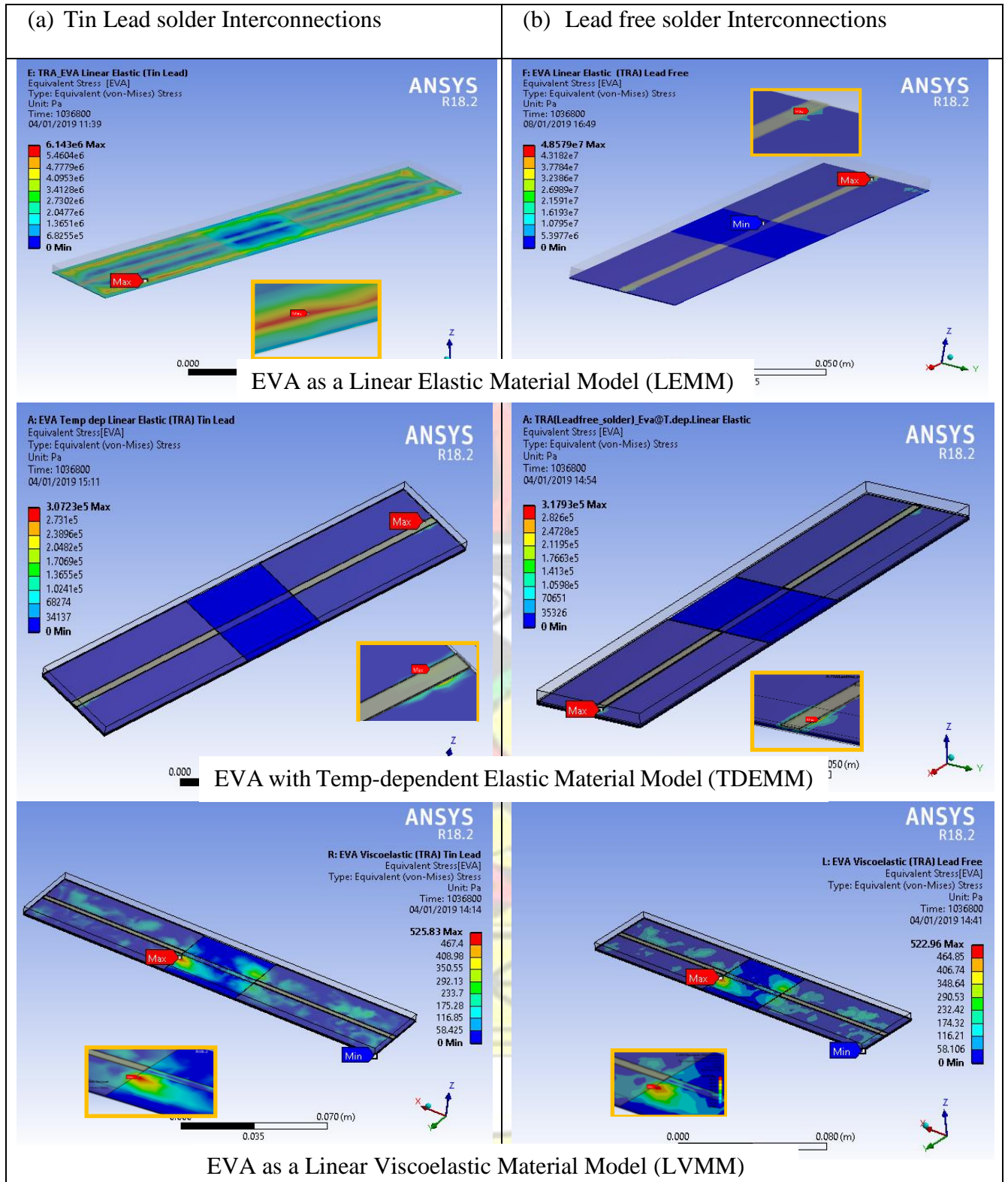


Figure 5 - 1: Equivalent von-Mises stress distribution in EVA for (a) tin-lead solder and (b) lead-free solder interconnection for different EVA material constitutive models.

CHAPTER FIVE: IMPACT OF CONSTITUTIVE BEHAVIOUR OF EVA ON SOLDERED INTERCONNECTIONS OF SPVM.

Another critical observation from the simulation results of the different material models is the region where the maximum stresses occur in the interconnections for the three different constitutive models of EVA. For the LEMMs the maximum stresses occur at different regions within the EVA material for the two types of interconnections under study. We observed from Figure 5-1 that the maximum stress occurs along a section of the EVA material away from the interconnection string for SnPb solder interconnection. However, for the Pb-free solder interconnection, the region of maximum stress in the EVA material is along the interconnect string. With the TDEMMs and LVMMs, the regions of maximum stress in the EVA is independent of the type of solder at the interconnection. The position of maximum stress (along the interconnection string) remained unchanged for both types of soldered interconnection investigated for TDEMMs. A similar observation for the LVMMs shows the position of maximum stress (cell gap region) remained unchanged for the two types of interconnecting solders. The stress contour plots from the three constitutive models for EVA show that the LVMMs presents lower maximum stresses at less critical regions (cell gap region). Presented in Figure 5-2 are the stress-time responses in the EVA over the 12-thermal cycles for the three constitutive models. For the LEMMs, higher stresses with nearly equal amplitude per cycle are observed for SnPb solder interconnection. On the other hand, with the Pb-free interconnection, the stress variation over the cycle show a gradual reduction in stress amplitude as the thermal cycle progresses.

CHAPTER FIVE: IMPACT OF CONSTITUTIVE BEHAVIOUR OF EVA ON SOLDERED INTERCONNECTIONS OF SPVM.

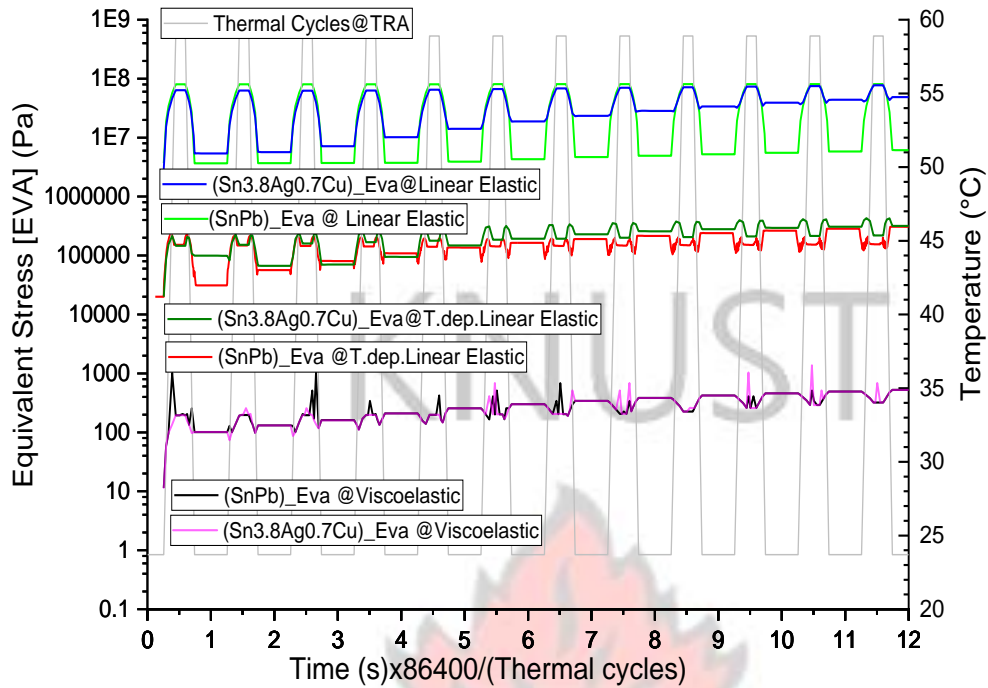


Figure 5-2: Equivalent von-Mises Stress in EVA versus Thermal Cycles @ TRA

For the TDEMMS, a gradual reduction in stress amplitude up to the third (3rd) thermal cycle was observed for both types of solder interconnections. Subsequently, the stress amplitudes assumed what appears like a constant value for the remaining cycles. Results from the LVMMs also show the stress profiles for the two types of interconnections almost tracking each other with the same amplitude over the 12-cycles with slightly higher stresses after the third thermal cycle. The stress amplitudes registered with LVMMs were relatively lower as compared with LEMMs and the TDEMMS. Another significant observation from the equivalent stress-time response curves is the position of maximum stress in a cycle. For LEMMs stresses peak at maximum temperatures and dwells with the hot temperature dwells. Stresses assume the lowest values at cold temperature dwells. For the TDEMMS the stresses peak and troughs within the hot temperature dwell. For the LVMMs the stresses show multiple spikes at hot temperature dwells within the cycle.

CHAPTER FIVE: IMPACT OF CONSTITUTIVE BEHAVIOUR OF EVA ON SOLDERED INTERCONNECTIONS OF SPVM.

Overall, the LVMMs impose significantly lower stresses from thermal cycling on the EVA material in the cell assembly compared with LEMMs and TDEMMs. In addition, the LVMMs show maximum stresses occurring at less critical positions within the cell (cell-gap region) as compared with the LEMMs and TDEMMs where the maximum stresses occur along the line of interconnection.

5.3.2 Evaluation of maximum principal strains in EVA.

In this section, the maximum principal elastic strain in the EVA material was evaluated over the 12 thermal cycles for the three constitutive models under study. The results are presented in Figure 5-3. The results show that maximum principal strains evaluated for LVMMs remain the highest with 1.2243 m/m and 1.2176 m/m for SnPb solder and Pb-free solder interconnection, respectively. Significantly lower strains are observed for TDEMMs with values of 0.0303294 m/m (for SnPb solder interconnection) and 0.030079 m/m (for Pb-free solder interconnection) at the end of the twelve thermal cycles. For the LEMMs, a maximum principal strain of 0.031942 m/m was evaluated for the Pb-free solder interconnection. However, the maximum principal strain was reduced by approximately 86% to 0.0044428 m/m when SnPb solder was used as the interconnection material.

For the TDEMMs (both PbSn and Pb-free) and LEMM with Pb-free solder interconnection, the critical region where peak values of maximum principal strains occurred were observed to be along the interconnection string. On the other hand, the critical region of maximum principal strains for LVMMs was found to be within the cell-to-cell gap. For LEMM with PbSn solder interconnection, the region of maximum principal strain in the EVA was found to be closer to the edge of the cell and away from the region of the interconnection string.

CHAPTER FIVE: IMPACT OF CONSTITUTIVE BEHAVIOUR OF EVA ON SOLDERED INTERCONNECTIONS OF SPVM.

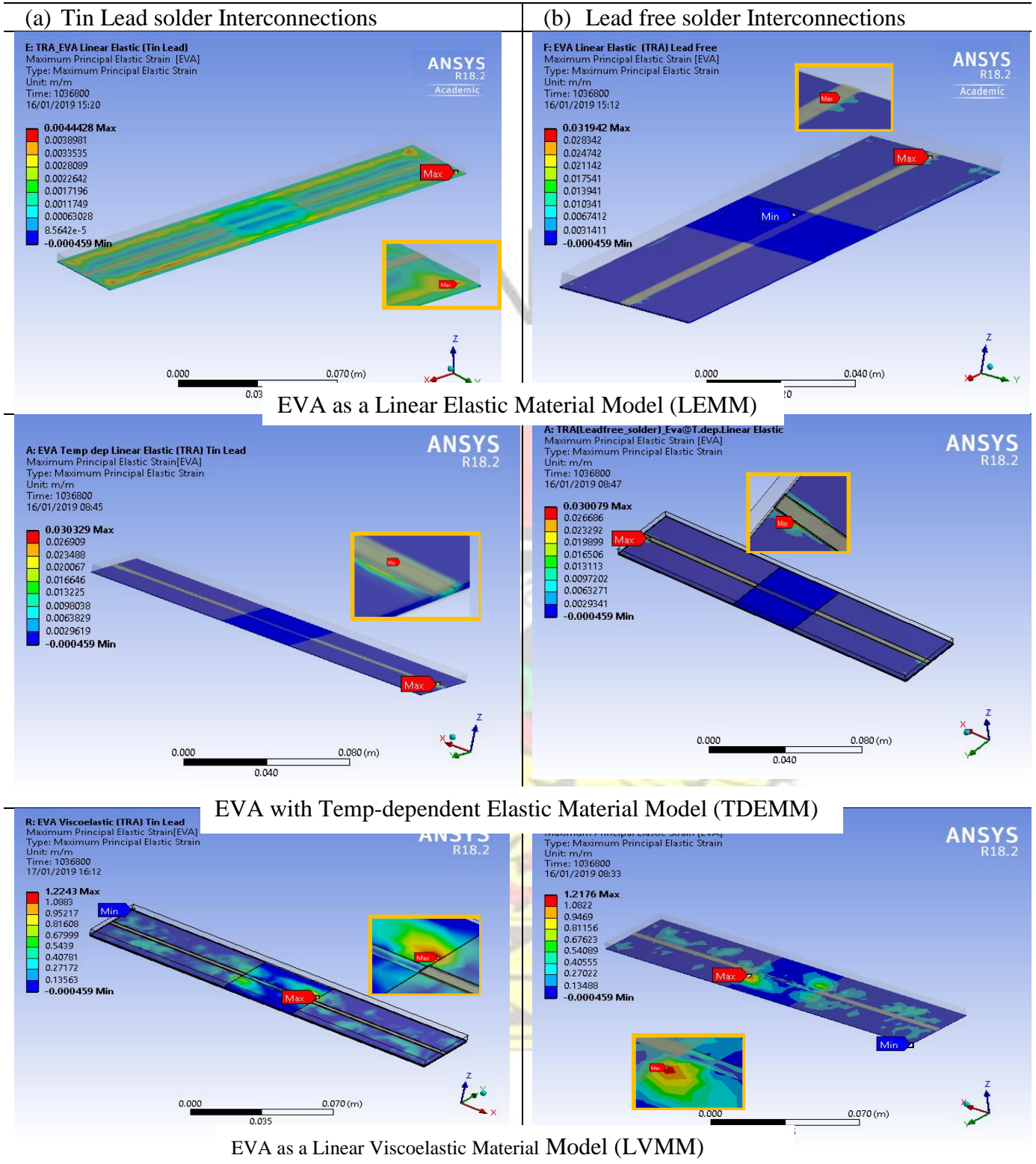


Figure 5-3: Maximum Principal Strains distribution in EVA material from a TRA Cycle

CHAPTER FIVE: IMPACT OF CONSTITUTIVE BEHAVIOUR OF EVA ON SOLDERED INTERCONNECTIONS OF SPVM.

The variation of maximum principal elastic strain over the twelve cycles for the six different models under consideration is presented in Figure 5-4.

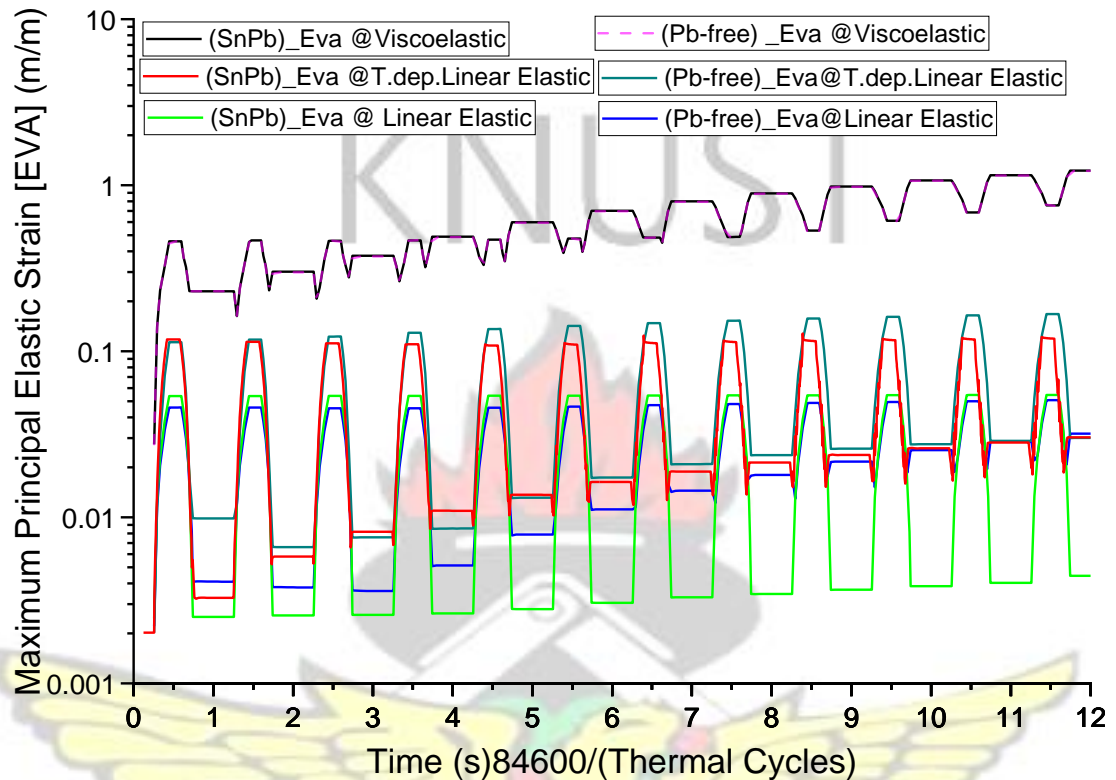


Figure 5-4: Maximum Principal Strain Cycles

The amplitude of the maximum principal strain remained constant for LEMM with SnPb solder interconnection. On the other hand, maximum principal strains of LEMM with Pb-free solder interconnection show constant strain amplitude up to the third thermal cycle and a gradual reduction in strain amplitude from cycle 3 to cycle 12. With the TDEMMS, the amplitudes of the maximum principal strains experience gradual reduction up to the sixth thermal cycle. Subsequently, the amplitudes remain constant for the rest of the cycles. The LVMMs, on the other hand, show maximum principal strains tracking and overlapping with a gradual rise over the twelve cycles.

CHAPTER FIVE: IMPACT OF CONSTITUTIVE BEHAVIOUR OF EVA ON SOLDERED INTERCONNECTIONS OF SPVM.

5.3.3 Study on time-dependent equivalent creep strain in Solder joint.

The integrity of soldered interconnections depends largely on the durability of the solder bond within an interconnection. Creep remains a key failure mechanism that affects solder materials. In this study, we evaluate the equivalent creep strain of the twelve cycles and analyse the results for the three different material models of EVA. The results are presented in Figures 5-5 and 5-6. The results from the equivalent creep strain evaluated at the end of the 12 thermal cycles and presented in Figure 5-5 show noticeable variations for the two types of solders and the different material models of EVA used for the study.

The contour plots show that creep strain effects recorded on the solder are lowest (0.002673 m/m) for SnPb-solder interconnections when LEMM is used to formulate the constitutive behaviour of the encapsulant (EVA) for the thermal cycling analysis. However, the equivalent creep strain is at the highest (0.10217 m/m) when the solder is replaced with a Pb-free solder (Sn3.8Ag0.7Cu). When the constitutive behaviour of EVA is changed to a TDEMM, the equivalent creep strains induced in the solder interconnections were found to be 0.012257 m/m and 0.016157 m/m for SnPb and Pb-free solder interconnections respectively. In the case of LVMMs, the creep strains induced in the solder at the end of the twelve thermal cycles were found to be relatively lower compared with that of the TDEMMs of EVA. The maximum equivalent creep strain registered in the solder for LVMMs of EVA was found to be 0.008097 m/m and 0.0097851 m/m for SnPb and Pb-free solder interconnections, respectively.

CHAPTER FIVE: IMPACT OF CONSTITUTIVE BEHAVIOUR OF EVA ON SOLDERED INTERCONNECTIONS OF SPVM.

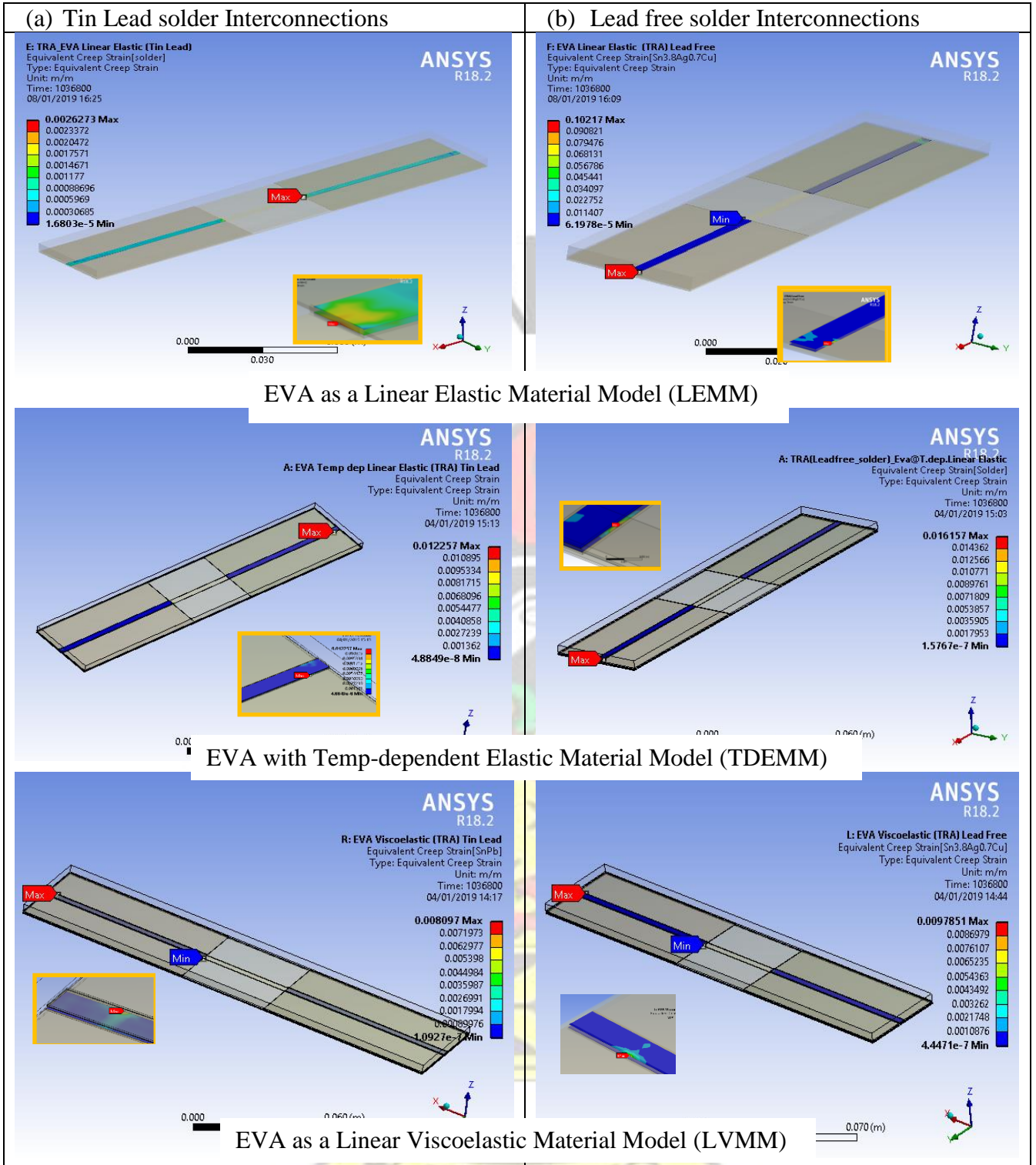


Figure 5-5: Equivalent Creep Strain Distribution in Interconnecting Solder

CHAPTER FIVE: IMPACT OF CONSTITUTIVE BEHAVIOUR OF EVA ON SOLDERED INTERCONNECTIONS OF SPVM.

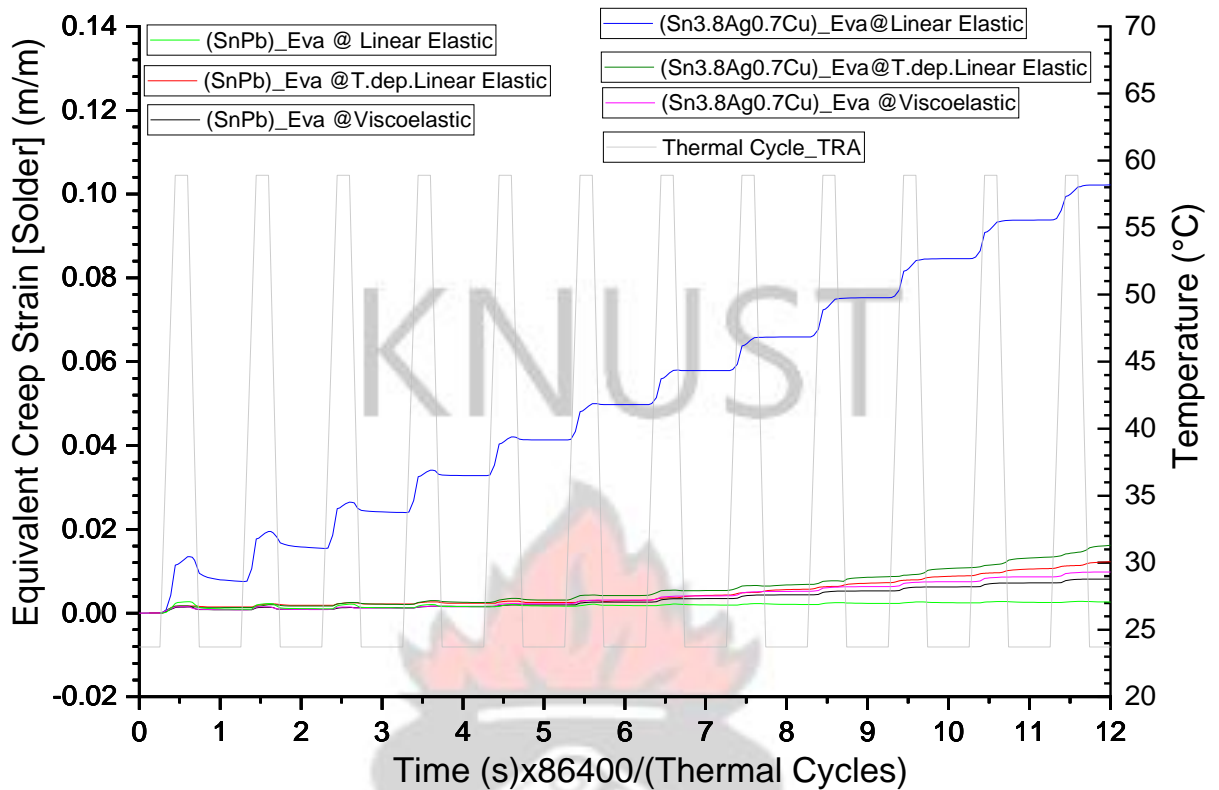


Figure 5-6: Time Response of Equivalent Creep Strain in Interconnecting Solder

Time-dependent plots of equivalent creep strain are presented in Figure 5-6 for the three different models of EVA. From Figure 5-6 the equivalent creep strain for LEMM of EVA with Pb-free solder interconnection rises sharply and nearly as a stepped function from the 1st to the 12th cycle departing sharply from all the other models. The plots further show that the equivalent creep strains for the different models of EVA (with the exception of LEMM with Pb-free solder) appear to track each other and nearly overlap up until the 5th thermal cycle. These results show that, for simulations of up to the 5th thermal cycle and with the exception of LEMM of EVA for Pb-free solder interconnection, the equivalent creep strain induced in the solder interconnection is not affected by the constitutive behaviour of EVA. From the 5th thermal cycle, we observe marginal variations in equivalent creep strain from the different constitutive models of EVA (excluding LEMM Pb-free solder interconnect). For EVA as a LEMM with SnPb

CHAPTER FIVE: IMPACT OF CONSTITUTIVE BEHAVIOUR OF EVA ON SOLDERED INTERCONNECTIONS OF SPVM.

solder interconnection, the equivalent creep strain remained the lowest throughout the 12th thermal cycles. The equivalent creep strains in the soldered interconnections (both SnPb and Pb-free solder interconnection) when EVA is modelled as a LVMM rose marginally from the 5th thermal cycle up to the 12th cycle with the creep strain in the Pb-free solder interconnect leading that of the SnPb solder interconnect. Similarly, when EVA is modelled as a TDEMM, the equivalent creep strains rise marginally from the 5th thermal cycle up to the 12th cycle.

5.3.4 Evaluation of Strain Energy and Strain Energy Density of Solder joint.

5.3.4.1 Evaluation of Strain Energy of Solder Joint

The strain energy generated in the solder joint at the end of 12th thermal cycles is presented in Figure 5-7 for the three different constitutive models of EVA (LEMM, TDEMM, LVMM) used in the study. We observed from Figure 5-7 that the strain energy generated in the solder (for the two types of soldered interconnections) remained the highest when LEMM is used for modelling the behaviour of the EVA material. The highest strain energy of 1.2284×10^{-7} J is registered in the LEMM with the Pb-free solder interconnection. For the LEMM with SnPb-solder interconnection, the maximum strain energy was found to be 2.8978×10^{-8} J. Using TDEMM to study the behaviour of EVA, the lowest strain energy values were generated in the solder joint for both types of interconnection. Furthermore, a similar trend was observed (as with the LEMMs) where the strain energy for SnPb-solder interconnection generated a relatively higher strain energy damage (1.6776×10^{-8} J) as compared with a strain energy damage of 1.2615×10^{-8} J in the Pb-free solder. The trend similarity continues with the LVMMs where the output from the contour plots shows maximum strain energy values of 2.5335×10^{-8} J and 1.5451×10^{-8} J for SnPb and Pb-free solder interconnections respectively.

CHAPTER FIVE: IMPACT OF CONSTITUTIVE BEHAVIOUR OF EVA ON SOLDERED INTERCONNECTIONS OF SPVM.

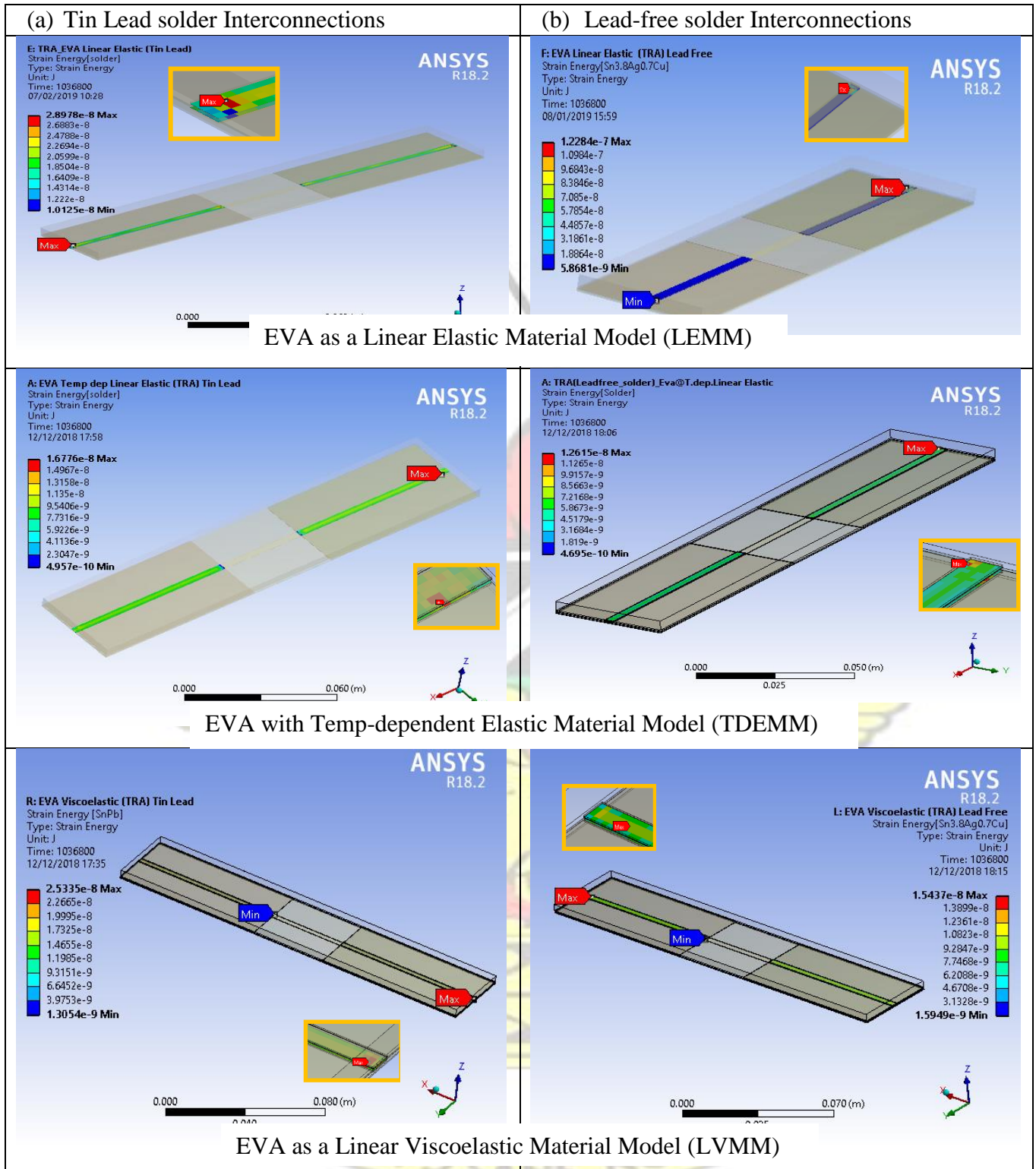


Figure 5-7: Strain Energy Distribution in solder for the different material models of EVA

CHAPTER FIVE: IMPACT OF CONSTITUTIVE BEHAVIOUR OF EVA ON SOLDERED INTERCONNECTIONS OF SPVM.

5.3.4.2 Evaluation of Strain Energy Density of a soldered joint.

Figure 5-8 (a) and (b) display a plot of strain energy density versus cycle time for 12-thermal cycles. The strain energy density is evaluated by dividing the strain energy density by the volume of interconnecting solder.

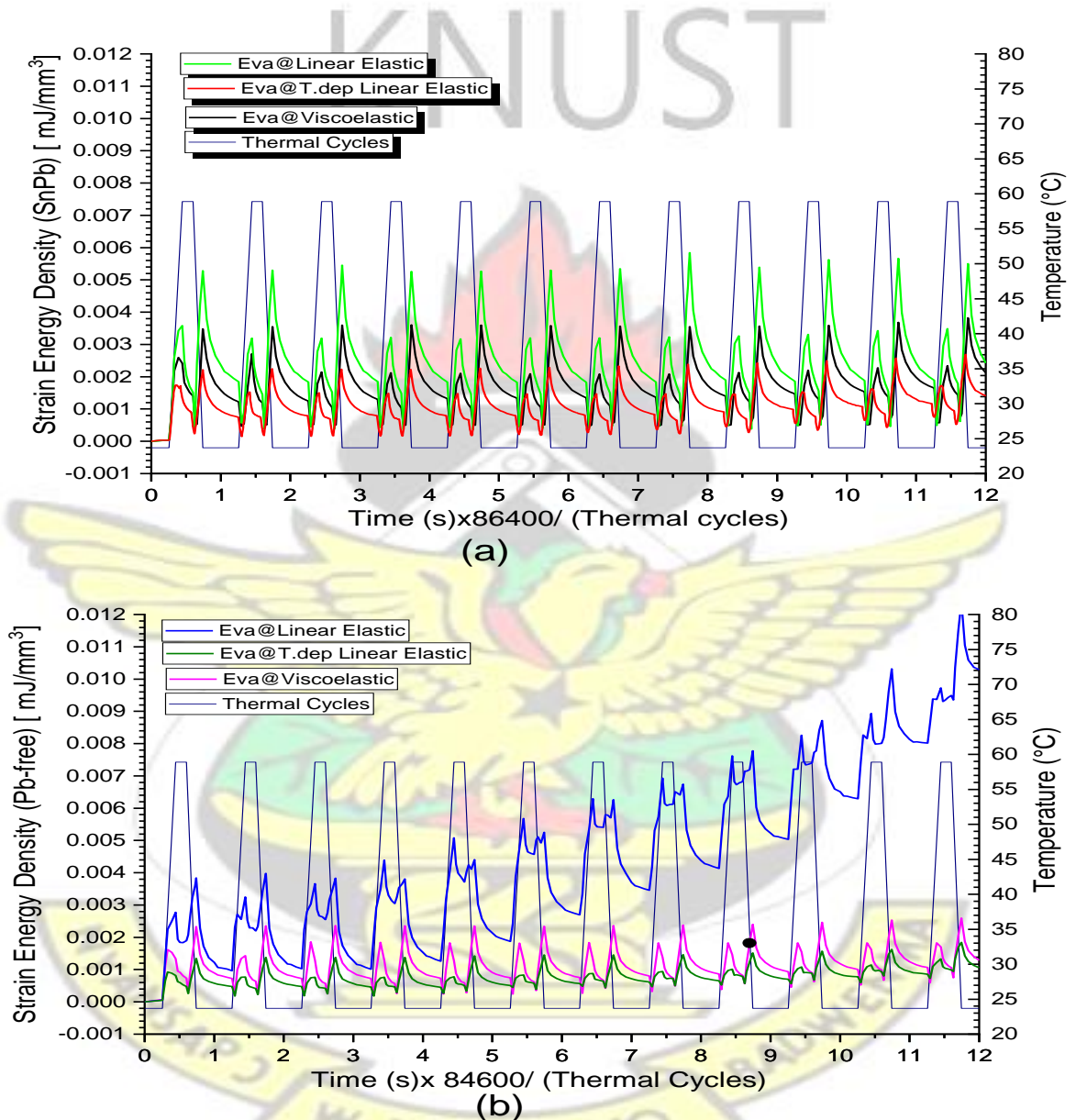


Figure 5-8: Strain Energy Density profiles versus thermal cycles

The response of strain energy density over the thermal cycles shows that for TDEMMs and LVMMs of EVA the strain energy density assumes higher amplitudes in the SnPb -solder compared with the Pb-free solder interconnection. Conversely, with the

CHAPTER FIVE: IMPACT OF CONSTITUTIVE BEHAVIOUR OF EVA ON SOLDERED INTERCONNECTIONS OF SPVM.

LEMMs, the strain energy density response shows relatively higher amplitudes of strain energy density for the Pb-free solder interconnection compared with the SnPb solder interconnection. With the Pb-free solder interconnection, the strain energy density for LEMM shows a steady rise in amplitude to a peak value of 0.012 mJ/mm^3 at the end of 12 thermal cycles. The LEMM with SnPb solder interconnect however shows a near constant amplitude per cycle over the whole of the 12 thermal cycles.

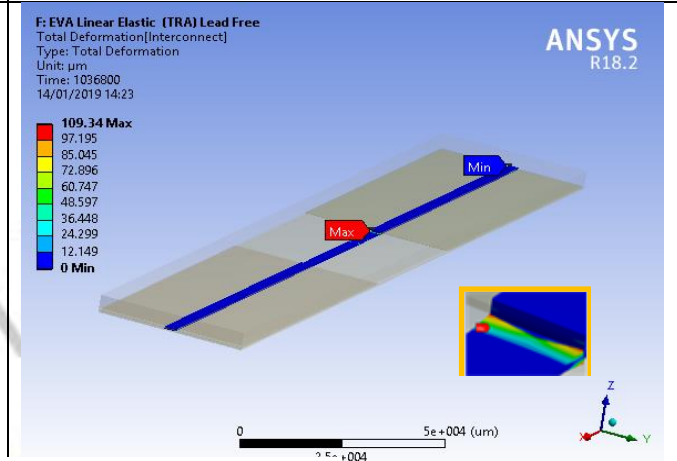
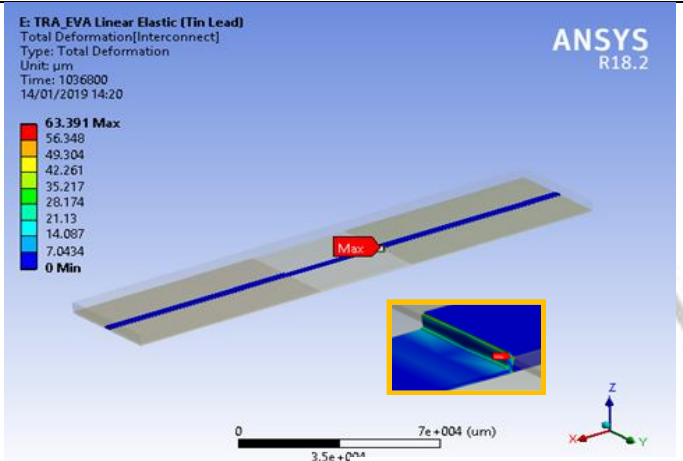
5.3.5 Study on interconnect deformation

In this section, we study the deformation resulting in the interconnection due to the temperature cycles. The interconnection consists of solder and its derivative IMCs (Cu_3Sn , Ag_3Sn) and copper ribbon. In Figure 5-9, we present contour plots of the total deformation of the interconnection at the end of 12 thermal cycles. As depicted in Figure 5-9, the peak values of the total interconnect deformation increased by 72.5 % from $63.391 \mu\text{m}$ for SnPb interconnection to $109.34 \mu\text{m}$ for Pb-free interconnection when LEMM is used to study the constitutive behaviour of the EVA material. A 48.9 % increase in peak values of the total interconnection deformation (from $87.69 \mu\text{m}$ for SnPb interconnect to $130.55 \mu\text{m}$) for the Pb-free interconnect was evaluated when a TDEMM is used to predict the behaviour of the EVA. For the LVMMs of EVA, the results from peak values of the total interconnect deformation show a relatively smaller increase of 5.2 % from $52.935 \mu\text{m}$ for SnPb interconnection to $55.691 \mu\text{m}$ for Pb-free interconnection. In all three cases of EVA, the peak values of the total deformation were registered in the copper ribbons.

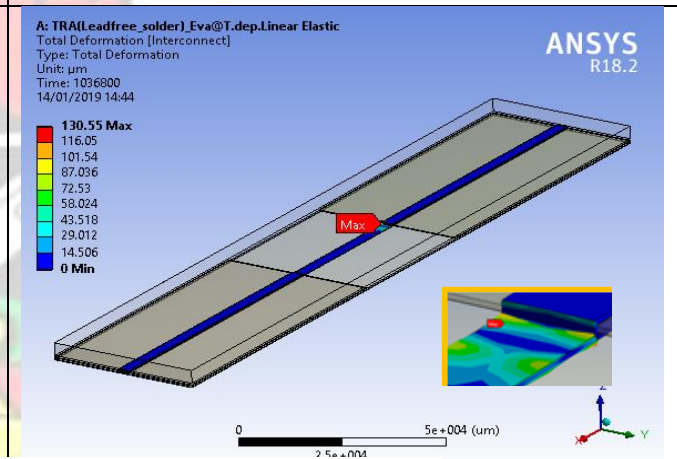
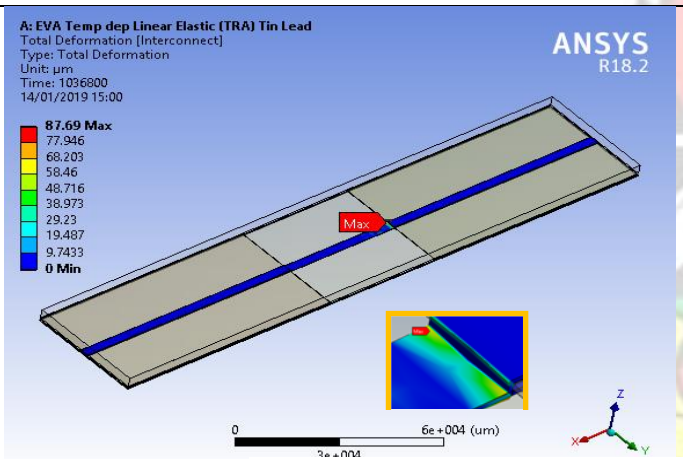
CHAPTER FIVE: IMPACT OF CONSTITUTIVE BEHAVIOUR OF EVA ON SOLDERED INTERCONNECTIONS OF SPVM.

(c) Tin Lead solder Interconnections

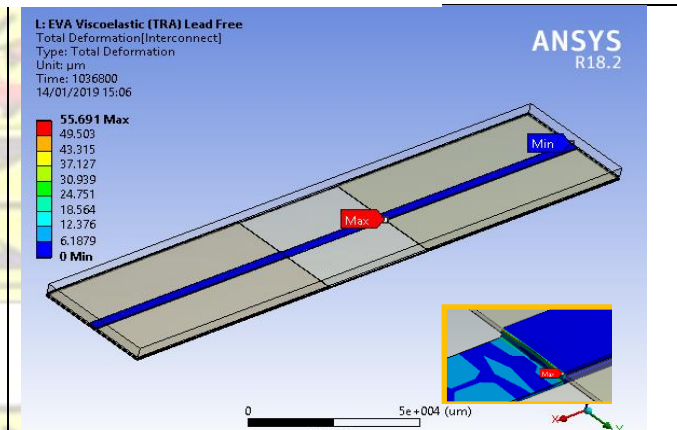
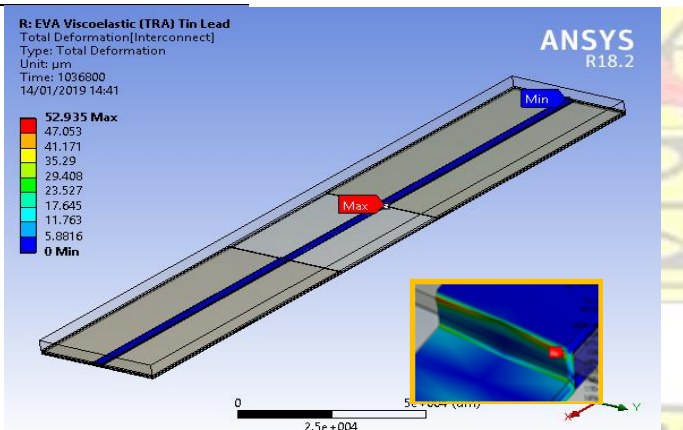
(d) Lead free solder Interconnections



EVA as a Linear Elastic Material Model (LEMM)



EVA with Temp-dependent Elastic Material Model (TDEMM)



EVA as a Linear Viscoelastic Material Model (LVMM)

Figure 5-9: Distribution of Total Deformation of Interconnection

CHAPTER FIVE: IMPACT OF CONSTITUTIVE BEHAVIOUR OF EVA ON SOLDERED INTERCONNECTIONS OF SPVM.

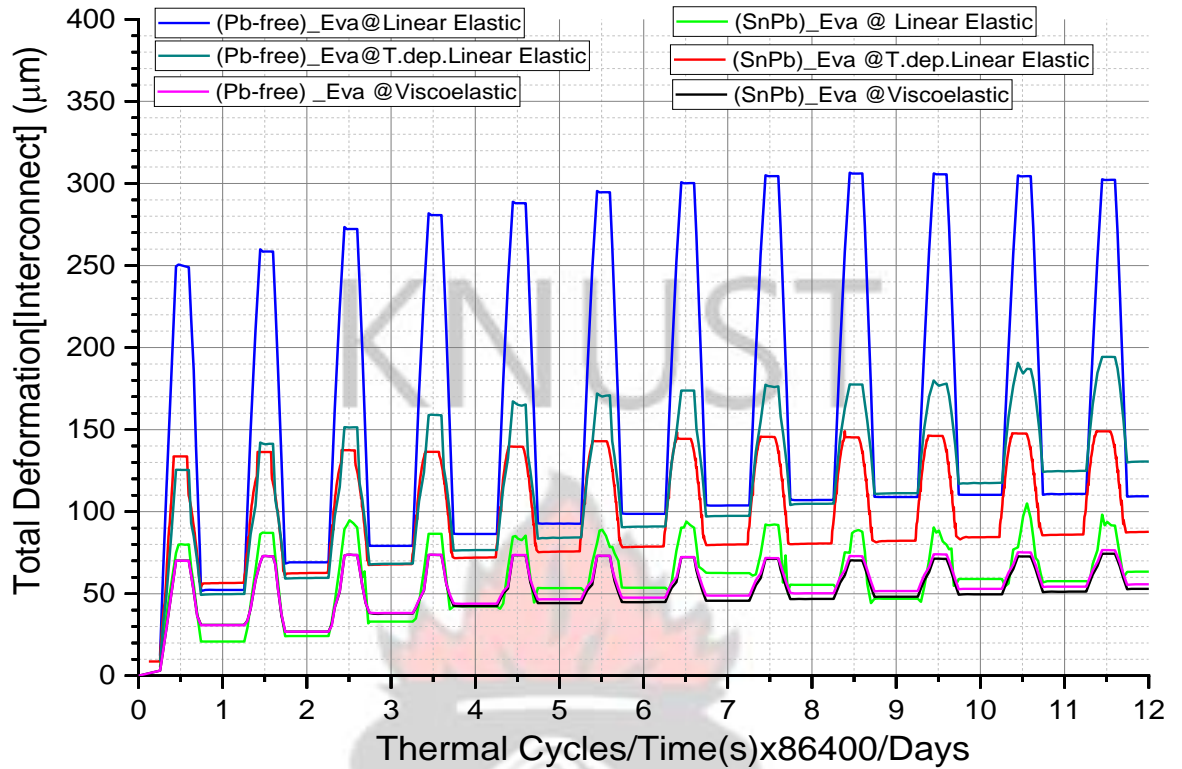


Figure 5-10: Total deformation Profiles of Interconnections versus Thermal Cycles

The total interconnection deformation is analysed over the 12 thermal cycles and presented in Figure 5-10 for the three constitutive models used for the study. For the EVA as a LEMM with Pb-free solder interconnection, the total interconnection deformation rises from a total deformation amplitude of 200 μm up to a maximum of 305 μm at the end of the 12 thermal cycles. However, for SnPb solder (with EVA as LEMM), a deformation amplitude of approximately 50 μm was observed at the start of the thermal cycle and maximum total deformation of 100 μm . In addition, the total interconnection deformation for TDEMMs was studied for the two different solder interconnections. Higher deformation amplitudes were observed for the Pb-free solder interconnections. Significant differences in deformation amplitudes are observed after the 3rd thermal cycle.

CHAPTER FIVE: IMPACT OF CONSTITUTIVE BEHAVIOUR OF EVA ON SOLDERED INTERCONNECTIONS OF SPVM.

An increase in deformation amplitude of 30 % from 150 μm (for SnPb interconnect) to 195 μm (for Pb-free interconnect) is observed at the end of the 12 thermal cycles.

The results from LVMMs show significantly lower interconnection deformations as compared with the LEMMs and TDEMMs. A maximum deformation amplitude of 50 μm is observed for the two types of interconnections (SnPb and Pb-free). The deformation profiles observed over the 12 thermal cycles show the two deformation cycles tracking each other and overlapping over the 12 thermal cycles. Here again, the LVMMs produce a very stable response to the interconnection deformation with a significantly lower total interconnection deformation compared with the LEMMs and TDEMMs.

5.4. Summary

The impact of the encapsulant (EVA) constitutive behaviour on the thermo-mechanical damage in crystalline silicon solar PV modules was examined by numerical investigation of interconnected and encapsulated solar cells with a front-to-back cell interconnection. The constitutive models proposed for EVA were; Linear Elastic Material Model (LEMM), Temperature-Dependent Linear Elastic Material Model (TDEMM) and Linear Viscoelastic Material Model (LVMM). The study investigated the encapsulant (EVA) response to equivalent von-Mises stress and maximum principal strains. Additionally, the study investigated the equivalent creep strain, strain energy and strain energy density generated in the solder joints within the interconnection. Finally, the study evaluated the total interconnect deformation from the different constitutive models of EVA presented.

Equivalent Von-Mises stresses evaluated show a very high value of 4.857×10^7 Pa in the EVA material using LEMM whereas the lowest equivalent stress of 525.83 Pa was

CHAPTER FIVE: IMPACT OF CONSTITUTIVE BEHAVIOUR OF EVA ON SOLDERED INTERCONNECTIONS OF SPVM.

registered in the EVA material when LVMM is utilized in the study of the EVA material. It was further observed that the position of maximum stress occurs at a less critical region (cell-gap region) for LVMMs compared with the LEMMs and the TDEMMs. For the LEMMs and TDEMMs, a change in the interconnecting solder material (from SnPb to Pb-free) show variations in maximum principal strain response.

Equivalent creep strain distribution in the solder for the three different EVA constitutive models (LEMM, TDEMM, LVMM) show that, with the exception of LEMM with Pb-free solder, there are no significant variations in equivalent creep strain response in the solders (SnPb and Pb-free) for up to the 5th thermal cycle. Beyond the 5th thermal cycles however, the creep strain in the solder remains consistently lower. Though the LEMM with SnPb-solder interconnection produces the lowest response, the creep response from LEMM with Pb-free solder appears to be extremely higher departing sharply from the trends displayed by the other material models. Furthermore, the strain energy distribution shows the highest strain energy output of 1.2284×10^{-7} J for a LEMM (Pb-free solder) and the lowest strain energy damage of 1.5451×10^{-8} J for a LVMM (Pb-free solder). In addition, the total interconnection deformation evaluated for the three different constitutive models shows that the LVMMs produce the lowest change in interconnection deformation (5.2 %) using different interconnecting solder materials. Overall, the LVMM of EVA offers a more stable material response for the study of the encapsulant constitutive behaviour in the thermo-mechanical analysis of c-Si SPVM. This study recommends the Linear Viscoelastic Material Model (LVMM) as a material model for predicting the behaviour of encapsulant (EVA) in c-Si solar cells.

CHAPTER SIX: LIFE PREDICTION OF Pb-FREE AND SnPb SOLDERED

JOINTS

6.1 Introduction

The drive towards clean energy has spurred the growth of photovoltaic power generation worldwide. Solar cells directly convert energy from the sun to electrical power. Thermo-mechanical deformation of constituent materials of solar cells during field operations due to exposure to thermal energy from the sun imposes reliability concerns to the modules. One of the key reliability concern is the degradation of solder in the interconnection.

Several researchers (Hasan and Arif, 2014, Kraemer, 2014, Lee and Tay, 2012, Dietrich et al., 2010, Wiese et al., 2010b, Wiese et al., 2009, Chen, 2008, Eitner et al., 2008, Eitner et al., Eitner et al., 2011b, Hasan et al., 2013) have conducted a number of studies (both numerically and experimentally) focusing on solar PV reliability improvement. The observed shortcoming of most geometric models used in these studies is the non-inclusion of intermetallic compound (IMC) layers in solder interconnection geometry. In addition, most researchers modelled EVA (ethylene vinyl acetate) as either linear elastic or temperature-dependent linear elastic. (Dietrich et al., 2010) performed a thermo-mechanical assessment of encapsulated solar cells by finite element simulation. They simulated various models from the lamination process starting at a curing temperature at 150 °C to thermal cycling at IEC 61215 test conditions. Subsequently, they conducted parametric studies on the cell thickness to access the thermo-mechanical behaviour of the cell string and the stress distribution in the silicon. However, the model used for the investigation was very simplified with the solder interconnection modelled as ‘interconnection paste’- neglecting the presence of intermetallic compounds (IMCs). (Wiese et al., 2009, Wiese et al., 2010b) investigated the constitutive behaviour of

CHAPTER SIX: LIFE PREDICTION OF Pb-FREE AND SnPb SOLDERED JOINTS

copper ribbons used in solar cell assembly process. The material models employed in the study show silicon (as linear elastic), silver (as linear elastic) and copper (as bilinear elastic-plastic). The geometric models used by (Wiese et al., 2009, Wiese et al., 2010b) were without solder and IMCs.

(Chen, 2008) investigated the residual stress and bow induced by soldering in the silicon cell interconnect. They developed a 2D shell model of a single cell with aluminum BSF, copper, and solder to determine induced damage from soldering. The authors modelled all the cell materials as temperature-independent elastic, perfectly plastic. Here again, the presence of IMCs in the copper-solder-silver interfaces were not accounted for. (Eitner et al., 2008) performed thermo-mechanical simulations of PV modules to optimize interconnects for back contact cells by modelling all the constituent materials of the cell as linear elastic. The authors modelled the PV cell interconnect string as a 2D model using a sub-structural modelling approach which was simplified to avoid computational complexity.

(Eitner et al., Eitner et al., 2011b) again investigated thermal stress and strain of solar cells using material models derived from experimental testing that best describe the true material mechanical behaviour. However, the model used in their investigation did not include solder with its IMCs. (Hasan et al., 2013, Hasan and Arif, 2014) performed finite element analysis and life prediction of PV modules. The model geometries used in these studies consisted of glass, encapsulant (EVA), interconnection (copper), cell (silicon) and backsheet. Though material mechanical behaviour was modelled as in (Eitner et al., Eitner et al., 2011b), the model was again simplified to exclude the solder interconnect and IMCs. On the other hand, (Zarmai et al., 2015a) performed an optimization study on solder interconnect in PV modules using Taguchi method. Though the geometric model used for the study included Cu_3Sn_5 IMC layer, the Ag_3Sn

CHAPTER SIX: LIFE PREDICTION OF Pb-FREE AND SnPb SOLDERED JOINTS

IMC layer was not included. Moreover, the study used linear elastic models to model the constitutive behaviour of all laminating materials except the solder, which exhibited creep.

From the studies reviewed, a number of researchers simplified geometric models to eliminate IMCs. The reported studies incorporating solder joints, unfortunately, ignored the presence of IMCs in the solder joint interface. The assumption advanced for the non-inclusion of IMCs in these studies is that the IMC layer is very thin ($\leq 6\mu\text{m}$) to contribute significantly to the solder joint damage. This assumption could potentially lead to inaccurate simulation results. IMC formation in solder joint interfaces is widely known for tin-based solder alloys and metallised copper bond pads. Another reason for eliminating IMCs in simulation by researchers is the resulting large number of mesh elements and nodes generated, which require HPC (High-Performance Computer) for a numerical solution. The HPC resources until recently were not readily available due to technological limitations. Other reasons such as unavailability of material property data on IMCs also accounted for their non-inclusion in previous numerical studies. Current advances in technology and materials engineering research have made available HPCs with superior computing power and material property data for the IMCs. The oversimplification of material behaviour and cell geometry has led to discrepancies in reported modelling results. Additionally, most modelling studies involved the use of IEC 61215 conditions for thermal cycling analysis. Very little attention is paid to actual field module temperature cycles (which are location-dependent) experienced by the PV modules.

In this study, a geometric model of a c-Si solar cell has been created which include all constituent materials as well as the solder and its derivative IMC layers. Subsequently,

CHAPTER SIX: LIFE PREDICTION OF Pb-FREE AND SnPb SOLDERED JOINTS

a finite element analysis (FEA) software (ANSYS v 18.2) has been used to simulate the thermo-mechanical response of the cell to field temperature cycles generated from in-situ climatic conditions in a sub-Saharan Africa ambient. Furthermore, we use the simulation results from the field temperature cycles to predict the life (number of cycles to failure) of the solder joints for both lead-free and SnPb solder alloys.

6.2 Methodology

The test rig for data collection and generation of test region thermal cycle profiles, the FEA methodology, material models and their properties have been discussed extensively in chapter 3. Eight geometric models (four in each case for Pb-free and PbSn interconnections) were generated for this study using the Constructive Solid Geometry (CSG) technique. In particular, a viscoelastic material model was used for the EVA. This was informed by the results of the studies from chapter 5. In this investigation, the behaviour of the soldered interconnection is examined under the thermal loads and boundary conditions from 2012, 2013, 2014 and TRA thermal cycles.

The study focused on investigating the impact of the thermal loads and boundary conditions of the various thermal cycles on the life (number of cycles to failure) of the soldered interconnections. The equivalent von-Mises stress, equivalent creep strain distribution and response, stress-strain hysteresis loops, accumulated creep energy density (ACED) distribution and response and the change in ACED response were investigated over the 12 thermal cycles.

Finally, the results from the change in ACED were used to predict the life of the solder interconnections to estimate how long the PV module could last under the thermal cycles generated from the outdoor weathering of the PV modules.

CHAPTER SIX: LIFE PREDICTION OF Pb-FREE AND SnPb SOLDERED JOINTS

6.3 Results and Discussion

6.3.1 Study on Von-Mises Equivalent stress of solder joint.

Figures 6-1 and 6-2 display the contour plots of equivalent Von-Mises stress distribution (after 12 thermal cycles) in the solder interconnector joining the copper ribbon to the silver busbars on the solar cell.

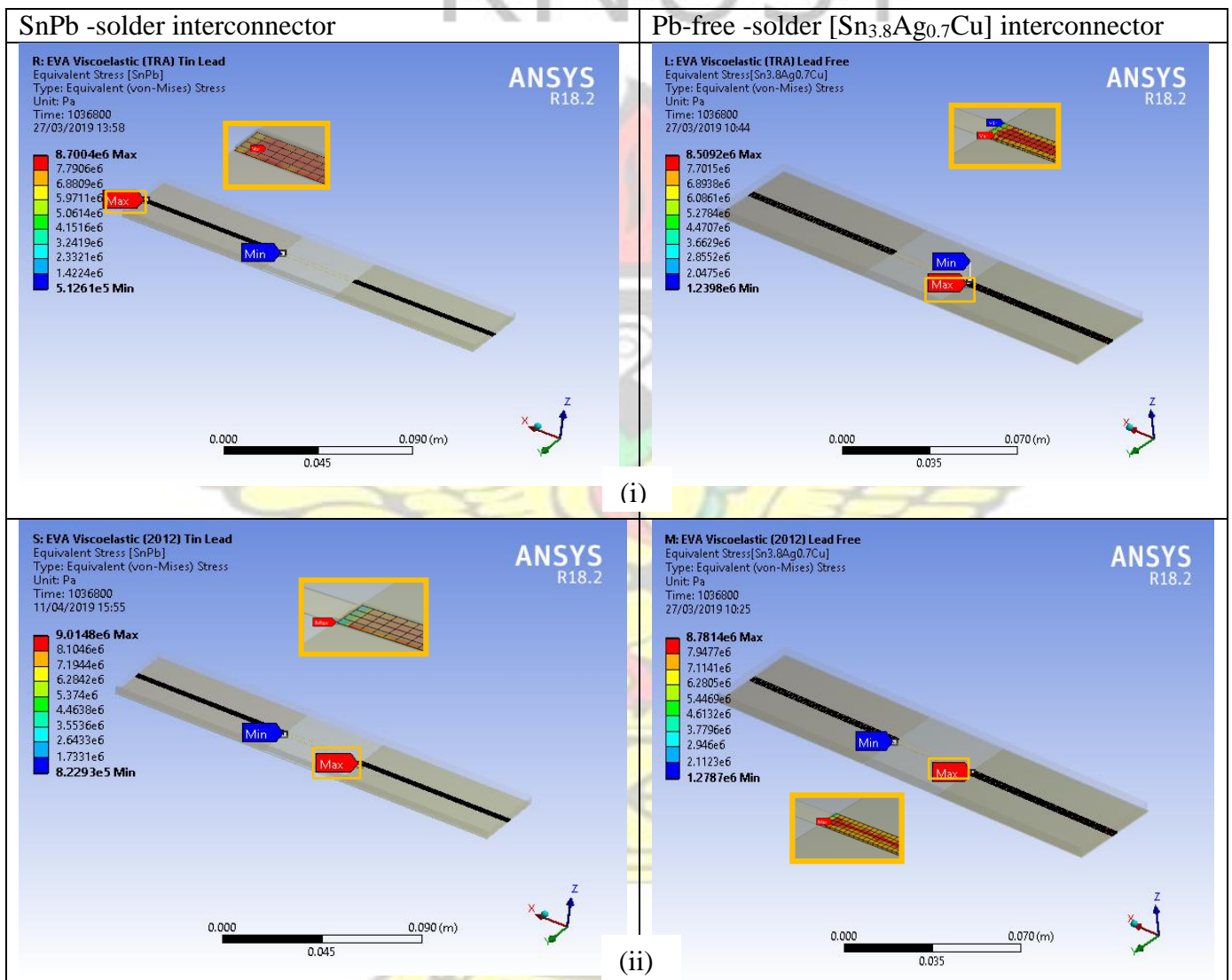


Figure 6-1 Equivalent von-Mises Stress Distribution on PbSn-solder and Pb-free (Sn_{3.8}Ag_{0.7}Cu) solder for: (i) TRA and (ii) 2012 thermal cycles.

CHAPTER SIX: LIFE PREDICTION OF Pb-FREE AND SnPb SOLDERED JOINTS

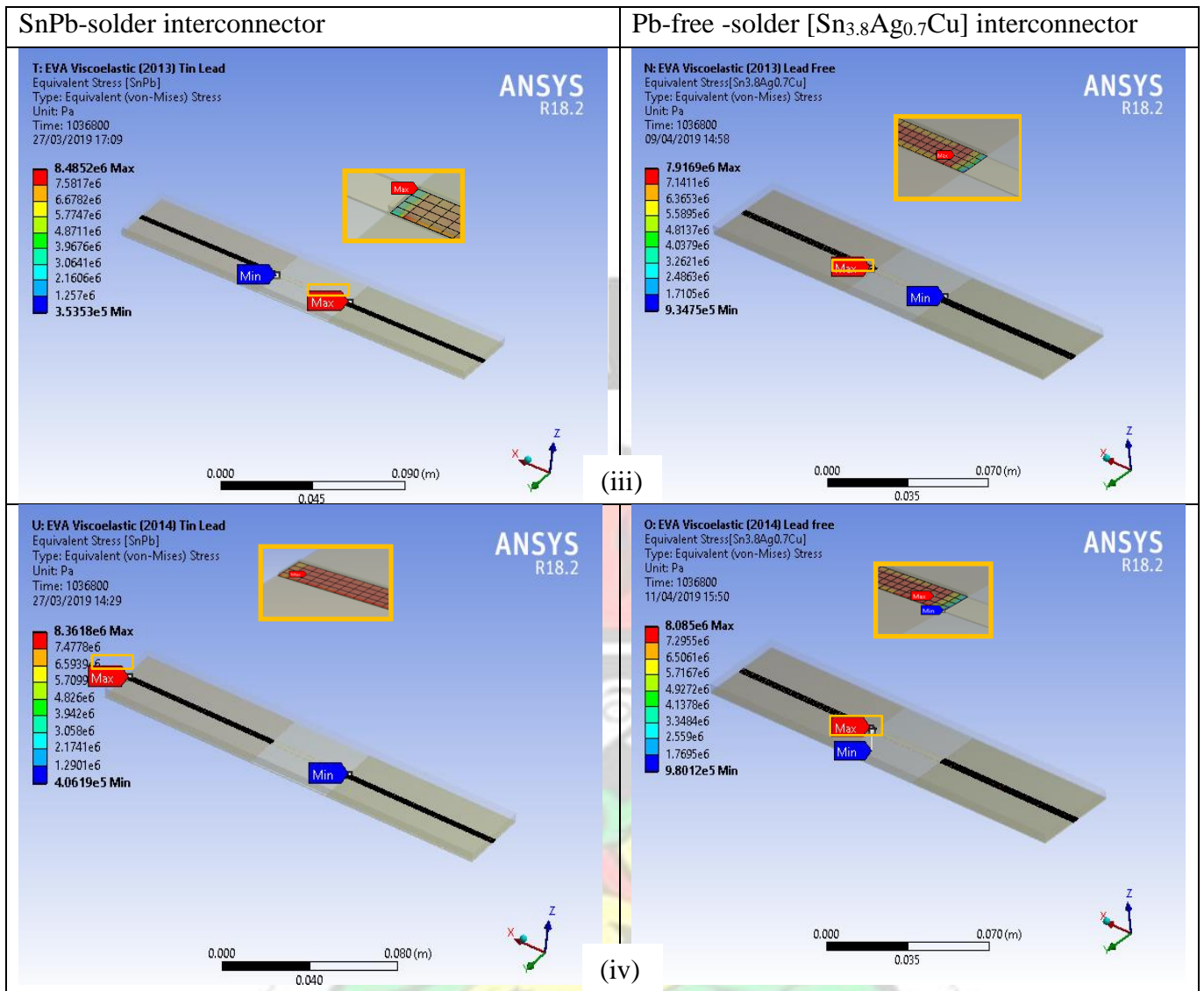


Figure 6-2 Equivalent von-Mises Stress Distribution on PbSn-solder and Pb-free (Sn_{3.8}Ag_{0.7}Cu) solder for: (iii) 2013 and (iv) 2014 thermal cycles.

Figure 6-3 also shows the stress response in the soldered interconnections over 12 cycles for the four different thermal cycle profiles generated from the real-time monitoring of installed PV modules at the test site. From the stress distribution in Figures 6-1 and 6-2, it is observed that the equivalent Von-Mises stresses generated in the SnPb-solder interconnection are generally higher than the stresses generated in the Pb-free solder interconnection for all the four (4) different thermal cycles simulated in this study.

CHAPTER SIX: LIFE PREDICTION OF Pb-FREE AND SnPb SOLDERED JOINTS

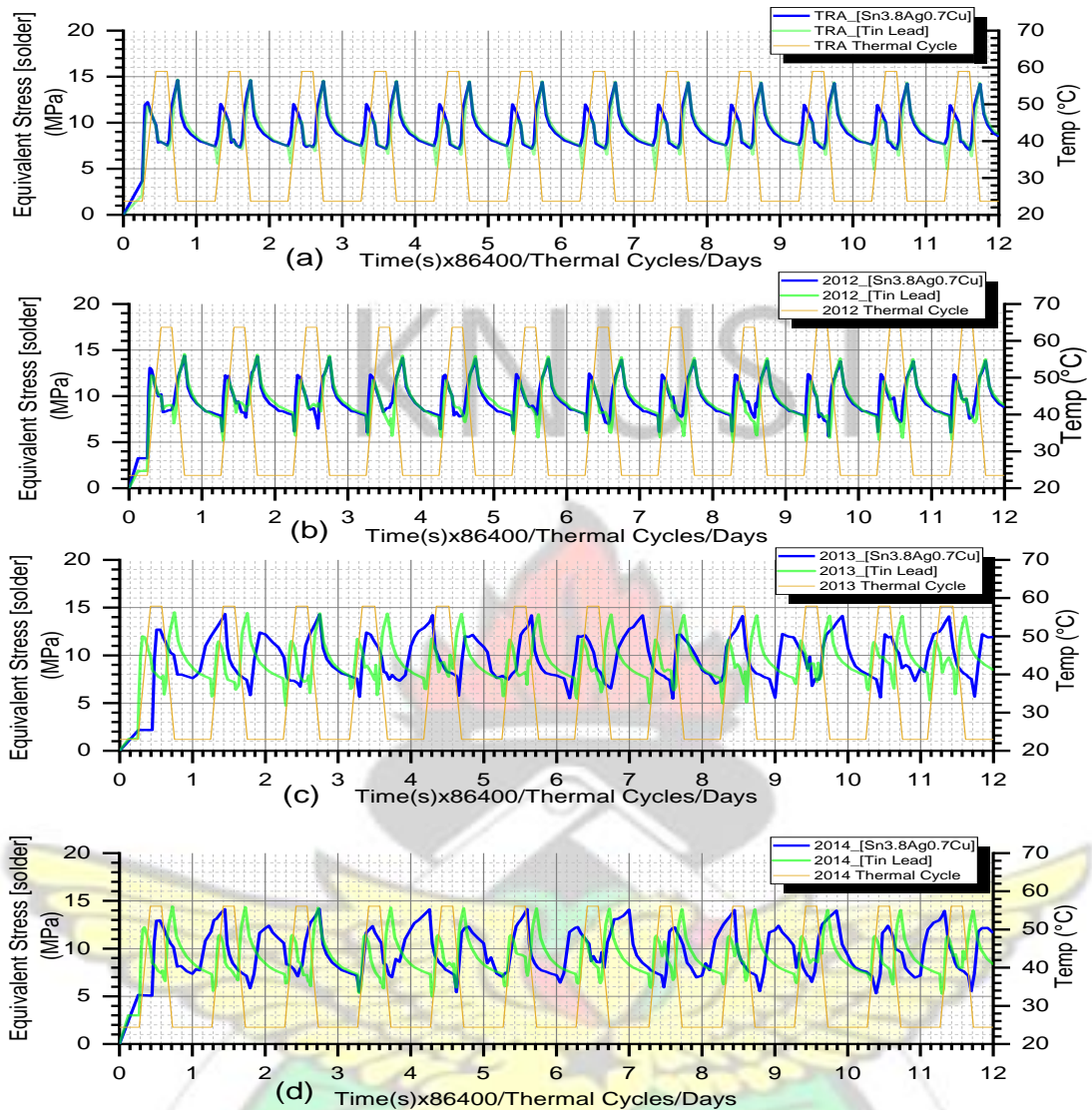


Figure 6-3 Equivalent non-Mises stress response of SnPb-solder and Pb-free (Sn_{3.8}Ag_{0.7}Cu) solders for: (a) TRA, (b) 2012, (c) 2013 and (d) 2014 thermal cycles.

The position of maximum and minimum stresses remained largely unchanged and was found to be closer to the cell gap region where the copper ribbon bends over to connect the adjacent cell (front-to-back interconnection). For the TRA thermal cycle loading, a reduction of 2.2 % in equivalent stress (from 8.7004 MPa to 8.5092 MPa) was observed when a SnPb-solder is replaced with a Pb-free (Sn_{3.8}Ag_{0.7}Cu) solder interconnector. A reduction of 2.5% (from 9.0148 MPa to 8.7814 MPa) in equivalent stress from the SnPb-solder to Pb-free solder interconnector was observed for the 2012 thermal cycle load profile. Furthermore, a higher reduction of 6.7% (from 8.4852 MPa to 7.9169

CHAPTER SIX: LIFE PREDICTION OF Pb-FREE AND SnPb SOLDERED JOINTS

MPa) in equivalent stress from PbSn-solder interconnector to a Pb-free solder interconnector was observed for the year 2013.

Furthermore, the year 2014 thermal cycle generated a reduction of 3.3 % (from 8.3618 MPa to 8.085 MPa) in equivalent stress when the interconnector was changed from SnPb -solder to Pb-free solder (Sn3.8Ag0.7Cu). Overall, the thermal cycle load profile for the year 2012 induced the maximum equivalent von-Mises stress (9.0148 MPa in SnPb -solder) whereas the 2013 thermal cycle induced the minimum equivalent stress of 7.9169 MPa in Pb-free solder interconnector. Typically, a daily thermal cycle can be sectioned into a five-load step cycle. The first load step involves the PV module experiencing near-constant temperature from midnight to early morning (cold dwell) to the point at which temperature begins to experience a gradual increase. The second load-step is where the PV module experiences gradual heating up to maximum temperature (ramp-up). The third load step occurs with PV modules soaks the peak temperature for uniform stress distribution within the cells (Hot dwell). The fourth step involves cooling of the PV module from the peak temperature to the lowest temperature (ramp down). The final daily load step involves PV module maintaining the lowest temperature up to the end of the cycle (cold dwell).

The equivalent von-Mises stress response in the solder over 12 thermal cycles (TRA, 2012, 2013 and 2014 thermal cycles) presented in Figure 6-3 shows that for both the SnPb and the Pb-free solder, the stresses rise to a peak value at a quarter-way through the first ramp-up step. Subsequently, the solders experience a gradual reduction in the equivalent stress as the heating progresses to a maximum cycle temperature (at the end of the first ramp-up). The next step in the thermal cycle depicts the highest temperature dwell step (hot dwell) where the equivalent stress in the solders show further decline

CHAPTER SIX: LIFE PREDICTION OF Pb-FREE AND SnPb SOLDERED JOINTS

up to the end of the hot dwell step. The decrease in stresses is identified as stress relaxation where the solder alloy microstructure attains thermal equilibrium. This subsequently relieves the internal stresses developed during the ramp-up step. During the cooling step (ramp down), the stresses in the solders increase gradually to a maximum peak value at the end of the ramp-down step. Finally, a reduction in stresses as the temperature dwells at the lowest value (cold dwell) up to the end of the cycle.

Generally, it was observed that the stresses generated in both solders show a near-constant amplitude (10 MPa) per cycle for the four different thermal cycles simulated. For the TRA and 2012 thermal cycle Profiles, the stresses in the two different solder alloys appear to track each other over the 12 cycles. This shows that the equivalent stresses developed in the solders remain the same for each time step. However, for the 2013 and 2014 thermal cycle profiles, the response of the Pb-free solder appears to be out-of-phase with that of the SnPb solder. Whilst the SnPb solder shows a consistent response across the four different thermal cycle profiles under this study, the Pb-free solder appears to display sensitivity to the 2013 and 2014 thermal cycles. In the next section, the solder interconnections response to creep strain will be studied.

6.3.2 Study on equivalent creep strain of solder joint.

Creep strain affects the reliability of soldered interconnections in the solar PV module. In this study, we assessed the impact of the two types of solders (SnPb and $\text{Sn}_{3.8}\text{Ag}_{0.7}\text{Cu}$ (Pb-free)). Creep damage distributions are depicted in Figures 6-4 and 6-5 on the two types of solders of the modelled quarter symmetry of the front-to-back solar cell interconnection subjected to the four different temperature load profiles (TRA, 2012, 2013, 2014).

CHAPTER SIX: LIFE PREDICTION OF Pb-FREE AND SnPb SOLDERED JOINTS

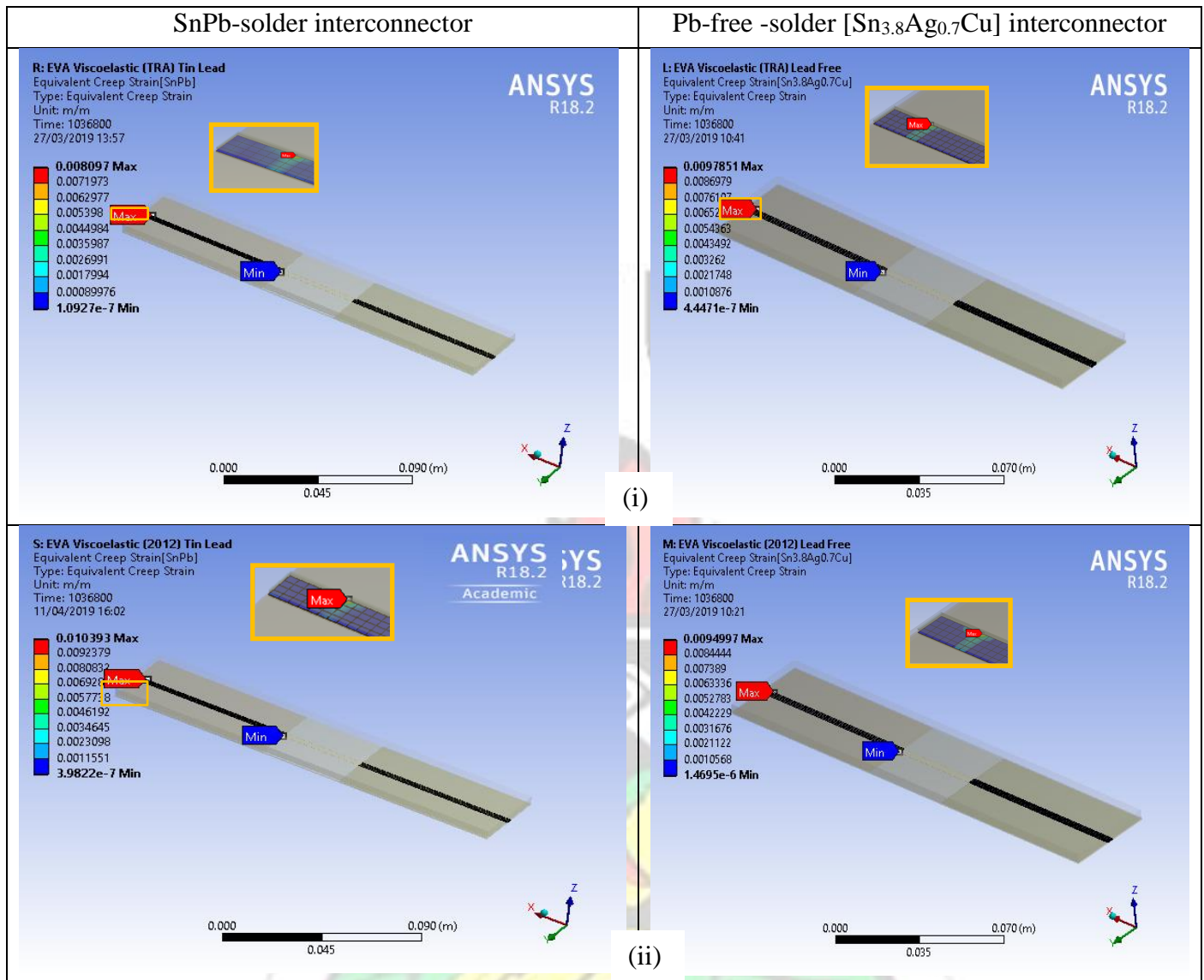


Figure 6-4 Equivalent Creep Strain distribution on PbSn-solder and Pb-free (Sn_{3.8}Ag_{0.7}Cu) Solder for: (i) TRA, (ii) 2012 thermal cycles

From Figures 6-4 and 6-5, a decrease in equivalent creep strain was observed for 2012, 2013, 2014 thermal cycles when the interconnecting solder is changed from SnPb to Pb-free solder. However, an increase in equivalent creep strain was observed when the solder was changed from SnPb to Pb-free solder under the TRA thermal cycle. Thus, the solder materials display some sensitivity to the thermal cycle parameters.

CHAPTER SIX: LIFE PREDICTION OF Pb-FREE AND SnPb SOLDERED JOINTS

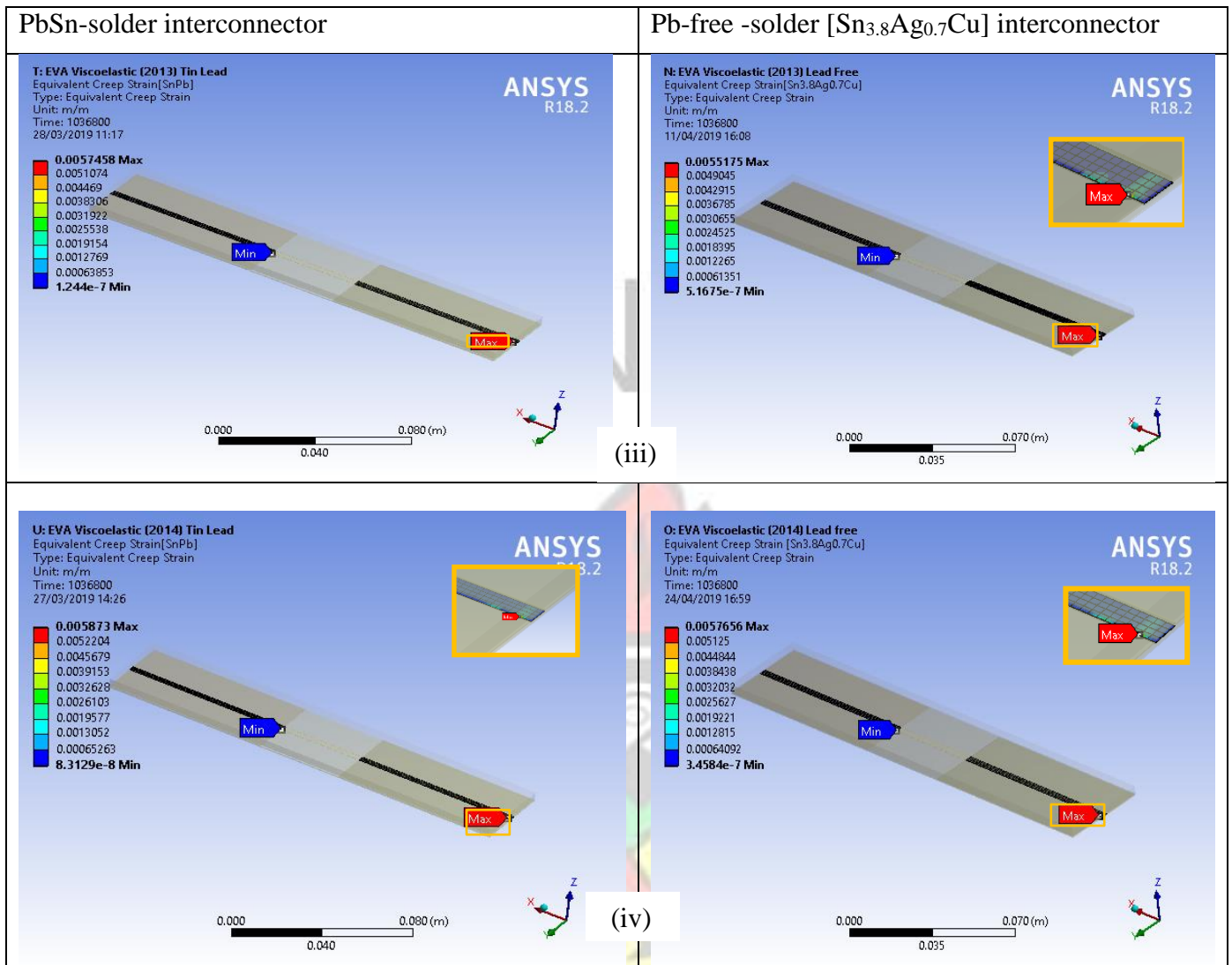


Figure 6-5 Equivalent Creep Strain distribution on PbSn-solder and Pb-free (Sn_{3.8}Ag_{0.7}Cu) Solder for: (iii) 2013 and (iv) 2014 Thermal cycles.

Depicted in Figure 6-6 is the variation of the creep strain induced in the solder interconnectors over the thermal cycles. In Figure 6-7, the creep strain responses from the respective thermal cycles (TRA, 2012, 2013 and 2014 thermal cycles) were superimposed on one another.

CHAPTER SIX: LIFE PREDICTION OF Pb-FREE AND SnPb SOLDERED JOINTS

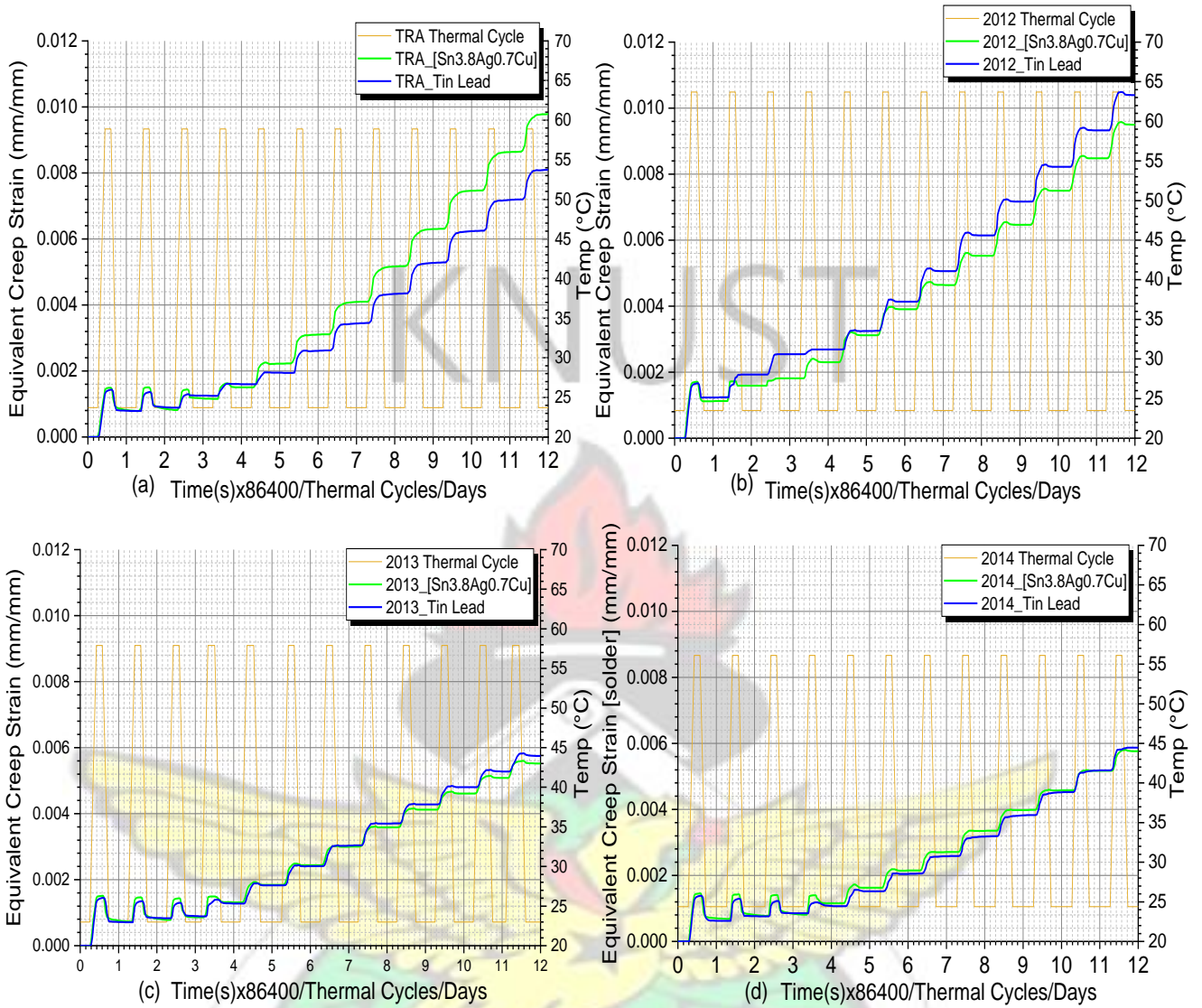


Figure 6-6 Equivalent Creep Strain Response of PbSn and Pb-free Solder interconnection versus Thermal cycles for: (a) TRA, (b) 2012, (c) 2013 and (d) 2014 thermal cycles

CHAPTER SIX: LIFE PREDICTION OF Pb-FREE AND SnPb SOLDERED JOINTS

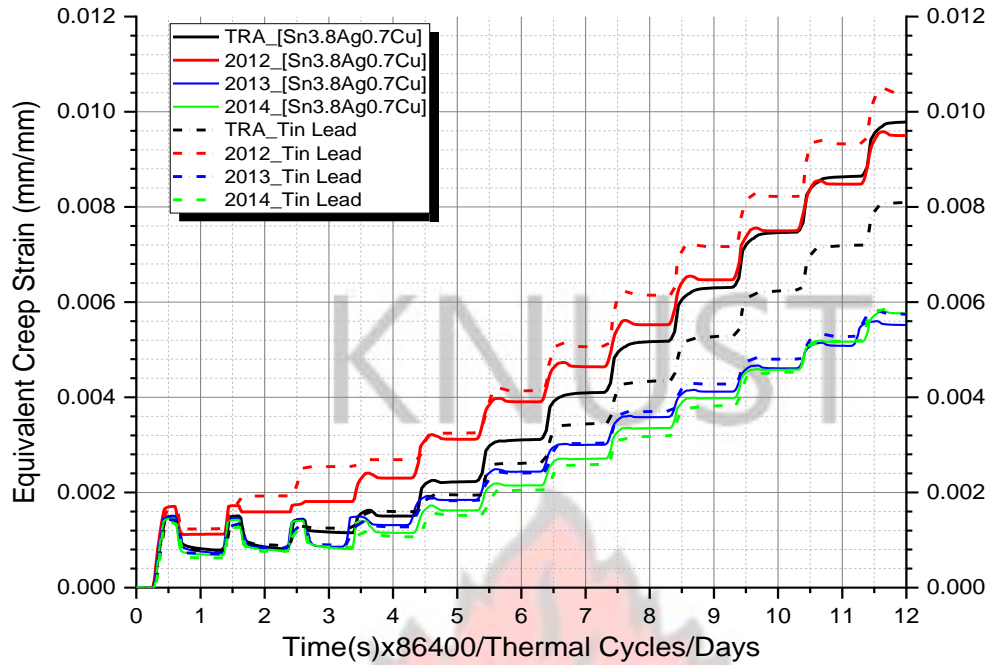


Figure 6-7 Superimposed Plots of Equivalent Creep Strain versus Thermal Cycles

The results from the creep strain distribution in Figures 6-4 and 6-5 show that, for the same thermal cycle, the creep strain decreases marginally when the SnPb solder interconnector is replaced with a Pb-free interconnector at the end of twelve thermal cycles for 2012, 2013 and 2014 thermal cycles. The TRA thermal cycle, on the other hand, shows a significant increase in equivalent creep strain (20%) from the SnPb solder to the Pb-free solder interconnect.

It was also observed from Figures 6-6 and 6-7 that the creep strain profiles in both the Pb-Sn solder and Pb-free solder vary with approximately equal amplitude per cycle (closely tracking each other over the 12 cycles) for the 2013 and 2014 thermal cycles. As with the TRA thermal cycle, creep strain response of the two solders appear to track each other with approximately equal creep strain amplitude up to the fourth (4th) thermal cycle. Subsequently, the Pb-free solder experiences a higher increase in creep strain per cycle compared with the SnPb solder.

CHAPTER SIX: LIFE PREDICTION OF Pb-FREE AND SnPb SOLDERED JOINTS

However, with the 2012 thermal cycle, a marked difference in creep strain response of the two solders was observed after the first (1st) thermal cycle. Furthermore, a higher increase in creep strain per cycle was registered in the SnPb compared with the Pb-free solder. These preliminary results indicate that Pb-free solder is a good substitute for SnPb solder in the manufacture of solar PV.

The outputs of the creep strain response curves over the different thermal cycles show that creep damage is sensitive to the thermal cycle parameters. Overall, the 2012 thermal cycle imposed the maximum creep damage of 0.010393 m/m on the SnPb-solder interconnection and the 2013 thermal cycle imposed the minimum creep damage of 0.0057458 m/m on the SnPb-solder interconnection. As with the Pb-free solder interconnection, the TRA thermal cycle imposed the maximum creep damage of 0.009785 m/m and the 2013 thermal cycle imposed the minimum creep damage of 0.0055175 m/m. Though creep strain provides an indication of the damage in solder interconnection, there exist superior damage indicators such as stress-strain hysteresis loop, accumulated creep strain and accumulated creep energy density, which are able to analyse the damage quantitatively. These damage indicators are discussed in subsequent sections.

6.3.3 Study on solder joint stress-strain hysteresis loops.

The stress-strain response of the solder interconnections to the thermal cycle loads are captured in plots shown in Figure 6-8. It can be seen in Figure 6-8 that as the plot continued, the trend evolves into a loop (hysteresis loop) which progresses as the number of thermal cycles increases. This observation is consistent with all the thermal cycles (TRA, 2012, 2013 and 2014 thermal cycles) used in this study. It was further observed that the extent of the loops varies from one thermal load cycle to the other.

CHAPTER SIX: LIFE PREDICTION OF Pb-FREE AND SnPb SOLDERED JOINTS

The extent of the loops provides an indication of the magnitude of the damage in the solder interconnection. The strain energy density dissipated per cycle can be calculated from the area of the loop formed per cycle.

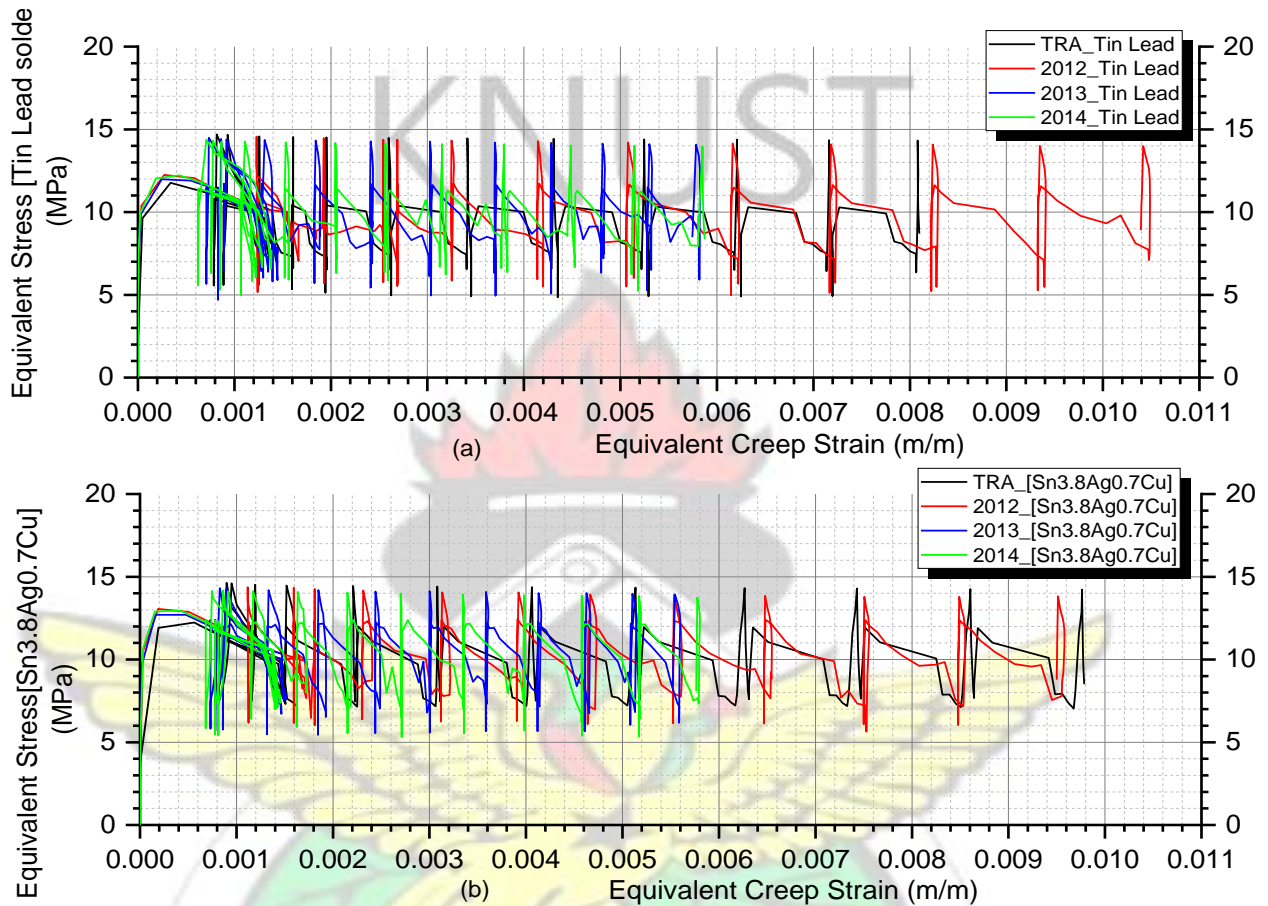


Figure 6-8 Plot of hysteresis loop (a) SnPb-solder interconnection (b) Pb-free solder interconnections.

The hysteresis loop formed from the stress-strain plots showed loops with constant stress amplitude of approximately 8 MPa for the respective temperature load cycles. For the SnPb-solder interconnection, the thermal load cycle for the year 2012 generated the most extensive loop with the highest strain range of 0.0105 m/m. Whilst the TRA load cycle generated a strain range of 0.0081 m/m, the 2013 and 2014 load cycles generated approximately equal strain range of 0.058 m/m. On the other hand, with the Pb-free solder interconnection, the extent of the hysteresis loops obtained for the TRA and 2012 load cycles were closely matched. The TRA cycle recorded the maximum

CHAPTER SIX: LIFE PREDICTION OF Pb-FREE AND SnPb SOLDERED JOINTS

strain range of 0.0098 m/m whereas the 2012 cycle recorded a strain range of 0.0096 m/m after twelve (12th) thermal cycles. Similarly, the extent of the hysteresis loops obtained from the 2013 and 2014 thermal cycles was closely matched.

The 2014 thermal cycles produced a relatively higher strain range of 0.058 m/m whereas the 2013 cycle generated a strain range of 0.056 m/m. From the profiles of the hysteresis plots from the different thermal load cycles, it can be predicted that the SnPb-solder interconnection will experience maximum creep damage which could lead to a lower number of stress cycles to failure (shorter joint life) in the 2012 thermal load cycle. On the other hand, the Pb-free solder will experience the minimum creep damage leading to a higher number of stress cycles to failure in the 2013 thermal load cycle. In the stress-strain hysteresis plot, the damage accumulation per cycle is computed by finding the area under the stress-strain loop that involves the integration of a higher-order polynomial function required to fit the hysteresis loop. The accuracy of this type of analysis remains a challenge. The next section discusses one of the key life prediction parameters (the accumulated creep strain (ϵ_{acc})).

6.3.4 Evaluation of Accumulated Creep Strain of Solder Interconnections

Apart from the energy density methods (strain energy density and creep energy density), the accumulated creep strain (ϵ_{acc}) remain one of the key life prediction parameters. The accumulated creep strain is evaluated using SEND CREEP command NLCREQ in Ansys. In this study, the accumulated creep strain damage in the two different solder interconnections (PbSn and Sn3.8Ag0.7Cu (Pb-free)) for the temperature load cycles (2012, 2013, 2014 and TRA thermal cycles) were evaluated.

The distributions of accumulated creep strain at the end of 12 thermal cycles are depicted in Figures 6-9 and 6-10. Also displayed in Figure 6-11 is the accumulated

CHAPTER SIX: LIFE PREDICTION OF Pb-FREE AND SnPb SOLDERED JOINTS

creep strain response over the 12 thermal cycles. Results from the distribution in Figures 6-9 and 6-10 show that for all the temperature cycles investigated, the creep strain generated in the Pb-free solder interconnection was found to be higher than that in the SnPb-solder interconnection.

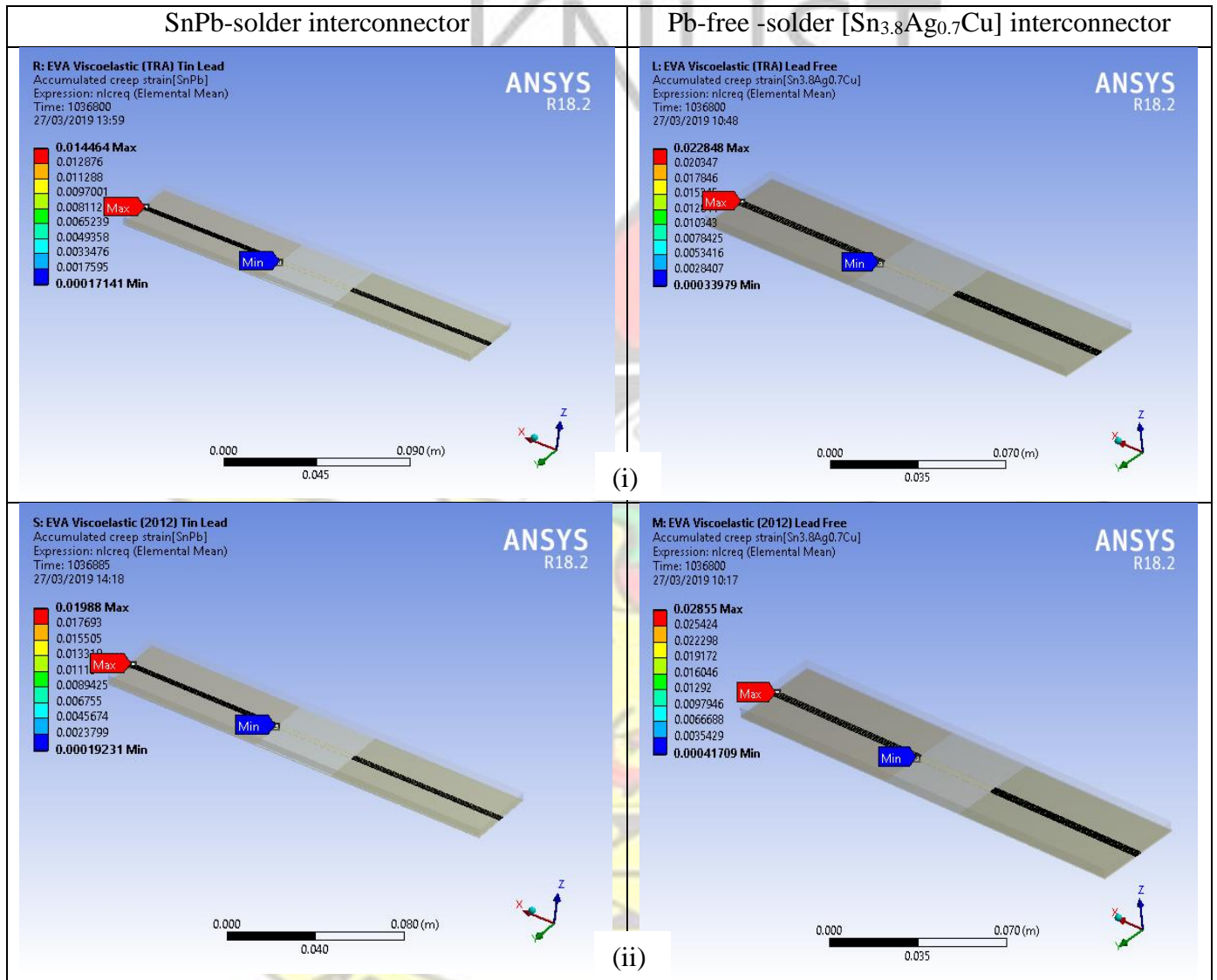


Figure 6-9 Accumulated Creep Strain Damage Distribution in PbSn and Pb-free Solder Interconnection for: (i) TRA and (ii) 2012 Thermal Cycles.

CHAPTER SIX: LIFE PREDICTION OF Pb-FREE AND SnPb SOLDERED JOINTS

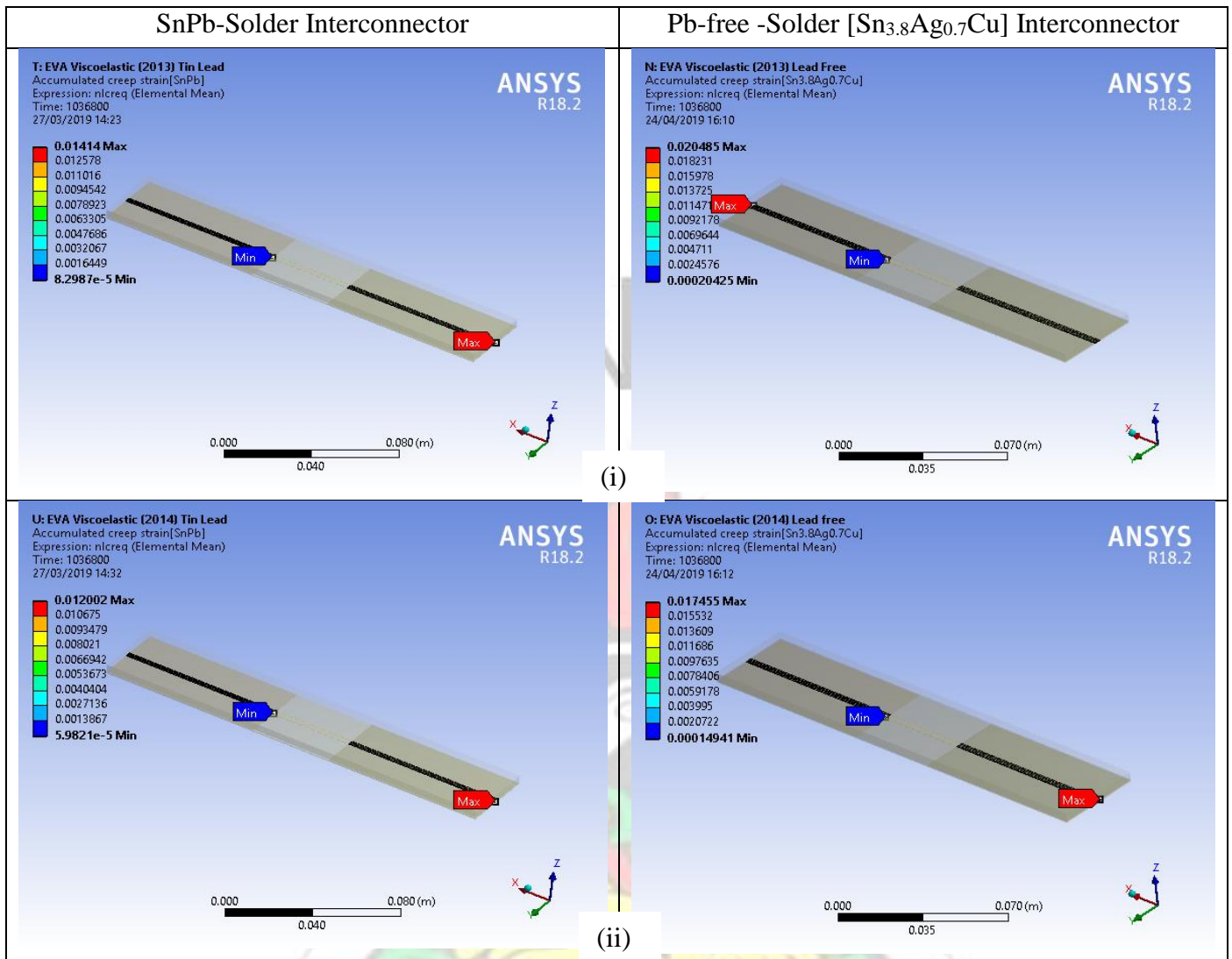


Figure 6 - 10 Accumulated Creep Strain damage distribution in PbSn and Pb-free solder interconnect for (i) 2013 and (ii) 2014 thermal cycles.

A maximum accumulated creep strain damage of 0.028555 mm/mm was generated in the Pb-free solder interconnection during the 2012 thermal load cycle and a minimum accumulated creep strain of 0.0120002 mm/mm in the SnPb-solder interconnection during the 2014 thermal load cycle. Overall, the 2012 thermal cycle induces the maximum accumulated creep strain in both interconnections (0.01968 mm/mm for SnPb-solder and 0.028555 mm/mm for Pb-free).

CHAPTER SIX: LIFE PREDICTION OF Pb-FREE AND SnPb SOLDERED JOINTS

Table 6-1 presents the percentage change in accumulated creep strain from SnPb-solder interconnection to Pb-free solder interconnection. It was observed that for 2012, 2013 and 2014 thermal cycles, the accumulated creep strain damage increases by an average value of 45 % when the interconnection solder is changed from SnPb-solder to Pb-free solder. However, the increase in accumulated creep strain was lower than the 57.96 % increase resulting from the TRA cycle.

Table 6 - 1: Percentage change in Accumulated creep Strain

Thermal Cycles		TRA	2012	2013	2014
Accumulated	SnPb-solder	0.014464	0.01988	0.01414	0.012002
Creep Strain (ϵ_{acc})	Sn _{3.8} Ag _{0.7} Cu	0.022848	0.02855	0.020485	0.017455
(mm/mm)					
% Change in Accumulated creep strain		57.96 %	43.61 %	44.87 %	45.43 %

The response of accumulated creep strain over the 12 thermal cycles presented in Figure 6-11 shows that, for up to the 3rd thermal cycle, the accumulated creep strain damage response in the Pb-free solder interconnection remained largely unchanged for 2013, 2014 and TRA cycles. However, variations in the accumulated creep strain response become more pronounced after the 3rd thermal cycle. At the end of the 12 thermal cycles, the damage accumulation in the Pb-free solder for the 2013 and 2014 thermal cycles was observed to be significantly below that of the TRA thermal cycle. However, with the same Pb-free solder interconnection, the accumulated creep strain damage per cycle from the 2012 thermal cycle was found to be relatively higher than that of the TRA thermal cycle.

CHAPTER SIX: LIFE PREDICTION OF Pb-FREE AND SnPb SOLDERED JOINTS

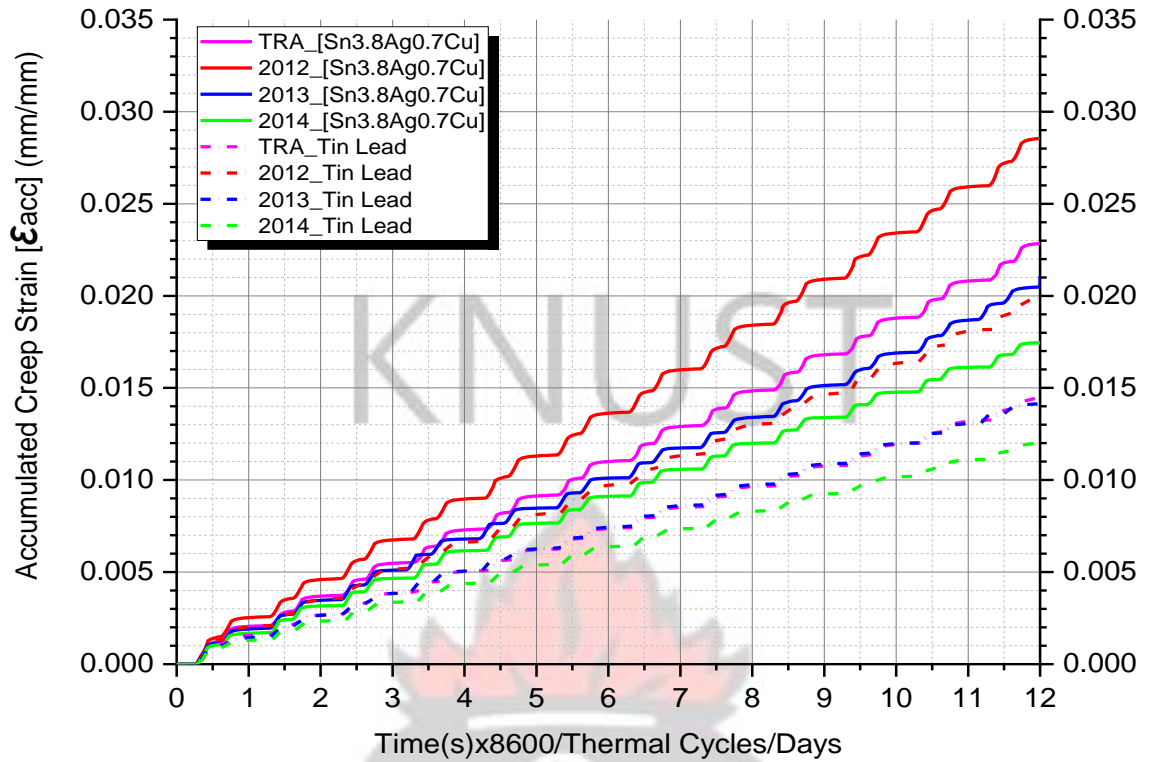


Figure 6-11 Accumulated creep Strain response for PbSn and Pb-free solder for: (a) TRA, (b) 2012, (c) 2013 and (d) 2014 thermal cycles

Similarly, with the SnPb-solder interconnection, the accumulated creep damage response remained approximately equal for up to the 2nd thermal cycle for 2013, 2014 and TRA cycles. The trend continues with the 2013 and TRA cycles which remain unchanged up to the end of the 12 thermal cycles. However, the accumulated creep strain response for the 2014 thermal cycle produced a relatively lower accumulated creep strain per cycle after the 2nd thermal cycle and up to the end of the 12 thermal cycles. This observation confirms what has been reported earlier by (Amalu and Ekere, 2012a) in which the authors observed that, for a given thermal loading cycle, more than 3 thermal cycles are required to clearly assess creep damage in solders. Fewer than 4 thermal cycles may generate misleading results. It was observed further that, the 2012 thermal cycle generated a relatively higher creep strain damage per cycle in the SnPb-solder interconnection.

CHAPTER SIX: LIFE PREDICTION OF Pb-FREE AND SnPb SOLDERED JOINTS

The results from the accumulated creep strain show that the fatigue life of Pb-free solder interconnections is expected to be relatively lower as compared with SnPb solder interconnects in the sub-Saharan Africa ambient. However, according to (Syed, 2006), the accumulated creep strain displays sensitivity to the type constitutive equation used in modelling the behaviour of the solder joint. Additionally, the accumulated creep strain is unable to capture damage resulting from low temperature dwells effectively. On the other hand, the accumulated creep energy density (W_{acc}) parameter is able to capture the damage from low-temperature dwells and does not display noticeable sensitivity to the constitutive model of the solder. Thus, the accumulated creep energy density offers a comparatively better parameter for fatigue life prediction in solder joints. In the next section, the accumulated creep energy density in the solder interconnections generated by the thermal cycles is evaluated.

6.3.5 Evaluation of the solder joint accumulated creep energy density

As stated in section 6.3.3, the response of accumulated creep energy density as a life prediction parameter provides the advantage of capturing the effect of low temperature dwell better than the accumulated creep strain. In this section, the accumulated creep energy density (ACED) was evaluated using creep work command NL CRWK in Ansys for 2012, 2013, 2014 and TRA thermal cycles. The distributions of the ACED at the end of 12 thermal cycles are presented in Figures 6-12 and 6-13. The distributions in Figures 6-12 and 6-13 show that the Pb-free solder interconnection experienced the maximum accumulated creep energy density of 0.29852 MJ/mm^3 . The SnPb-solder interconnection, on the other hand, experiences a maximum accumulated creep energy density of 0.19779 MJ/mm^3 .

CHAPTER SIX: LIFE PREDICTION OF Pb-FREE AND SnPb SOLDERED JOINTS

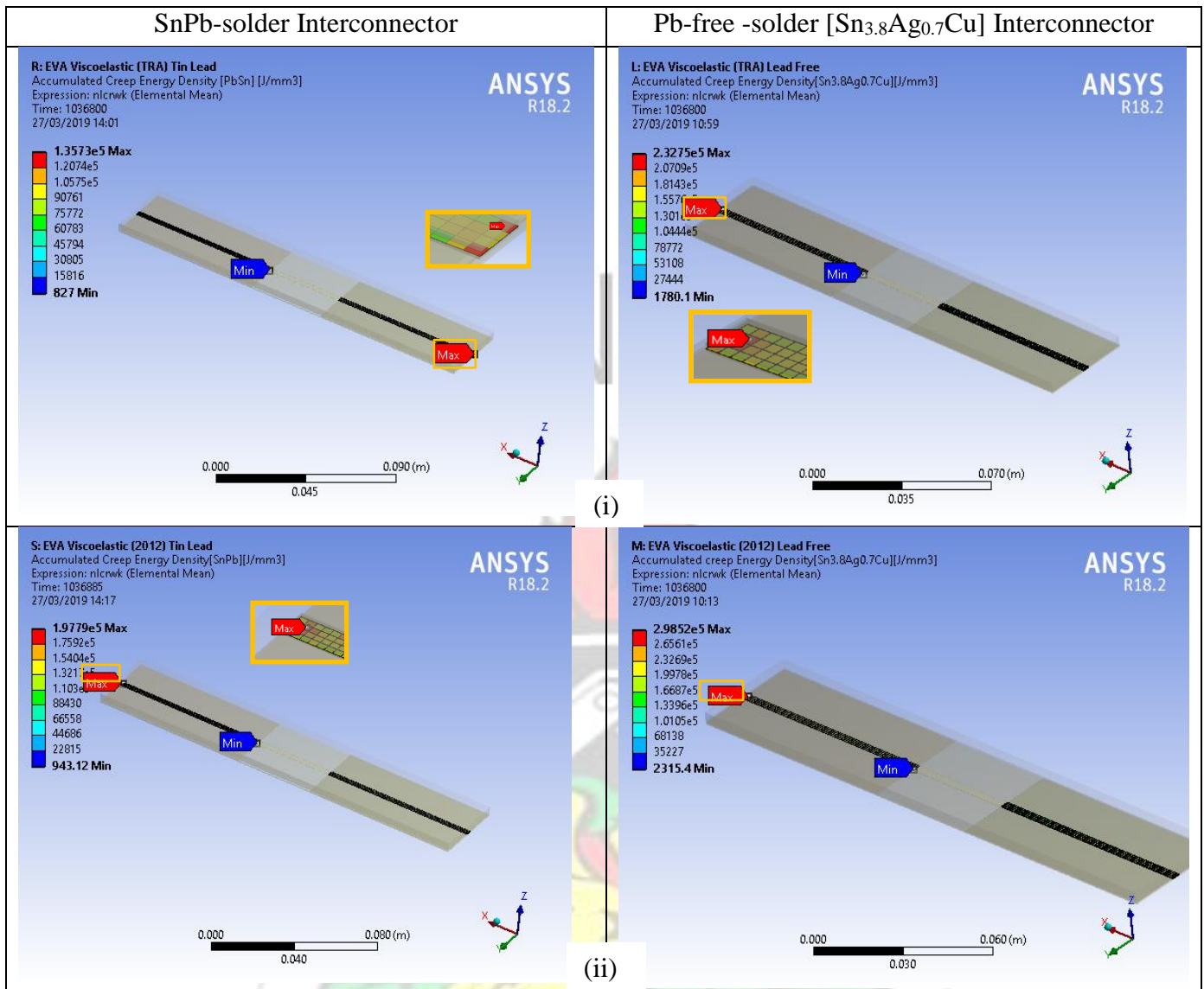


Figure 6 - 12 Accumulated Creep Energy Density Distribution at the end of 12 Thermal cycles for; (i) TRA and (ii) 2012 Thermal cycles

These peak values of accumulated creep energy density occur at the end of the 2012 thermal cycle. Thus, with the four thermal cycles under the study, the 2012 thermal cycle produced the highest damaging effect in terms of creep energy density. On the other hand, the 2014 thermal cycle produced the lowest creep damaging effect for the two types of soldered interconnections.

CHAPTER SIX: LIFE PREDICTION OF Pb-FREE AND SnPb SOLDERED JOINTS

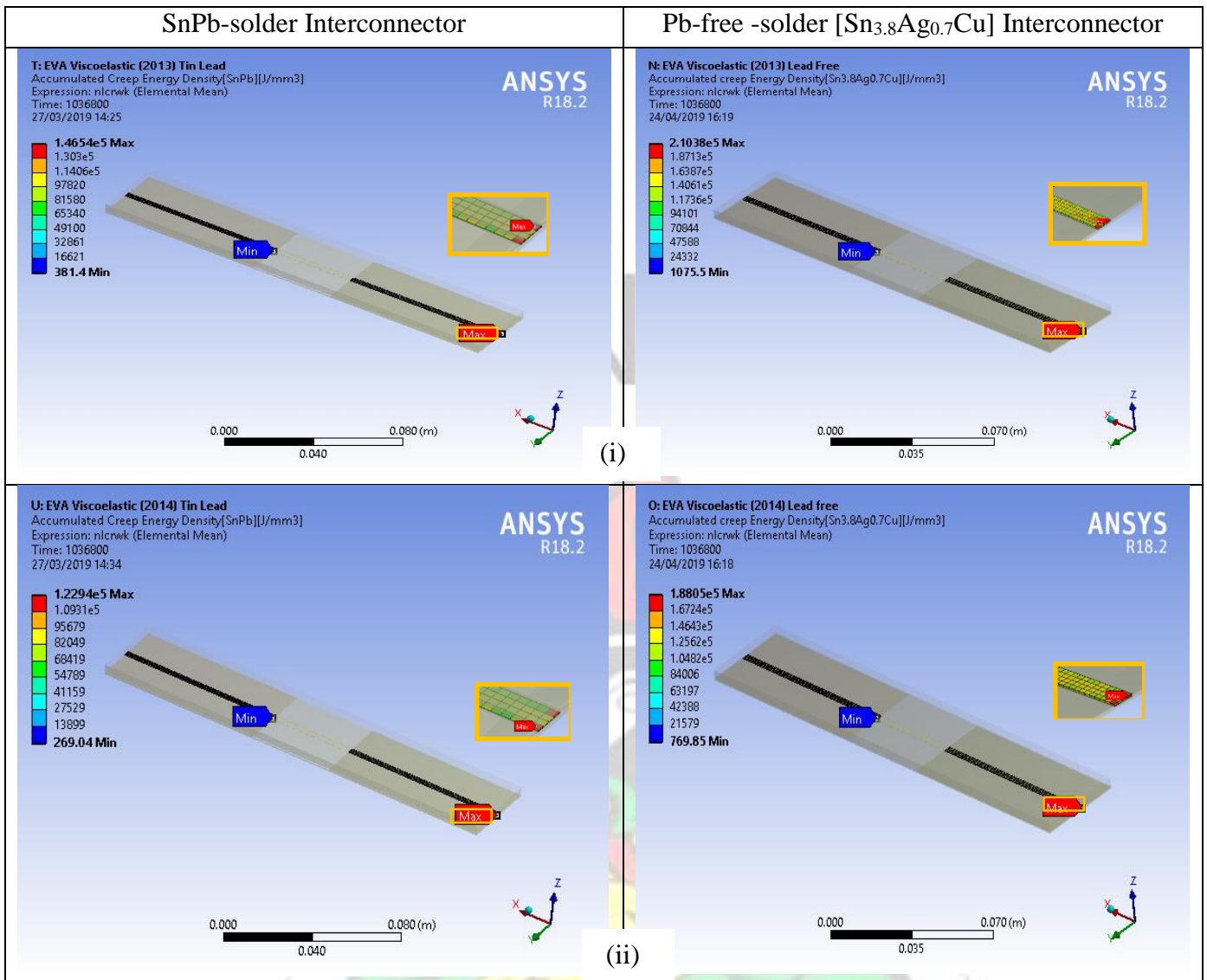


Figure 6 - 13 Accumulated Creep Energy Density Distribution at the end of 12 Thermal cycles for; (i) 2013 and (ii) 2014 thermal cycles.

Figure 6-14 presents a column plot of accumulated creep energy density at the end of 12 thermal cycles for the four thermal cycle profiles under study. The distribution in Figure 6-14 shows a maximum percentage change of 71.4 % in accumulated creep energy density from SnPb-solder to the Pb-free solder interconnection during the TRA thermal cycle.

On the other hand, the 2013 thermal cycle recorded a minimum of 43.56 % change in accumulated creep strain energy density. Thus, the TRA thermal cycle display a

CHAPTER SIX: LIFE PREDICTION OF Pb-FREE AND SnPb SOLDERED JOINTS

relatively higher sensitivity to the solder interconnection material properties while the 2013 thermal cycle display a relatively lower sensitivity to solder interconnection material property.

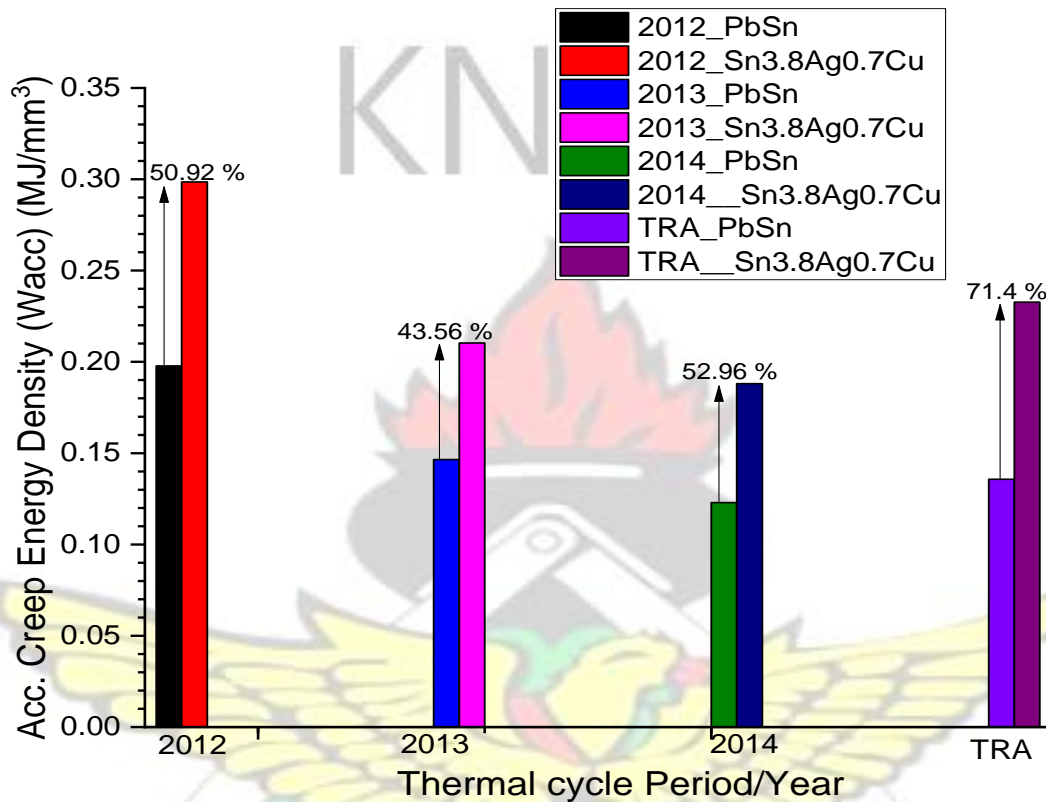


Figure 6 - 14 Column distribution of Accumulated Creep Energy Density for 2012, 2013, 2014 and TRA thermal cycles.

The time-dependent accumulated creep energy density over the various thermal cycle profiles for the two different solder interconnection materials is presented in Figure 6-15. It was observed from Figure 6-15 that, with the Pb-free solder interconnection, the accumulated creep energy density profiles for 2013 and TRA thermal cycles remained approximately equal for up to six thermal cycles.

CHAPTER SIX: LIFE PREDICTION OF Pb-FREE AND SnPb SOLDERED JOINTS

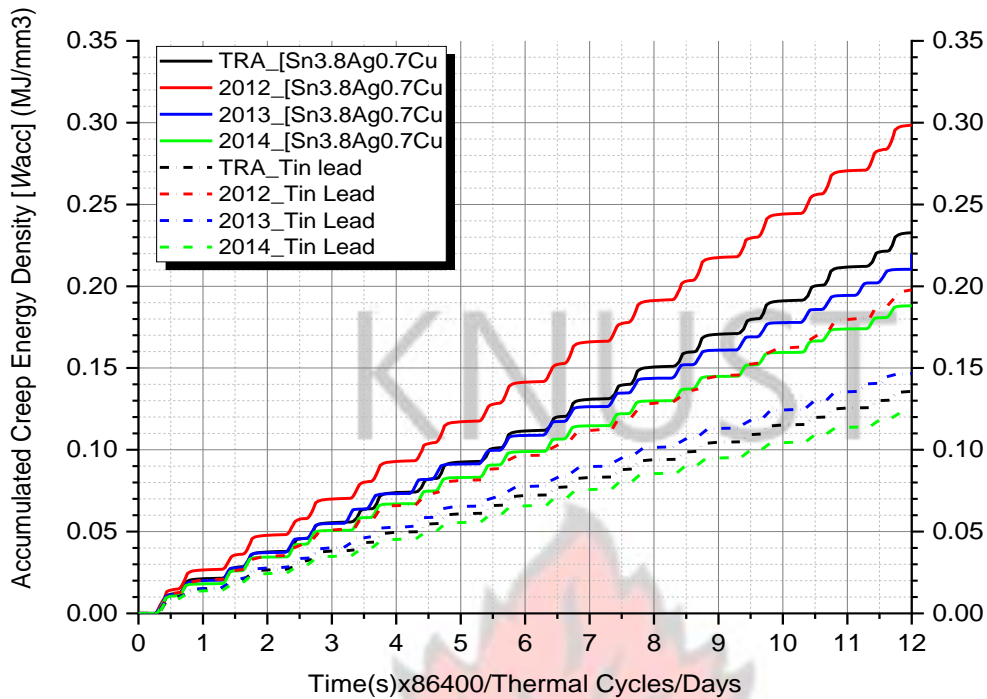


Figure 6 - 15 Accumulated Creep Energy Density (ACED) response over the 12 thermal cycles for: (a) TRA, (b) 2012, (c) 2013 and (d) 2014 thermal cycles

With the SnPb-solder interconnection, the accumulated creep energy density profiles for 2013 and TRA remained the same for up to the 3rd thermal cycle. Furthermore, from the 6th thermal cycle to the end of the 12th thermal cycle, the ACED profile generated in the Pb-free interconnection during the TRA cycle shows a higher ACED per cycle over that generated by the 2013 cycle. In contrast, beyond the 3rd thermal cycle, the ACED profile for the TRA thermal cycle generated in the SnPb-solder interconnection shows a lower ACED over the 2013 thermal cycle. The results show that more than six thermal cycles are required to quantify damage in the solder interconnection from ACED accurately. In the subsequent section, the accumulated creep energy density generated over the 12 thermal cycles is used as a parameter to predict the fatigue life of the soldered interconnection for the four thermal cycle profiles (2012, 2013, 2014 and TRA).

6.3.6 Life Prediction of Soldered Joint in Cell Interconnection

A number of life prediction models by several researchers including; (Kilinski et al., 1991, Pang et al., 1998, Yeo et al., 1996, Pang, 1997, Knecht and Fox, 1991, Syed, 1996, Syed, 1997, Syed et al., 1999, Syed, 2004, Syed, 2006, Akay et al., 1997, Liang et al., 1997, Wu et al., 1998, Gustafsson, 1998, Pan, 1994, Stolkarts et al., 1998, Mei, 1996) have been used to evaluate the life of soldered joints. In this study, the Syed's (Syed, 2006) model was used to predict the life of the solder interconnections. Syed's model is based on creep strain energy density that relates to the deformation stored internally throughout the volume of the joint during thermal loading. This model offers a more robust damage indicator in the solder joint since creep strain energy density captures the entire deformation in the joint. In this section, we predict the life of the solder interconnects using the accumulated creep energy density per cycle (W_{acc}) in (Syed, 2006) updated life prediction model given by:

$$N_f = (0.0069W_{acc})^{-1} \quad (6.1)$$

In practice, the change in accumulated creep energy density per cycle (ΔW_{acc}) averaged over the volume of solder is used for predicting the cycles of failure. The (ΔW_{acc}) is obtained by computing the average change in creep energy density (ΔW_{ave}) from the finite element analysis (FEA) results and then normalised with the volume of the solder used in generating the geometric model. Thus

$$\Delta W_{ave} = \frac{\sum_i^n W_2^i V_2^i}{\sum_i^n V_2^i} - \frac{\sum_i^n W_1^i V_1^i}{\sum_i^n V_1^i} \quad (6.2)$$

Where W_2^i , W_1^i is the total ACED in one element at the end and the starting point of one thermal cycle, respectively. V_2^i , V_1^i is the volume of element at the end and start point of one cycle respectively, and n is the number of selected elements used.

CHAPTER SIX: LIFE PREDICTION OF Pb-FREE AND SnPb SOLDERED JOINTS

Figure 6-16 presents the change in accumulated creep energy density over the thermal cycles under study. As observed from Figure 6-16, the change in accumulated creep energy density reduces sharply in the solder interconnections from the first to the second thermal cycle for all four thermal cycle profiles considered. For the Pb-free solder interconnection, the change in ACED increases steadily after the second thermal cycle for both the 2012 and TRA thermal cycles. However, with the 2013 and 2014 thermal the change in ACED decreases further but marginally after the second thermal cycle. Similar trends in the change in ACED were observed in the SnPb solder interconnection for 2012, 2013 and 2014 thermal cycles. The TRA thermal cycle, on the other hand, generated an alternating increase and decrease in the change in ACED per cycle in the SnPb solder interconnect. Overall, the change in ACED in Pb-free solder interconnections was observed to be relatively higher than the change in ACED registered in the SnPb solder interconnects for all the four different thermal cycles under study.

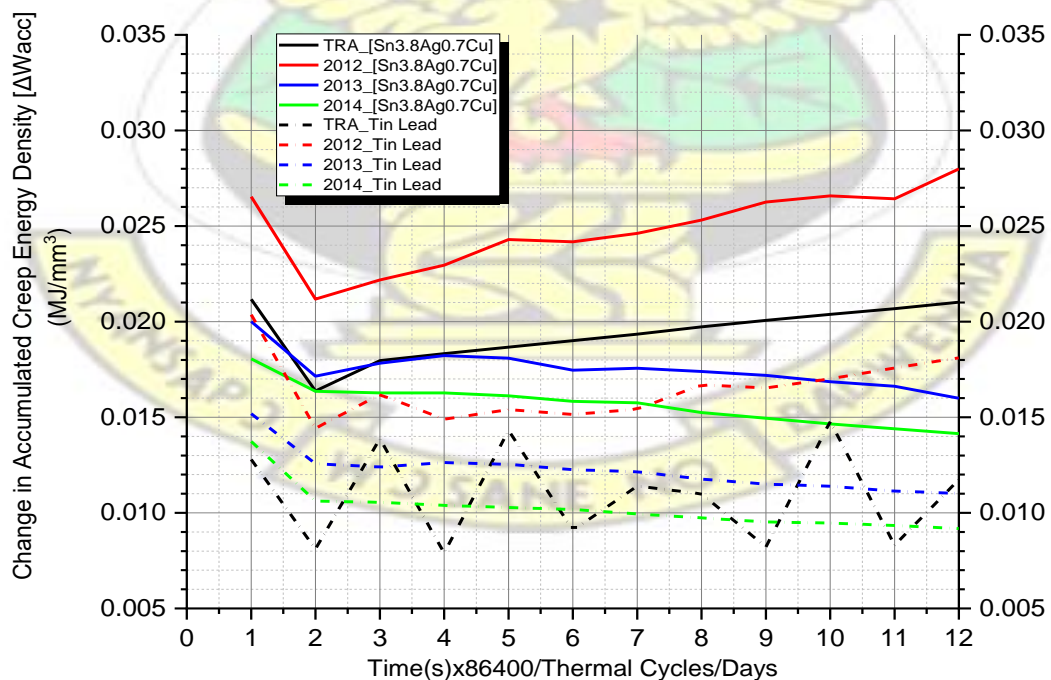


Figure 6-16: Change in Accumulated Creep Energy Density vrs Thermal Cycles for; 2012, 2013, 2013, 2014 and TRA thermal cycles.

CHAPTER SIX: LIFE PREDICTION OF Pb-FREE AND SnPb SOLDERED JOINTS

The accumulated creep energy density per cycle (W_{acc}) is computed from the relation:

$$W_{acc} = \frac{\sum_{c_1}^{c_n} \Delta W_{acc}}{c_n} \quad (6.3)$$

Where c_1 is the cycle number for the first thermal cycle and, c_n is the cycle number for the n^{th} thermal cycle. For this study involving 12 thermal cycles: $c_1=1$ and $c_n=12$. Thus, we have

$$W_{acc} = \frac{\sum_1^{12} \Delta W_{acc}}{12} \quad (6.4)$$

The cycle time used in this study is 86400 s (24 hrs or 1 day). Additionally, (Guyenot et al., 2011) reported that, within a temperature change of about 50 °C, PV modules generally experience one and a half (1.5) thermal cycles per day. Thus, the expected life of interconnects (in years) is evaluated as:

$$L_{years} = \frac{\left(\frac{N_f}{1.5}\right)}{365} \quad (6.5)$$

Table 2 presents the results from the evaluation of W_{acc} , N_f and L_{years} from equations (6.3), (6.4) and (6.5) respectively. Figure 6-17 presents a histogram of the distribution of fatigue life (years/cycles).

CHAPTER SIX: LIFE PREDICTION OF Pb-FREE AND SnPb SOLDERED JOINTS

Table 6 - 2: Expected Life of solder interconnects from outdoor module temperature cycle profiles

Thermal Cycles		2012	2013	2014	TRA
Accumulated Creep Energy Density per cycle (W_{acc}) / $MJmm^3$	Sn3.8Ag0.7Cu	0.02488	0.01753	0.01567	0.01934
	SnPb	0.01648	0.01221	0.01024	0.01131
Expected Life (N_f) / cycles	Sn3.8Ag0.7Cu	5825	8267	9249	7494
	SnPb	8794	11870	14,153	12814
Expected Life (L_{years}) / years	Sn3.8Ag0.7Cu	10.64	15.1	16.89	13.69
	SnPb	16.06	21.68	25.85	23.4

From table 6-2 and figure 6-17, the maximum accumulated creep energy density per cycle in the 2012 thermal cycle on the Pb-free interconnection produced a fatigue life of 5825 cycles (10.64 years) and the minimum accumulated creep energy density per cycle in 2014 produced a fatigue life of 14153 cycles (25.85 years) in the SnPb interconnection.

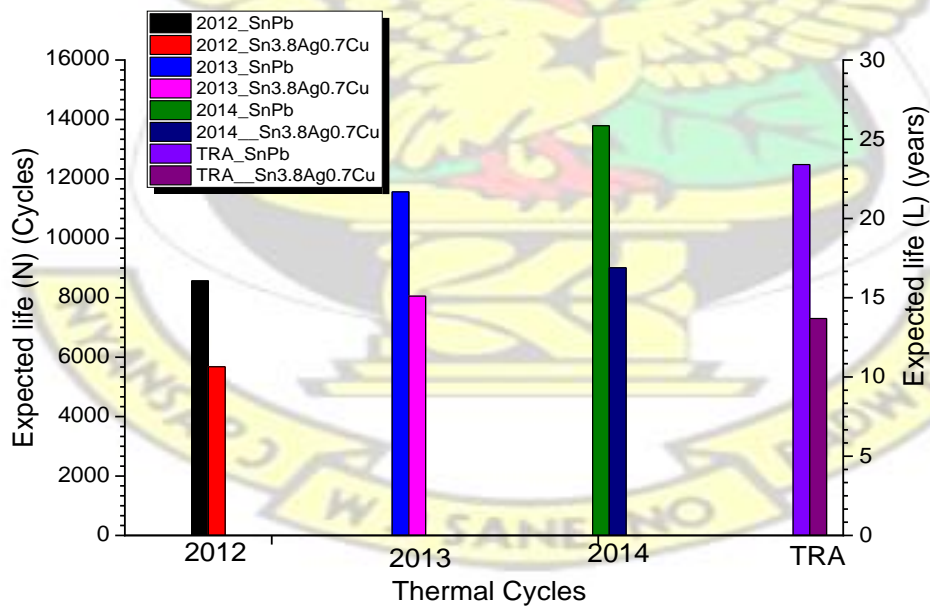


Figure 6 - 17 Expected Life of solder interconnection under 2012, 2013, 2014 and TRA thermal cycling.

CHAPTER SIX: LIFE PREDICTION OF Pb-FREE AND SnPb SOLDERED JOINTS

The results from the life prediction study correlate with a study by (Guyenot et al., 2011) where the authors estimated the life of PV modules operating per day with an average temperature gradient of about 50 °C as 13688 cycles (25 years). In addition, the results are in close agreement with (Köhl et al., 2009) who reported 10950 cycles in a four-year German project. Furthermore, related studies from (Kumar and Sarkan, 2013) who recorded a minimum life of 11497 cycles (21 years) under constant stress accelerated life test on 20 PV modules for stress-related failure closely matches with results from this study.

6.4. Summary

In this study, the life of solder interconnection in solar PV is predicted for both SnPb solder and a Pb-free solder. The study utilized thermal cycle loads generated by real-time monitoring of module temperatures on installed PV modules for the years 2012, 2013 and 2014. Additionally, a test region average (TRA) thermal cycle was utilized in the study. Results from the numerical study show that the 2012 thermal cycle induced the maximum stress and creep strain damage of 9.0148 MPa and 0.010393 m/m, respectively. The maximum stress and creep strain were registered in the SnPb-solder interconnection. On the other hand, the minimum equivalent stress and creep strain damage of 7.9169 MPa and 0.0055175 m/m were generated in the Pb-free solder interconnection during the 2013 thermal cycle. These results were confirmed by the stress-strain hysteresis loops generated by the respective thermal cycles, which showed the 2012 thermal cycle as developing the most extensive loop during the 2012 thermal cycle. In addition, accumulated creep strain results evaluated show that the Pb-free solder interconnection accumulated the highest creep strain damage for 2012, 2013 and 2014 thermal cycles. During these three thermal cycles (2012, 2013 and 2014), the average percentage change in accumulated creep damage from the SnPb solder

CHAPTER SIX: LIFE PREDICTION OF Pb-FREE AND SnPb SOLDERED JOINTS

interconnection to Pb-free solder was found to be approximately 45%. However, the change in accumulated creep strain was found to be relatively higher (57.96 %) across the two types of solder interconnections during the TRA thermal cycle.

Subsequently, results from the life prediction show that the solder interconnects will achieve the maximum life (cycles/years) under the 2014 thermal cycle loading. In particular, the SnPb solder interconnection is expected to achieve 14,153 cycles (25.85 years) whilst the Pb-free solder interconnection is expected to achieve 9249 cycles (16.89 years). Additionally, with the TRA cycle, the Pb-free and Pb-Sn solder interconnections are expected to achieve 7944 cycles (13.69 years) and 12814 cycles (23.4 years) respectively. The study show that Pb-Sn solder interconnections are likely to exhibit superior reliability over the Pb-free solder interconnections at the KNUST test site in sub-Saharan Africa.



CHAPTER SEVEN: EFFECTS OF TEMPERATURE RAMPS AND DWELLS ON DAMAGE OF SOLDERED INTERCONNECTIONS

7.1 Introduction

The reliability of soldered interconnections of solar PV modules and other electronic devices are usually assessed using accelerated thermal cycling tests. The control and acceleration parameters that are utilized in thermal cycling tests include dwell-times, ramp-rates, maximum and minimum ramp temperatures, mean temperature and cycle time. Figure 7-1 shows relationships between the thermal cycle parameters.

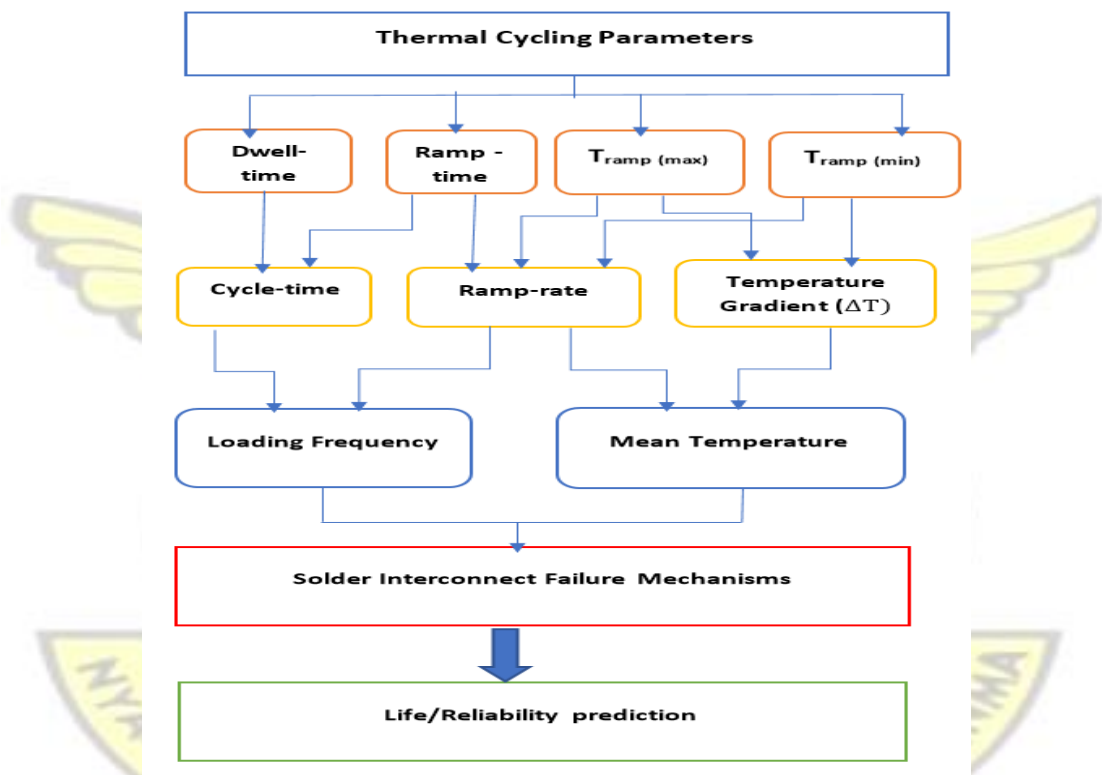


Figure 7-1: Relationships between Thermal Cycle Parameters

(Bath et al., 2005, Sharma and Dasgupta, 2002) in their respective studies compared dwell-times of 10-minute to over 30-minutes. Studies on relatively shorter dwell times and dwell-time intervals have also been carried out by (Pan et al., 2005, Bingting et al., 2006). (Clech, 2005) proposed an optimum dwell time of 10 minutes for BGA assemblies based on highest damage rate. A dwell-time of 8-10 minutes at the highest

CHAPTER SEVEN: EFFECTS OF TEMPERATURE RAMPS AND DWELLS ON DAMAGE OF SOLDERED INTERCONNECTIONS

ramp has been recommended by (Zhai and Blish, 2003). (Zhai and Blish, 2003) further observed that with dwell-times beyond 20 minutes, the effect on the acceleration factor becomes insignificant since the induced stresses tend to stabilize. A number of related studies (Xuejun et al., 2005, Sahasrabudhe et al., 2003, Manock et al., 2007) however reported a decrease in lifetime with increasing dwell-time. (Xuejun et al., 2005) in their study of effects of dwell times and ramp rates on Lead-free solder joints in FCBGA packages reported a decrease in fatigue life with an increase in dwell time from 15-to-30 minutes and up until 90 minutes. Results from (Sahasrabudhe et al., 2003) show a strong dependency of dwell-time on initiation of failures. (Sahasrabudhe et al., 2003) observed that the longer dwell-times lead to earlier failures as compared with shorter dwell-times. (Manock et al., 2007) compared 10, 30 and 60 minutes dwells with 10 minute ramps between (0°C - 100°C) temperature boundaries. Their results show a decrease in characteristic lifetime in cycles-to-failure with increase in dwell time.

A number of studies have reported conflicting outcomes on the effects of ramp rate on fatigue life of solder joints but a significant majority (Clech, 2005, Dusek et al., 2005, Ghaffarian, 2001, Lau and Dauksher, 2005, Qi et al., 2006) agree that the number of cycles to failure decreases with increase in ramp rate. For instance (Lau and Dauksher, 2005) reported in their findings indicating that a fewer number of cycles to failure under thermal shock compared with temperature cycling conditions. Additionally, (Ghaffarian, 2001) observed that (10 to 15°C/min) thermal shock condition will produce less cycles-to-failure than a temperature cycling conditions of (2 to 5°C/min). Furthermore, (Qi et al., 2006) reported that (95 °C/min) caused more damage than a lower ramp rate of (14°C/min). The reported differences in cycles-to-failure are

CHAPTER SEVEN: EFFECTS OF TEMPERATURE RAMPS AND DWELLS ON DAMAGE OF SOLDERED INTERCONNECTIONS

explained by the resulting large change in creep strain energy density per cycle at faster ramp rates.

(Bouarroudj et al., 2008, Schubert et al., 2003) reported in their respective studies that test conditions with higher mean temperature leads to significantly shorter lifetimes than test conditions with lower mean temperature. The observed differences in the reported lifetime of solder joints relates to the impact of temperature on the mechanical properties of solder. Research reports that the mean temperature influences the width and height of the stress/strain hysteresis loop produced in thermal cycling of the solder interconnection. (Clech, 2005) studied the mean temperature effects of Lead-free and SnAgCu assemblies and suggested that a minimum lifetime for SnAgCu solder interconnection exist when the mean temperature of a thermal cycle profile falls in the range of about 50 °C to 65 °C. (Classe and Sitaraman, 2003, Morris et al., 1991) have all suggested that at lower dwell temperature the dwell phase is insensitive to duration since there is minimal amount of accumulated visco-plastic strain. However, (Syed, 2010) in estimating acceleration factors for lead-free solders reported that dwell-time at lower temperature contributes significantly to failure mechanism when accumulated creep strain is used as the damage indicator in thermal cycling. Syed also observed that high temperature dwell is the lowest contributor to accumulated creep strain and therefore placing too much emphasis on high temperature dwells could be misleading.

All the studies reviewed involved different materials and packages such as PCBs, IGBTs, and BGAs. Results of investigations into effects of ramp rates, dwell times and temperature gradients on solar PV cell interconnections are scarcely available. In this

CHAPTER SEVEN: EFFECTS OF TEMPERATURE RAMPS AND DWELLS ON DAMAGE OF SOLDERED INTERCONNECTIONS

study, the contributions of ramp rates and dwell times to the degradation of soldered interconnections of c-Si PV modules under field temperature cycling is investigated.

7.2 Methodology

In this investigation, geometric models of solar cells interconnected using two different solder formulations namely; $Pb_{60}Sn_{40}$ and $Sn_{3.8}Ag_{0.7}Cu$ as interconnecting materials. Four geometric models were generated for the study of each type of solder interconnection. In addition, four temperature load profiles (2012, 2013, 2014 and TRA thermal cycles) generated from a three-year real-time monitoring of installed PV modules at the test site. The generalized Garafalo Arrhenius model was used in the study of the creep behaviour of the solders. IMC's of $6\mu m$ thickness comprising of Cu_3Sn_5 and Ag_3Sn on either side of the solder material were used to completely model the interconnection. The material models used for the different laminating materials of the solar cell as well as the general FEM methodology have been extensively discussed in the chapter 3 and shall not be repeated here.

In a single thermal cycle, the damage accumulation occurs at various load steps defined in the cycle. In this study, a typical daily temperature cycle shown in Figure 7-2 has five (5) load steps that can be defined as; 1st Cold dwell load step, Ramp-up load step, Hot dwell load step, Ramp-down load step, and 2nd Cold dwell step. Each of these five load steps generated different damage profiles in the soldered interconnection.

**CHAPTER SEVEN: EFFECTS OF TEMPERATURE RAMPS AND DWELLS
ON DAMAGE OF SOLDERED INTERCONNECTIONS**

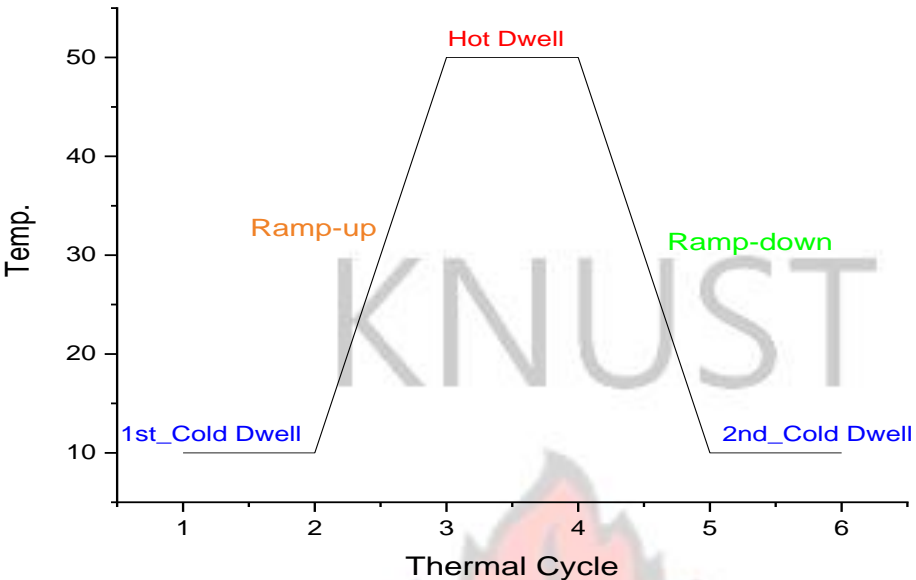
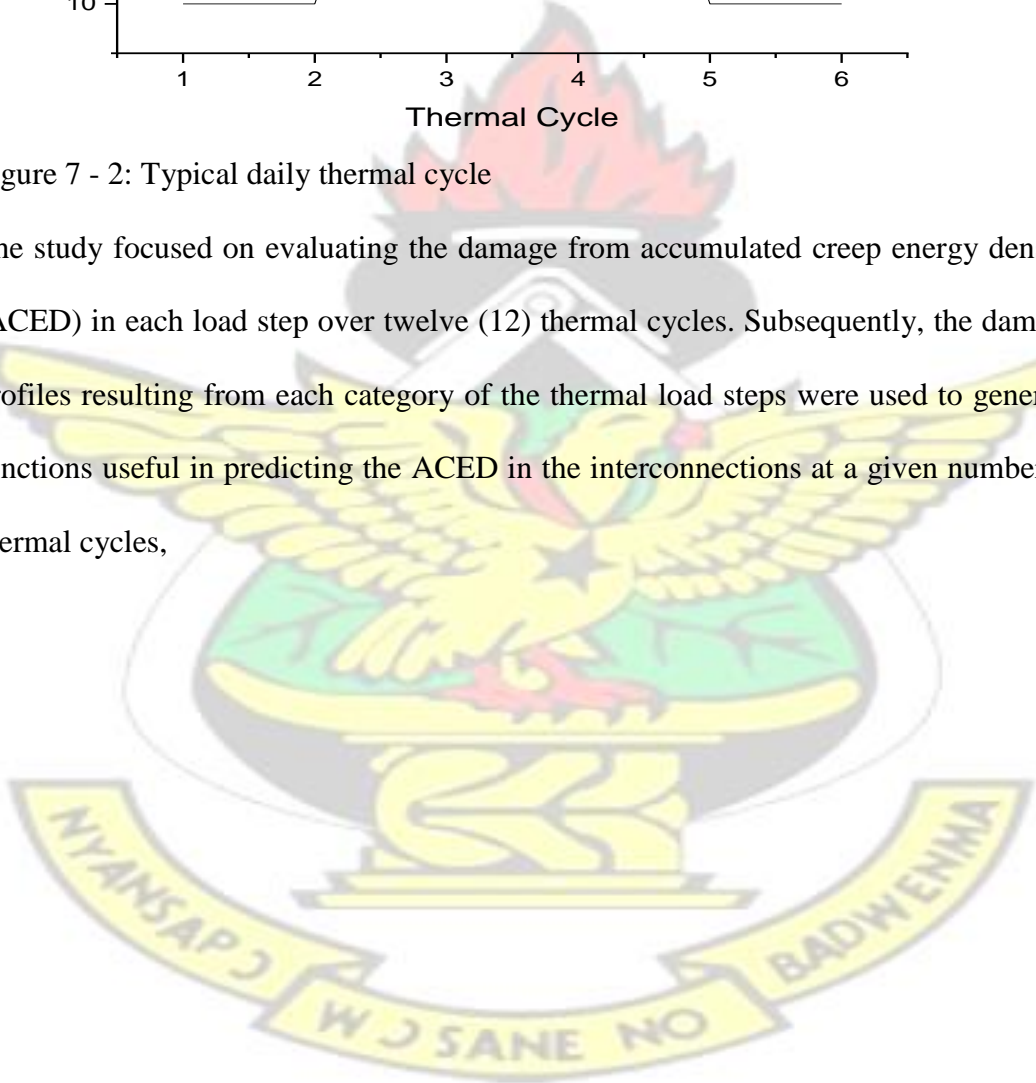


Figure 7 - 2: Typical daily thermal cycle

The study focused on evaluating the damage from accumulated creep energy density (ACED) in each load step over twelve (12) thermal cycles. Subsequently, the damage profiles resulting from each category of the thermal load steps were used to generate functions useful in predicting the ACED in the interconnections at a given number of thermal cycles,



CHAPTER SEVEN: EFFECTS OF TEMPERATURE RAMPS AND DWELLS ON DAMAGE OF SOLDERED INTERCONNECTIONS

7.3 Results and discussions

7.3.1 Evaluation of change in Accumulated Creep Energy Density (ACED) of solder joint.

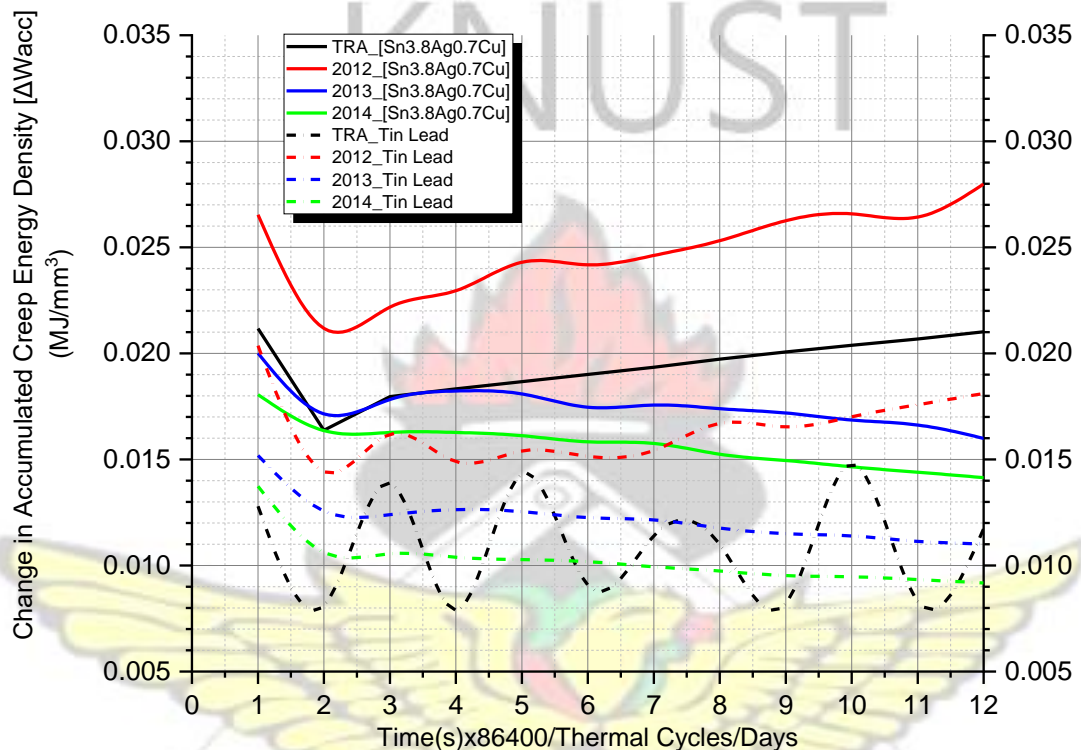


Figure 7-3: Change in ACED over daily thermal cycles

The change in accumulated creep energy density (ACED) is evaluated by computing the difference between the damage accumulated in the solder interconnection from a thermal cycle and the next higher thermal cycle. In this study, we compute the change in the ACED per cycle for the two different types of interconnect solder and present the response of the solder interconnection to creep damage in Figure 7-3. The damage profiles from Figure 7-3 have been discussed in chapter 6. To study the effect of ramp rates and dwell times on the total damage index, it is important to examine the percentage damage contribution of each of these load steps within the cycle. In the next section, we study the creep damage distribution from the daily thermal cycle profiles.

CHAPTER SEVEN: EFFECTS OF TEMPERATURE RAMPS AND DWELLS ON DAMAGE OF SOLDERED INTERCONNECTIONS

7.3.2 Study on Creep Damage distribution from Thermal cycles

The distribution of the percentage changes in ACED shows that the ramp-up load step contributes the highest percentage (approximately 50%) of the accumulated damage in the first thermal cycle for all the four different thermal cycle profiles under study (TRA, 2012, 2013 and 2014 thermal cycles). However, the distributions change after the first thermal cycle showing varied responses from the different thermal cycles and thermal load steps. For every thermal cycle, the combined effect of ramp-up load step and ramp-down load step accounted for at least 80 % of the damage in the two types of soldered interconnections. Another key observation reveals that the damage contribution from the hot dwell load step and cold dwell load step are significantly higher in the SnPb solder interconnections than in the Pb-free interconnections for all the thermal cycles considered in the study. The subsequent sub-sections discuss the damage distribution from the four thermal cycles.

7.3.2.1 Damage Distribution from TRA thermal cycle

The damage distribution from the TRA thermal cycle is displayed in Figure 7-4. From Figure 7-4, the ramp-up load step contributed to approximately 36 % of creep damage per cycle in both the SnPb and Pb-free solder interconnections during the TRA thermal cycle. Additionally, the creep damage distribution in both interconnections from the TRA thermal cycle shows that the contribution to creep damage from the ramp-down load step remained the highest from the second thermal cycle up to the end of the 12 thermal cycles. The results from the TRA thermal cycle show that, from the second thermal cycle, the contribution of the ramp-down load step to creep damage is slightly higher (approximately 40%) in the Pb-free solder interconnection than the creep

CHAPTER SEVEN: EFFECTS OF TEMPERATURE RAMPS AND DWELLS ON DAMAGE OF SOLDERED INTERCONNECTIONS

damage registered in the SnPb solder interconnection (approximately 37%) from the same ramp-down load step.

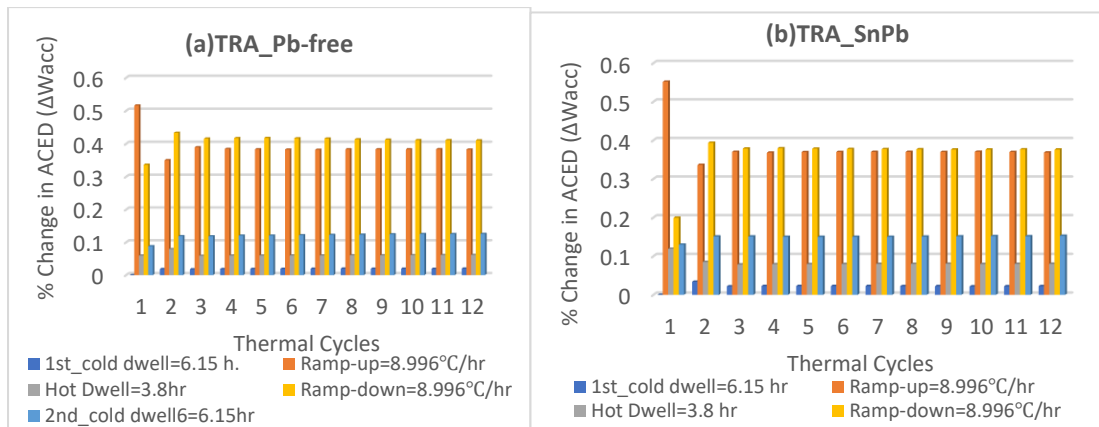


Figure 7-4: Change in ACED distribution from TRA thermal cycle for (a) Pb-free (b) PbSn interconnections

The contribution of the 1st Cold dwell load steps accounted for the lowest percentage (3 %) of the creep damage per cycle. On the other hand, the 2nd Cold dwell step accounted for about 12 % in Pb-free solder interconnection and 15% in SnPb solder interconnection respectively. Additionally, the hot dwell load step accounted for about 5% and 8% of creep damage per cycle in the Pb-free and SnPb interconnections respectively.

7.3.2.2 Damage Distribution from 2012 thermal cycle

The damage distribution from the 2012 thermal cycle displayed in Figure 7-5 showed that, after the first thermal cycle, the damage contribution from the ramp-up load step stabilizes at approximately 35% in the Pb-free interconnection. On the other hand, the damage contribution from the ramp-up load step increases after stabilizing around 30% in the second (2nd) and third (3rd) thermal cycle in the SnPb interconnection. It rises to a peak value of 40 % at the fifth (5th) and sixth (6th) thermal cycle. Subsequently, the damage from the ramp-up load step declined from the seventh (7th) thermal cycle and

CHAPTER SEVEN: EFFECTS OF TEMPERATURE RAMPS AND DWELLS ON DAMAGE OF SOLDERED INTERCONNECTIONS

again stabilized at 30% from the eighth (8th) cycle up to the eleventh (11th) thermal cycle.

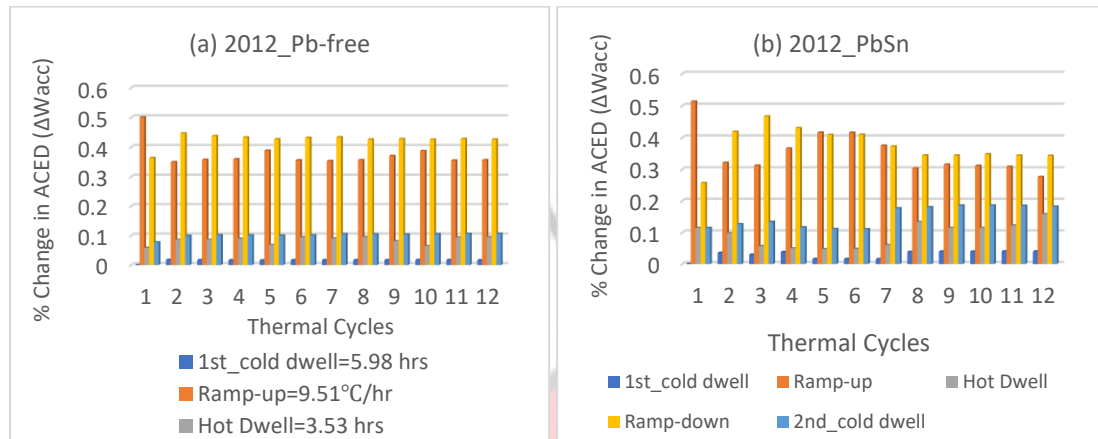


Figure 7-5: Change in ACED distribution from TRA thermal cycle for: (a) Pb-free (b) PbSn interconnections

The ramp-down load step contributed approximately 42% of the damage accumulation per cycle in the Pb-free soldered interconnection. The damage within the Pb-free interconnection from the hot dwell load step contributed approximately 8% of the accumulated damage per cycle. The 1st cold dwell step contribution to the damage per cycle remained the lowest (at 2%) whilst the 2nd cold dwell step accounted for 10% of the damage in the Pb-free soldered interconnection.

The damage distribution in the SnPb soldered interconnection from the 2012 thermal cycling showed that the damage contribution from the ramp-up load step peaked at the 5th and 6th thermal cycles with nearly 40% of the damage contribution. Subsequently, the damage contribution declined to an average value of 30% after the 7th thermal cycle. The 2nd_cold dwell step and the hot dwell load step generated significant creep damage in the SnPb soldered interconnection after the 6th thermal cycle with 15% and 10% contribution per cycle respectively.

CHAPTER SEVEN: EFFECTS OF TEMPERATURE RAMPS AND DWELLS ON DAMAGE OF SOLDERED INTERCONNECTIONS

7.3.2.3 Damage distribution from 2013 thermal cycle

The damage distribution of ACED from the 2013 thermal cycle displayed in Figure 7-6 shows a nearly equal percentage distribution in creep damage for ramp-up (heating) and ramp-down (cooling) load steps in both types of interconnection after the first thermal cycle.

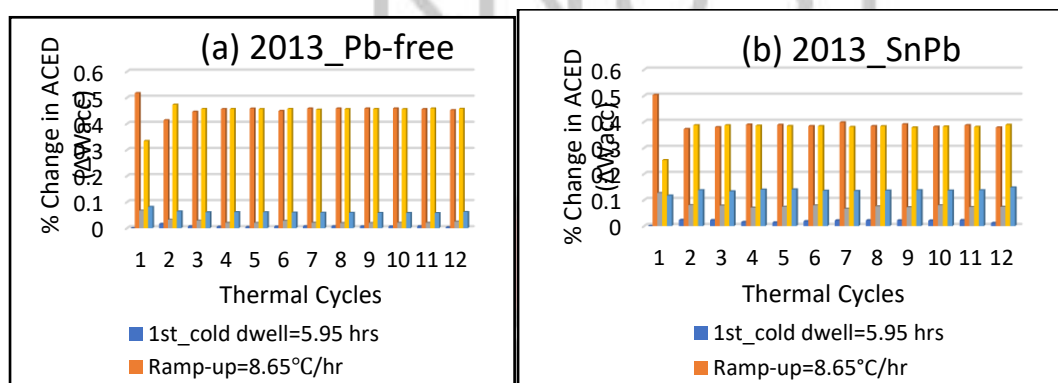


Figure 7-6: Change in ACED distribution from 2013 thermal cycle for: (a) Pb-free (b) PbSn interconnections

The ACED from the heating and cooling load steps accounted for about 88% of the total accumulated creep damage in the Pb-free solder interconnection. Similarly, the heating and cooling load step show accounted for 78 % of the total accumulated damage in the PbSn solder interconnection. The remaining three load steps (1st cold dwell, 2nd cold dwell and hot dwell) contributed 12% and 22% of the accumulated creep damage in the Pb-free and PbSn solder interconnections respectively.

7.3.2.4 Damage distribution from 2014 thermal cycle

The damage distribution from the 2014 thermal cycle shown in Figure 7-7 display similar trends as in the 2013 thermal cycle with the combined accumulated creep energy damage from the heating and cooling load step accounting for 90% of the total accumulated creep energy damage in the Pb-free interconnection. A similar damage

CHAPTER SEVEN: EFFECTS OF TEMPERATURE RAMPS AND DWELLS ON DAMAGE OF SOLDERED INTERCONNECTIONS

distribution can be observed in the PbSn interconnection where the heating and cooling load steps accounted for 76% of the total damage.

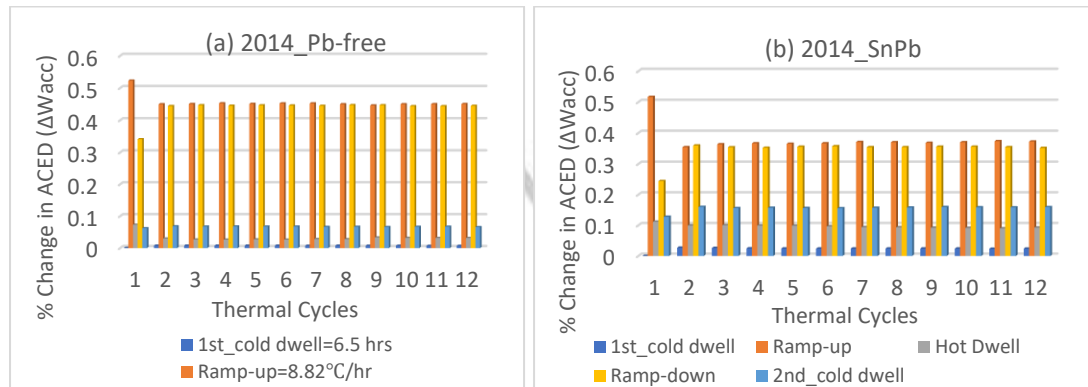


Figure 7-7: Change in ACED distribution from 2013 thermal cycle for: (a) Pb-free (b) PbSn interconnections

The damage from hot and cold dwell periods in the SnPb interconnections recorded the significant value of 24 % whereas a relatively lower percentage of 10 % was generated in the Pb-free solder. The damage distribution from the four thermal cycles (TRA, 2012, 2013 and 2014) studied shows that the ACED is sensitive to the thermal cycle parameters of dwell time and temperature ramp rate. To quantify the effect of ramp rates and dwell times of the thermal cycle on the damage accumulation, it is imperative to study the damage profiles resulting from both ramp rates and dwell times in order to generate some functional relationships between them as well as the total accumulated creep energy density. The next section discusses the damage accumulation profiles from the five thermal load steps.

7.3.3 Study on Damage Accumulation profile at Temperature Load Steps

7.3.3.1 Damage profile at Cold dwell load step at the start of Thermal Cycle

The change in ACED in the soldered interconnections from the cold dwell load steps across the four thermal cycles (2012, 2013, 2014 and TRA) is presented in Figure 7-8.

CHAPTER SEVEN: EFFECTS OF TEMPERATURE RAMPS AND DWELLS ON DAMAGE OF SOLDERED INTERCONNECTIONS

The first cold dwell load step in each thermal cycle generated the minimum ACED within the soldered interconnections. The contribution to damage from the first cold dwell step in each thermal cycle remained insignificant.

The damage accumulation profiles in the Pb-free interconnections from 2012, 2014 and TRA thermal cycles exhibited clear similarities across the 12 cold dwell load steps corresponding to the start of each cycle. Generally, they showed a sharper rise in the change in ACED from the end of the first load step up to the end of the 2nd cold dwell load step corresponding to the start of the second thermal cycle. Subsequently, they exhibited a drop in ACED at the third cold dwell load step. After the 3rd cold dwell load step, the changes in ACED from the respective thermal cycle loads assumed polynomial profiles.

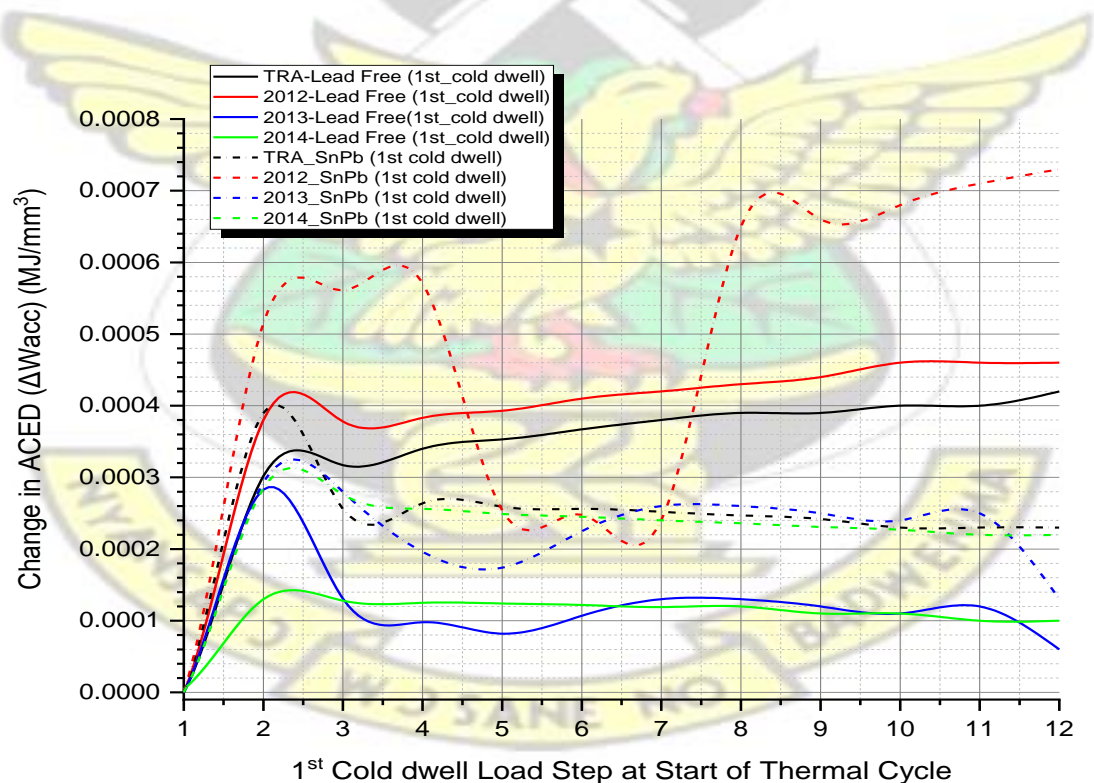


Figure 7-8: Damage Accumulation from cold dwell at start of thermal cycle (1st Cold dwell load step)

CHAPTER SEVEN: EFFECTS OF TEMPERATURE RAMPS AND DWELLS ON DAMAGE OF SOLDERED INTERCONNECTIONS

The damage profiles in Pb-free solder interconnections from 2014 and TRA thermal cycles trends closely with the damage profile in Pb-free solder interconnections. On the other hand, the damage profile in SnPb and Pb-free interconnections from the 2013 thermal cycle declined further from the 3rd cold dwell load step through to the 5th load step.

Furthermore, the damage profile assumed a steady rise from the 5th cold dwell load step up to the 7th thermal cycle. Subsequently, the damage profiles in both interconnections assumed stagnation from the 7th cold dwell load step to the end of the 11th load step, and finally the profiles dropped sharply at the end of the 12th cold dwell load step. The damage profile in SnPb interconnection from 2012 thermal cycle displayed a fluctuating profile up to the 9th cold dwell step. After the 9th cold dwell load step, the profile assumed a steady rise up to the end of the 12th thermal cycle. Results from this study showed that, the change in ACED from the cold temperature dwell at the start of each thermal cycle in SnPb interconnections for all four thermal cycling conditions were generally higher than that in Pb-free interconnections.

CHAPTER SEVEN: EFFECTS OF TEMPERATURE RAMPS AND DWELLS ON DAMAGE OF SOLDERED INTERCONNECTIONS

7.3.3.2 Damage at Cold Dwell load step at the end of thermal cycles

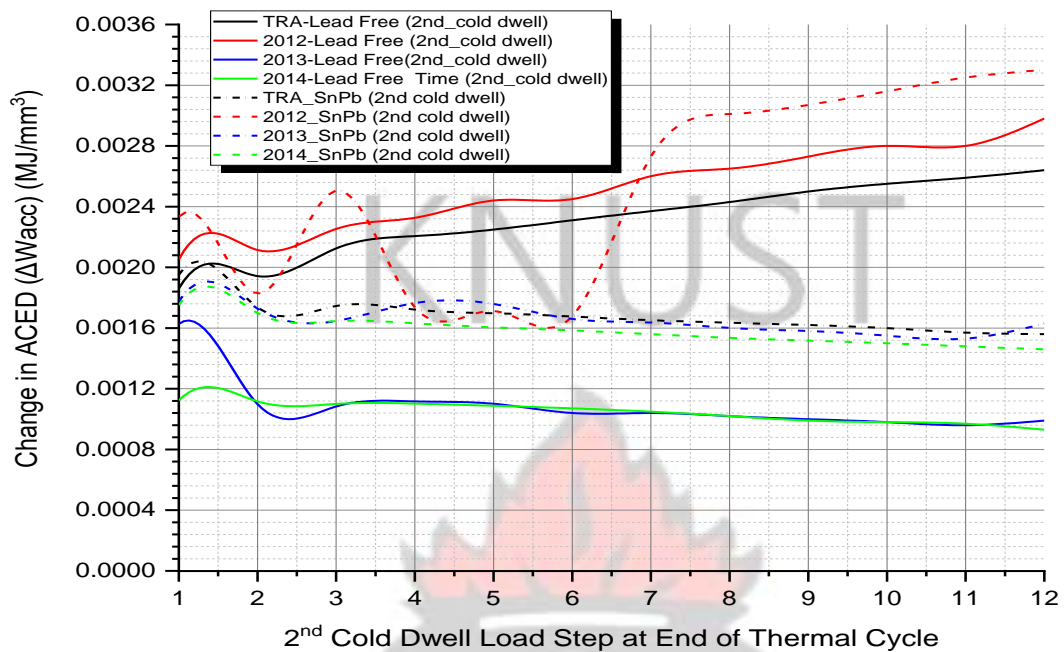


Figure 7-9: Damage Accumulation from cold dwell at end of thermal cycle (2nd Cold dwell load step)

The change in ACED profiles during the end of each thermal cycle (cold dwell at the start of thermal cycles) displayed in Figure 7-9 showed similarities to the cold dwell load steps at the start of the thermal cycle. The distinction observed revealed that, for the cold dwell steps at the end of each cycle, the change in ACED registered a peak value initially at the end of the 1st dwell load step as against the second dwell load step registered from Figure 7-8.

Additionally, the change in ACED generated per load step during the temperature dwells at the end of the thermal cycles were observed to be relatively higher than that at the start of the thermal cycle (1st cold dwell load steps).

CHAPTER SEVEN: EFFECTS OF TEMPERATURE RAMPS AND DWELLS ON DAMAGE OF SOLDERED INTERCONNECTIONS

7.3.3.3 Damage profile at maximum Temperature Dwell (Hot Dwell load step)

The damage profiles depicted in Figure 7-10 from maximum temperature dwell (hot dwell load steps) showed similar trends except for the profile generated from the 2012 thermal cycle.

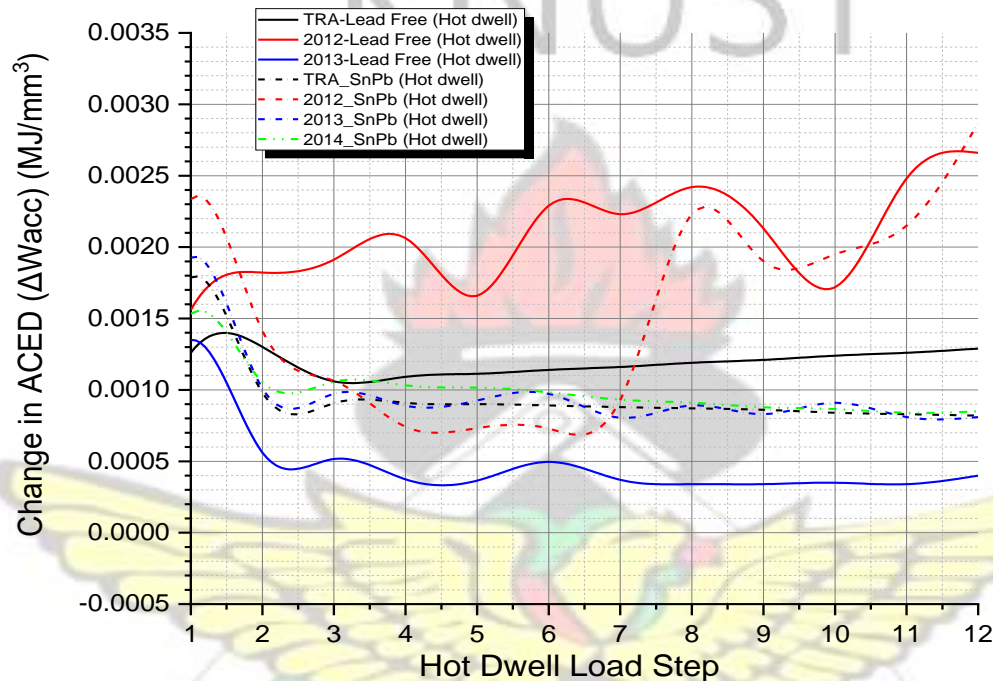


Figure 7-10: Damage Accumulation from hot dwell load step

The damage profiles from the 2012 (SnPb), 2013, 2014 and TRA (SnPb) thermal cycles in Figure 7-10 showed sharp increases in change in ACED to peak values at the end of the first (1st) hot dwell load step, followed by a corresponding sharp drop at the end of the 2nd hot dwell load step. Furthermore, relatively higher amplitudes in change in ACED were observed for SnPb solder interconnects across all the thermal cycles at the end of the second hot dwell temperature load step. Subsequently, the profiles (from 2013, 2014 and TRA (SnPb) thermal cycles) showed approximately linear trends from the third thermal cycle onwards. On the other hand, the damage profiles from the 2012 thermal cycles exhibited non-linearity in the damage profiles for the two types of

CHAPTER SEVEN: EFFECTS OF TEMPERATURE RAMPS AND DWELLS ON DAMAGE OF SOLDERED INTERCONNECTIONS

interconnections after the 2nd hot dwell. The damage profile TRA(Pb-free) assumed a steady decline from the second hot dwell load step up to the end of the 3rd hot dwell load step, followed by a steady rise up to the end of the 12th thermal cycle. The damage profiles at temperature ramps are discussed in the next sub-section.

7.3.3.4 Damage Profile at Heating (Ramp Up) load step

The ramp-up load steps displayed in Figure 7-11 generated relatively higher change in ACED per cycle within the Pb-free interconnects than in the SnPb interconnections. This is in sharp contrast with the cold dwell load steps where the damage profiles exhibited relatively higher change in ACED within the SnPb interconnections. Within the Pb-free interconnections, the damage profiles from all four thermal cycles (2012, 2013, 2014 and TRA) exhibited a sharp increase in ACED at the end of the first load step. Subsequently the damage profile experience a gradual drop in amplitude for up to the 4th thermal cycle. However, a steady increase in ACED was observed for the TRA and 2012 thermal cycle whilst marginal declines were observed for the 2013 and 2014 thermal cycles.

**CHAPTER SEVEN: EFFECTS OF TEMPERATURE RAMPS AND DWELLS
ON DAMAGE OF SOLDERED INTERCONNECTIONS**

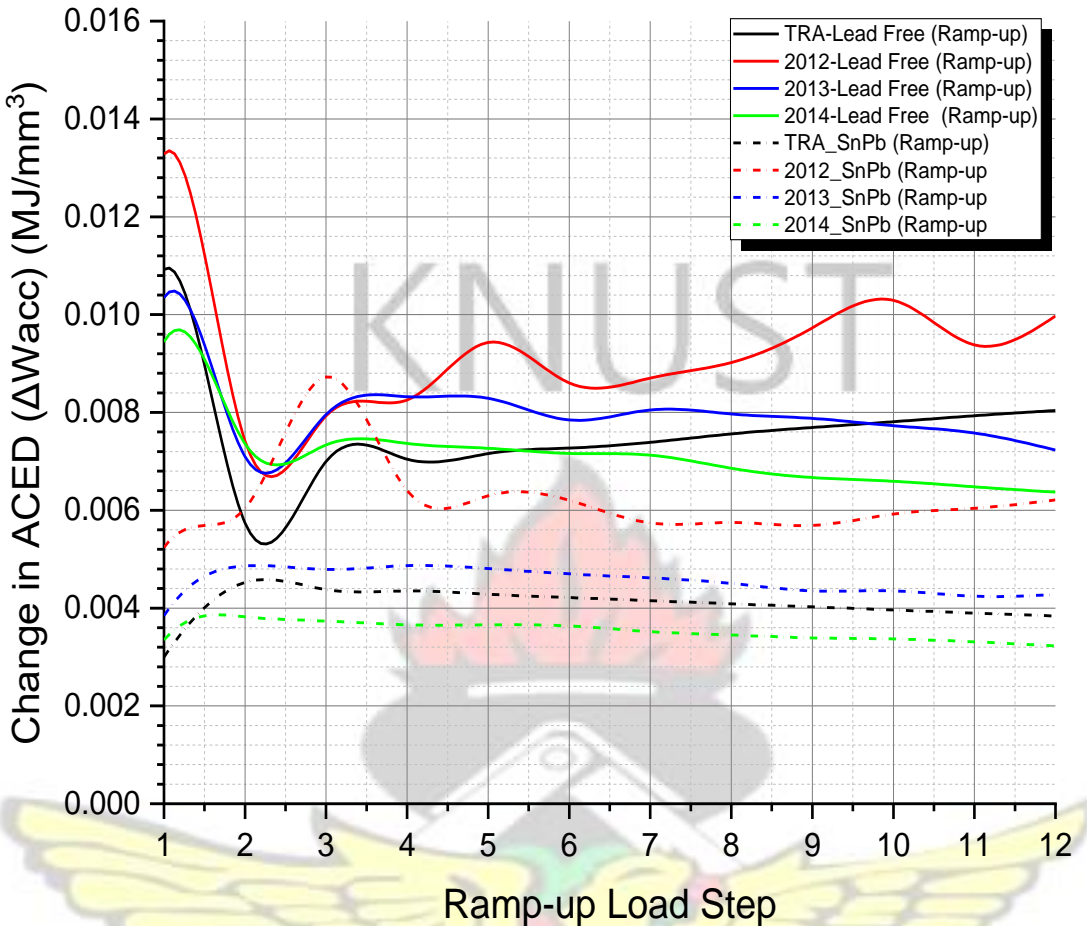


Figure 7-11: Damage Accumulation from Ramp-up load step

On the other hand, within the SnPb interconnections, the change in ACED per cycle remained constant after a steady rise to the 2nd ramp-up load step across the 2013, 2014 and TRA thermal cycles. More so, the damage profile in SnPb interconnection from the 2012 thermal cycle appear to trend closely with the profile from the Pb-free interconnection.

CHAPTER SEVEN: EFFECTS OF TEMPERATURE RAMPS AND DWELLS ON DAMAGE OF SOLDERED INTERCONNECTIONS

7.3.3.5 Damage Profile at Cooling Ramp Down load step

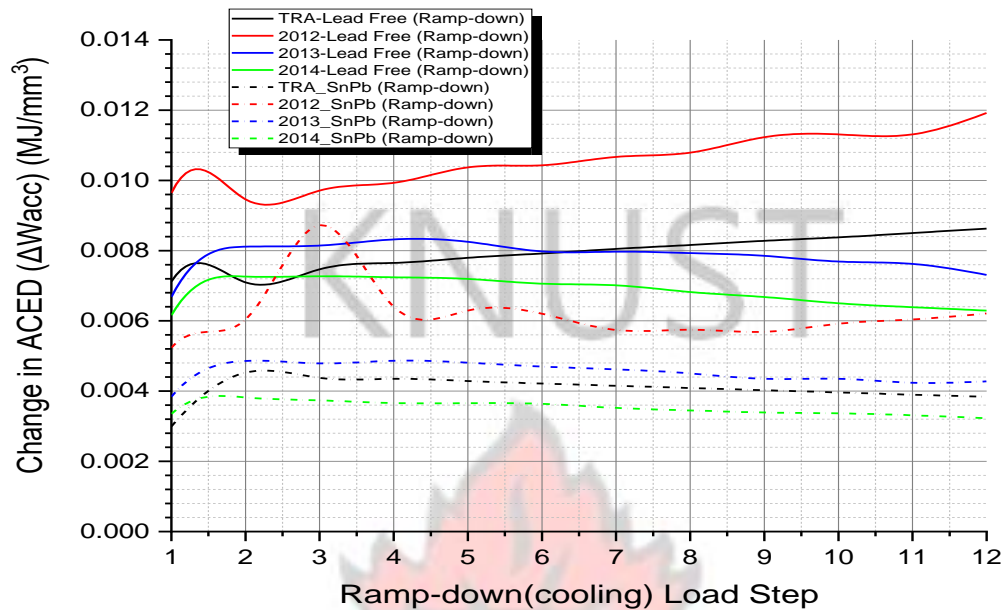


Figure 7-12: Damage Accumulation from Ramp-up load step

The damage profiles resulting from ramp-down Load steps displayed in Figure 7-12 showed more linearity across the 12 load steps compared with the damage profiles at the ramp-up load steps. The change in ACED in both Pb-free and SnPb interconnections from 2013 and 2014 thermal cycles showed a steady rise up to the 2nd load step. Subsequently, they assumed marginal decline up to the 12th ramp-down load step. The TRA thermal cycle imposed a similar damage profile in the SnPb interconnection. On the other hand, the damage profile in the Pb-free interconnection from the TRA and 2012 thermal cycles showed a sharp rise up to peak values at mid-way into the 2nd ramp-down load step. Subsequently, the change in ACED drops at the end of the 2nd ramp-down load step, followed by a steady rise up to the end of the 12th thermal cycle from the TRA and 2012 thermal cycles. In the next section, a damage function from summation of ACED from the various load steps is generated to predict the life of interconnections from ACED damage under thermal cycling.

CHAPTER SEVEN: EFFECTS OF TEMPERATURE RAMP AND DWELLS ON DAMAGE OF SOLDERED INTERCONNECTIONS

7.3.4 Generating Accumulated Creep Damage Functions for Soldered Joint Life Prediction

In this section the damage profiles from change in ACED from the five different load steps in each cycle are predicted as functions of the respective load steps using polynomial and logarithmic functions to approximate the trend lines from data points generated by the FEA results.

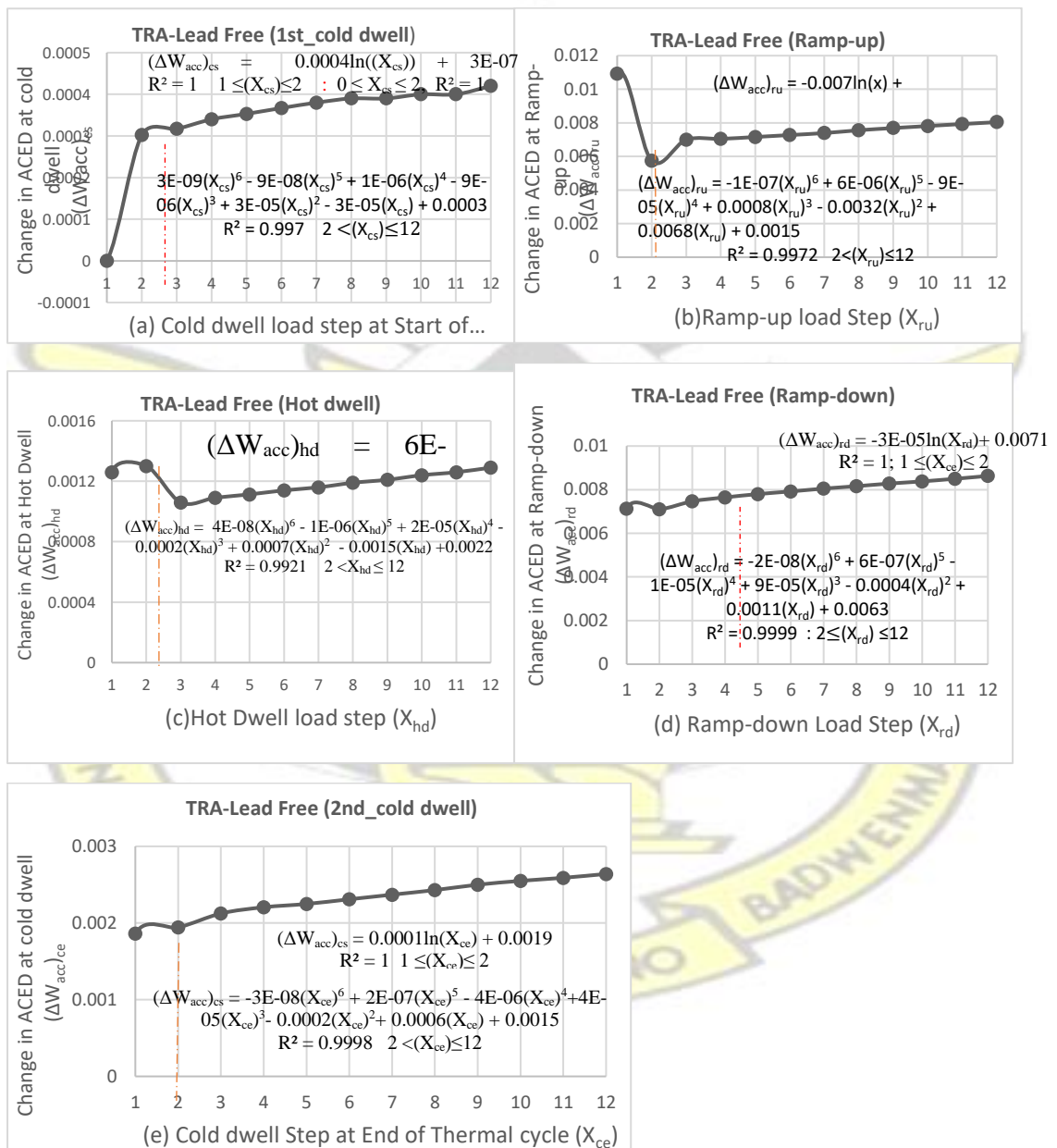


Figure 7 - 13: Change in ACED in Pb-free solder (a) 1St Cold Dwell (b) Ramp-up (c) Hot Dwell(d) Ramp-down (e) 2nd Cold Dwell

CHAPTER SEVEN: EFFECTS OF TEMPERATURE RAMPS AND DWELLS ON DAMAGE OF SOLDERED INTERCONNECTIONS

The TRA thermal cycle is used as the representative thermal cycle to generate the functions for the solder joint life prediction. Figures 7-13 and 7-14 display the damage profiles together with their respective functions for prediction.

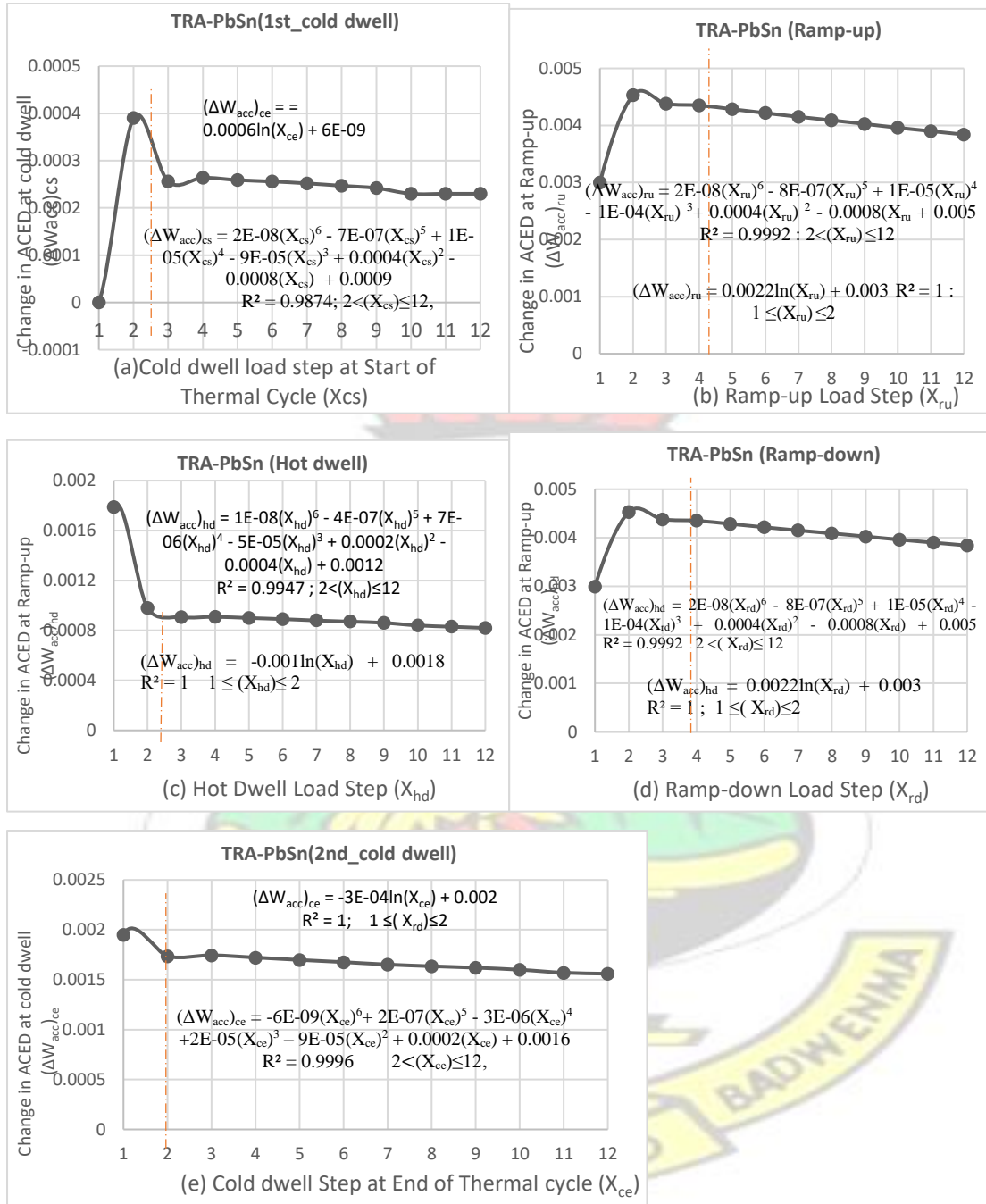


Figure 7 - 14: Change in ACED in PbSn Solder (a)1st cold Dwell (b) Ramp-up (c) Hot Dwell (d) Ramp-down (e) 2nd Cold Dwell

CHAPTER SEVEN: EFFECTS OF TEMPERATURE RAMPS AND DWELLS ON DAMAGE OF SOLDERED INTERCONNECTIONS

It was also observed that all the damage profiles approximated logarithmic functions at the second dwell/ramp load step. Beyond the second dwell/ramp load step the ACED profiles approximated six-order polynomial functions. Results from the regression analysis show that all the logarithmic functions provided perfect fit to each data set with a co-efficient of determination value of one ($R^2 = 1$). The six-order functions also provided nearly perfect fits to the data sets with ($R^2=0.9874$) being the widest spread.

In general, the trends from the change in ACED profiles can be predicted by a step function as:

$$(\Delta W_{acc})_{ij} = \begin{cases} f_1(X_{ij}) & 1 \leq X_{ij} \leq 2 \\ f_2(X_{ij}) & 2 < X_{ij} \leq 12 \end{cases} \quad (7.1)$$

Where the subscripts 'ij' denote the damage corresponding to a particular load step.

The following variables can be defined to correspond to the dwell/ramp load steps:

X_{cs} - cold dwell load step at start of each thermal cycle (1st cold dwell)

X_{ce} - cold dwell load step at the end of each thermal cycle (2nd cold dwell)

X_{ru} - load steps from temperature ramp-ups

X_{rd} - load steps from temperature ramp-downs

X_{hd} - load steps from hot dwell

$(\Delta W_{acc})_{cs}$ - change in ACED from 1st cold dwell

$(\Delta W_{acc})_{ce}$ - change in ACED from 2nd cold dwell

$(\Delta W_{acc})_{ru}$ - change in ACED from temperature ramp-ups

$(\Delta W_{acc})_{rd}$ - change in ACED from temperature ramp-downs

$(\Delta W_{acc})_{hd}$ - change in ACED from hot dwells

**CHAPTER SEVEN: EFFECTS OF TEMPERATURE RAMPS AND DWELLS
ON DAMAGE OF SOLDERED INTERCONNECTIONS**

7.3.4.1 Damage Functions for Pb-free Soldered Interconnections

The damage functions displayed on Figures 7-13 and 7-14 can be written as:

$$(\Delta W_{acc})_{cs}|_{Pb-free} = \begin{cases} 0.0004 \ln(X_{cs}) + 3E - 7 & 1 \leq X_{cs} \leq 2 \\ 3E - 09(X_{cs})^6 - 9E - 08(X_{cs})^5 + 1E - 06(X_{cs})^4 - 9E - 06(X_{cs})^3 \\ + 3E - 05(X_{cs})^2 - 3E - 05(X_{cs}) + 0.0003 & 2 < X_{cs} \leq 12 \end{cases} \quad (7.2)$$

$$(\Delta W_{acc})_{ru}|_{Pb-free} = \begin{cases} -0.0071 \ln(X_{ru}) + 0.0109 & 1 \leq X_{ru} \leq 2 \\ -1E - 07(X_{ru})^6 + 6E - 06(X_{ru})^5 - 9E - 05(X_{ru})^4 \\ + 0.0008(X_{ru})^3 - 0.0032(X_{ru})^2 + 0.0068(X_{ru}) + 0.0015 & 2 < X_{ru} \leq 12 \end{cases} \quad (7.3)$$

$$(\Delta W_{acc})_{hd}|_{Pb-free} = \begin{cases} 6E - 05 \ln(X_{hd}) + 0.0013 & 1 \leq X_{hd} \leq 2 \\ 4E - 08(X_{hd})^6 - 1E - 06(X_{hd})^5 + 2E - 05(X_{hd})^4 \\ - 0.0002(X_{hd})^3 + 0.0007(X_{hd})^2 - 0.0015(X_{hd}) + 0.0022 & 2 < X_{hd} \leq 12 \end{cases} \quad (7.4)$$

$$(\Delta W_{acc})_{rd}|_{Pb-free} = \begin{cases} -3E - 05 \ln(X_{rd}) + 0.007 & 1 \leq X_{rd} \leq 2 \\ -2E - 08(X_{rd})^6 + 6E - 07(X_{rd})^5 - 1E - 05(X_{rd})^4 \\ + 9E - 05(X_{rd})^3 - 0.0004(X_{rd})^2 + 0.0011(X_{rd}) + 0.0063 & 1 \leq X_{rd} \leq 12 \end{cases} \quad (7.5)$$

$$(\Delta W_{acc})_{ce}|_{Pb-free} = \begin{cases} 0.0001 \ln(X_{ce}) + 0.0019 & 1 \leq X_{hd} \leq 2 \\ -3E - 08(X_{ce})^6 + 2E - 07(X_{ce})^5 - 4E - 06(X_{ce})^4 \\ + 4E - 05(X_{ce})^3 - 0.0002(X_{ce})^2 + 0.0006(X_{ce}) + 0.0015 & 2 < X_{hd} \leq 12 \end{cases} \quad (7.6)$$

**CHAPTER SEVEN: EFFECTS OF TEMPERATURE RAMPs AND DWELLS
ON DAMAGE OF SOLDERED INTERCONNECTIONS**

7.2.4.2 Damage Functions for PbSn Interconnections

$$\begin{aligned}
 & (\Delta W_{acc})_{cs}|_{SnPb} \\
 & = \begin{cases} 0.0006\ln(X_{cs}) + 6E - 09 & 1 \leq X_{cs} \leq 2 \\ 2E - 08(X_{cs})^6 - 7E - 07(X_{cs})^5 + 1E - 05(X_{cs})^4 \\ -9E - 05(X_{cs})^3 + 0.0004(X_{cs})^2 - 0.0008(X_{cs}) + 0.0009 & 2 < X_{cs} \leq 12 \end{cases} \quad (7.7)
 \end{aligned}$$

$$\begin{aligned}
 & (\Delta W_{acc})_{ru}|_{SnPb} \\
 & = \begin{cases} 0.0022\ln(X_{ru}) + 0.003 & 1 \leq X_{ru} \leq 2 \\ 2E - 08(X_{ru})^6 - 8E - 07(X_{ru})^5 + 1E - 5(X_{ru})^4 \\ -1E - 04(X_{ru})^3 + 0.0004(X_{ru})^2 - 0.0008(X_{ru}) + 0.005 & 2 < X_{ru} \leq 12 \end{cases} \quad (7.8)
 \end{aligned}$$

$$\begin{aligned}
 & (\Delta W_{acc})_{hd}|_{SnPb} \\
 & = \begin{cases} -0.001\ln(X_{hd}) + 0.0018 & 0 \leq X_{hd} \leq 2 \\ 1E - 08(X_{hd})^6 - 4E - 07(X_{hd})^5 + 7E - 06(X_{hd})^4 \\ -5E - 05(X_{hd})^3 + 0.0002(X_{hd})^2 - 0.0004(X_{hd}) + 0.0012 & 2 < X_{hd} \leq 12 \end{cases} \quad (7.9)
 \end{aligned}$$

$$\begin{aligned}
 & (\Delta W_{acc})_{rd}|_{SnPb} \\
 & = \begin{cases} 0.0022\ln(X_{rd}) + 0.003 & 0 \leq X_{rd} \leq 2 \\ 2E - 08(X_{rd})^6 - 8E - 07(X_{rd})^5 + 1E - 05(X_{rd})^4 \\ -1E - 04(X_{rd})^3 + 0.0004(X_{rd})^2 - 0.0008(X_{rd}) + 0.005 & 2 < X_{rd} \leq 12 \end{cases} \quad (7.10)
 \end{aligned}$$

$$\begin{aligned}
 & (\Delta W_{acc})_{ce}|_{SnPb} \\
 & = \begin{cases} -3E - 04\ln(X_{cs}) + 0.002 & 1 \leq X_{cs} \leq 2 \\ -6E - 09(X_{cs})^6 + 2E - 07(X_{cs})^5 - 3E - 06(X_{cs})^4 + 2E - 05(X_{cs})^3 \\ -9E - 05(X_{cs})^2 - 0.0002(X_{cs}) + 0.0016 & 2 < X_{cs} \leq 12 \end{cases} \quad (7.11)
 \end{aligned}$$

Subsequently, the ACED over the 12 thermal cycles is written as:

$$\sum_1^{12} (\Delta W_{acc}) = \sum_1^{12} [(\Delta W_{acc})_{cs} + (\Delta W_{acc})_{ru} + (\Delta W_{acc})_{hd} + (\Delta W_{acc})_{rd} + (\Delta W_{acc})_{ce}]$$

**CHAPTER SEVEN: EFFECTS OF TEMPERATURE RAMPS AND DWELLS
ON DAMAGE OF SOLDERED INTERCONNECTIONS**

$$= \sum_1^{12} \left[[(\Delta W_{acc})_{cs} + (\Delta W_{acc})_{ce}]_{cold\ dwells} + [(\Delta W_{acc})_{ru} + (\Delta W_{acc})_{rd}]_{temp.\ ramps} \right] + [(\Delta W_{acc})_{hd}]_{hot\ dwell} \quad (7.12)$$

The temperature dwells and ramps occur at equal time steps (time intervals) respectively. Thus, the damage prediction functions can be simplified by representing the load steps for the temperature dwells and ramps with single variables as:

$$X_{cs} = X_{ce} = X$$

$$X_{ru} = X_{rd} = Y$$

$$X_{hd} = Z$$

The prediction functions are combined and simplified in sub-sections 7.3.4.3 and 7.3.4.4.

7.3.4.3 Damage in Pb-free Interconnections

$(\Delta W_{acc})_{cold\ dwells|Pb-free}$

$$= \begin{cases} 0.0005 \ln(X) + 0.0019 & 1 \leq X \leq 2 \\ -2.7E - 08(X)^6 + 1.1E - 07(X)^5 - 3E - 06(X)^4 + 3.9E - 05(X)^3 \\ -1.7E - 04(X)^2 + 5.7E - 04(X) + 0.0018 & 2 < X \leq 12 \end{cases} \quad (7.13)$$

$(\Delta W_{acc})_{ramps|Pb-free}$

$$= \begin{cases} -7.13E - 03 \ln(X_{rd}) + 0.0179 & 1 \leq X_{rd} \leq 2 \\ -1.2E - 07(X_{rd})^6 + 6.6E - 07(X_{rd})^5 - 1E - 04(X_{rd})^4 + 8.9E - 04(X_{rd})^3 \\ -0.003(X_{rd})^2 + 0.0079(X_{rd}) + 0.0078 & 1 \leq X_{rd} \leq 12 \end{cases} \quad (7.14)$$

**CHAPTER SEVEN: EFFECTS OF TEMPERATURE RAMPs AND DWELLS
ON DAMAGE OF SOLDERED INTERCONNECTIONS**

$$= \begin{cases} 6E - 05\ln(Z) + 0.0013 & 1 \leq Z \leq 2 \\ 4E - 08(Z)^6 - 1E - 06(Z)^5 + 2E - 05(Z)^4 - 0.0002(Z)^3 \\ + 0.0007(Z)^2 - 0.0015(Z) + 0.0022 & 2 < Z \leq 12 \end{cases} \quad (7.15)$$

7.3.4.4 Damage in Pb-Sn Interconnections

$(\Delta W_{acc})_{cold\ dwells|_{SnPb}}$

$$= \begin{cases} 0.0003\ln(X) + 0.002 & 1 \leq X \leq 2 \\ 1.4E - 08(X)^6 - 5E - 07(X)^5 + 7E - 06(X)^4 - 7E - 05(X)^3 \\ + 0.00031(X)^2 - 0.001(X) + 0.0025 & 2 < X \leq 12 \end{cases} \quad (7.16)$$

$(\Delta W_{acc})_{ramps|_{SnPb}}$

$$= \begin{cases} 0.0044\ln(Y) + 0.006 & 1 \leq Y \leq 2 \\ 4E - 08(Y)^6 - 16E - 07(Y)^5 + 2E - 05(Y)^4 + 7.29E - 04(Y)^3 \\ + 0.0008(Y)^2 - 0.0016(Y) + 0.01 & 2 < Y \leq 12 \end{cases} \quad (7.17)$$

$(\Delta W_{acc})_{hot\ dwells|_{SnPb}}$

$$= \begin{cases} -0.001\ln(Z) + 0.0018 & 1 \leq Z \leq 2 \\ 1E - 08(Z)^6 - 4E - 07(Z)^5 + 7E - 06(Z)^4 \\ - 5E - 05(Z)^3 + 0.0002(Z)^2 - 0.0004(Z) + 0.0012 & 2 < Z \leq 12 \end{cases} \quad (7.18)$$

A further simplification of the damage prediction functions is achieved by substituting the different variables for dwells and ramps with a single variable 'L_s' such that:

$$X=Y=Z= L_s;$$

Where L_s is defined as the number of thermal load steps involved in generating ACED damage profile. Thus, the total ACED function over the 12 cycles is given as;

Pb-free solder interconnection:

**CHAPTER SEVEN: EFFECTS OF TEMPERATURE RAMPES AND DWELLS
ON DAMAGE OF SOLDERED INTERCONNECTIONS**

$(\Delta W_{acc})_{total} |_{Pb-free}$

$$= \begin{cases} -0.00657 \ln(L_s) + 0.00211 & 1 \leq L_s \leq 2 \\ -1.07E - 07(L_s)^6 + 5.71E - 06(L_s)^5 - 8.3E - 05(L_s)^4 \\ -0.0002(L_s)^3 - 0.00307(L_s)^2 + 0.00697(L_s) + 0.0118 & 2 < L_s \leq 12 \end{cases} \quad (7.19)$$

SnPb solder interconnection:

$(\Delta W_{acc})_{total} |_{SnPb}$

$$= \begin{cases} 0.0037 \ln(L_s) + 0.0098 & 1 \leq L_s \leq 2 \\ 6.4E - 08(L_s)^6 - 2.5E - 06(L_s)^5 + 3.4E - 05(L_s)^4 \\ -3.2E - 04(L_s)^3 + 0.00131(L_s)^2 - 0.003(L_s) + 0.0137 & 2 < L_s \leq 12 \end{cases} \quad (7.20)$$

The above equations (7.19 & 7.20) are used as damage prediction functions to estimate the ACED per cycle (W_{acc}) in the solder interconnections for the test region. From equation 6.2 in chapter six (6) we have:

$$W_{acc} = \frac{\sum_{1}^{12} \Delta W_{acc}}{12} \quad (6.2)$$

Thus, W_{acc} is computed by summing up the step functions generated within the limits of the thermal cycle number as:

$W_{acc} |_{Pb-free}$

$$= \sum_{L_s=1}^2 [-0.00657 \ln(L_s) + 0.00211] + \sum_{L_s=3}^{12} [-1.07E - 07(L_s)^6 + 5.71E - 06(L_s)^5 - 8.3E - 05(L_s)^4 - 0.0002(L_s)^3 - 0.00307(L_s)^2 + 0.00697(L_s) + 0.0118] \quad (7.21)$$

$W_{acc} |_{SnPb}$

$$= \sum_{L_s=1}^2 [0.0037 \ln(L_s) + 0.0098] + \sum_{L_s=3}^{12} [6.4E - 08(L_s)^6 - 2.5E - 06(L_s)^5 + 3.4E - 05(L_s)^4 - 3.2E - 04(L_s)^3 + 0.00131(L_s)^2 - 0.003(L_s) + 0.0137] \quad (7.22)$$

CHAPTER SEVEN: EFFECTS OF TEMPERATURE RAMPS AND DWELLS ON DAMAGE OF SOLDERED INTERCONNECTIONS

Thus, equations 7.21 and 7.22 can be used to predict the total damage from ACED in both Pb-free and SnPb interconnections in c-Si photovoltaic cells installed at the test site for any proposed number of thermal cycles. Subsequently, the expected life (number of cycles to failure) of the soldered interconnection from the estimated thermal cycles can be computed. This is useful since the FEA simulation from less number of thermal cycles generate several gigabits of data, which require huge computing storage on a hard drive.

7.4 Summary

In this study, the damage distribution from FEA of c-Si solar cell interconnections from thermal cycling loads generated by real-time outdoor weathering of PV modules were analysed. The results show that the ramp-down (cooling) load steps generated the highest damage in the solder interconnections. This is followed closely by the ramp-up load steps. Overall, the two load steps accounted for average values of 78% and 88% of the total damage per cycle in the SnPb and Pb-free solder interconnections respectively. It was observed further that, the 1st cold dwell load steps generated the lowest change in ACED in the interconnections.

A study of the damage profiles from the five different load steps in each thermal cycle showed that, the first two thermal cycles can be predicted using logarithmic functions and the remaining ten thermal cycles predicted using six-order polynomial functions. Finally, ACED functions were generated to predict the creep damage in both Pb-free and SnPb solder interconnections from the test site. The damage functions provide useful relations for the prediction of the life (number of cycles to failure) of interconnections from the temperature load cycles at the test site. This study when repeated for other locations could generate the damage functions for the location.

**CHAPTER SEVEN: EFFECTS OF TEMPERATURE RAMPS AND DWELLS
ON DAMAGE OF SOLDERED INTERCONNECTIONS**

KNUST



CHAPTER 8- CONCLUSIONS AND RECOMMENDATIONS FOR FURTHER WORK

8.1 Conclusions

A numerical study on the reliability of soldered interconnections of C-Si solar cells has been conducted. The Study utilized a three-year data (2012 – 2014) from outdoor weathering of PV modules to generate temperature cycle profiles to serve as thermal loads and boundary conditions for the investigation of the thermo-mechanical response of the soldered interconnections when subjected to real outdoor conditions. The appropriate constitutive models of constituent materials forming a typical solar cell were utilized to generate accurate material responses to evaluate the damage from the thermal cycles. The conclusions from this study are summarised as follows:

- i. Analysis of the data on temperature variation and thermally induced stresses demonstrates that the region has a profile with a ramp rate of $8.996\text{ }^{\circ}\text{C}/\text{hr}$, a hot dwell time of 228 minutes, a cold dwell time of 369 minutes. Maximum and minimum module temperatures of $58.9\text{ }^{\circ}\text{C}$ and $23.7\text{ }^{\circ}\text{C}$, respectively; and a cycle time of 86400 s.
- ii. Comparison with the IEC 61215 standards for terrestrial PV modules qualification revealed percentage changes of - 91 %, 2180 %, 3590 %, 747 % for the ramp rate, dwell (hot and cold) and cycle times, respectively. The generated in-situ temperature cycle profile is predicted to qualify accurately c-Si PV modules operating in the sub-Saharan African test site.
- iii. Results from the numerical study showed that the constitutive behaviour of the encapsulant has a significant impact on equivalent von-Mises stress and

CHAPTER 8- CONCLUSIONS AND RECOMMENDATIONS FOR FURTHER WORK

maximum principal strains on the encapsulant. In addition, the constitutive behaviour of the encapsulant influenced the creep strain on interconnecting solder and total deformation of the cell interconnections (copper ribbon, Silver fingers, solder). From simulation results, the LVMM of the EVA produced the most consistent response to thermo-mechanical damage from the TRA thermal cycle.

- iv. The damage response from accumulated creep energy density shows that more than six thermal cycles are required to accurately predict the damage in the interconnections by the respective thermal cycle profiles.
- v. Subsequently, results from the life prediction show that the solder interconnections will achieve the maximum life (cycles/years) under the 2014 thermal cycle loading. The SnPb solder interconnection is expected to achieve 14,153 cycles (25.85 years) whilst the Pb-free solder interconnect is expected to achieve 9249 cycles (16.89 years). Additionally, with the TRA cycle, the Pb-free and SnPb solder interconnections are expected to achieve 7944 cycles (13.69 years) and 12814 cycles (23.4 years) respectively. The study showed that SnPb solder interconnections are likely to exhibit superior reliability over the Pb-free solder interconnections in the sub-Saharan Africa test region.
- vi. The study on damage accumulation over the load steps showed that the ramp-down (cooling) load steps remained the most critical load step in the thermal cycling of solder interconnections in SPV modules. This is followed closely by the ramp-up load steps. Overall, the two load steps accounted for average values of 78% and 88% of the total damage per cycle in the SnPb and Pb-free solder

CHAPTER 8- CONCLUSIONS AND RECOMMENDATIONS FOR FURTHER WORK

interconnections respectively. On the other hand, the 1st cold dwell load steps remain the least critical load step for damage accumulation in thermal cycling of SPV cell interconnections.

- vii. Furthermore, the study on damage accumulation profiles over the load steps from solder interconnections in SPV modules installed in the test region showed that, up to the first load step, the damage profile can be predicted using a logarithmic function whilst the remaining cycles can be predicted by a six-order polynomial function.

8.2 Recommendations for Further Work

With reference to the findings from this study, the following recommendations are proposed:

- i. The systematic technique employed in this study to generate the in-situ temperature cycle profile would be useful to the thermo-mechanical reliability research community. It is therefore recommended that photovoltaic design and manufacturing engineers harness the information to create a climate-specific robust c-Si PV module.
- ii. Results from the FE modeling provide new knowledge which may be harnessed to improve the reliability and increase the mean-time-to-failure of the PV modules operating in the region.
- iii. Overall, the LVMM of EVA offers a more stable material response for the study of the encapsulant constitutive behaviour in the thermo-mechanical analysis of c-Si SPVM. It is recommended that the Linear Viscoelastic Material Model

CHAPTER 8- CONCLUSIONS AND RECOMMENDATIONS FOR FURTHER WORK

(LVMM) is used as a material model for predicting the behaviour of encapsulant (EVA) in c-Si solar cells.

- iv. The damage functions provide useful relations for the prediction of the life (number of cycles to failure) of interconnections from the temperature load cycles at the test site. This study when repeated for other locations could generate the damage functions for each location.



REFERENCE

- Akay, H., Zhang, H. & Paydar, N. 1997. Experimental correlations of an energy-based fatigue life prediction method for solder joints. *Advances in Electronic Packaging, ASME-EEP*, 19, 1567-1574.
- Alam, M., Chan, Y. & Hung, K. 2002. Reliability study of the electroless Ni–P layer against solder alloy. *Microelectronics Reliability*, 42, 1065-1073.
- Almeida, R. H., Narvarte, L. & Lorenzo, E. 2018. PV arrays with delta structures for constant irradiance daily profiles. *Solar Energy*, 171, 23-30.
- Amagai, M. 1999. Chip Scale Package (CSP) solder joint reliability and modeling. *Microelectronics Reliability*, 39, 463-477.
- Amalu, E. H. & Ekere, N. 2012a. Damage of lead-free solder joints in flip chip assemblies subjected to high-temperature thermal cycling. *Computational Materials Science*, 65, 470-484.
- Amalu, E. H. & Ekere, N. N. 2012b. High temperature reliability of lead-free solder joints in a flip chip assembly. *Journal of Materials Processing Technology*, 212, 471-483.
- Amalu, E. H. & Ekere, N. N. 2016. Modelling evaluation of Garofalo-Arrhenius creep relation for lead-free solder joints in surface mount electronic component assemblies. *Journal of Manufacturing Systems*, 39, 9-23.
- Amalu, E. H., Hughes, D. J., Nabhani, F. & Winter, J. 2018. Thermo-mechanical deformation degradation of crystalline silicon photovoltaic (c-Si PV) module in operation. *Engineering Failure Analysis*, 84, 229-246.
- Ametektest Accessed: 2017 January 10. <http://www.ametektest.com/learningzone/testtypes/peel-strength-testing>.
- Andrei, C., Hoge, I. & Dobrescu, V. 1982 Photodegradation and photostabilization of the ethylene-vinyl acetate copolymers. *Proc. IUPAC, 28th Macromol. Symp.*, 329.
- Anguera, E. & Estrada, C. A. 2018. A new approach for evaluating flux uniformity for dense array concentrator photovoltaic cells. *Solar Energy*, 171, 330-342.
- Arangú, A. V., Ponce-Alcántara, S. & Sánchez, G., 2014. Optical characterization of backsheets to improve the power of photovoltaic modules. *Proceedings of the 8th International Photovoltaic Power Generation Conference and Exhibition, SNEC, Shanghai, China.*, 20-22.
- Armstrong, S. & Hurley, W. 2010. A thermal model for photovoltaic panels under varying atmospheric conditions. *Applied Thermal Engineering*, 30, 1488-1495.
- Assmus, M., Jack, S., Weiss, K. A. & Koehl, M. 2011. Measurement and simulation of vibrations of PV-modules induced by dynamic mechanical loads. *Progress in Photovoltaics: Research and Applications*, 19, 688-694.
- Baccouch, C., Sakli, H., Bouchouicha, D. & Aguilu, T. 2016 Patch antenna based on a photovoltaic solar cell grid collection. *Progress in Electromagnetic Research Symposium (PIERS)*,. IEEE, 164-165.
- Badiee, A., Ashcroft, I. & Wildman, R. D. 2016. The thermo-mechanical degradation of ethylene vinyl acetate used as a solar panel adhesive and encapsulant. *International Journal of Adhesion and Adhesives*, 68, 212-218.

REFERENCE

- Balaska, A., Tahri, A., Tahri, F. & Stambouli, A. B. 2017. Performance assessment of five different photovoltaic module technologies under outdoor conditions in Algeria. *Renewable Energy*, 107, 53-60.
- Bath, J., Sethuraman, S., Zhou, X., Willie, D., Hyland, K., Newman, K., Hu, L., Love, D., Reynolds, H. & Kochi, K. 2005. Reliability evaluation of lead-free SnAgCu PBGA676 components using tin-lead and lead-free SnAgCu solder paste. *Proceedings of SMTAI*, 891-901.
- Beaucarne, G. 2016. Materials challenge for shingled cells interconnection. *Energy Procedia*, 98, 115-124.
- Behnken, H., Apel, M. & Franke, D. 2003. Simulation of mechanical stress during bending tests for crystalline wafers. *Photovoltaic Energy Conversion, 2003. Proceedings of 3rd World Conference on*, IEEE, 1308-1311.
- Bennett, I. G. B., Olson, C. & Goris, M. 2013. Compatibility of copper-electroplated cells with metal wrap-through module materials. *Photovolt Int.*
- Bergenthal, J. 1995. Reflow Soldering Process Considerations for Surface Mount Application. pgs 2-3.
- Biancardo, M., Taira, K., Kogo, N., Kikuchi, H., Kumagai, N., Kuratani, N., Inagawa, I., Imoto, S. & Nakata, J. 2007. Characterization of microspherical semi-transparent solar cells and modules. *Solar Energy*, 81, 711-716.
- Bingting, H., Jiemin, Z., Ping, Z. & Ying, Y. 2006. The effect of accelerated thermal cycle parameters and the geometry dimensions on solder joint reliability. *Conference on High Density Microsystem Design and Packaging and Component Failure Analysis, 2006. HDP'06., 27-28 June 2006.* 242-246.
- Blieske, U., Doege, T., Gayout, P., Neander, M., Neumann, D. & Prat, A. 2003. Light-trapping in solar modules using extra-white textured glass. *Photovoltaic Energy Conversion, Proceedings of 3rd World Conference on, 2003.* IEEE, 188-191.
- Bone, V., Pidgeon, J., Kearney, M. & Veeraragavan, A. 2018. Intra-hour direct normal irradiance forecasting through adaptive clear-sky modelling and cloud tracking. *Solar Energy*, 159, 852-867.
- Bordihn, S., Mertens, V., Cieslak, J., Zimmermann, G., Lantzsich, R., Scharf, J., Geißler, S., Hörnlein, S., Neuber, M. & Laube, S. 2016. Status of industrial back junction n-type Si solar cell development. *Energy Procedia*, 92, 678-683.
- Borri, C., Gagliardi, M. & Paggi, M. 2018. Fatigue crack growth in Silicon solar cells and the hysteretic behaviour of busbars. *Solar Energy Materials and Solar Cells*, 181, 21-29.
- Bosco, N. & Kurtz, S. 2010. Quantifying the Weather: an analysis for thermal fatigue. *Proceedings of the PV Module Reliability Workshop, Golden, CO,*
- Bouarroudj, M., Khatir, Z., Ousten, J.-P. & Lefebvre, S. 2008. Temperature-level effect on solder lifetime during thermal cycling of power modules. *IEEE Transactions on device and materials reliability*, 8, 471-477.
- Bower, A. F. 2009. *Applied mechanics of solids*, CRC press.
- Boyd, R. H. & Pant, P. K. 1991. Molecular packing and diffusion in polyisobutylene. *Macromolecules*, 24, 6325-6331.
- Brady, G. S., Clauser, H. R. & Vaccari, J. A. 1956. *Materials handbook*, McGraw-hill.

REFERENCE

- Braun, S., Hahn, G., Nissler, R., Pönisch, C. & Habermann, D. 2013. Multi-busbar solar cells and modules: high efficiencies and low silver consumption. *Energy Procedia*, 38, 334-339.
- Brueckner, R. 1991. Glasses and Amorphous Materials. *Materials Science and Technology: A Comprehensive Treatment, Vol. 9.* Wiley-VCH.
- Buck, T., Kopecek, R., Libal, J., Petres, R., Peter, K., Rover, I., Wambach, K., Geerligs, L. J., Wefringhaus, E. & Fath, P. 2006. Large Area Screen Printed N-Type MC-SI Solar cells With B-Emitter: Efficiencies Close to 15% and Innovative Module Interconnection. Photovoltaic Energy Conversion, Conference Record of the 2006 IEEE 4th World Conference on, May 2006. 1060-1063.
- Bultman Jh, W. A., Brieko, M.w., Hoornstra, J. & Burgers, Ar, Dijkstra, 2012. Pin-up module: a design for higher efficiency, easy module manufacturing, and attractive appearance.
- Bultman, J. H., Brieko, M. W., Burgers, A. R., Hoornstra, J., Tip, A. C. & Weeber, A. W. 2001. Interconnection through vias for improved efficiency and easy module manufacturing of crystalline silicon solar cells. *Solar Energy Materials and Solar Cells*, 65, 339-345.
- Bultman, J., Eikelboom, D., Kinderman, R., Tip, A., Weeber, A., Meuwissen, M., Van Den Nieuwenhof, M., Michiels, P., Schoofs, C. & Schuurmans, F. 2002. Selecting optimal interconnection methodology for easy and cost-efficient manufacturing of the pin-up module. Proceedings of the PV In Europe—From PV Technology to Energy Solutions, Rome, 761-764.
- Bultman, J., Weeber, A., Brieko, M., Hoornstra, J., Burgers, A., Dijkstra, J., Tip, A. & Schuurmans, F., 2000. Pin up module: a design for higher efficiency, easy module manufacturing, and attractive appearance. Proceedings of the 16th EPVSC, Glasgow, 1210-1213.
- Cañete, C., Carretero, J. & Sidrach-De-Cardona, M. 2014. Energy performance of different photovoltaic module technologies under outdoor conditions. *Energy*, 65, 295-302.
- Chaboche, J.-L. & Rousselier, G. 1983. On the plastic and viscoplastic constitutive equations—Part II: application of internal variable concepts to the 316 stainless steel. *Journal of Pressure Vessel Technology*, 105, 159-164.
- Chan, Y., So, A. C. & Lai, J. 1998. Growth kinetic studies of Cu–Sn intermetallic compound and its effect on shear strength of LCCC SMT solder joints. *Materials Science and Engineering: B*, 55, 5-13.
- Chaturvedi, P., Hoex, B. & Walsh, T. M. 2013. Broken metal fingers in silicon wafer solar cells and PV modules. *Solar Energy Materials and Solar Cells*, 108, 78-81.
- Che, F. & Pang, J. H. 2013. Fatigue reliability analysis of Sn–Ag–Cu solder joints subject to thermal cycling. *IEEE Transactions on Device and Materials Reliability*, 13, 36-49.
- Chen, C.-H., Lin, F.-M., Hu, H.-T. And Yeh, F.-Y. 2008 Residual stress and bow analysis for silicon solar cell induced by soldering. International symposium on solar cell technologies, 4-6 December., Taipei, Taiwan, pp.1-3.
- Chen, X., Church, K., Yang, H., Cooper, I. B. & Rohatgi, A., 2011. Improved front side metallization for silicon solar cells by direct printing. Photovoltaic Specialists Conference (PVSC), 2011 37th IEEE, 2011. IEEE, 003667-003671.
- Cheng, Z., Wang, G., Chen, L., Wilde, J. & Becker, K. 2000. Viscoplastic Anand model for solder alloys and its application. *Soldering & Surface Mount Technology*, 12, 31-36.

REFERENCE

- Choi, W. K., Jang, S.-Y., Kim, J. H., Paik, K.-W. & Lee, H. M. 2002. Grain morphology of intermetallic compounds at solder joints. *Journal of materials research*, 17, 597-599.
- Classe, F. C. & Sitaraman, S. K. 2003 Asymmetric accelerated thermal cycles: An alternative approach to accelerated reliability assessment of microelectronic packages. *Electronics Packaging Technology*, 2003 5th Conference (EPTC 2003),. IEEE, 81-89.
- Clech, J.-P. 2005 Acceleration factors and thermal cycling test efficiency for lead-free Sn-Ag-Cu assemblies. *Proceedings, SMTA international conference, Chicago, IL*, 902-917.
- Commission, I. E. 2005. Crystalline silicon terrestrial photovoltaic (PV) modules—design qualification and type approval. *International Standard IEC*, 61215, 04.
- Corporation, D. C. 2013. Accessed: 2017 January 14. Electrically Conductive Adhesives. https://www.dowcorning.com/content/solar/solarproducts/Electrically_Conductive_Adhesives.aspx.
- Cuddalorepatta, G., Dasgupta, A., Sealing, S., Moyer, J., Tolliver, T. & Loman, J. Durability of Pb-Free solder connection between copper interconnect wire and crystalline silicon solar cells. *Thermal and Thermomechanical Phenomena in Electronics Systems*, 2006. IThERM '06. The Tenth Intersociety Conference on, May 30 2006-June 2 2006 2006. 1232-1239.
- Cuddalorepatta, G., Dasgupta, A., Sealing, S., Moyer, J., Tolliver, T. & Loman, J. 2010. Durability of Pb-free solder between copper interconnect and silicon in photovoltaic cells. *Progress in Photovoltaics: Research and Applications*, 18, 168-182.
- Cuddihy, E., Coulbert, C., Gupta, A. & Liang, R. 1986. Electricity from photovoltaic solar cells: flat-plate solar array project final report. Volume VII: Module encapsulation.
- Cuddihy, E., Coulbert, C., Liang, R., Gupta, A., Willis, P. & Baum, B. 1983. Applications of ethylene vinyl acetate as an encapsulation material for terrestrial photovoltaic modules.
- Darveaux, R. & Banerji, K. 1992. Constitutive relations for tin-based solder joints. *IEEE Transactions on Components, Hybrids, and Manufacturing Technology*, 15, 1013-1024.
- Davis, K. O., Rodgers, M. P., Scardera, G., Brooker, R. P., Seigneur, H., Mohajeri, N., Dhare, N. G., Wohlgemuth, J., Schneller, E., Shiradkar, N., Rudack, A. C. & Schoenfeld, W. V. 2016. Manufacturing metrology for c-Si module reliability and durability Part II: Cell manufacturing. *Renewable and Sustainable Energy Reviews*, 59, 225-252.
- De Jong, P. C., Eikelboom, D., Wienke, J., Brieko, M. & Kloos, M. Low-stress interconnections for solar cells. Presented at the 20th European Photovoltaic Solar Energy Conference and Exhibition, 2005. 10.
- De Jong, P., Eikelboom, D., Kinderman, R., Tip, A., Bultman, J., Meuwissen, M. & Van Den Nieuwenhof, M. 2004. Single-step laminated full-size PV modules made with back-contacted mc-Si cells and conductive adhesives. *19th EPVSEC, Paris*, 2145.
- Deenapanray, P. N., Athukorala, C., Macdonald, D., Jellett, W., Franklin, E., Everett, V., Weber, K. & Blakers, A. 2006. Reactive ion etching of dielectrics and silicon for photovoltaic applications. *Progress in Photovoltaics: Research and Applications*, 14, 603-614.
- Deng, X., Koopman, M., Chawla, N. & Chawla, K. K. 2004. Young's modulus of (Cu, Ag)-Sn intermetallics measured by nanoindentation. *Materials Science and Engineering: A*, 364, 240-243.

REFERENCE

- Deng, X., Piotrowski, G., Williams, J. & Chawla, N. 2003. Influence of initial morphology and thickness of Cu₆Sn₅ and Cu₃Sn intermetallics on growth and evolution during thermal aging of Sn-Ag solder/Cu joints. *Journal of electronic materials*, 32, 1403-1413.
- Deng, X., Sidhu, R., Johnson, P. & Chawla, N. 2005. Influence of reflow and thermal aging on the shear strength and fracture behavior of Sn-3.5 Ag solder/Cu joints. *Metallurgical and materials transactions A*, 36, 55-64.
- Deplanque, S., Nuchter, W., Spraul, M., Wunderie, B., Dudek, R. & Michel, B. Relevance of primary creep in thermo-mechanical cycling for life-time prediction in Sn-based solders. EuroSimE 2005. Proceedings of the 6th International Conference on Thermal, Mechanical and Multi-Physics Simulation and Experiments in Micro-Electronics and Micro-Systems, 2005., 18-20 April 2005 2005. 71-78.
- Di Paola, M., Pinnola, F. P. & Zingales, M. 2013. A discrete mechanical model of fractional hereditary materials. *Meccanica*, 48, 1573-1586.
- Di Paola, M., Pirrotta, A. & Valenza, A. 2011. Visco-elastic behavior through fractional calculus: an easier method for best fitting experimental results. *Mechanics of materials*, 43, 799-806.
- Dietrich, S., Pander, M., Sander, M., Schulze, S. H. & Ebert, M. Mechanical and thermomechanical assessment of encapsulated solar cells by finite-element-simulation. 2010. 77730F-77730F-10.
- Dumbleton, A. F. Z. D. P. 2012. *Photovoltaic Module Weather Durability & Reliability Testing* [Online]. Solar Energy Competence Center, Atlas Material Testing Technology LLC, IL USA. Available: http://solar durability.com/filestore/186/atlas25plus_whitepaper_final30.pdf [Accessed 03/07 2016].
- Dusek, M., Wickham, M. & Hunt, C. 2005. The impact of thermal cycling regime on the shear strength of lead-free solder joints. *Soldering & surface mount technology*, 17, 22-31.
- Dutta, I. 2003. A constitutive model for creep of lead-free solders undergoing strain-enhanced microstructural coarsening: A first report. *Journal of Electronic Materials*, 32, 201-207.
- Ehrenstein, G. 1999. „Polymerwerkstoffe: Struktur. Eigenschaften, Anwendung“, Hanser, München, Wien, 73-85.
- Eikelboom, D., Bultman, J., Schönecker, A., Meuwissen, M., Van Den Nieuwenhof, M. & Meier, D. Conductive adhesives for low-stress interconnection of thin back-contact solar cells. Photovoltaic Specialists Conference, 2002. Conference Record of the Twenty-Ninth IEEE, 2002. IEEE, 403-406.
- Eitner, U. & Rendler, L. 2014. Peel Testing of Ribbons on Solar Cells at Different Angles: Consistent Comparison by Using Adhesive Fracture Energies. *Proc. of the 29th EUPVSEC, Amsterdam*, 3406-3408.
- Eitner, U. 2011. *Thermomechanics of photovoltaic modules*. Dr.-Ing., Martin-Luther-Universität Halle-Wittenberg.
- Eitner, U., Altermatt, P. P., Kontges, M., Meyer, R. & Brendel, R. 2008. A modeling approach to the optimization of interconnects for back contact cells by thermomechanical simulations of photovoltaic modules. 23rd European Photovoltaic Solar Energy Conference (EU PVSEC), Valencia, Spain, September 1-5.
- Eitner, U., Kajari-Schröder, S., Köntges, M. & Altenbach, H. 2011. *Thermal Stress and Strain of Solar Cells in Photovoltaic Modules*.

REFERENCE

- Eitner, U., Kajari-Schröder, S., Köntges, M. & Altenbach, H. 2011a. Thermal stress and strain of solar cells in photovoltaic modules. *Shell-like Structures*, 453-468.
- Eitner, U., Kajari-Schroder, S., Kontges, M. & Brendel, R. 2010. Non-linear mechanical properties of ethylene-vinyl acetate (EVA) and its relevance to thermomechanics of photovoltaic modules. 25th European Photovoltaic Solar Energy Conference (EU PVSEC), Valencia, Spain, September, 6-10.
- Eitner, U., Köntges, M. & Brendel, R. 2009. Measuring thermomechanical displacements of solar cells in laminates using digital image correlation. Photovoltaic Specialists Conference (PVSC), 34th IEEE, 2009. IEEE, 001280-001284.
- Eitner, U., Pander, M., Kajari-Schröder, S., Köntges, M. & Altenbach, H. 2011b. Thermomechanics of PV modules including the viscoelasticity of EVA. 26th European Photovoltaic Solar Energy Conference and Exhibition, Hamberg, Germany, 3267-3269.
- Elibol, E., Özmen, Ö. T., Tutkun, N. & Köysal, O. 2017. Outdoor performance analysis of different PV panel types. *Renewable and Sustainable Energy Reviews*, 67, 651-661.
- Emanuel, N. N. M. & Buchachenko, A. L. 1987. *Chemical physics of polymer degradation and stabilization*, VSP.
- Faes, A., Levrat, M. D., J. J. Champlaud, A. Lachowicz, J. Geissbühler, N. Badel, H. Watanabe, T., Söderström, Y. Y., J. Ufheil, P. Papet, B. Strahm, J. Hermans, A. Tomasi, Y. Baumgartner, J. Cattin, M. & Kiaee, A. H.-W., J. Fleischer, P.V. Fleischer, A. Tsuno, C. Ballifs, 2016. Advanced metallization enabled by smart-wire interconnection for silicone heterojunction cell, Presentation at 6th Workshop on Metallization and Interconnection for Crystalline Silicon Solar Cells., *Energy Procedia*, 98, 2-11.
- Faes, A., Despeisse, M., Levrat, J., Champlaud, J., Badel, N., Kiaee, M., Söderström, T., Yao, Y., Grischke, R. & Gragert, M. 2014. SmartWire solar cell interconnection technology. Proc. 29th Eur. Photovoltaic Sol. Energy Conf, 2555-2561.
- Fields, R.J. S. R. L. *Mechanical Properties of Solder* [Online]. Available: http://www.metallurgy.nist.gov/mechanical_properties/solderpaper.html. [Accessed: 2017 January 17.].
- Franklin, E., Blakers, A., Weber, K., Everett, V. & Deenapanray, P. 2006. Towards a Simplified 20% Efficient Sliver Cell. Photovoltaic Energy Conversion, Conference Record of the 2006 IEEE 4th World Conference on, May 2006. 980-983.
- Gabor, A. M., Ralli, M., Montminy, S., Alegria, L., Bordonaro, C., Woods, J., Felton, L., Davis, M., Atchley, B. & Williams, T. 2006. Soldering induced damage to thin Si solar cells and detection of cracked cells in modules. 21st European Photovoltaic Solar Energy Conference, Dresden, Germany, September. 4-8.
- Gee, J. M., Schubert, W. K. & Basore, P. A. 1993. Emitter wrap-through solar cell. Photovoltaic Specialists Conference, Conference Record of the Twenty Third IEEE, 1993. IEEE, 265-270.
- Geipel, T., Moeller, M., Walter, J., Kraft, A. & Eitner, U. 2017. Intermetallic compounds in solar cell interconnections: Microstructure and growth kinetics. *Solar Energy Materials and Solar Cells*, 159, 370-388.
- Ghaffarian, R. 2001. Effect of thermal cycling ramp rate on CSP assembly reliability. Electronic Components and Technology Conference, 2001. Proceedings., 51st, IEEE, 1170-1174.

REFERENCE

- Glunz, S., Preu, R. & Biro, D. 2012. 16: Crystalline Silicon Solar Cells—State-of-the-Art and Future Developments. *Comprehensive renewable energy*, 1, 353-387.
- Gochermann, H. 1990. Apparatus for welding components together with the use of ultrasound. Google Patents.
- Gonzalez, M., Govaerts, J., Labie, R., De Wolf, I. & Baert, K. 2011. Thermo-mechanical challenges of advanced solar cell modules. Thermal, Mechanical, and Multi-Physics Simulation and Experiments in Microelectronics and Microsystems (EuroSimE), 12th International Conference on, 18-20 April 2011 2011. 1/7-7/7.
- Granek, F. & Reichel, C. 2010. Back-contact back-junction silicon solar cells under UV illumination. *Solar Energy Materials and Solar Cells*, 94, 1734-1740.
- Greenwood, J. 1988. Silicon in mechanical sensors. *Journal of Physics E: Scientific Instruments*, 21, 1114.
- Grossiord, N., Kroon, J. M., Andriessen, R. & Blom, P. W. 2012. Degradation mechanisms in organic photovoltaic devices. *Organic Electronics*, 13, 432-456.
- Grunow, P., Clemens, P., Hoffmann, V., Litzenburger, B. & Podlowski, L. 2005. Influence of micro cracks in multi-crystalline silicon solar cells on the reliability of PV modules. *Proceedings of the 20th EUPVSEC*, 2042-2047.
- Guo, J.-H. & Cotter, J. E. 2004. Laser-grooved backside contact solar cells with 680-mV open-circuit voltage. *IEEE Transactions on Electron Devices*, 51, 2186-2192.
- Gustafsson, G. 1998. Solder joint reliability of a lead-less RF-transistor. Electronic Components & Technology Conference, 48th IEEE, 1998. IEEE, 87-91.
- Guyenot, M., Peter, E., Zerrer, P., Kraemer, F. & Wiese, S. 2011. Enhancing the lifetime prediction methodology for photovoltaic modules based on electronic packaging experience. 2011 12th Intl. Conf. on Thermal, Mechanical & Multi-Physics Simulation and Experiments in Microelectronics and Microsystems, 18-20 April 2011 1/4-4/4.
- Hall, R. & Soltys, T. 1980. Polka dot solar cell. 14th Photovoltaic Specialists Conference, 550-553.
- Hasan, M. K. & Sasaki, K. 2016. Thermal deformation analysis of tabbed solar cells using solder alloy and conductive film. *Journal of Mechanical Science and Technology*, 30, 3085-3095.
- Hasan, O. & Arif, A. F. M. 2014. Performance and life prediction model for photovoltaic modules: Effect of encapsulant constitutive behavior. *Solar Energy Materials and Solar Cells*, 122, 75-87.
- Hasan, O., Arif, A. F. M. & Siddiqui, M. U. 2013. Finite Element Modeling, Analysis, and Life Prediction of Photovoltaic Modules. *Journal of Solar Energy Engineering*, 136, 021022-021022.
- Hendrichs, M., Thaidigsmann, B., Fellmeth, T., Nold, S., Spribille, A., Herrmann, P., Mittag, M., Hädrich, I., Eitner, U. & Clement, F. 2013. Cost-optimized metallization layout for metal wrap through (MWT) solar cells and modules. Proceedings of the 28th European photovoltaic solar energy conference and exhibition, Paris, 1524-1528.
- Herrmann, W., Bogdanski, N., Reil, F., Köhl, M., Weiss, K. A., Assmus, M. & Heck, M. PV 2010. module degradation caused by thermomechanical stress: real impacts of outdoor weathering versus accelerated testing in the laboratory. 77730I-77730I-9.
- Hoenig, R., Clement, F., Menkoe, M., Retzlaff, M., Biro, D., Preu, R., Neidert, M., Henning, A., Mohr, C. & Zhang, W. 2010. Paste development for screen printed mc-Si MWT

REFERENCE

- solar cells exceeding 17% efficiency. Photovoltaic Specialists Conference (PVSC), 2010 35th IEEE, IEEE, 003167-003172.
- Hongtao, M., Suhling, J. C., Lall, P. & Bozack, M. J. 2006. Reliability of the aging lead free solder joint. Electronic Components and Technology Conference, 2006. Proceedings. 56th, 0-0 0 16 pp.
- Hornbogen, E. & Warlimont, H. 2006. *Metalle*, Springer.
- Huang, C. K., Sun, K. W. & Chang, W. L. 2012. Efficiency enhancement of silicon solar cells using a nano-scale honeycomb broadband anti-reflection structure. *Optics Express*, 20, A85-A93.
- Hulstrom, R. 2005. Pv Module Reliability R & D Project Overview. United States. Department of Energy.
- I. Rogelj, P. Z., P. Eiselt, 2012. PV Ribbon design specification. *Overview of Product specification and Comparison of production processes*. China: SOLARCON.
- IBM. Available: <https://www.ibm.com/analytics/spss-statistics-software> [Accessed October 20th 2017].
- IEC 61215 1993. Crystalline silicon terrestrial PVmodules. *Design qualification and type approval*. Geneva, Switzerland: IEC.
- Ike, C. 2013. The effect of temperature on the performance of a photovoltaic solar system in Eastern Nigeria. *Res Inven: Int J Eng Sci*, 3, 10-14.
- Jamaly, M. & Kleissl, J. 2017. Spatiotemporal interpolation and forecast of irradiance data using Kriging. *Solar Energy*, 158, 407-423.
- Jamaly, M. & Kleissl, J. 2018. Robust cloud motion estimation by spatio-temporal correlation analysis of irradiance data. *Solar Energy*, 159, 306-317.
- Jellinek, H. H. G. 1989. *Degradation and stabilization of polymers: a series of comprehensive reviews*, Elsevier Science Ltd.
- Jeong, J.-S., Park, N. & Han, C. 2012. Field failure mechanism study of solder interconnection for crystalline silicon photovoltaic module. *Microelectronics Reliability*, 52, 2326-2330.
- Jones, D. R. & Ashby, M. F. 2011. *Engineering materials 1: An introduction to properties, applications and design*, Elsevier.
- Kajari-Schröder, S., Kunze, I., Eitner, U. & Köntges, M. 2011. Spatial and orientational distribution of cracks in crystalline photovoltaic modules generated by mechanical load tests. *Solar Energy Materials and Solar Cells*, 95, 3054-3059.
- Kankam, S. & Boon, E. K. 2009. Energy delivery and utilization for rural development: Lessons from Northern Ghana. *Energy for sustainable development*, 13, 212-218.
- Karekezi, S. 2002. Poverty and energy in Africa—a brief review. *Energy Policy*, 30, 915-919.
- Kemauor, F., Obeng, G. Y., Brew-Hammond, A. & Duker, A. 2011. A review of trends, policies and plans for increasing energy access in Ghana. *Renewable and sustainable energy reviews*, 15, 5143-5154.
- Kempe, M. D. 2006. Modeling of rates of moisture ingress into photovoltaic modules. *Solar Energy Materials and Solar Cells*, 90, 2720-2738.

REFERENCE

- Kempe, M., Dameron, A., Moricone, T. & Reese, M. 2010. Evaluation and modeling of edge-seal materials for photovoltaic applications. Photovoltaic Specialists Conference (PVSC), 35th IEEE, 2010. IEEE, 000256-000261.
- Kerschaver, E. V. & Beaucarne, G. 2006. Back-contact solar cells: a review. *Progress in Photovoltaics: Research and Applications*, 14, 107-123.
- Kiefer, F., Ulzhofer, C., Brendemuhl, T., Harder, N. P., Brendel, R., Mertens, V., Bordihn, S., Peters, C. & Muller, J. W. 2011. High Efficiency N-Type Emitter-Wrap-Through Silicon Solar Cells. *IEEE Journal of Photovoltaics*, 1, 49-53.
- Kilinski, T. J., Lesniak, J. R. & Sandor, B. I. 1991. Modern approaches to fatigue life prediction of SMT solder joints. *Solder joint reliability*. Springer.
- Kim, N. & Han, C. 2013. Experimental characterization and simulation of water vapor diffusion through various encapsulants used in PV modules. *Solar Energy Materials and Solar Cells*, 116, 68-75.
- Klengel, R., Petzold, M., Schade, D. & Sykes, B. 2011. Improved testing of soldered busbar interconnects on silicon solar cells. Microelectronics and Packaging Conference (EMPC), 18th European, 2011. IEEE, 1-5.
- Kluska, S. F., Hermle, G. M. & Glunz, S.W. 2008. Loss Analysis of High-Efficiency Back-Contact Back-Junction Silicon Solar Cells. 23rd European Photovoltaic Solar Energy Conference and Exhibition, 1-5 September 2008, Valencia, Spain 2CV.5.4 Spain. 1590 - 1595.
- Knecht, S. & Fox, L. 1991. Integrated matrix creep: application to accelerated testing and lifetime prediction. *Solder Joint Reliability*. Springer.
- Koch, S., Kupke, J., Tornow, D., Schoppa, M., Krauter, S. & Grunow, P. 2010. Dynamic mechanical load tests on crystalline silicon modules. 25th European Photovoltaic Solar Energy Conference–Valencia.
- Köhl, M., Weiss, K., Heck, M. & Philipp, D. 2009. PV reliability: Results of a German four-year joint project Part I: accelerated ageing tests and modelling of degradation. European Photovoltaic Solar Energy Conference and Exhibition, 24th.
- Kohn, C., Kübler, R., Krappitz, M., Kleer, G., Reis, I., Retzlaff, M., Erath, D. & Biro, D. Influence of the metallization process on the strength of silicon solar cells. 24th European Photovoltaic Solar Energy Conference, 2009. 25.
- Köntges, M., Kunze, I., Kajari-Schröder, S., Breitenmoser, X. & Bjørneklett, B. 2011. The risk of power loss in crystalline silicon based photovoltaic modules due to micro-cracks. *Solar Energy Materials and Solar Cells*, 95, 1131-1137.
- Kontges, M., Kurtz, S., Packard, C., Jahn, U., Berger, K., Kato, K., Friesen, T., Liu, H. & Van Iseghem, M. 2014. Performance and reliability of photovoltaic systems—subtask 3.2: review of failures of photovoltaic modules. *External final report by international energy agency (IEA) for photovoltaic power systems programme (PVPS)*.
- Köntges, M., Siebert, M., De La Dedicación Rodríguez, A., Denz, M., Wegner, M., Illing, R. & Wegert, F. 2013. Impact of transportation on silicon wafer-based PV modules. Proc. 28th Eur. Photovoltaic Sol. Energy Conf, 2960-2967.
- Kopecek, R., Buck, T., Kränzl, A., Libal, J., Peter, K., Schneider, A., Sánchez-Friera, P., Röver, I., Wambach, K. & Wefringhaus, E. 2006a. Module interconnection with alternate p- and n-type Si solar cells. *Proc. 21th EUPVSC Dresden Germany*.

REFERENCE

- Kopecek, R., Buck, T., Libal, J., Rover, I., Wambach, K., Geerligs, L. J., Sanchez-Friera, P., Alonso, J., Wefringhaus, E. & Fath, P. 2006b. Large Area Screen Printed N-Type Silicon Solar Cells with Rear Aluminium Emitter: Efficiencies Exceeding 16%. Photovoltaic Energy Conversion, Conference Record of the 2006 IEEE 4th World Conference on, May 2006 1044-1047.
- Kopecek, R., Libal, J., Buck, T., Peter, K., Wambach, K., Acciarri, M., Binetti, S., Geerligs, L. & Fath, P. 2005. N-type multicrystalline silicon: material for solar cell processes with high efficiency potential. Conference Record of the Thirty-first IEEE Photovoltaic Specialists Conference, 2005. IEEE, 1257-1260.
- Kraemer, F. W., S. 2014. FEM stress analysis of various solar module concepts under temperature cycling load. Thermal, mechanical and multi-physics simulation and experiments in microelectronics and microsystems (eurosime), 2014 15th international conference on, 7-9 April 2014 1-8.
- Kraemer, F., Wiese, S., Peter, E. & Seib, J. 2013. Mechanical problems of novel back contact solar modules. *Microelectronics Reliability*, 53, 1095-1100.
- Kray, D., Dicker, J., Rein, S., Kamerewerd, F., Osswald, D., Schäffer, E., Glunz, S. & Willeke, G. 2001. High-efficiency emitterwrap-through cells. *Proceedings of the 17th EPVSC, Munich*, 1299-1302.
- Kumar, S. & Jung, J. 2013. Mechanical and electronic properties of Ag₃Sn intermetallic compound in lead free solders using ab initio atomistic calculation. *Materials Science and Engineering: B*, 178, 10-21.
- Kumar, S. & Sarkan, B. 2013. Design for reliability with weibull analysis for photovoltaic modules. *Int. J. Curr. Eng. Technol*, 3, 129-134.
- Lamers, M., Tjengdrawira, C., Koppes, M., Bennett, I., Bende, E., Visser, T., Kossen, E., Brockholz, B., Mewe, A. & Romijn, I. 2012. 17.9% Metal-wrap-through mc-Si cells resulting in module efficiency of 17.0%. *Progress in Photovoltaics: Research and Applications*, 20, 62-73.
- Lau, J. & Dauksher, W., 2005. Effects of ramp-time on the thermal-fatigue life of SnAgCu lead-free solder joints. In *Electronic Components and Technology Conference* (Vol. 55, 2. 1292). IEEE; 1999.
- Lee, Y. & Tay, A. A. O. 2012. Finite Element Thermal Analysis of a Solar Photovoltaic Module. *Energy Procedia*, 15, 413-420.
- Leistiko, O. 1994. The waffle: a new photovoltaic diode geometry having high efficiency and backside contacts. Photovoltaic Energy Conversion, 1994., Conference Record of the Twenty Fourth. IEEE Photovoltaic Specialists Conference-1994, 1994 IEEE First World Conference on, IEEE, 1462-1465.
- Liang, J., Gollhardt, N., Lee, P., Heinrich, S. & Schroeder, S. 1997. An integrated fatigue life prediction methodology for optimum design and reliability assessment of solder interconnections. *Advances in electronic packaging*, 2, 1583-1592.
- Liang, M., Ren, S., Fan, W., Xin, X., Shi, J. & Luo, H. 2017. Rheological property and stability of polymer modified asphalt: Effect of various vinyl-acetate structures in EVA copolymers. *Construction and Building Materials*, 137, 367-380.
- Liu, J., Lai, Z., Kristiansen, H. & Khoo, C. 1998. Overview of conductive adhesive joining technology in electronics packaging applications. Adhesive Joining and Coating Technology in Electronics Manufacturing, 1998. Proceedings of 3rd international Conference on, IEEE, 1-18.

REFERENCE

- Lohmuller, E., Thaidigsmann, B., Pospischil, M., Jager, U., Mack, S., Specht, J., Nekarda, J., Retzlaff, M., Krieg, A. & Clement, F. 2011. 20% efficient passivated large-area metal wrap through solar cells on boron-doped Cz silicon. *IEEE Electron Device Letters*, 32, 1719-1721.
- Lundberg, J., Mooney, E. & Rogers, C. 1969. Diffusion and solubility of methane in polyisobutylene. *Journal of Polymer Science Part A-2: Polymer Physics*, 7, 947-962.
- Lyon, K., Salinger, G., Swenson, C. & White, G. 1977. Linear thermal expansion measurements on silicon from 6 to 340 K. *Journal of Applied Physics*, 48, 865-868.
- Ma, H., Suhling, J. C., Lall, P. & Bozack, M. J. Reliability of the aging lead free solder joint. 56th Electronic Components and Technology Conference 2006, 2006. IEEE, 16 pp.
- Macben, M., Nelson, Timonah, Mutua, Benedict, Ismael, Abisai 2015. Degradation Prevalence Study of Field-Aged Photovoltaic Modules Operating Under Kenyan Climatic Conditions *Science Journal of Energy Engineering* 3, 1-5.
- Manock, J., Coyle, R., Vaccaro, B., McCormick, H., Popowich, R., Fleming, D., Read, P., Osenbach, J. & Gerlach, D. 2007. Effect of temperature cycling parameters on the solder joint reliability of a Pb-free PBGA package. *Proceedings of SMTAI*, 564-573.
- McCormick, P. G. & Suehrcke, H. 2018. The effect of intermittent solar radiation on the performance of PV systems. *Solar Energy*, 171, 667-674.
- Mckellar, J. F. & Allen, N. S. 1979. *Photochemistry of man-made polymers*, Applied Science Publishers.
- Mei, Z. 1996. TSOP solder joint reliability. Electronic Components and Technology Conference, 1996. Proceedings., 46th, IEEE, 1232-1238.
- Mei, Z., Sunwoo, A. & Morris, J. 1992. Analysis of low-temperature intermetallic growth in copper-tin diffusion couples. *Metallurgical Transactions A*, 23, 857-864.
- Meier, R., Kraemer, F., Wiese, S., Wolter, K.-J. & Bagdahn, J. 2010. Reliability of copper-ribbons in photovoltaic modules under thermo-mechanical loading. Photovoltaic Specialists Conference (PVSC), 35th IEEE, 2010. IEEE, 001283-001288.
- Meydbray, Y., Wilson, K., Brambila, E., Terao, A. & Daroczi, S. 2007. Solder joint degradation in high efficiency all back contact solar cells. Proceedings of the 22th European Photovoltaic Solar Energy Conference, Milan, Italy, September, 3-7.
- Miao, H.-W. & Duh, J. G. 2001. Microstructure evolution in Sn–Bi and Sn–Bi–Cu solder joints under thermal aging. *Materials chemistry and physics*, 71, 255-271.
- Mickiewicz, R., Li, B., Doble, D., Christian, T., Lloyd, J., Stokes, A., Voelker, C., Winter, M., Ketola, B. & Norris, A. 2011. Effect of encapsulation modulus on the response of PV modules to mechanical stress. Proceedings of 26th European Photovoltaic Solar Energy Conference and Exhibition, Hamburg, 3157-3161.
- Mohamed, M., Hilali, B. & Ajeet Rohatgi, T. 2004. A Review and Understanding of Screen-Printed Contacts and Selective-Emitter Formation 14th Workshop on Crystalline Silicon Solar Cells and Modules, August 8-11 Winter Park, Colorado 1-11.
- Morgensen, P. E. Blieske, M., Neander, U. M., Toelle R. & Palm, J. 2004. Large area glass coating for thin film CIGS module production. In: Proceedings of the 19th European Photovoltaic Solar Energy Conference, Paris. pp. 1905–1908.
- Morita, K., Inoue, T., Kato, H., Tsuda, I. & Hishikawa, Y. 2003. Degradation factor analysis of crystalline-Si PV modules through long-term field exposure test. *Photovoltaic Energy*

REFERENCE

- Conversion, Proceedings of 3rd World Conference on, 18-18 May 2003. 1948-1951 Vol.2.
- Morlier, A., Haase, F. & M, K. 2015. Impact of Cracks in Multicrystalline Silicon Solar Cells on PV Module Power; A Simulation Study Based on Field Data. *IEEE Journal of Photovoltaics*, 5, 1735-1741.
- Morris, J., Tribula, D., Summers, T. & Grivas, D. 1991. The role of microstructure in thermal fatigue of Pb-Sn solder joints. *Solder Joint Reliability*. Springer.
- Moyer, J., Zhang, W., Kurtz, E., Tavares, R., Buzby, D. & Kleinbach, S. 2010. The role of silver contact paste on reliable connectivity systems. 25th European Photovoltaic Solar Energy Conference and Exhibition, Valencia, Spain,
- Musallam, M. & Johnson, C. M. 2012. An Efficient Implementation of the Rainflow Counting Algorithm for Life Consumption Estimation. *IEEE Transactions on Reliability*, 61, 978-986.
- Neander, M., Gromball, F., Neumann, D., Harder, N.-P. & Nositschka, W. A. 2006. Anti-reflective-coating tuned for higher solar module voltage. Photovoltaic Energy Conversion, Conference Record of the 2006 IEEE 4th World Conference on, IEEE, 2070-2072.
- Neuhaus, D.-H. & Münzer, A. 2008. Industrial silicon wafer solar cells. *Advances in OptoElectronics*, 2007.
- Nicht Auf Den Aufschwung, W. S. 2008. *Bildungschancen jetzt nutzen!*
- Niclas, D. W. 2016. *What is a solar busbar and how does it work* [Online]. Available: <http://sinovoltaics.com/technology/solar-cell-busbar-3bb-5bb-or-0bb/> [Accessed 24th April 2018].
- Nieland, S., Baehr, M., Boettger, A., Ostmann, A. & Reichl, H. 2007. Advantages of microelectronic packaging for low-temperature lead-free soldering of thin solar cells. 22nd European Photovoltaic Solar Energy Conference and Exhibition,
- Novotny, M., Jakubka, L., Cejtchaml, P. & Szendiuch, I. 2006. Thermomechanical stressing of solar cells. Thermal, Mechanical, and Multiphysics Simulation and Experiments in Micro-Electronics and Micro-Systems, 2006. EuroSime 2006. 7th International Conference on, 24-26 April 2006 1-4.
- Obeng, G. & Evers, H. D. 2010. Impacts of public solar PV electrification on rural micro-enterprises: The case of Ghana. *Energy for Sustainable Development*, 14, 223-231.
- Obeng, G. Y., Evers, H. D., Akuffo, F., Braimah, I. & Brew-Hammond, A. 2008. Solar photovoltaic electrification and rural energy-poverty in Ghana. *Energy for Sustainable Development*, 12, 43-54.
- Ogbomo, O. O., Amalu, E. H., Ekere, N. N. & Olagbegi, P. O. 2018. Effect of operating temperature on degradation of solder joints in crystalline silicon photovoltaic modules for improved reliability in hot climates. *Solar Energy*, 170, 682-693.
- Ogochukwu, E. S. 2013. Laser Soldering.
- Ojo, S. O. & Paggi, M. 2016. A thermo-visco-elastic shear-lag model for the prediction of residual stresses in photovoltaic modules after lamination. *Composite Structures*, 136, 481-492.

REFERENCE

- Owen-Bellini, M., Zhu, J., Betts, T. R. & Gottschalg, R. 2015. Environmental Stress Potentials of Different Climatic Regions. Proc. 31st European PV Solar Energy Conference, 1854-1857.
- Paggi, M. & Sapora, A. 2015. An accurate thermoviscoelastic rheological model for ethylene-vinyl acetate based on fractional calculus. *International Journal of Photoenergy*, 2015.
- Paggi, M., Kajari-Schröder, S. & Eitner, U. 2011. Thermomechanical deformations in photovoltaic laminates. *The Journal of Strain Analysis for Engineering Design*, 46, 772-782.
- Pan, N., Henshall, G., Billaut, F., Dai, S., Strum, M., Benedetto, E. & Rayner, J. 2005. An acceleration model for Sn-Ag-Cu solder joint reliability under various thermal cycle conditions. *Proceedings of SMTAI*, 876-883.
- Pan, T.Y. 1994. Critical accumulated strain energy (case) failure criterion for thermal cycling fatigue of solder joints. *Journal of Electronic Packaging*, 116, 163-170.
- Pang, H. 1997. Temperature cycling fatigue analysis of fine pitch solder joints. *Proc. of Interpack'97*, 2, 1495-1500.
- Pang, H., Tan, K., Shi, X. & Wang, Z. 2001a. Microstructure and intermetallic growth effects on shear and fatigue strength of solder joints subjected to thermal cycling aging. *Materials Science and Engineering: A*, 307, 42-50.
- Pang, J. H. L., Chong, D. Y. R. & Low, T. H. 2001b. Thermal cycling analysis of flip-chip solder joint reliability. *IEEE Transactions on Components and Packaging Technologies*, 24, 705-712.
- Pang, J. H., Low, T., Xiong, B. & Che, F. 2003. Design for reliability (DFR) methodology for electronic packaging assemblies. *Electronics Packaging Technology, 2003 5th Conference (EPTC 2003)*, IEEE, 470-478.
- Pang, J. H., Tan, T.-I. & Sitaraman, S. 1998. Thermo-mechanical analysis of solder joint fatigue and creep in a flip chip on board package subjected to temperature cycling loading. *Electronic Components & Technology Conference, 1998. 48th IEEE*, IEEE, 878-883.
- Park, N., Han, C. & Kim, D. 2013. Effect of moisture condensation on long-term reliability of crystalline silicon photovoltaic modules. *Microelectronics Reliability*, 53, 1922-1926.
- Park, N., Jeong, J. & Han, C. 2014. Estimation of the degradation rate of multi-crystalline silicon photovoltaic module under thermal cycling stress. *Microelectronics Reliability*, 54, 1562-1566.
- Peike, C., Hoffmann, S., Hülsmann, P., Thaidigsmann, B., Weiß, K. A., Koehl, M. & Bentz, P. 2013. Origin of damp-heat induced cell degradation. *Solar Energy Materials and Solar Cells*, 116, 49-54.
- Pingel, S., Zemen, Y., Frank, O., Geipel, T. & Berghold, J. 2009a. Mechanical stability of solar cells within solar panels. *Proc. of 24th EUPVSEC*, 3459-3464.
- Pingel, S., Zemen, Y., Frank, O., Geipel, T. & Berghold, J. 2009b. Mechanical stability of solar cells within solar panels. *Proceedings of the 24th EUPVSEC, WIP, Dresden, Germany*, 3459-3464.
- Pintat, T., Wellinger, K. & Gimmel, P. 2000. *Werkstofftabellen der Metalle. Auflage. Stuttgart: Alfred Kröner.*
- Popovich, V. A., Maris, M. P. F. H. L. V., Janssen, M., Bennett, I. J. & Richardson, I. M. 2013. Understanding the Properties of Silicon Solar Cells Aluminium Contact Layers and Its Effect on Mechanical Stability. *Materials Sciences and Applications*, Vol.04No.02, 10.

REFERENCE

- POREX. 2017. *Porous Plastics* [Online]. POREX. Available: <http://www.porex.com/technologies/materials/porous-plastics/ethyl-vinyl-acetate/> [Accessed 03/08/2017 2017].
- Prakash, K. & Sritharan, T. 2001. Interface reaction between copper and molten tin–lead solders. *Acta Materialia*, 49, 2481-2489.
- Pratt, R. E., Stromswold, E. I. & Quesnel, D. J. 1994. Mode I fracture toughness testing of eutectic Sn-Pb solder joints. *Journal of Electronic Materials*, 23, 375-381.
- Protsenko, P., Terlain, A., Traskine, V. & Eustathopoulos, N. 2001. The role of intermetallics in wetting in metallic systems. *Scripta Materialia*, 45, 1439-1445.
- PV Education Accessed: 2017 January 10. <http://www.pveducation.org/pvcdrom/design/metal-grid-pattern>.
- PV Education. 2013. *Single Crystalline Silicon* [Online]. Available: <http://www.pveducation.org/pvcdrom/manufacturing/single-crystalline-silicon> [Accessed 8/4/2017 2017].
- Qi, Y., Lam, R., Ghorbani, H. R., Snugovsky, P. & Spelt, J. K. 2006. Temperature profile effects in accelerated thermal cycling of SnPb and Pb-free solder joints. *Microelectronics Reliability*, 46, 574-588.
- Quansah, D. A. & Adaramola, M. S. 2018. Ageing and degradation in solar photovoltaic modules installed in northern Ghana. *Solar Energy*, 173, 834-847.
- Quintana, M. A., King, D. L., McMahon, T. J. & Osterwald, C. R. 2002. Commonly observed degradation in field-aged photovoltaic modules. Photovoltaic Specialists Conference, 2002. Conference Record of the Twenty-Ninth IEEE, 19-24 May 2002 1436-1439.
- Raga, A., & Carlson, K. 2011. Accessed: 2017 January 17. Selective Soldering by Laser. http://www.us-tech.com/Relld/.../selective_soldering_by_laser.htm.
- Reil, F., Sepanski, A., Herrmann, W., Althaus, J., Vaaßen, W. & Schmidt, H. 2012. Qualification of arcing risks in PV modules. Photovoltaic Specialists Conference (PVSC), 2012 38th IEEE, IEEE, 000727-000730.
- Ren21 2014. ECOWAS Renewable Energy and Energy Efficiency - Status Report. Paris: UNIDO.
- Roberts, R. 1981. Thermal expansion reference data: silicon 300-850 K. *Journal of Physics D: Applied Physics*, 14, L163.
- Roos, E., Maile, K. & Seidenfuß, M. 2017. *Werkstoffkunde für Ingenieure: Grundlagen, Anwendung, Prüfung*, Springer-Verlag.
- Rosenthal, A. L., Thomas, M. G. & Durand, S. J. 1993. A ten year review of performance of photovoltaic systems. Photovoltaic Specialists Conference, 1993., Conference Record of the Twenty Third IEEE, 10-14 May 1993 1289-1291.
- Rubin, L. & Schneider, A. 2007. Interconnection Technology for Conventional and Concentrator Modules (Solar Cells). LEOS -IEEE Lasers and Electro-Optics Society Annual Meeting Conference Proceedings.
- Saga, T. 2010. Advances in crystalline silicon solar cell technology for industrial mass production. *NPG Asia Materials*, 2, 96-102.
- Sahasrabudhe, S., Monroe, E., Tandon, S. & Patel, M. 2003. Understanding the effect of dwell time on fatigue life of packages using thermal shock and intrinsic material behavior.

REFERENCE

- 53rd Electronic Components and Technology Conference, Proceedings., 27-30 May 2003 2003. 898-904.
- Sangaj, N. S. & Malshe, V. 2004. Permeability of polymers in protective organic coatings. *Progress in Organic Coatings*, 50, 28-39.
- Sathyanarayana, P., Ballal, R., Ps, L. S. & Kumar, G. 2015. Effect of Shading on the Performance of Solar PV Panel. *Energy and Power*, 5, 1-4.
- Schmidhuber, H., Klappert, S., Stollhof, J., Erfurt, G., Eberspächer, M. & Preu, R. 2005. Laser soldering—a technology for better contacts. Proceedings of the 20th European photovoltaic solar energy conference, Barcelona, Spain, 1997-2000.
- Schmitt, F., Priessner, A., Kramer, B. & Gillner, A. 2008. Application report-Laser joining photovoltaic modules-With new laser sources and integrated process control systems, optimized thermal management of the interconnection process can be provided. *Industrial Laser Solutions for Manufacturing*, 23, 20.
- Schneller, E. J., Brooker, R. P., Shiradkar, N. S., Rodgers, M. P., Dhare, N. G., Davis, K. O., Seigneur, H. P., Mohajeri, N., Wohlgemuth, J., Scardera, G., Rudack, A. C. & Schoenfeld, W. V. 2016. Manufacturing metrology for c-Si module reliability and durability Part III: Module manufacturing. *Renewable and Sustainable Energy Reviews*, 59, 992-1016.
- Schonecker, A., Eikelboom, D., Manshanden, P., Goris, M., Wyers, P., Roberts, S., Bruton, T., Jooss, W., Faika, K. & Kress, A. 2002. Ace designs: the beauty of rear contact solar cells. Photovoltaic Specialists Conference, Conference Record of the Twenty-Ninth IEEE, 2002. IEEE, 106-109.
- Schubert, A., Dudek, R., Auerswald, E., Gollhardt, A., Michel, B. & Reichl, H. 2003. Fatigue life models for SnAgCu and SnPb solder joints evaluated by experiments and simulation. Electronic Components and Technology Conference, Proceedings. 53rd, 2003. IEEE, 603-610.
- Schubert, A., Dudek, R., Walter, H., Jung, E., Gollhardt, A., Michel, B. & Reichl, H. 2002. Reliability assessment of flip-chip assemblies with lead-free solder joints. 52nd Electronic Components and Technology Conference 2002. (Cat. No.02CH37345), 2002 1246-1255.
- Schulte-Huxel, H., Blankemeyer, S., Merkle, A., Steckenreiter, V., Kajari-Schröder, S. & Brendel, R. 2015. Interconnection of busbar-free back contacted solar cells by laser welding. *Progress in Photovoltaics: Research and Applications*, 23, 1057-1065.
- Shackelford, J. F., Han, Y. H., Kim, S. & Kwon, S. H. 2016. *CRC materials science and engineering handbook*, CRC press.
- Sharma, P. & Dasgupta, A. 2002. Micro-Mechanics of Creep-Fatigue Damage in PB-SN Solder Due to Thermal Cycling—Part II: Mechanistic Insights and Cyclic Durability Predictions From Monotonic Data. *Journal of Electronic Packaging*, 124, 298-304.
- Shioda, T. & Zenkoh, H. 2012. Influence of elastic modulus of encapsulant on solder bond failure of c-Si PV modules. Photovoltaic Module Reliability Workshop,
- Siewert, T. S. L., Smith, D.R. & Madeni J. C. 2002. Database for Solder Properties with Emphasis on New Lead-free Solders. February 11, 2002 ed. Colorado: National Institute of Standards and Technology & Colorado School of Mines.
- Sitaraman, S. K. & Kacker, K. 2005. Thermomechanical Reliability Prediction of Lead-Free Solder Interconnects. *Lead-Free Solder Interconnect Reliability*, 181.

REFERENCE

- Skoczek, A., Sample, T. & Dunlop, E. D. 2009. The results of performance measurements of field-aged crystalline silicon photovoltaic modules. *Progress in Photovoltaics: Research and Applications*, 17, 227-240.
- Song, W. J. R., Tippabhotla, S. K., Tay, A. A. O. & Budiman, A. S. 2018. Numerical Simulation of the Evolution of Stress in Solar Cells During the Entire Manufacturing Cycle of a Conventional Silicon Wafer Based Photovoltaic Laminate. *IEEE Journal of Photovoltaics*, 8, 210-217.
- Sørensen, B. & Watt, G. 2006. Trends in Photovoltaic Applications, Survey report of selected IEA countries between 1992 and 2005.
- Stolkarts, V., Moran, B. & Keer, L. 1998. Constitutive and damage model for solders. *Electronic Components & Technology Conference*, 1998. 48th IEEE, IEEE, 379-385.
- Syed, A. 1997. Factors affecting creep-fatigue interaction in eutectic Sn/Pb solder joints. *Advances in Electronic Packaging*. ASME.
- Syed, A. 2001. Predicting solder joint reliability for thermal, power, and bend cycle within 25% accuracy. 2001 Proceedings. 51st Electronic Components and Technology Conference (Cat. No.01CH37220), 2001 255-263.
- Syed, A. Accumulated creep strain and energy density based thermal fatigue life prediction models for SnAgCu solder joints. *Electronic Components and Technology Conference*, 2004. Proceedings. 54th, 2004. IEEE, 737-746.
- Syed, A. Limitations of Norris-Landzberg equation and application of damage accumulation based methodology for estimating acceleration factors for Pb free solders. *Thermal, Mechanical & Multi-Physics Simulation, and Experiments in Microelectronics and Microsystems (EuroSimE)*, 2010 11th International Conference on, 26-28 April 2010 2010. 1-11.
- Syed, A. R. Thermal fatigue reliability enhancement of plastic ball grid array (PBGA) packages. *Electronic Components and Technology Conference*, 1996. Proceedings., 46th, 1996. IEEE, 1211-1216.
- Syed, A. Updated Life Prediction Models for Solder Joints with Removal of Modeling Assumptions and Effect of Constitutive Equations. *Thermal, Mechanical and Multiphysics Simulation and Experiments in Micro-Electronics and Micro-Systems*, 2006. EuroSime 2006. 7th International Conference on, 24-26 April 2006 2006. 1-9.
- Syed, A., PANCZAK, T., DARVEAUX, R., LEE, S., LEE, C. & PARTRIDGE, J. 1999. Solder Joint Reliability of ChipArray BGA. *Journal of Surface Mount Technology*, 12, 1-7.
- Taira, K., Inagawa, I., Imoto, S. & Nakata, J. 2008. Proprietary Sphelar® technology for sustainable living in the 21ST century. *Proceedings of ECOpole*, 2, 141--146.
- Tang, H. & Basaran, C. 2003. A Damage Mechanics-Based Fatigue Life Prediction Model for Solder Joints. *Journal of Electronic Packaging*, 125, 120-125.
- Thaidigsmann, B., Greulich, J., Lohmüller, E., Schmeißer, S., Clement, F., Wolf, A., Biro, D. & Preu, R. 2012. Loss analysis and efficiency potential of p-type MWT-PERC solar cells. *Solar Energy Materials and Solar Cells*, 106, 89-94.
- The Engineering Toolbox* [Online]. Available: http://www.engineeringtoolbox.com/young-modulus-d_417.html [Accessed April 24th 2018].
- Tossa, A. K., Soro, Y., Thiaw, L., Azoumah, Y., Sicot, L., Yamegueu, D., Lishou, C., Coulibaly, Y. & Razongles, G. 2016. Energy performance of different silicon photovoltaic technologies under hot and harsh climate. *Energy*, 103, 261-270.

REFERENCE

- Tu, K. & Thompson, R. 1982. Kinetics of interfacial reaction in bimetallic Cu-Sn thin films. *Acta Metallurgica*, 30, 947-952.
- Walsh, T. M., Xiong, Z., Khoo, Y. S., Tay, A. A. & Aberle, A. G. 2012. Singapore modules-optimised PV modules for the tropics. *Energy Procedia*, 15, 388-395.
- Weber, K., Everett, V., Macdonald, J., Blakers, A. W., Deenapanray, P. & Babaei, J. 2004. Modelling of silver modules incorporating a lambertian rear reflector.
- Weeber, A. W., Kinderman, R., Tool, C. J. J., Granek, F. & Jong, P. C. D. How to achieve 17% cell efficiencies on large back-contacted mc-Si solar cells. Photovoltaic Energy Conversion, Conference Record of the 2006 IEEE 4th World Conference on, May 2006 2006. 1048-1051.
- Wendt, J., Träger, M., Mette, M., Pfennig, A. & Jäckel, B. 2009. The link between mechanical stress induced by soldering and micro damages in silicon solar cells. *Proc. of 24th EUPVSEC*, 3420-3423.
- Wenham, S. R., Green, M. A. & Watt, M. E. 1994. Applied Photovoltaics, Center for Photovoltaic Devices and Systems. *University of New South Wales, Sydney, Australia*.
- Wiese, S. & Wolter, K. J. 2004. Microstructure and creep behaviour of eutectic SnAg and SnAgCu solders. *Microelectronics Reliability*, 44, 1923-1931.
- Wiese, S., Kraemer, F., Betzl, N. & Wald, D. 2010a. Interconnection technologies for photovoltaic modules - analysis of technological and mechanical problems. 2010 11th International Thermal, Mechanical & Multi-Physics Simulation, and Experiments in Microelectronics and Microsystems (EuroSimE), 26-28 April 2010 1-6.
- Wiese, S., Meier, R. & Kraemer, F. 2010b. Mechanical behaviour and fatigue of copper ribbons used as solar cell interconnectors. Thermal, Mechanical & Multi-Physics Simulation, and Experiments in Microelectronics and Microsystems (EuroSimE), 2010 11th International Conference on, 26-28 April 2010 1-5.
- Wiese, S., Meier, R., Kraemer, F. & Bagdahn, J. 2009. Constitutive behaviour of copper ribbons used in solar cell assembly processes. Thermal, Mechanical and Multi-Physics simulation and Experiments in Microelectronics and Microsystems, 2009. EuroSimE 2009. 10th International Conference on, IEEE, 1-8.
- Wikipedia 2017. https://en.wikipedia.org/wiki/Reflow_soldering.
- Wilde, J., Becker, K., Thoben, M., Blum, W., Jupitz, T., Wang, G. & Cheng, Z. N. 2000. Rate dependent constitutive relations based on Anand model for 92.5 Pb5Sn2. 5Ag solder. *IEEE transactions on Advanced Packaging*, 23, 408-414.
- Willeke, G. P. & Weber, E. R. 2013. *Advances in photovoltaics*, Newnes.
- Williams, M. L., Landel, R. F. & Ferry, J. D. 1955. The temperature dependence of relaxation mechanisms in amorphous polymers and other glass-forming liquids. *Journal of the American Chemical society*, 77, 3701-3707.
- Wirth, H. 2010. Lasers in Wafer-based PV Module Production. *Laser Technik Journal*, 7, 36-38.
- Wu, S. X., Chin, J., Grigorich, T., Wu, X., Mui, G. & Yeh, C. P. 1998. Reliability analysis for fine pitch BGA package. Electronic Components & Technology Conference, 1998. 48th IEEE, IEEE, 737-741.

REFERENCE

- Wu, W. Q., Chen, D., Caruso, R. A. & Cheng, Y. B. 2017. Recent progress in hybrid perovskite solar cells based on n-type materials. *Journal of Materials Chemistry A*, 5, 10092-10109.
- Xu, H. & Jiang, X. 2017. Creep constitutive models for viscoelastic materials based on fractional derivatives. *Computers & Mathematics with Applications*, 73, 1377-1384.
- Xuejun, F., Rasier, G. & Vasudevan, V. S. 2005. Effects of Dwell Time and Ramp Rate on Lead-Free Solder Joints in FCBGA Packages. Proceedings Electronic Components and Technology, 2005. ECTC '05., 31 May-3 June 2005 901-906.
- Yeo, C., Mhaisalkar, S. & Pang, H. 1996. Solder joint reliability study of 256 Pin, 0.4 mm pitch, PQFP. Electronic Components and Technology Conference, Proceedings., 46th, 1996. IEEE, 1222-1231.
- Yoon, S., Chen, Z., Osterman, M., Han, B. & Dasgupta, A. 2005. Effect of Stress Relaxation on Board Level Reliability of Sn Based Pb-Free Solders. Proceedings Electronic Components and Technology, 2005. ECTC '05., May 31 2005-June 3 2005 1210-1214.
- Zarmai, M. T., Ekere, N. N., Oduoza, C. F. & Amalu, E. H. 2015a. Optimization of thermo-mechanical reliability of solder joints in crystalline silicon solar cell assembly. *Microelectronics Reliability*.
- Zarmai, M. T., Ekere, N. N., Oduoza, C. F. & Amalu, E. H. 2015b. A review of interconnection technologies for improved crystalline silicon solar cell photovoltaic module assembly. *Applied Energy*, 154, 173-182.
- Zemen, Y., Teusch, H., Kropke, G., Pingel, S. & Held, S. 2012. The Impact of Busbar Surface Topology and Solar Cells Soldering Process. Proceedings of 27th European Photovoltaic Solar Energy Conference and Exhibition. Frankfurt, Germany, 24-28.
- Zhai, C. J. & Blish, R. 2003. Board level solder reliability versus ramp rate and dwell time during temperature cycling. *IEEE transactions on device and materials reliability*, 3, 207-212.
- Zhai, C. J., Sidharth & Blish, R. 2003. Board level solder reliability versus ramp rate and dwell time during temperature cycling. *IEEE Transactions on Device and Materials Reliability*, 3, 207-212.
- Zhang, L., Han, J. G., He, C. W. & Guo, Y. H. 2013. Reliability behavior of lead-free solder joints in electronic components. *Journal of Materials Science: Materials in Electronics*, 24, 172-190.
- Zhang, L., Han, J.-G., Guo, Y. & He, C. W. 2014. Anand model and FEM analysis of SnAgCuZn lead-free solder joints in wafer level chip scale packaging devices. *Microelectronics Reliability*, 54, 281-286.
- Zhang, Q., Dasgupta, A. & Haswell, P. 2004. Partitioned viscoplastic-constitutive properties of the Pb-free Sn₃.9Ag₀.6Cu solder. *Journal of Electronic Materials*, 33, 1338-1349.
- Zhang, Y., Cai, Z., Suhling, J. C., Lall, P. & Bozack, M. J. 2008. The effects of aging temperature on SAC solder joint material behavior and reliability. 58th Electronic Components and Technology Conference, 2008. IEEE, 99-112.
- Zhao, J., Wang, A. & Campbell, P. 1999. A 19.8% efficient honeycomb multi-crystalline silicon solar cell with improved light trapping. *IEEE Transactions on Electron Devices*, 46, 1978-1983.

APPENDICES

APPENDIX A

RAINFLOW COUNTING ALGORITHM

USAGE:

To call the function in a script on array of turning points <array_ext>:

```
import rainflow as rf
array_out = rf.rainflow(array_ext)
```

DEPENDENCIES:

- Numpy

```
from random import choice
```

```
from threading import Thread
```

```
import numpy as np
```

```
class Valley(object):
```

```
    def __init__(self, value, index, sig):
```

```
        self.__value__ = value
```

```
        self.index = index
```

```
        self.__parent_signal__ = sig
```

```
        self.position = [value]
```

```
        self.index_of_position = [index]
```

```
        self.pos_dict = {index: value}
```

```
        self.terminate = False
```

```
@property
```

```
def value(self):
```

```
    return self.__value__
```

```
@property
```

```
def range(self):
```

```
    return round(abs(self.value - self.position[-1]), 1)
```

```
@property
```

```
def parent_signal(self):
```

APPENDICES

```
    return self.__parent_signal__
def plot(self, axes):
    print('Plotting Valley at index {}'.format(self.index))
    x = []
    y = []
    shapes = ['s', '^', '*', 'o', '.', 'v', '<', '>', '1', '2', '3', '4',
              '8', 'p', 'P', 'h', 'H', '+', 'x', 'X', 'D', 'd', '|', '_']
    colors = ['y', 'm', 'c', 'r', 'g', 'b', 'k']
    shape = choice(shapes)
    color = choice(colors)
    for i, index in enumerate(self.index_of_position):
        if self.position[i] != self.position[i-1] and i > 0:
            m = (self.parent_signal[index]-self.parent_signal[index - 1])
            c = self.parent_signal[index] - m*index
            y += [self.position[i-1]]
            x += [(y[-1] - c)/m]
            y += [self.position[i]]
            x += [(y[-1] - c)/m]
        else:
            x += [index]
            y += [self.position[i]]
    axes.plot(x, y, color)
    axes.plot(x[-1], y[-1], color + shape)
    axes.plot(x[0], y[0], color + shape)
class Peak(object):
    def __init__(self, value, index, sig):
        self.__value__ = value
        self.index = index
        self.__parent_signal__ = sig
        self.position = [value]
        self.index_of_position = [index]
        self.pos_dict = {index: value}
```

APPENDICES

```
self.terminate = False

@property
def value(self):
    return self.__value__

@property
def range(self):
    return round(abs(self.value - self.position[-1]), 1)

@property
def parent_signal(self):
    return self.__parent_signal__

def plot(self, axes):
    print('Plotting Peak at index {}'.format(self.index))
    x = []
    y = []
    shapes = ['s', '^', '*', 'o', '!', 'v', '<', '>', '1', '2', '3', '4',
              '8', 'p', 'P', 'h', 'H', '+', 'x', 'X', 'D', 'd', '|', '_']
    colors = ['y', 'm', 'c', 'r', 'g', 'b', 'k']
    shape = choice(shapes)
    color = choice(colors)
    for i, index in enumerate(self.index_of_position):
        if self.position[i] != self.position[i-1] and i > 0:
            m = (self.parent_signal[index]-self.parent_signal[index - 1])
            c = self.parent_signal[index] - m*index
            y += [self.position[i-1]]
            x += [(y[-1] - c)/m]
            y += [self.position[i]]
            x += [(y[-1] - c)/m]
        else:
            x += [index]
            y += [self.position[i]]
    axes.plot(x, y, color)
    axes.plot(x[-1], y[-1], color + shape)
```

APPENDICES

```
axes.plot(x[0], y[0], color + shape)
def isvalley(index, signal):
    try:
        if signal[index+1] > signal[index]:
            return True
    except IndexError:
        if signal[index-1] > signal[index]:
            return True
    return False
def eval_peaks(peaks_extremes, sig):
    """
    Rainflow codes for the evaluation of valleys
    INPUT
    peaks_extreme: List containing only Valley objects
    sig: Original list or tuple from which valleys_extreme was created
    OUTPUT
    None
    """
    print('Inside peak function')
    for a, peak in enumerate(peaks_extremes):
        print('Peak at index {}'.format(peak.index))
        con_sigs = sig[peak.index+1:]
        for con_sig, _ in enumerate(con_sigs):
            if not peak.terminate:
                peak.index_of_position += [con_sig+peak.index+1]
                if not isvalley(con_sig+peak.index + 1, sig):
                    peak.position += [peak.position[-1]]
                    peak.pos_dict[peak.index_of_position[-1]] = peak.position[-1]
                if con_sigs[con_sig] >= peak.value:
                    peak.terminate = True
```

APPENDICES

```
        break
    else:
        c_peaks = peaks_extremes[:a]
        max_ind = max(peak.index_of_position)
        if con_sigs[con_sig] < peak.position[-1]:
            peak.pos_dict[peak.index_of_position[-1]]
                = con_sigs[con_sig]
            peak.position += [con_sigs[con_sig]]

    else:
        peak.pos_dict[peak.index_of_position[-1]]
            = peak.position[-1]
        peak.position += [peak.position[-1]]
        for c_peak in c_peaks[::-1]:
            if max(c_peak.index_of_position) >= max_ind:
                c_peak_pos = c_peak.pos_dict[max_ind-1]
                peak.terminate = True if c_peak_pos > \
                    peak.position[-1] else peak.terminate
                peak.position[-1] = c_peak_pos if c_peak_pos > \
                    peak.position[-1] else peak.position[-1]
                peak.pos_dict[peak.index_of_position[-1]] = c_peak_pos if \
                    c_peak_pos > peak.position[-1] else peak.position[-1]
            else:
                break
    print('Exiting Peak Function')
```

```
def eval_valleys(valleys_extreme, sig):
```

```
    ""
```

Rainflow codes for the evaluation of valleys

INPUT

valleys_extreme: List containing only Valley objects

APPENDICES

sig: Original list or tuple from which valleys_extreme was created

OUTPUT

None

"""

```
print('Inside Valleys function')
```

```
# Loop through all valley objects
```

```
for a, valley in enumerate (valleys_extreme):
```

```
    print('Valley at index {}'.format(valley.index))
```

```
    # Considers signals that come after selected valley
```

```
    con_sigs = sig[valley.index+1:]
```

```
    # Loops through the selected signal
```

```
    for con_sig, _ in enumerate(con_sigs):
```

```
        if not valley.terminate: # While the cycle hasn't ended
```

```
            # Jump to the next extrema and append the index of the next extrema to the  
            valley's index property
```

```
            valley.index_of_position += [con_sig+valley.index+1]
```

```
            # Check to see if the next extrema is a valley
```

```
            if isvalley(con_sig+valley.index + 1, sig):
```

```
                # Append the value of the next extrema to the position property of the  
                valley
```

```
                valley.position += [valley.position[-1]]
```

```
                # Also append it to the post_dict dictionary with the index as  
                key
```

```
                valley.pos_dict[valley.index_of_position[-1]
```

```
                    ] = valley.position[-1]
```

```
                # Terminate if the value of the current valley is greater than the value of  
                the considered extrema
```

```
                if con_sigs[con_sig] <= valley.value:
```

```
                    valley.terminate = True
```

```
                    break
```

```
            else: # If the next extrema is a peak
```

```
                c_valleys = valleys_extreme[:a] # Select only valleys that come before  
                valley being analysed
```

```
                max_ind = max(valley.index_of_position)
```

APPENDICES

```
if con_sigs[con_sig] > valley.position[-1]:
    valley.pos_dict[valley.index_of_position[-1]
                    ] = con_sigs[con_sig]
    valley.position += [con_sigs[con_sig]]
else:
    valley.pos_dict[valley.index_of_position[-1]
                    ] = valley.position[-1]
    valley.position += [valley.position[-1]]
for k in c_valleys[::-1]:
    if max(k.index_of_position) >= max_ind:
        k_pos = k.pos_dict[max_ind-1]
        valley.terminate = True if k_pos <= \
            valley.position[-1] else valley.terminate
        valley.position[-1] = k_pos if k_pos <= \
            valley.position[-1] else valley.position[-1]
        valley.pos_dict[valley.index_of_position[-1]] = k_pos if k_pos \
            <= valley.position[-1] else valley.position[-1]
    else: # If the valley has terminated, skip the entire loop
        break
print('Exiting Valley function')
def rainflow(sig):
    """
    Find and plot rainflow parameters
    INPUTS
    List or tuple sig: List or tuple containing series signal
    OUTPUTS:
    Tuple sig: Original inputted list
    List peaks: A list containing
    """
    new_sig = []
    for i, signal in enumerate(sig):
        try:
```

APPENDICES

```
# Attempt to round of to a 1 decimal place
new_sig += [round(float(signal), 1)]
except ValueError:
    pass
# Convert signal into a tuple of extrema
sig = tuple(sig2ext(new_sig))

# Create a Valley and Peak objects from the extrema signal
valleys = []
peaks = []
for i, value in enumerate(sig[:-1]):
    if isvalley(i, sig):
        valleys += [Valley(value, i, sig)]
    else:
        peaks += [Peak(value, i, sig)]
# Run independent rainflow code of separate threads
p = Thread(target=eval_peaks, args=(peaks, sig))
v = Thread(target=eval_valleys, args=(valleys, sig))
p.start()
v.start()
# Join the two threads to the main thread
p.join()
v.join()
return sig, peaks, valleys
def sig2ext(sig):
    """
    Returns a list of all local minima and maxima in input list
    Inputs: A list or a tuple of signals
    Output: A list of local extrema signals
    This code is a slightly modified form which only accepts one signal
    """
    w1 = np.diff(sig)
```

APPENDICES

```
w = [True] + [True if w1[i]*w1[i+1] <=
               0 else False for i in range(len(w1)-1)] + [True]
ext = [sig[i] for i, val in enumerate(w) if val is True]
```

```
w1 = np.diff(ext)
w = [True] + [False if w1[i] == 0 and w1[i+1] ==
               0 else True for i in range(len(w1)-1)] + [True]
ext1 = [ext[i] for i, val in enumerate(w) if val is True]
```

```
ext = ext1
w = [True] + [False if ext[i] == ext[i+1]
               else True for i in range(len(ext)-1)]
ext1 = [ext[i] for i, val in enumerate(w) if val is True]
ext = ext1
```

```
del ext1
```

```
if len(ext) > 2:
```

```
    w1 = np.diff(ext)
    w = [True] + [True if w1[i]*w1[i+1] <
                  0 else False for i in range(len(w1)-1)] + [True]
```

```
    ext1 = [ext[i] for i, val in enumerate(w) if val is True]
```

```
    ext = ext1
```

```
    del ext1
```

```
return ext
```

APPENDICES

ALGORITHM FOR COMPUTING TEMPERATURE DWELLS

```
% import data and find size
data = xlsread('C:\Users\Kurt\Documents\MATLAB\editedData.xlsx', 2);
data12 = data(1:287, :);
data13 = data(288:652, :);
data14 = data(653:1017, :);
data15 = data(1018:end, :);

dim = size(data);

% find daily maximum and daily minimum
maximums = zeros(dim(1), 1);
minimums = zeros(dim(1), 1);

for i = 1 : dim(1)
    maximums(i) = max(data(i, :));
    minimums(i) = min(data(i, :));
end

% - find maximum year by year data (segregate data into year by year)
max12 = max(max(data12));
max13 = max(max(data13));
max14 = max(max(data14));
max15 = max(max(data15));

n12 = size(data12);
n13 = size(data13);
n14 = size(data14);
n15 = size(data15);

% Clear isnan values
```

APPENDICES

```
for i = 1 : dim(1)
    for j = 1 : dim(2)
        if isnan(data(i,j))
            data(i,j) = (data(i+1,j)+data(i-1,j))/2;
        end
    end
end

% - find daily range (maximum - minimum)
rangeData = range(data');
range12 = range(data12');
range13 = range(data13');
range14 = range(data14');
range15 = range(data15');

% - find the rate in degree Celcius per hour for every 5 minutes
% ratesPer5mins = zeros(dim(1)*dim(2)-1 : 1);
% transData = data';
%
% for i = 1 : dim(1)*dim(2)-1
%     ratesPer5mins(i) = (transData(i+1) - transData(i))*60/5;
% end

% - split data into 2 from the max and plot cooling rate and heating rate
% - find the cooling in 5 minute intervals with degree Celcius per hour
% units (ie multiply by 60) then we can plot the data
cooling = cell(dim(1), 1);
heating = cell(dim(1), 1);
heatrate = cell(dim(1), 1);
coolrate = cell(dim(1), 1);
for i = 1:dim(1)
    [val, idx] = max(data(i,:));
```

APPENDICES

```
heating{i} = data(i, 1:idx);
heatrate{i} = diff(heating{i})*60/5;
cooling{i} = data(i, idx:end);
coolrate{i} = diff(cooling{i})*60/5;
end

% - We need ramp rates per year
heatramp12 = [];
coolramp12 = [];
for i = 1:n12(1)
    heatramp12 = horzcat(heatramp12, heatrate{i});
    coolramp12 = horzcat(coolramp12, coolrate{i});
end
averageHeatRate12 = mean(heatramp12);
averageCoolRate12 = mean(coolramp12);
% heatramp12 = heatramp12(heatramp12~=0.000001)';
% coolramp12 = coolramp12(coolramp12~=0.000001)';

heatramp13 = [];
coolramp13 = [];
for i = n12(1)+1:n12(1)+n13(1)
    heatramp13 = horzcat(heatramp13, heatrate{i});
    coolramp13 = horzcat(coolramp13, coolrate{i});
end
averageHeatRate13 = mean(heatramp13);
averageCoolRate13 = mean(coolramp13);
% heatramp13 = heatramp13(heatramp13>0.000001)';
% coolramp13 = coolramp13(coolramp13>0.000001)';

heatramp14 = [];
coolramp14 = [];
for i = n12(1)+n13(1)+1:n12(1)+n13(1)+n14(1)
```

APPENDICES

```
    heatramp14 = horzcat(heatramp14, heatrate{i});
    coolramp14 = horzcat(coolramp14, coolrate{i});
end
averageHeatRate14 = mean(heatramp14);
averageCoolRate14 = mean(coolramp14);
% heatramp14 = heatramp14(heatramp14>0.000001);
% coolramp14 = coolramp14(coolramp14>0.000001);
heatramp15 = [];
coolramp15 = [];
for i = n12(1)+n13(1)+n14(1)+1:n12(1)+n13(1)+n14(1)+n15(1)
    heatramp15 = horzcat(heatramp15, heatrate{i});
    coolramp15 = horzcat(coolramp15, coolrate{i});
end
averageHeatRate15 = mean(heatramp15);
averageCoolRate15 = mean(coolramp15);
% heatramp15 = heatramp15(heatramp15>0.000001);
% coolramp15 = coolramp15(coolramp15>0.000001);
xlswrite('Absolute Cooling Rate.xlsx', horzcat(coolramp12(coolramp12<0),
heatramp12(heatramp12<0)), 1)
xlswrite('Absolute Cooling Rate.xlsx', horzcat(coolramp13(coolramp13<0),
heatramp13(heatramp13<0)), 2)
xlswrite('Absolute Cooling Rate.xlsx', horzcat(coolramp14(coolramp14<0),
heatramp14(heatramp14<0)), 3)
xlswrite('Absolute Cooling Rate.xlsx', horzcat(coolramp15(coolramp15<0),
heatramp15(heatramp15<0)), 4)

xlswrite('Absolute Heating Rate.xlsx', horzcat(coolramp12(coolramp12>0),
heatramp12(heatramp12>0)), 1)
xlswrite('Absolute Heating Rate.xlsx', horzcat(coolramp13(coolramp13>0),
heatramp13(heatramp13>0)), 2)
xlswrite('Absolute Heating Rate.xlsx', horzcat(coolramp14(coolramp14>0),
heatramp14(heatramp14>0)), 3)
xlswrite('Absolute Heating Rate.xlsx', horzcat(coolramp15(coolramp15>0),
heatramp15(heatramp15>0)), 4)
```

APPENDICES

```
xlswrite('Range.xlsx', rangeData', 1)
```

```
xlswrite('Range.xlsx', range12', 2)
```

```
xlswrite('Range.xlsx', range13', 3)
```

```
xlswrite('Range.xlsx', range14', 4)
```

```
xlswrite('Range.xlsx', range15', 5)
```

KNUST



APPENDICES

APPENDIX B

MAPDL COMMANDS FOR ANSYS FEA

OUTRES,ERASE

OUTRES,BASIC

CUTCONTROL, CRPLIMIT, 0.25, EXPRATIO

CUTCONTROL, PLSLIMIT, 0.15

CUTCONTROL, CRPLIMIT, 5000, IMPRATIO

CUTCONTROL,CRPLIMIT , 5000, STSLIMIT

CUTCONTROL,CRPLIMIT , 5000, STNLIMIT

SHPP,OFF,,NOWARN

ANSYS SOLUTION OPTIONS

PROBLEM DIMENSIONALITY.....3-D

DEGREES OF FREEDOM..... UX UY UZ

ANALYSIS TYPE.....STATIC (STEADY-STATE)

OFFSET TEMPERATURE FROM ABSOLUTE ZERO 273.15

EQUATION SOLVER OPTION.....SPARSE

PLASTIC MATERIAL PROPERTIES INCLUDED.....YES

CREEP MATERIAL PROPERTIES INCLUDED.....YES

NEWTON-RAPHSON OPTION.....FULL

GLOBALLY ASSEMBLED MATRIX.....SYMMETRIC

Small sliding logic is assumed

Contact algorithm: Augmented Lagrange method

Contact detection at: Gauss integration point

Aggressive variation of contact stiffness is activated,

Contact stiffness factor FKN 0.10000

The resulting initial contact stiffness 0.19027E+13

Default penetration tolerance factor FTOLN 0.10000

The resulting penetration tolerance 0.14681E-03

Default opening contact stiffness OPSF will be used.

Default tangent stiffness factor FKT 1.0000

Default elastic slip factor SLTOL 0.50000E-02

The resulting elastic slip tolerance 0.24469E-04

Update contact stiffness at each iteration

Default Max. friction stress TAUMAX 0.10000E+21

Average contact surface length 0.48938E-02

APPENDICES

Average contact pair depth 0.14681E-02
User defined pinball region PINB 0.20000E-02
Initial penetration/gap is excluded.
Bonded contact (always) is defined.

ANSYS LOAD STEP OPTIONS

LOAD STEP NUMBER..... 2
TIME AT END OF THE LOAD STEP..... 2940.0
AUTOMATIC TIME STEPPING..... ON
INITIAL NUMBER OF SUBSTEPS..... 5
MAXIMUM NUMBER OF SUBSTEPS..... 1000
MINIMUM NUMBER OF SUBSTEPS..... 1
MAXIMUM NUMBER OF EQUILIBRIUM ITERATIONS.... 15
STEP CHANGE BOUNDARY CONDITIONS..... NO
TERMINATE ANALYSIS IF NOT CONVERGED.....YES (EXIT)
CREEP CRITERION..... 1.0000
CONVERGENCE CONTROLS
LABEL REFERENCE TOLERANCE NORM MINREF
F 5000. 0.5000E-02 2 -1.000
COPY INTEGRATION POINT VALUES TO NODE.....YES, FOR ELEMENTS
WITH
ACTIVE MAT. NONLINEARITIES
PRINT OUTPUT CONTROLS.....NO PRINTOUT
DATABASE OUTPUT CONTROLS
ITEM FREQUENCY COMPONENT
ALL NONE
NSOL ALL
RSOL ALL
NLOA ALL
STRS ALL
EPEL ALL
EPPL ALL
EPTH ALL
EPCR ALL

